

---

# **Deep learning for satellite imagery:**

## **A climatology of tropical cyclone rainband morphology**

---

ANNA VAUGHAN

Masters Thesis submitted as part of the M.Sc. degree in the School of Earth Sciences, The  
University of Melbourne

December 3, 2018

I certify that this thesis contains less than 25,000 words

Anna Vaughan

# Acknowledgements

I would first like to thank my supervisors Professor Kevin Walsh and Dr Jeff Kepert for their guidance with this project over the past two years. Their encouragement, patience and generosity with their knowledge and time has contributed immensely to this work.

Thank you to Professor Chun-Chieh Wu and everyone at the Typhoon Dynamics Research Centre (TDRC) at National Taiwan University (NTU) for their assistance with this project and for inspiring me to pursue this degree in Meteorology after studying at NTU in 2016. I am particularly grateful for the opportunity to visit the TDRC in February 2018. The knowledge I gained during this visit was invaluable to this thesis.

This work would not have been possible without the generosity of a number of people and organisations in sharing software and data. I would particularly like to thank Professor Wayne Hayes at the University of California, Irvine and Dr Darren Davis at Google for generously allowing me to use the SpArcFiRe software as part of this project.

I would like to acknowledge generous financial support from the University of Melbourne in the form of a Future Generations Scholarship. Both financial support and the provision of educational and training activities from the Australian Research Council Centre for Climate System Science (ARCCSS) have contributed greatly to this project.

# Abstract

Secondary eyewall formation is a common process of structural change in tropical cyclones. Previous work has qualitatively suggested that a secondary eyewall forms from the axisymmetrisation of pre-existing spiral rainbands, in particular the stationary banding complex. However, the evolution of rainband morphology prior to secondary eyewall formation has not been quantified. Limited progress in this area is primarily related a lack of objective methods to describe TC banding structure, and subsequent lack of understanding of the climatological morphology of rainbands.

In this study, we construct an objective system for classifying the structure of a tropical cyclone from 85-92GHz passive microwave satellite imagery. A fully automated implementation of this technique is developed using a novel combination of a convolutional neural network and unsupervised clustering. This classification system is used to compile a climatology of rainband morphology in all tropical cyclones globally between 2012 and 2014, and quantify changes in morphology prior to secondary eyewall formation.

We find that a stationary banding complex is present in only 37% of passive microwave images. The geometry of the principal rainband varies widely between storms, with crossing angles (azimuthal extents) ranging from 0.02 to 53.40 degrees (0.49 to 9.89 radians). Of 41 secondary eyewall formation events in the climatology, 79% of develop from pre-existing stationary banding complexes. Within 6 hours of secondary eyewall formation, the rainband crossing angle (azimuthal extent) is preferentially lower (higher) than the sample average.

The impact of the large scale environmental conditions at each stage of this axisymmetrisation process is discussed. These results are applied together with the rainband climatology to develop a statistical model using gradient boosted decision tree learning to predict secondary eyewall formation events. This model has a probability of detection of 66% and false alarm rate of 2%, providing a skilful forecasting tool.

# Contents

## 1 Introduction

- 1.1 Motivation
- 1.2 Aims
- 1.3 Thesis Structure

## 2 Background and Literature Review

- 2.1 TC structure
- 2.2 Rainbands
  - 2.2.1 Terminology
  - 2.2.2 IC rainbands
  - 2.2.3 OC rainbands
  - 2.2.4 The principal rainband (PRB)
  - 2.2.5 Mesoscale convective complexes
- 2.3 Secondary Eyewall Formation (SEF)
  - 2.3.1 Definition and kinematic structure
  - 2.3.2 Dynamics
- 2.4 Classifying TC structure
- 2.5 Environmental conditions and TC structure
- 2.6 Significance and innovation

## 3 Datasets

- 3.1 Observing TC structure
- 3.2 PMW dataset
  - 3.2.1 PMW data sources
  - 3.2.2 PMW data processing
  - 3.2.3 Interpretation of PMW images
- 3.3 Environmental data
  - 3.3.1 SHIPS
  - 3.3.2 Shear profiles

## 4 Classifying TC Structure

- 4.1 Definitions
  - 4.1.1 TC scale convective structure
  - 4.1.2 Secondary Eyewalls
  - 4.1.3 Rainbands
  - 4.1.4 SBCs
- 4.2 Classification Scheme
- 4.3 Validation dataset
- 4.4 Automated Classification
  - 4.4.1 Image processing for TCs
  - 4.4.2 Automated classification
  - 4.4.3 Output
- 4.5 Verification
- 4.6 Conclusion

## 5 Results chapter: Climatology of rainband morphology

- 5.1 Dataset
- 5.2 Storm scale classifications
- 5.3 TC scale convective classifications
- 5.4 Rainband geometry
  - 5.4.1 Logarithmic spiral fit verification
  - 5.4.2 Crossing angle
  - 5.4.3 Azimuthal extent
- 5.5 SEF
  - 5.5.1 Rainbands prior to SEF
- 5.6 Summary

## 6 Results chapter: Impact of Environmental Conditions on Rainband Evolution

- 6.1 Methodology
- 6.2 Dynamics
  - 6.2.1 TC scale Convective structure
  - 6.2.2 Principal rainband formation (PRBF)
  - 6.2.3 PRB geometry
  - 6.2.4 SEF
- 6.3 A Statistical Model for SEF
  - 6.3.1 Model description
  - 6.3.2 SEF Model
- 6.4 Conclusion

## 7 Conclusion and Future Work

- 7.1 Conclusion
- 7.2 Application of Methodology
  - 7.2.1 Satellite dataset
  - 7.2.2 Structural classification methodology
- 7.3 Future work
  - 7.3.1 Extension of the climatology
  - 7.3.2 Numerical simulations
  - 7.3.3 High resolution observations

## Appendices

### A Multichannel satellite products

- A.1 Multichannel satellite products
- A.2 Observing convective structure

### B Shear Profiles

### C Mask-RCNN training

- C.1 Network overview
- C.2 Network tuning

### D SpArcFiRe clustering software

- D.1 SpArcFiRe
- D.2 Alterations to the original clustering scheme

# List of Figures

- 2.1 Schematic of different rainband types showing (a) A TC with IC spiral rainbands, an OC rainband and a mesoscale convective complex. (b) A TC with a SBC. (c) A TC with a SE and spiral banding.
- 2.2 Schematic of the terminology used in this study for different parts of the SBC.
- 2.3 Schematic of the structure of a PRB. (a) Precipitation structure of a typical PRB, showing convective cells upwind and stratiform precipitation downwind, together with a tangential jet oriented along the band. (b) Cross section of PRB structure showing the overturning circulation, with the IED and LLD (dashed arrows), radial circulation (grey arrow) and tangential jet (J). From Didlake et al. (2009).
- 2.4 Schematic of SBC formation, showing convection developing in the downshear right quadrant of the tilted vortex and being cyclonically advected to the downshear left. Low level shading represents the distortion of the equivalent potential temperature field, and dashed contours the positive vorticity anomalies associated with the vortex tilt. From Riemer (2016).
- 3.1 Example of clear concentric eyewalls together with a PRB viewed on 89GHz PMW imagery in Hurricane Genevieve at 19:53UTC on the 08/08/2014.
- 4.1 Flow chart of the TC classification process.
- 4.2 Examples of TCs classified in each of the four structural groups. (A) No bands type, showing from left to right cases with (i) convection with no clear banding structure, (ii) eyewall with no clear banding structure and (iii) annular configuration. (B) No classification type, showing three examples of cases with irregular convection and no clear eyewall structure. (C) Sheared type, showing three examples of TCs with convection confined to 180° on one side of the TC. (D) Rainbands type, showing three cases with clearly defined spiral banding structure.
- 4.3 Four examples of SEs on 89GHz PMW imagery.
- 4.4 Example of a triple concentric eyewall configuration, with concentric eyewalls indicated by white dashed lines observed in Typhoon Bolaven at 23:29UTC on the 25/08/2012.

- 4.5 Cases with clear spiral structure but poorly defined individual rainbands. Clockwise from top left. Example of a rainband merging with an upwind mesoscale convective complex. Example of clear spiral banding structure within which it is difficult to isolate the extent of individual bands. Two examples of sub banding structure within a PRB.
- 4.6 Examples of typical SBCs included in the PMW dataset.
- 4.7 Flow chart outlining the rainband morphology classification scheme.
- 4.8 Example of the distinction between the eyewall (within the innermost dashed circle), IC (within the second dashed circle) and OC (outside of both circles) rainband regions.
- 4.9 Example of a stationary banding complex with (A) one PRB and one secondary rainband identified and (B) the ICA parameter shown as red dashed lines.
- 4.10 Example of the MATLAB implementation of the command line classification process on an AMSRE image of Hurricane Marie (2014) at 09:03UTC on the 23/08/2014.
- 4.11 Similarities in spiral structure between a TC and spiral galaxy M51. Image retrieved from <https://www.nasa.gov/feature/goddard/2017/messier-51-the-whirlpool-galaxy>
- 4.12 Overview of the automated classification technique.
- 4.13 Image of Typhoon Megi at 09:13UTC on the 26/09/2016 used to demonstrate the stages of the automated classification system.
- 4.14 Example of Mask-RCNN output for identifying an eyewall and SE in the example image. Eyewall masks and bounding boxes displayed using code adapted from Ye (2018).
- 4.15 The three stages of CLAHE pre-processing, from left to right: the original image, output after the first application of the CLAHE filter and output after the second application of the CLAHE filter.
- 4.16 Stages of image pre-processing, showing (1) the original image, (2) original image R channel after eyewall masking using mask output from mask-RCNN, (3) resized image, (4) after first application of CLAHE, (5) after second application of CLAHE and finally (6) the preprocessing output after unsharp masking and thresholding.
- 4.17 Examples of successful identifications of (a) a small eyewall and (b) A large eyewall and (c) example of a false negative with a banding eyewall. Eyewall masks and bounding boxes are displayed using software adapted from Ye (2018).

- 4.18 Examples of MASK-RCNN output for (a) a large elliptical SE, (b) an incomplete SE, (c) a classical circular SE, (d) example of false negative with indistinct inner eyewall, (e) example of a false positive in a PRB with a symmetric moat, (f) example of model successfully rejecting a moat as a SE. Eyewall masks and bounding boxes are displayed using software adapted from (Ye, 2018).
- 4.19 Examples of successful rainband segmentations. Different rainbands are shown in different colours using code adapted from the SpArcFiRe project (Davis and Hayes 2014). Images show (L-R original 89GHz satellite image, cropped and masked image prior to preprocessing to demonstrate rainband locations and output of the rainband clustering. Examples show (a) successful clustering of a poorly defined bands within a SBC, (b) successful identification of a lone PRB and (c, d) successful segmentation of multiple spiral bands.
- 4.20 Examples demonstrating limitations of the clustering scheme. As in Figure 4.18, in clustering images each rainband is identified by a different colour, with clustering plots produced using the SpArcFiRe software (Davis and Hayes, 2014). For each case, images show (L-R original 89GHz satellite image, cropped and masked image prior to preprocessing to demonstrate rainband locations and output of the rainband clustering. Images show examples of (a) difficulties in accurately identifying rainbands where the geometry varies significantly along the band, (b) a rainband with highly irregular geometry that is not correctly identified, (c) poorly defined diffuse rainbands that are not accurately identified.
- 5.1 Tracks of the 106 TCs included in the sample, together with approximate locations of the basins considered in this climatology. Tracks are taken from the IBTrACS dataset (Knapp et al. 2010).
- 5.2 TC scale convective classifications for the climatology, showing the number of PMW images classed as no classification, no bands, sheared and bands.
- 5.3 Latitude distributions (taken from IBTrACS) for the no classification, no bands, sheared and bands groups.
- 5.4 Percentages of PMW images classified as no classification, no bands, sheared and bands in the NATL, EPAC, WPAC and SHEM basins.
- 5.5 Geographic locations of PRBF events included in the sample, marked in red. Locations taken from the IBTrACS dataset linearly interpolated to the time of the first PMW overpass classified as containing a PRB.
- 5.6 Scatter plot showing the relationship between crossing angle ( $\aleph$ ) and azimuthal extent ( $\Psi$ ) for all rainbands in the sample.
- 5.7 Crossing angle ( $\aleph$ ) distribution for all bands (top), together with (a) Example of a TC with crossing angle  $4.59^\circ$  and (b) Example of a TC with a crossing angle of  $49^\circ$ .

- 5.8 Crossing angle distributions for the IC, OC, PRB and ICA groups.
- 5.9 Crossing angle ( $\aleph$ ) distributions for different band types in the NATL, EPAC, WPAC and SHEMA basins for the IC, OC and PRB groups, together with the ICA parameter and all bands group. Note the different scales for different band types.
- 5.10 Crossing angle ( $\aleph$ ) distributions by basin for PRB (Left) and ICA (Right).
- 5.11 Azimuthal extent ( $\Psi$ ) distribution for all bands (top), together with (a) Example of a TC with azimuthal extent 7.01 radians and (b) Example of a TC with an azimuthal extent of 3.12 radians.
- 5.12 Azimuthal extent ( $\Psi$ ) distribution for the IC, OC, PRB and ICA groups.
- 5.13 Azimuthal extent ( $\Psi$ ) distributions for different band types in the NATL, EPAC, WPAC and SHEMA basins for the IC, OC and PRB groups, together with the ICA parameter and all bands group. Note the different scales for different band types.
- 5.14 Azimuthal extent ( $\Psi$ ) distributions by basin for PRB (Left) and ICA (Right).
- 5.15 Locations of the 41 SEF events included in the sample. Locations are taken from IBTrACS interpolated to the time of the first PMW overpass containing the SE.
- 5.16 KDE probability plots showing distributions of ICA parameter geometry for (from left to right): Images 0-6 hours prior to SEF, images 6-12hrs prior to SEF, all images with a PRB that do not evolve into a SE within 24hrs.
- 6.1 Examples of differences in distributions in SHIPS parameters between TC scale convective classifications. (a,b) No classification compared to rainbands for VMAX. (c,d) No bands compared to rainbands for VMPI. (e,f) No bands compared to rainbands for RSST. (g,h) Sheared compared to rainbands for SHRD.
- 6.2 SHIPS histograms comparing the PRBF and no PRBF groups for (a, b) VMAX, (c, d) VMPI, (e, f) PSLV, (g, h) CD26, (i, j) R000.
- 6.3 Mean shear profiles for the (a) u-component and (b) v-component of the wind relative to the 850-200hPa deep layer shear vector for the no PRBF group (blue) and PRBF group (red).
- 6.4 Deep layer shear relative mean direction at different heights for (left) PRBF and (right) No PRBF.
- 6.5 Schematic of flux asymmetries in the vortex under the influence of VWS for (a) counter aligned low level environmental flow and (b) aligned low level environmental flow. The vortex circulation is shown in black, low level environmental flow in blue and the deep layer shear vector in red. Positive (negative) surface flux anomalies are indicated with red (blue) shading.
- 6.6 SHIPS histograms comparing cases with crossing angles in the first quartile (left) fourth quartile (right) for (a, b) VMAX, (c, d) SHRD and (e, f) R000.

- 6.7 SHIPS histograms comparing cases with PRB azimuthal extent in the first quartile (left) and fourth quartile (right) for (a, b) VMAX, (c, d) VMPI, (e, f) SHRD and (g, h) RHRI.
- 6.8 Mean shear profiles for the (a) u-component and (b) v-component of the wind relative to the 850-200hPa shear vector for the low azimuthal extent group (blue) and high azimuthal extent group (red).
- 6.9 Schematic of different azimuthal extents for (a) low level flow to the right of the deep layer shear and (b) low level flow to the left of the deep layer shear. The vortex circulation is shown in black, low level environmental flow in blue and the deep layer shear vector in red. Positive (negative) surface flux anomalies are indicated with red (blue) shading.
- 6.10 SHIPS histograms comparing the SEF (left) and no SEF (right) groups for (a, b) VMAX, (c, d) D200, (e, f) SHRD, (g, h) RHRI.
- 6.11 Macro-F1 score evolution for SEF model tuning with tree depths ranging from 3-6 and ensemble sizes from 50-500.
- 6.12 SHAP values for the SHIPS predictors, ICA crossing angle (ca) and ICA azimuthal extent (az) in the SEF model. Graphic generated using the python SHAP library Lundberg and Lee (2017).
- 6.13 SHAP interaction values for ICA crossing angle (ca) and azimuthal extent (az). Graphic generated using the python SHAP library Lundberg and Lee (2017)
- 6.14 Example of the SEF model correctly predicting two SEF events in Typhoon Jelawat (2012), showing (top) model predictions of the probability of SEF occurring within 24 hours as a function of time, and (bottom) selected PMW images corresponding to different predictions. Blue marks indicate the time of each satellite overpass, red lines indicate the time of SEF and red shading the duration of the SE. On the PMW images, white dashed lines indicate the extent of the PRB or SE.
- 7.1 WRF output showing evolution towards a secondary eyewall in the control simulation. Fields are model calculated reflectivity in dBz at the lowest model level.
- 7.2 Example of a composite radar image for normalised downshear left radar reflectivity (dBz) at 0-6 hours prior to SEF.
- A.1 AMSR-2 satellite images of Typhoon Neptak at 04:02UTC on the 0507/2016, showing from left to right, mutichannel 89GHz, multichannel 37GHz and novel four channel composite.
- A.2 Example of clear concentric eyewalls together with a PRB viewed on PMW imagery in Hurricane Genevieve at 19:53 on the 08/08/2014.

- A.3 Example of poor agreement between radar and satellite for outer rainband and SE identification. Images are of typhoon Nepartak at 03:40UTC on 07/07/2016 as seen on land based radar (left) and 89GHz SSMI (right). Both the outer rainbands and the SE observed on the radar image are not evident on the coarse resolution SSMI image.
  - A.4 Example of rainbands visible on multichannel imagery but not on 89GHz imagery in hurricane Matthew at 18:43UTC on 02/10/2016.
  - A.5 Example of a warm rainband observed on an AMSR-2 image that has no signal at the 89GHz wavelength.
- B.1 Example of vortex removal with  $k = 18$  truncation for Hurricane Gonzalo (2014), at 26.3W, 28.3N on 15/10/2014 at 18:00UTC, showing the original ERAI 850hPa reanalysis field (left) and corresponding field with the vortex removed after low pass filtering (right).
  - B.2 Deep layer shear magnitude time series calculated from ERA interim reanalysis for TC Jasmine (2012) at different wavenumber truncations.
- C.1 Mask-RCNN network architecture.
  - C.2 Resnet 50 heads only training and validation losses. Values are smoothed with a 0.8 strength filter as used in Tensorboard.
  - C.3 Resnet 50 all layers training and validation losses. Values are smoothed with a 0.8 strength filter as used in Tensorboard.
  - C.4 Resnet 100 heads only training and validation losses. Values are smoothed with a 0.8 strength filter as used in Tensorboard.
  - C.5 Resnet 100 all layers training and validation losses. Values are smoothed with a 0.8 strength filter as used in Tensorboard.

# List of Tables

- 3.1 Specifications of the PMW sensors and satellites included in the dataset
- 3.2 The 15 SHIPS predictors included in the analysis. Descriptions adapted from Regional and Mesoscale Meteorology Branch (2018).
- 4.1 Output from the classification algorithm, showing each rainband in a different colour, together with the crossing angle and azimuthal extent of each band. Rainband clusters are shown using software adapted from the SpArcFiRe project (Davis and Hayes 2014). Eyewall masks and bounding boxes are displayed using software adapted from (Ye, 2018).
- 4.2 Validation statistics for Mask-RCNN eyewall identification.
- 4.3 Validation statistics for rainband identification.
- 5.1 Sample sizes for the climatology, showing the total numbers of TCs, PMW images, total rainbands, SBCs, IC and OC bands for each of the five basins analysed.
- 5.2 Coincidence of different banding types including IC only, OC only, IC and OC (IC+OC) and neither inner or OC (None) for images with and without a SBC.
- 5.3 Mean RMS errors (km) for logarithmic spiral fits for different band types.
- 5.4 Number of TCs, individual SEF events and total PMW overpasses included in each time period prior to SEF.
- 5.5 Median ICA crossing angle ( $\aleph$ ), azimuthal extent ( $\Psi$ ) and percentage of images with an SBC at different times prior to SEF.
- 6.1 Differences in statistically significant SHIPS predictors between the PRBF and no PRBF groups.
- 6.2 Differences in statistically significant SHIPS predictors between the low crossing angle and high crossing angle groups.
- 6.3 Differences in statistically significant SHIPS predictors between the low azimuthal extent and high azimuthal extent groups.
- 6.4 Differences in statistically significant SHIPS predictors between the SEF and no SEF groups.

- 6.5 Confusion matrices for SEF models using a dummy classifier, the KS09 classifier, the new model with rainband predictors excluded and the new model with all predictors.
- C.1 Losses at the optimum network configuration for each of the four backbone options. All loss values are taken at the optimum epoch for  $valloss$ , which was the point at which the validation loss began to increase, indicating overfitting.

# List of Abbreviations

TC	TC
SEF	SEF
ERC	Eyewall Replacement Cycle
SBC	Stationary Banding Complex
PRB	Principal Rainband
PRBF	Principal Rainband Formation
IC	Inner Core
OC	Outer Core
PV	(Ertel) Potential Vorticity
PMW	Passive Microwave
VRW	Vortex Rossby Wave
SDW	Shear-Induced Deformation Wave
RMW	Radius of Maximum Winds
TRMM	Tropical Rainfall Measuring Mission
TMI	TRMM Microwave Imager
AMSR-2	Advanced Microwave Scanning Radiometer 2
GCOMW-1	Global Change Observation Mission for Water
SSMI	Special Sensor Microwave Imager
SSMIS	Special Sensor Microwave Imager/Sounder
DMSP	Defence Meteorological Satellite Program

PCT	Polarisation Corrected Temperature
IBTrACS	International Best Tracks for Climate Stewardship
PPS	Precipitation Processing System
SHIPS	Statistical Hurricane Intensity Prediction Scheme
NCEP-FNL	National Centres for Environmental Prediction Final (reanalysis)
ERA-I	ERA-Interim (reanalysis)
CLAHE	Contrast Limited Adaptive Histogram Equalisation
CNN	Convolutional Neural Network
Mask-RCNN	Mask Region Proposal Convolutional Neural Network
FPN	Feature Pyramid Network
ROI	Region Of Interest
SpArcFiRe	Spiral Arc Fitting and Reporting Algorithm
TP	True Positives
FP	False Positives
TN	True Negatives
FN	False Negatives
POD	Probability of Detection
FAR	False Alarm Rate
SHAP	SHapely Additive exPlanations
XGBoost	eXtreme Gradient Boosting
SMOTE	Synthetic Minority Oversampling Technique
RMSE	Root Mean Squared Error
KS-test	Kolmogorov - Smirnov test
MWU-test	Mann-Whitney-U test
NATL	North Atlantic
EPAC	Eastern Pacific

WPAC Western Pacific

SHEM Southern Hemisphere

# Chapter 1

## Introduction

### 1.1 Motivation

Understanding the incidence and dynamics of variations in the convective structure of Tropical Cyclones (TC) is vital for improving forecasting of intensity (Dvorak, 1975; Velden et al., 2006), size (Huang et al., 2012), storm surge (Irish et al., 2008), wind radii (Knaff et al., 2014) and surface wave height (Lazarus et al., 2013). Two frequently observed changes in convective morphology are Secondary Eyewall Formation (SEF; Willoughby et al. 1982) and the development of a stationary banding complex (SBC; Willoughby et al. 1984). SEF occurs when outer rainbands coalesce to form a new eyewall concentric to the existing inner eyewall. An SBC is a mesoscale wavenumber one convective asymmetry that remains stationary relative to the vortex.

Increases in TC size (Huang et al., 2012; Bell et al., 2012), intensity (Willoughby and Black, 1996; Sitkowski et al., 2011) and integrated kinetic energy (Maclay et al., 2008) occur during SEF. Understanding the processes driving these changes is vital from the perspective of operational forecasting, yet SEF remains difficult to predict (Kossin and Sitkowski, 2009, 2012; Kossin and DeMaria, 2016), and the dynamical processes responsible for the development of the SE are not well understood (Wu et al., 2016). Observational and modelling studies of SEF have qualitatively suggested that the SE develops from the axisymmetrization of pre-existing spiral rainbands. In particular, case studies have documented SEs developing from the amplification and axisymmetrization of a SBC (Houze et al., 2007; Hence and Houze, 2008; Didlake and Houze, 2009, 2013a; Qiu and Tan, 2013; Didlake et al., 2018).

Differences in the precipitation and kinematic structure of rainbands in different regions of the vortex, and the orientation of the SBC relative to the deep layer environmental shear have been extensively studied. However, these studies focus on compositing techniques, as opposed to observing the morphology at the level of individual rainbands. Understanding of the de-

velopment and evolution of individual bands is derived either from case studies (Barnes et al., 1983; Powell, 1990a,b; Houze et al., 2006), or composite profiles that do not capture the morphology of the rainband. Limited work has focussed on the banding structure prior to SEF (Didlake et al., 2018). However, the explicit role of the pre-existing rainband geometry in the axisymmetrisation process has not been quantitatively documented beyond case studies. Similarly, the climatological incidence of the SBC and other rainband configurations, as well as the geometry of a typical rainband, has not been investigated.

## 1.2 Aims

The overarching aim of this thesis is to quantify how the rainband morphology of a TC evolves prior to SEF, and use this to predict imminent SEF events. Specifically, the four scientific questions answered in this thesis are:

1. What is the morphology of a typical spiral rainband, and how does this vary geographically?
2. What is the typical evolution of rainband morphology prior to SEF, and does this differ substantially from the climatological average?
3. Do the large scale environmental conditions influence the axisymmetrisation process?
4. Is it possible to use information about the environmental conditions and rainband morphology to reliably predict SEF?

These questions are answered in five steps. Firstly, a TC centred 85-89GHz passive microwave (PMW) dataset suitable for viewing TC structure is compiled. A novel objective technique is then developed to automatically classify TC structure from a PMW image. This technique is used to construct a 3-year climatology of TC rainband morphology. Finally, a statistical model is developed to predict imminent SEF events.

## 1.3 Thesis Structure

Chapter 2 presents a review of current understanding of TC structure and an overview of background literature important in the context of this study. This chapter has a particular focus on the proposed role of rainbands in SEF. Chapter 3 presents an overview of datasets used in this study, including the construction of PMW images for observing the convective structure of a TC. Chapter 4 describes a classification system for TC structure, together with a fully automated implementation for PMW satellite imagery. Results are presented in Chapters

5 and 6. Chapter 5 presents a climatology of different rainband structures, and documents the typical evolution of the banding pattern prior to SEF. Chapter 6 assesses the impact of the environmental conditions on each stage of the SEF process, and uses this information to create a statistical model for predicting SEF events. Finally, conclusions and directions for future work are discussed in Chapter 7.

# Chapter 2

## Background and Literature Review

### 2.1 TC structure

The structure of a mature TC has been extensively documented (e.g Houze, 2010). At the centre of the TC is the eye, a convection-free region of subsidence surrounded by a quasi-circular ring of deep convection known as the eyewall. Outside of this are the rainbands, quasi-spiral areas of convective and stratiform precipitation that typically propagate outwards from the inner core (IC). Radar and satellite observations have demonstrated that rainband structure varies considerably between TCs. A schematic of the different rainband types introduced in this section is shown in Figure 2.1.

Rainbands in the IC and outer core (OC) of the TC have distinct structures (Wexler, 1947; Figure 2.1 (a)). The IC rainbands are sheared, transient bands which propagate outwards from the eyewall within 150km of the radius of maximum winds (RMW; Wang, 2009). In contrast, the outer rainbands form at a radius greater than 200km, and consist of cellular convection with a structure similar to a squall line (Houze, 2010; Yu et al., 2018). The IC (OC) bands have a more stratiform (convective) precipitation structure. This suggests that the IC bands form within the region primarily controlled by the vortex circulation, while the OC bands are governed by squall line dynamics (Kummerow et al., 1998; Cecil et al., 2002; Cecil and Zipser, 2002).

A variation on this classification is the formation of a SBC (Willoughby et al. 1984). In contrast to the transient IC and OC bands, the SBC remains quasi-stationary and persists on a timescale of 24 hours. The SBC consists of the principal rainband (PRB), the largest band within the TC, together with several small secondary bands joined to the inner edge (Figure 2.1 (b)). The PRB may be connected to the eyewall by secondary bands, or separated by a convection-free moat. Another common structural change in a mature TC is SEF, where convection from pre-existing rainbands is axisymmetrised into a ring of deep convection concentric to the original

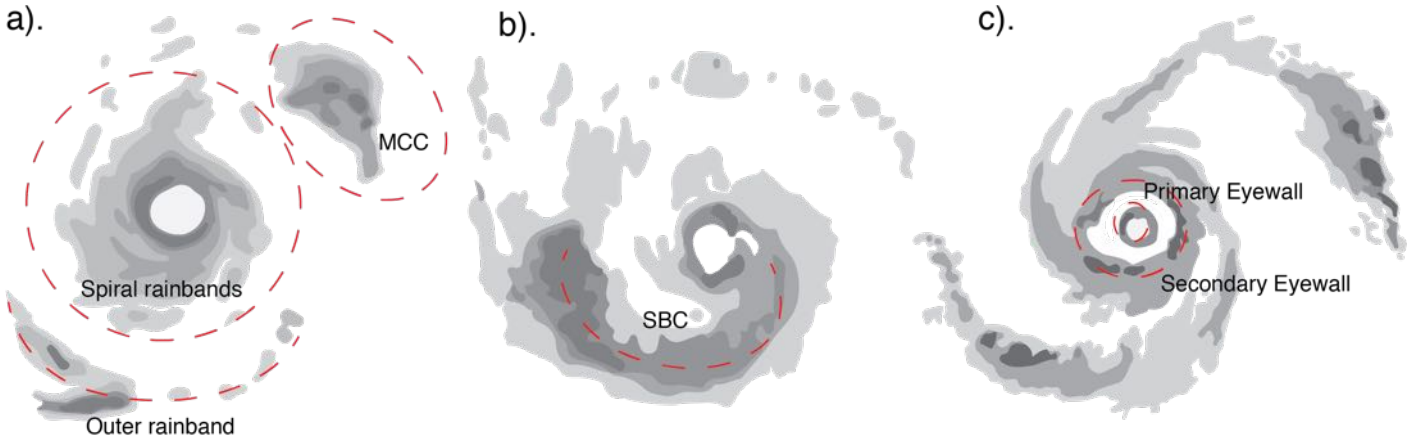


*Figure 2.1: Schematic of different rainband types showing (a) A TC with IC spiral rainbands, an OC rainband and a mesoscale convective complex. (b) A TC with a SBC. (c) A TC with a SE and spiral banding.*

eyewall, known as a secondary eyewall (SE; Willoughby et al. 1982; Figure 2.1 (c)).

In certain conditions, rainband activity may be suppressed. One such class of TCs are annular hurricanes (Knaff et al., 2003, 2008), characterised by a large eyewall, intense symmetric vortex structure and suppressed rainband activity. Similar storm structures with limited rainband activity, but lacking the characteristic large eye of annular hurricanes may also develop in regions with low environmental relative humidity (Chen et al. 2012).

The kinematic structure and dynamics of these different types of rainbands and SEs are discussed in Sections 2.2 and 2.3.

## 2.2 Rainbands

### 2.2.1 Terminology

A schematic of terms used in this thesis to refer to the SBC is shown in Figure 2.2. Downwind (upwind) is used with respect to the low level inflow, and refers to the end of the rainband closest to (furthest from) the eye. The inner (outer) edge of the rainband is used to refer to the edge of the band closest to (furthest from) the TC centre. Finally, the term ‘moat’ is used qualitatively to describe the region of raised brightness temperature on the inner side of a PRB or SE. The terms ‘band’ and ‘rainband’ are used interchangeably, and are both understood to refer to a spiral rainband. Throughout this study, TCs are assumed to be located in the Northern Hemisphere unless otherwise stated.

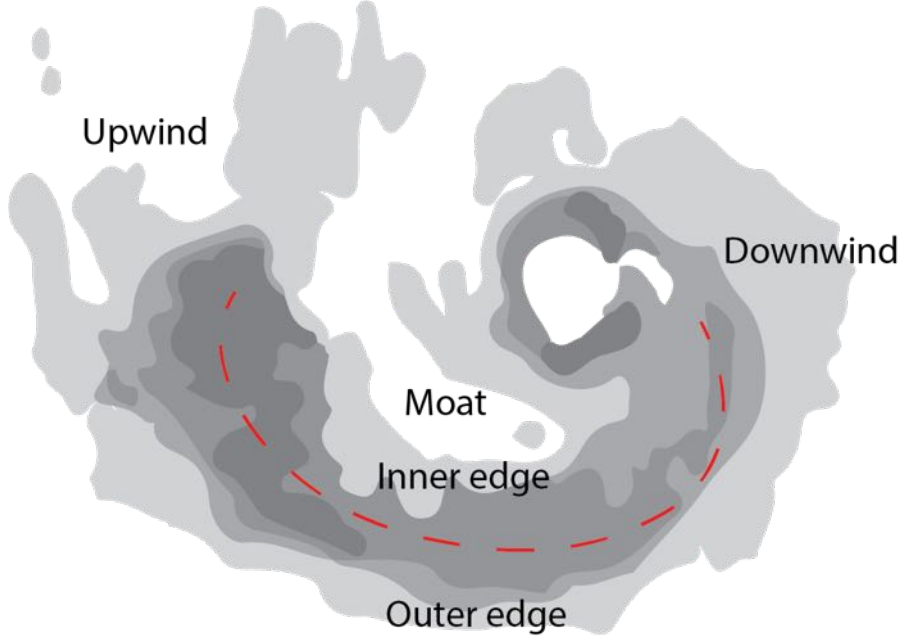


*Figure 2.2: Schematic of the terminology used in this study for different parts of the SBC.*

### 2.2.2 IC rainbands

The IC rainbands occur within a radius of 2-3 times the RMW. This region is characterised by the development of a rapid filamentation zone (Rozoff et al., 2006; Wang, 2008a), a region of strain dominated flow where convective disturbances are filamented by strong radial wind shear. Early studies primarily attributed these bands to gravity waves forced by the latent heating in the eyewall (Kurihara, 1976; Willoughby, 1978), however recent work has demonstrated that their propagation speed is inconsistent with gravity waves (Sawada and Iwasaki, 2010). The accepted explanation for the dynamical origin of the IC rainbands is that they are Vortex Rossby Waves (VRWs) propagating on the gradient of potential vorticity outside the eyewall (Guinn and Schubert, 1993; Montgomery and Kallenbach, 1997). Although the theoretical formalism of VRWs was developed in a dry, barotropic framework, studies using full physics models (Wang, 2002a,b) and observational analyses (Corbosiero et al., 2006) have demonstrated that the propagation characteristics of wavenumber two and three IC modes are consistent with convectively coupled VRWs.

An alternative viewpoint is that the IC rainbands result from shear induced deformation waves. Using a full physics simulation, Moon and Nolan (2015a,b) observed IC bands with propagation characteristics inconsistent with either gravity waves or VRWs. These bands were proposed to develop from convection originating in the upshear quadrants that is deformed into a spiral shape as it is advected around the vortex within the rapid filamentation zone.

### 2.2.3 OC rainbands

In contrast, relatively little is known about the dynamics of the OC rainbands. Yu et al. (2018), used dual Doppler radar retrievals to document the kinematic structure of 50 individual rainbands from 22 typhoons approaching Taiwan, finding that 58% of the bands had kinematic and thermodynamic characteristics similar to that of a squall line. These bands were propagating at approximately  $20ms^{-1}$  away from the vortex. It is unclear to what extent these results are true for TCs over open ocean or making landfall in other regions, as the topography of Taiwan has significant impacts on rainband structure (Chang et al., 1993).

### 2.2.4 The principal rainband (PRB)

The kinematic and thermodynamic structure of the PRB and SBC is well understood. Studies using pseudo-dual Doppler techniques (Barnes et al., 1983; Powell, 1990a,b), as well as high resolution radar such as in the Hurricane Rainband and Intensity Change Experiment (RAINEX; Houze et al. 2006) field campaign have flown purpose designed missions to observe the SBC. The precipitation structure of the PRB is primarily convective (stratiform) at the upwind (downwind) end of the band (Jorgensen, 1984). Convective cells develop at the upwind end of the band, propagate down the band at 80% of the mean tropospheric wind speed (Powell, 1990a), and collapse into stratiform precipitation at the downwind end (Figure 2.3 (a)). The cross-band structure is convective on the inner edge and stratiform on the outer edge (Hence and Houze, 2008).

A distinct circulation structure is observed within the PRB (Figure 2.3 (b)). Similar to the eyewall, an overturning secondary (i.e radial) circulation develops within the rainband, the depth of which is constrained by the upper level outflow (Barnes et al., 1983). Two distinct downdrafts are observed: the lower level downdraft (LLD) and inner edge downdraft (IED). The LLD originates within the low level inflow above the boundary layer. Air flowing radially inwards is forced downwards and cools due to precipitation drag and evaporative cooling (Zipser, 1977; Barnes et al., 1983; Powell, 1990a; Didlake and Houze, 2009). This transports low potential temperature air into the boundary layer, decreasing the intensity of the TC (Powell, 1990b; Riemer and Laliberté, 2015). The IED originates within the upper level outflow layer (Didlake and Houze, 2009). Air flowing radially outwards is forced downwards by a combination of the buoyancy pressure gradient field induced by the overturning circulation within the PRB and evaporative cooling (Didlake and Houze, 2009). This downdraft creates a sharp reflectivity gradient on the inner edge of the band.

An important kinematic feature within a PRB is the tangential wind jet oriented along the axis of the band (Jorgensen, 1984). Samsury and Zipser (1995) documented the climatological prevalence of tangential jets in TC rainbands, defining a rainband as a region of enhanced

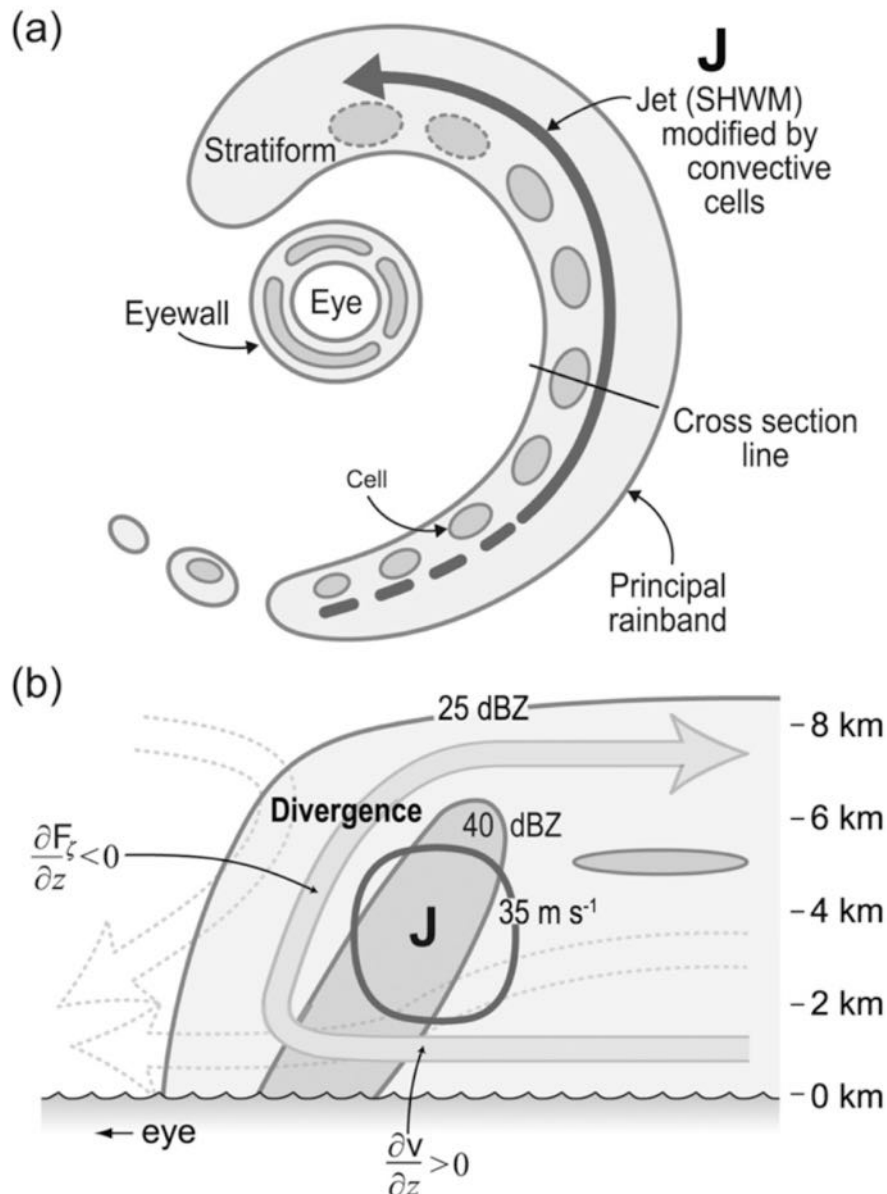


Figure 2.3: Schematic of the structure of a PRB. (a) Precipitation structure of a typical PRB, showing convective cells upwind and stratiform precipitation downwind, together with a tangential jet oriented along the band. (b) Cross section of PRB structure showing the overturning circulation, with the IED and LLD (dashed arrows), radial circulation (grey arrow) and tangential jet (J). From Didlake et al. (2009).

reflectivity on airborne radar. They demonstrated that over 70% of tangential jets are associated with a rainband, however just 29% of rainbands have a tangential jet. Dynamically, this jet is similar to the rear inflow jet of a squall line (Lafore and Moncrieff, 1989), occurring in response to mid-tropospheric PV anomalies at the stratiform end of the band (May and Holland, 1999; Franklin et al., 2006). The PV anomalies at the stratiform end of a PRB are sufficient to generate a secondary tangential wind maximum within several hours (May, 1996; May and Holland, 1999). Once the jet has formed, it intensifies both via stratiform processes and through the mid-level vorticity accumulation induced by the transverse circulation (Hence and Houze, 2008). Tangential wind jets may also be observed in the upwind convective portion of the rainband, however these are associated with individual cells, and are therefore dynamically distinct from the stratiform jet (Didlake and Houze, 2013a).

The structure of a PRB organizes on three distinct scales: the scales of the SBC, sub-band features and individual cells (May, 1996). Sub-bands are smaller scale rainbands propagating within the quasi-stationary PRB. The typical structure and dynamical role of these sub-bands remains unclear. May and Holland (1999) first documented sub bands in TC Lawrence (1990), observing convective lines oriented at 45 degrees to the axis of the main band propagating down-band at approximately 8m/s. The propagation characteristics of these bands were demonstrated to be consistent with gravity waves generated by convection within the eyewall. Tang et al. (2018) presented a case study of a sub-band within the PRB of typhoon Hagiput (2008). They observed multiple sub-bands of scale 140 by 20km, with propagation characteristics similar to gravity waves. These sub-bands were shown to have a dynamic and thermodynamic structure similar to a squall line with trailing stratiform precipitation.

In addition to the sub band structure within the PRB, the band itself is constantly evolving as part of the SBC. Willoughby et al. (1984) first noted the continually evolving nature of the SBC, with secondary bands continually forming and the structure and orientation of the PRB changing. Occasionally, a secondary rainband will propagate outwards from the eyewall, amplify and eventually replace the PRB (May, 1996). This process of PRB replacement has also been observed in numerical simulations. Li et al. (2017) documented three possible paths to PRB formation and replacement within a pre-existing SBC. The first path involved the amplification and outward propagation of a VRW, similar to that observed by May (1996). The second and third paths both involved the amplification of shear induced deformation waves (Moon and Nolan, 2015a) into a PRB. In the second path, a single deformation wave formed in the upshear left quadrant amplified within the rapid filamentation zone and developed into the PRB. In the third path, multiple shear induced deformation bands propagated downwind, coalesced into a single band and replaced the PRB.

There is still no consensus as to the dynamics responsible for the formation of the SBC. Current understanding suggests that the development and orientation of the SBC is related to the mag-

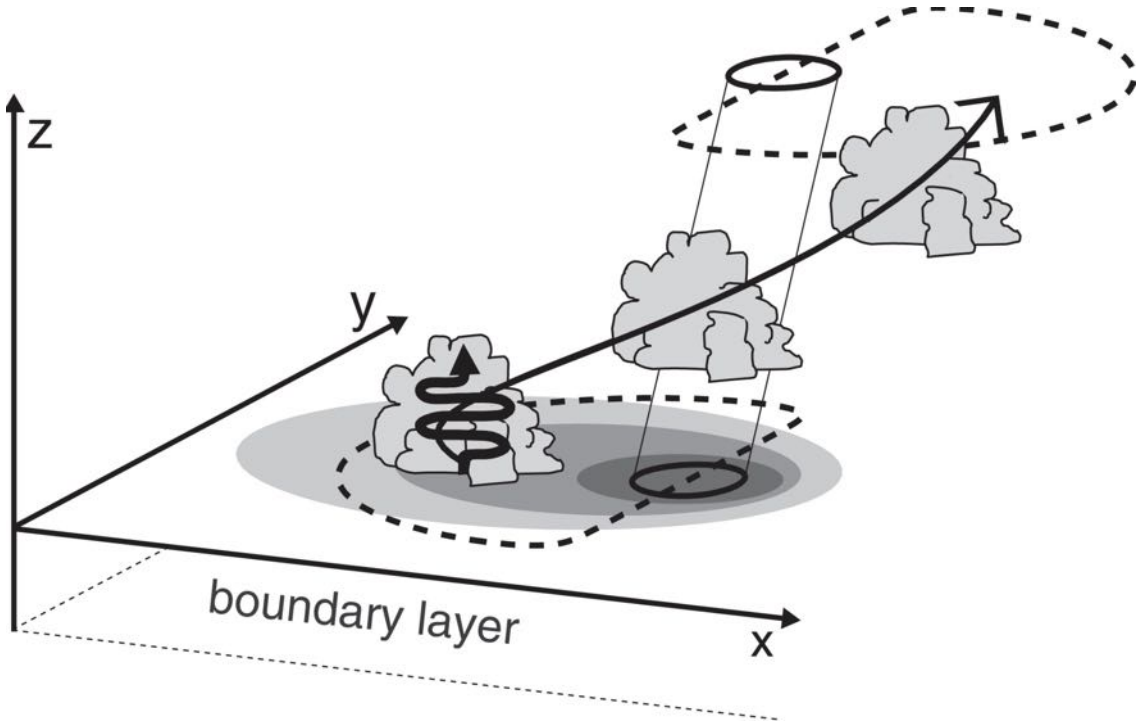


*Figure 2.4: Schematic of SBC formation, showing convection developing in the downshear right quadrant of the tilted vortex and being cyclonically advected to the downshear left. Low level shading represents the distortion of the equivalent potential temperature field, and dashed contours the positive vorticity anomalies associated with the vortex tilt. From Riemer (2016).*

nitude of the deep layer vertical wind shear (VWS), as discussed in further detail in Section 2.5. Both observations (Willoughby et al., 1984) and numerical simulations Riemer and Montgomery (2011) have demonstrated that the SBC forms on the thermodynamic boundary between the vortex moist envelope and the drier environmental air. Riemer (2016) suggested that the SBC develops as a result of the downshear right overlap of a region of high vorticity resulting from the downshear tilt of the vortex and positive equivalent potential temperature anomaly arising from the distortion of the moist envelope. This creates an environment favourable for deep convection, and a vorticity perturbation large enough to force ascent via frictional convergence within the boundary layer (Figure 2.4).

## 2.2.5 Mesoscale convective complexes

Not all structures outside the eyewall are readily classified as rainbands. In many cases, extensive regions of convection develop that do not have a clearly defined banding structure, known as Mesoscale Convective Complexes (MCCs, Lee et al. 2012). A ten year climatology of Western Pacific TCs demonstrated that these convective complexes may merge with the eyewall, or evolve from a distant rainband at large radius (Lee et al. 2012). In this climatology, 22% of TCs developed at least one MCC during their lifetime, with a mean duration of 10.3hrs.

## 2.3 Secondary Eyewall Formation (SEF)

### 2.3.1 Definition and kinematic structure

SEF occurs when rainbands organise into a quasi-circular ring of deep convection concentric to the original eyewall, collocated with secondary horizontal wind and potential vorticity (PV) maxima (Willoughby et al., 1982). Between these convective rings is the moat, a region of subsidence dynamically and thermodynamically similar to the eye. (Houze et al., 2007). The formation of the SE is preceded by the broadening of the tangential wind field, quantified by an expansion in the radius of 34kt winds (Bell et al., 2012). The structure of the SE during SEF differs from that of a single primary eyewall. TRMM precipitation radar observations reveal that the hydrometer structure of a SE is similar to a rainband in the upper troposphere and an eyewall in the lower troposphere (Hence and Houze, 2011). This supports the idea that SEs develop from the bottom up axisymmetrization of pre-existing rainbands.

High resolution Doppler radar observations have demonstrated that the SE is composed of convective cells with no preferred orientation embedded within uniform stratiform precipitation (Didlake and Houze, 2011). The shear-induced convective asymmetry is at a maximum in the downshear left quadrant for the inner eyewall, however is at a maximum in the downshear right quadrant in the developing outer eyewall, possibly as a result of interactions with a pre-existing SBC (Hence and Houze, 2012b; Didlake et al., 2017). The structure of the primary eyewall is identical to that of a single eyewalled storm, but with shallower convection (Houze et al., 2007; Hence and Houze, 2012b).

SEF is frequently followed by an eyewall replacement cycle (ERC), where the SE contracts inwards and intensifies as the primary eyewall dissipates. During this process, the maximum intensity of the storm increases during SEF, decreases as the primary eyewall begins to dissipate and then increases as the SE strengthens (Willoughby et al., 1982; Sitkowski et al., 2011). At the conclusion of the ERC, the TC is left weaker with a broader tangential wind field and larger RMW.

### 2.3.2 Dynamics

There is no accepted dynamical theory of SEF (Wu et al., 2016). Qualitatively, climatologies using PMW imagery and radar case studies have suggested that the SE forms from the axisymmetrisation of convection in pre-existing spiral rainbands (Hawkins and Helveston, 2008; Hence and Houze, 2008). Many theories of SEF therefore focus on the potential roles of spiral bands from both a symmetric and asymmetric perspective, which will be discussed in this section.

A theory relating SEF to the IC rainbands is that SEF occurs as a result of energy transport by

VRWs. Montgomery and Kallenbach (1997) proposed that VRWs propagating on the PV gradient outside the eyewall drive SEF through wave-mean flow interaction at the wave stagnation radius (the radius at which the group velocity vanishes). Modelling experiments in both full physics and barotropic frameworks have used Empirical Normal Mode techniques to confirm that the leading modes are primarily VRWs and that SEF occurs at their stagnation radius (Abarca and Corbosiero, 2011; Martinez et al., 2010, 2011; Menelaou et al., 2012). This hypothesis has been questioned in recent work, however. Judt and Chen (2010) used full physics simulations of hurricane Rita (2005) to demonstrate that a strong moat region with zero PV gradient formed prior to SEF, preventing VRW activity at the SEF radius. Similarly Sun et al. (2013) found that VRW activity had minimal impact on SEF in a full physics simulation of typhoon Sinlaku (2008).

One school of thought is that SEF is driven by the balanced vortex response to the projection of diabatic heating and vorticity anomalies in rainbands onto the azimuthal mean. Diabatic heating associated with convection in the bands is sufficient to explain the broadening of the tangential wind field that precedes SEF (Fudeyasu and Wang, 2011). Shapiro and Willoughby (1982) first showed that the balanced response to heat and momentum sources in the outer vortex could generate a secondary tangential wind maximum. Rozoff et al. (2012) verified this theoretical work using a cloud resolving model, suggesting that the enhanced inertial stability associated with the broadening wind field is important in confining the secondary tangential wind maximum to a narrow region. Judt and Chen (2010) focussed on the PV distributions in the OC rainbands, demonstrating that PV accumulation within the rainband region could trigger SEF. Zhu and Zhu (2014) also noted the importance of diabatic heating within the rainbands, suggesting that SEF occurs only when the rainband convection surpasses a certain intensity. The hydrometer structure of the rainbands is also important in the SEF process (Tyner et al., 2018).

More recently, the role of asymmetric dynamics has been recognised. Case studies of SEF events in hurricanes Rita (2005; Houze et al., 2007, Didlake and Houze, 2011; Bell et al., 2012; Didlake and Houze, 2013) and Earl (2010; Didlake et al. 2018) demonstrated that the SEs in these two TCs formed from the axisymmetrisation of a pre-existing SBC. In both of these cases, a strong mid-level mesoscale descending inflow jet developed in the downshear-left quadrant, descending into the boundary layer and creating a local vorticity maximum at the radius of the incipient SE. Didlake et al. (2018) suggested that this jet acts to accelerate the tangential circulation in the downshear left quadrant, after which SEF is triggered by axisymmetric processes. Qiu and Tan (2013) observed a similar inflow pattern in a numerical simulation, suggesting that this works in conjunction with axisymmetric boundary layer mechanisms to trigger SEF by enhancing inflow on the opposite side of the TC. The formation of an SBC prior to SEF has also been observed in other numerical simulations (Fang and Zhang, 2012; Zhang et al., 2017a). Moon and Nolan (2010) used idealised numerical simulations to model the response of the

tangential wind field to asymmetric rainband heating, finding heating associated with spiral banding is sufficient to spin up a secondary tangential circulation on the opposite side of the vortex which persists even after the heating is removed.

Considerable work has focussed on the potential role of boundary layer dynamics in SEF. Although absolute angular momentum is not conserved in the boundary layer, if the inflow is sufficiently strong parcels are advected inwards with minimal loss of angular momentum (Smith et al., 2009), spinning up supergradient tangential flow in the IC. Based on observations of typhoon Sinlaku (2008; Wu et al. 2012), Huang et al. (2012) suggested that enhanced inflow in response to rainband heating spins up a supergradient tangential circulation at the SEF radius via this mechanism. The development of the supergradient secondary tangential wind maximum results in boundary layer convergence, deep convection, and eventually SEF. This process has also been observed in other numerical simulations (Wang et al., 2018b; Huang et al., 2018). An alternative viewpoint is that SEF is driven by the boundary layer response to vorticity anomalies in the outer regions of the storm (Kepert, 2013; Kepert and Nolan, 2014; Kepert, 2017). At large radii, boundary layer dynamics are sufficient to generate significant frictional updrafts in response to small anomalies in the vorticity gradient. This creates favourable conditions for deep convection, further enhancing the vorticity anomaly and leading to a positive feedback resulting in SEF. This mechanism has been observed to operate in response to vorticity anomalies in the SBC in numerical simulations (Zhang et al., 2017a).

The large scale environmental conditions can also enhance rainband activity and subsequently trigger SEF. Vortex response to changes in VWS (Hogsett and Zhang, 2009; Zhang et al., 2017a) increased rainband activity in regions of higher environmental relative humidity (Hill and Lackmann, 2009) and enhanced surface fluxes (Xu and Wang, 2010; Cheng and Wu, 2018) have all been shown to increase the likelihood of SEF. It is noted that other theories for SEF have been proposed that do not explicitly invoke the role of rainbands. These include beta skirt axisymmetrisation (Terwey and Montgomery, 2008), interaction with upper level troughs (Nong and Emanuel, 2003; Komaromi and Doyle, 2018), and interaction between outflow and upper tropospheric jets (Dai et al., 2017).

## 2.4 Classifying TC structure

SEs are readily identified using PMW imagery. Satellite climatologies have investigated the characteristics of SEF events, finding that the probability of SEF increases with storm size (Ge et al., 2016), intensity (Hawkins and Helveston, 2004) and time spent at maximum intensity (Kuo et al., 2009). Significant differences in the prevalence of SEF exist between basins (Hawkins and Helveston, 2004). SEF is estimated to occur in 75% of Western Pacific, 40% of Southern hemisphere, 65% of Eastern Pacific and 70% of North Atlantic TCs with a maximum

lifetime intensity greater than 110 knots (Hawkins and Helveston, 2004; Hawkins et al., 2006; Hawkins and Helveston, 2008). Subsequent to SEF, observed structural evolutions include ERC, dissipation of the outer eyewall, long lived concentric eyewalls, multiple SEF and ERC events and transition to an annular hurricane (Hawkins and Helveston, 2008; Wang, 2008b). Yang et al. (2013) quantitatively examined the likelihood of these scenarios, finding that an ERC eventuates in 62% of SEF events.

In contrast, the climatological differences in rainband morphology have not been well documented. In a series of radar studies, Senn et al. (1957) documented the geometric properties of rainbands in different regions of storms within the Gulf of Mexico. Fitting log spirals to individual bands, they found that bands in the inner (outer) regions typically have lower (higher) crossing angle. Senn and Hiser (1959) attempted to study the evolution of different banding patterns on radar, however noted that it was difficult to unambiguously isolate individual bands was difficult as they tended to merge within large complexes of precipitation with poorly defined banding structure.

An alternative to isolating individual bands is to utilise structural ‘shape’ metrics to quantify the asymmetry and organisation of the storm. Shape metrics such as the dispersion, asymmetry and fragmentation have been used to analyse precipitation structure on radar (Matyas, 2007), reanalysis (Zick and Matyas, 2016) and satellite (Matyas, 2014) data. These metrics have been used to quantify the effect of environmental conditions on storm asymmetry (Matyas, 2008, 2009, 2010) and assess the spatial extent of rainfall structures (Zhou and Matyas, 2017). More recently, alternative metrics have been used to quantify rainfall asymmetry at different stages of the TC lifecycle (Deng and Ritchie, 2018).

## 2.5 Environmental conditions and TC structure

The primary environmental factor influencing TC structure is the magnitude and direction of the deep layer VWS. A TC is typically weaker in stronger VWS (DeMaria, 1996), and develops a wavenumber one convective asymmetry (Frank and Ritchie, 1999) with a maximum in the downshear left quadrant (Hence and Houze, 2012a). In vertically sheared flow, a vortex will initially tilt downshear as the upper level core is passively advected downstream (Jones, 1995). This induces a low level PV anomaly upshear, and upper level PV anomaly downshear, resulting in cyclonic flow anomalies which cause the vortex to precess in an anticlockwise direction. In practice, vortices will reach an equilibrium state tilt oriented downshear left (Corbosiero and Molinari, 2003; Riemer and Montgomery, 2011) due to VRW damping (Reasor et al., 2004), though the efficiency and impact of this process depends on the characteristics of the radial PV profile and the distribution of pre existing convection (Reasor et al., 2004; Mallen et al., 2005).

In the majority of previous work, the primary focus has been on the relationship between TC structure and the magnitude of the shear vector. More recently, it has become clear that the characteristics of the shear profile and direction of the shear have significant implications for TC structure. The direction of surface flow relative to the deep layer shear vector impacts vortex symmetry by inducing anomalies in surface flux distributions (Rappin and Nolan, 2012; Chen et al., 2018). Changes in shear depth (Finocchio et al., 2016) and direction (Onderlinde and Nolan, 2014, 2016) also influence the structural asymmetries of a TC.

Although shear is typically the dominant factor in determining TC structure, other parameters also impact the distribution of convection. TC motion induces convective asymmetries as a result of boundary layer convergence (Shapiro, 1983), though these are typically secondary to the effects of VWS (Thomsen et al., 2015). Increased environmental relative humidity (Hill and Lackmann, 2009), convectively available potential energy (CAPE; Wada et al. 2012) and relative sea surface temperature (Lin et al., 2015) enhance rainband activity, increasing the overall size of a TC.

## 2.6 Significance and innovation

From Section 2.3.2, it is clear that there is no consensus as to which dynamical processes are responsible for SEF. Understanding these processes is critical for forecasting SEF events, and in turn improving forecasts of intensity and storm surge. A particular knowledge gap is that while it is accepted that rainbands are important in the process of SEF, their precise role is unclear. Qualitative work has suggested that the SE is formed by axisymmetrisation, however knowledge of this process is limited to case studies. Moreover, knowledge of rainband morphology in general is lacking. Difficulties in isolating individual rainbands have restricted a majority of previous studies to compositing techniques or structural metrics which are unsuitable for gaining insight into the evolution of individual rainbands.

This study addresses these issues by using machine learning techniques to develop a first objective method for classifying TC morphology at the level of the geometry of individual rainbands. Many of the computer vision techniques employed in this analysis have not previously been used in meteorology. Application of this technique allows for the geometry and evolution of individual rainbands to be assessed for the first time.

The rainband climatology developed in this study has important implications for evaluating the potential likelihood of the large number of competing SEF hypotheses, and improving knowledge of rainband dynamics and formation. A specific practical application of this technique is demonstrated in Chapter 6, with the construction of a skilful model to predict SEF events.

# Chapter 3

## Datasets

In order to construct a climatology of TC structure, it is necessary to have a dataset with global coverage and sufficient spatial and temporal resolution to resolve changes in convective structure. This chapter describes the development of multichannel PMW satellite products used for rainband and eyewall identification in this study, together with information about datasets used to quantify the large scale environmental conditions.

### 3.1 Observing TC structure

Despite advances in remote sensing technology, observing the IC structure of a TC remains challenging. This is primarily due to the upper level cirrus canopy that develops within the outflow layer above a mature TC, obscuring the lower level structure at infrared (IR) and visible wavelengths (Kossin et al., 2007). The geostationary IR and visible channels widely used in other remote sensing climatologies are therefore unsuitable for identifying IC rainbands and SEs. Techniques using multichannel IR brightness temperature and water vapour imagery may be used to observe convection. Unfortunately, however, these products are either limited to daylight hours, or are not of sufficient quality for identifying individual rainbands (Sanabia et al., 2015). Alternative methods of viewing TC structure are using land based and airborne radar, and microwave satellites.

Aircraft reconnaissance data provides the highest resolution observations of TC structure. Aircraft fly routine reconnaissance missions into storms within the Gulf of Mexico, and sporadic missions in other basins (Elsberry and Harr, 2008; Chan and Kepert, 2010). In a typical mission, an aircraft remains in the storm for four to six hours, flying two complete transects through the eye. All aircraft take measurements of vertical and tangential wind together with various thermodynamic variables at flight level. Certain missions are also equipped with doppler radar. Although this dataset provides high resolution observations within the IC, each flight

only provides a snapshot of the storm structure at a particular time. This dataset is therefore unsuitable for constructing a climatology of band evolution. Land based doppler radars have limited range, and therefore have similar issues.

The only data source that is both suitable for classifying TC structure and has quasi-regular global coverage is microwave satellite imagery. At microwave frequencies, instruments are unaffected by the small ice crystals in the cirrus outflow, and can therefore observe the convective structure. A drawback is that no geostationary satellites are equipped with microwave instruments, resulting in irregular temporal sampling.

The highest spatial resolution is obtained using active microwave instruments. Synthetic Aperture Radar (SAR) instruments include RADARSAT (Raney et al., 1991) and the Environmental Satellite (ENVISAT; Gardini et al. 1995). These satellites have spatial resolutions ranging from 50-400m (Lee et al., 2017), and have previously been used to investigate sub-rainband scale morphology in TCs (Li et al., 2013), observe rainbands (Quilfen et al., 2006) and reconstruct the low level wind field (Horstmann et al., 2005). Attempts were made to use SAR data for this climatology, however all available instruments have swath widths between 200 and 400km, typically too narrow to include the entire rainband field. Spaceborne radar, for example the Tropical Rainfall Measuring Mission (TRMM; Kummerow et al. 1998) Precipitation Radar also provide global high resolution datasets, however the temporal sampling of these instruments is too irregular for a global climatology.

The only data source with quasi-regular global coverage suitable for observing TC convective structure is PMW data. PMW data has been collected continuously from 1981 to the present day. From 1998-2018, at least 6 separate platforms have transmitted data simultaneously at any given time. Although all PMW sensors are on satellites in either low earth, polar or sun synchronous orbits, the swath widths are wide enough to regularly capture the entire rainband field of a given TC (Table 3.1). Although morphed products are available that standardise the microwave temporal resolution, for example the Morphed Integrated Microwave Imagery TC (MIMIC-TC; Wimmers and Velden, 2010), these archives are of low quality, and are hence not used in this study.

## 3.2 PMW dataset

### 3.2.1 PMW data sources

For this study, a 20 year TC-centred PMW dataset is compiled. As high spatial resolution is required, cross track scanning instruments are excluded from the dataset, as the spatial resolution rapidly degrades off nadir (Liang, 2017). This dataset therefore consists of observations

from all available conical scanning PMW sensors operating between 1998 and 2018; a total of six different instruments operating on 13 individual platforms. The instruments and satellites included are the:

- TRMM Microwave Imager (TMI) on the Tropical Rainfall Measuring Mission (TRMM) satellite (Kummerow et al., 1998).
- Advanced Microwave Scanning Radiometer 2 (AMSR-2) on the Global Change Observation Mission for Water (GCOMW-1) satellite (Maeda et al., 2016).
- Advanced Microwave Scanning Radiometer E (AMSR-E) on the Aqua satellite (Japan Aerospace Exploration Agency, 2005)
- Special Sensor Microwave Imager (SSMI) on the Defence Meteorological Satellite Program (DMSP) F11, F13, F14 and F15 satellites (Hollinger et al., 1990).
- Special Sensor Microwave Imager/Sounder (SSMIS) on the Defence Meteorological Satellite Program (DMSP) F16, F17, F18 and F19 satellites (Hollinger et al., 1990).
- GPM Microwave Imager (GMI) on the Global Precipitation Mission satellite (Hou et al., 2014).

Specifications of these instruments are summarised in Table 3.1. Data is taken from the NASA Precipitation Processing System STORM archive (hereafter referred to as the PPS dataset), using the level 1C products for each instrument (National Aeronautics and Space Agency, 2018).

Each of the six instruments has multiple channels and polarisations, ranging from 19GHz to 183GHz. The most frequently used bands for observing convection are 36.5-37GHz (37GHz hereafter) and 85-92GHz (89GHz hereafter). Typically, PMW products combine multiple channels into false colour products to eliminate interference from features such as the ocean surface. As part of this study, three multichannel products were trialled. For observing rainbands and SEs, optimum results were obtained using three channel false colour 89GHz imagery. For a full description of different products developed and trialled for this task, see Appendix A.

Together, this constellation of satellites has a mean revisit time of 3 hours (Flaming, 2004), though data gaps may be up to 12 hours. Given that the structure of a PRB evolves on a timescale of at least 6 hours (Wang et al., 2018a; Tang et al., 2018) and SEs on a timescale of at least 12 hours (Sitkowski et al., 2011) this resolution is sufficient for observing the evolution of these phenomena.

Sensors included in the PMW dataset					
Satellite	Instrument	Swath width	Data availability	Channel	Resolution
TRMM	TMI	880km	07/12/1997 - 08/04/2015	85GHz	8km×6km
				37GHz	18km×10km
GPM	GMI	931km	04/03/2014 - present	89GHz	7km×4km
				36.5GHz	15km×9km
GCOMW1	AMSR2	1450km	02/07/2012 - present	89GHz	6km×4km
				36.5GHz	15km×9km
AQUA	AMSRE	1450km	04/05/2002 - 4/10/2012	89GHz	6km×4km
				36.5GHz	14km×8km
DMSP F11	SSMI	1700km	01/12/1991 - 01/05/2000	85.5GHz	15km×13km
				37GHz	37km×28km
DMSP F13	SSMI	1700km	01/05/1995 - 01/11/2009	85.5GHz	15km×13km
				37GHz	37km×28km
DMSP F14	SSMI	1700km	01/05/1997 - 01/08/2008	85.5GHz	15km×13km
				37GHz	37km×28km
DMSP F15	SSMI	1700km	01/12/1995 - present	85.5GHz	15km×13km
				37GHz	37km×28km
DMSP F16	SSMIS	1700km	04/05/2002 - 4/10/2012	92GHz	15km×13km
				37GHz	37km×28km
DMSP F17	SSMIS	1700km	19/03/2008 - present	92GHz	15km×13km
				37GHz	37km×28km
DMSP F18	SSMIS	1700km	08/03/2010 - present	92GHz	15km×13km
				37GHz	37km×28km
DMSP F19	SSMIS	1700km	18/12/2014 - 11/02/2016	92GHz	15km×13km
				37GHz	37km×28km

Table 3.1: Specifications of the PMW sensors and satellites included in the dataset

### 3.2.2 PMW data processing

For each swath in the PPS dataset, the International Best Tracks for Climate Stewardship (IBTrACS; Knapp et al. 2010) dataset is used to identify any TCs with a centre fix within the swath and intensity greater than 65kts at the time of the satellite overpass. Both the horizontally and vertically polarised brightness temperature data for each TC contained within the swath is then isolated and regridded to a  $1500 \times 1500$ km cartesian grid at 2km resolution using bi-cubic spline interpolation. The choice of 2km resolution is made to be consistent with other PMW image archives, which have a resolution of 1-2km (Turk et al., 1999; Knapp, 2008).

Within the raw PPS dataset, quality control is pre-imposed for incidences such as failure of a given channel. Other possible sources of error including sun glint and warm load intrusion are flagged for each data point. To assess the fidelity of each brightness temperature image, the pointwise quality control flags were interpolated to the image domain. Analysis of one year (2012) of the dataset revealed that less than 1% of images are affected by warm load intrusion or sunglint. As these effects are crudely corrected for within the raw dataset (National Aeronautics and Space Agency, 2018), points with these quality flags are retained.

Parallax is an important consideration in assessing the uncertainty in the regridded dataset. The PMW instruments have viewing angles between  $52^\circ$  and  $55^\circ$ . Parallax differences will therefore arise depending on the relative heights of different rainbands. Assuming a height difference of 10km between upper and lower level rainbands (Wimmers and Velden, 2010), this gives a parallax error of around 10km. As this is small compared to the length of the bands (approximately 250km), parallax error is not corrected for, and the TC is assumed to be centred with respect to the upper level reflectivity signature.

Another consideration in standardising the dataset across instruments is the differences in brightness temperature retrievals resulting from frequency differences between instruments. Comparisons of brightness temperature datasets from TMI at 85GHz and SSMIS at 92GHz have demonstrated that these differences may be up to 10K (Yang et al., 2014). This effect is corrected for in the PPS dataset for the 85-92GHz channels, which have been recalibrated to 89GHz using histogram matching (Berg et al., 2016).

This dataset is referred to as ‘the PMW dataset’ hereafter.

### 3.2.3 Interpretation of PMW images

The 89GHz product used in this study is based on the product described by Lee et al. (2002). The red (R) blue (B) and green (G) channels of the false colour image are constructed according

to the following specifications:

$$R = (290 - PCT_{89}) \times \frac{255}{130}, R < 160 = 255, R > 290 = 0$$

$$G = 255 - (290 - 89_{vpol}) \times \frac{255}{20}, G < 270 = 0, G > 270 = 255$$

$$B = 255 - (300 - 89_{hpol}) \times \frac{255}{60}, B < 240 = 0, B > 300 = 255$$

where  $89_{vpol}$  is the 89GHz vertical polarisation brightness temperature channel,  $89_{hpol}$  is the 89GHz horizontal polarisation brightness temperature channel and  $PCT_{89}$  is the 89GHz polarisation corrected temperature (PCT), defined by:

$$PCT_{89} = 1.818 \times 89_{vpol} - 0.818 \times 89_{hpol}$$

The scaling for the red channel is different to the original product outlined by Lee et al. (2002). Here, the lower end of the PCT range is reduced to 160K, providing greater contrast between rainbands and eyewalls, and allowing for easier discrimination between individual bands in intense storms where red channel in the original product is saturated. A PCT of less than 255K has been established as the upper threshold for precipitation (Spencer et al., 1989). A final constraint is therefore imposed that the PCT must be less than 255K for a pixel to be classified as raining:

$$PCT_{89} < 255K$$

An example of one of the resulting PMW images is shown in Figure 3.1. In this image red pixels indicate areas of rain, and green and blue indicate low level warm clouds or the underlying surface.

### 3.3 Environmental data

Two data sources are used to describe the state of the large scale environment for each TC. The first of these is the statistical hurricane intensity prediction scheme (SHIPS; DeMaria and Kaplan 1994, 1999; DeMaria et al. 2005) predictors. Additional shear profiles are calculated from ERA interim reanalyses to assess the impact of environmental flow in greater detail.

#### 3.3.1 SHIPS

The SHIPS dataset is used to describe the storm averaged environmental conditions in the vicinity of a given TC. The dataset consists of the storm centred averages of 89 environmental variables calculated 6 hourly from the National Center for Environmental Prediction (NCEP)

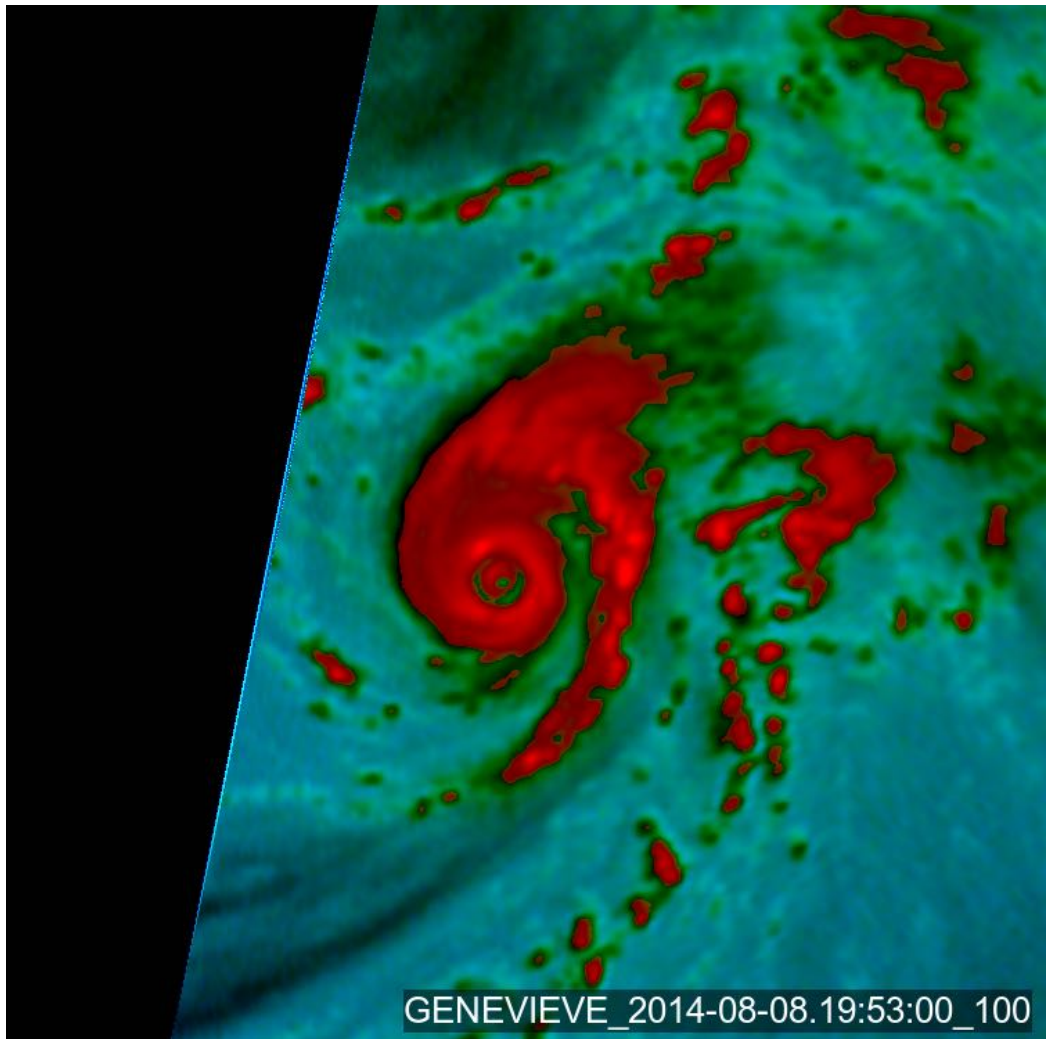


Figure 3.1: Example of clear concentric eyewalls together with a PRB viewed on 89GHz PMW imagery in Hurricane Genevieve at 19:53UTC on the 08/08/2014.

reanalysis (Kalnay et al., 1996) and operational models (Regional and Mesoscale Meteorology Branch, 2018). This dataset has previously been used for the statistical prediction of SEF (Kossin and Sitkowski, 2009, 2012; Kossin and DeMaria, 2016) and rapid intensification (Kaplan and DeMaria, 2003; Kaplan et al., 2010, 2015).

Examples of variables included in the full SHIPS dataset include the VWS direction and magnitude at different heights, maximum potential intensity and relative humidity. The dataset also includes predictors derived from principal component analysis of infrared channel brightness temperature data. These satellite-based predictors are excluded from the analysis in this study, as they are not independent of the TC morphology.

Many predictors within the complete SHIPS dataset are collinear, for example the maximum velocity and minimum sea level pressure. To avoid this issue and ensure consistency with the dataset size, a representative subset of 15 SHIPS predictors are selected for analysis and model construction. The predictors included are shown in Table 3.2. These include the current storm intensity (VMAX), Emanuel maximum potential intensity (VMPI; Emanuel 1986), deep layer shear magnitude (SHRD), 200hPa divergence (D200), sea surface temperature (RSST), depth of the 26 degree isotherm (CD26), vertical mass flux (VMFX), time since storm genesis (HIST), vertical temperature gradient (TGRD), 0-500hPa helicity (HE05), pressure level of the steering flow (PSLV), mid tropospheric relative humidity (RHHI), vertical potential temperature difference (EPOS), 1000hPa relative humidity (R000) and 1000hPa potential temperature (E000). These predictors are all derived from reanalyses and operational model output, with the exception of RSST and CD26, which are taken from Navy Coupled Ocean Data Assimilation (NCODA; Metzger et al. 2014).

In reality, there will be a time lag in the adjustment of the TC morphology to changes in the environmental conditions. To assess whether this had any impact on the results, the analysis using this dataset in Chapter 6 was repeated with the predictors calculated at -6 hours, -12 hours, and the six and 12 hour differences. In all cases, no substantial differences were observed. In order to limit the size of the predictor pool, only predictors at the current time were used.

### 3.3.2 Shear profiles

As discussed in Section 2, the orientation and development of convective asymmetries in TCs are primarily controlled by the magnitude, direction and profile of the deep layer VWS (Willoughby et al., 1984; Frank and Ritchie, 1999; Hence and Houze, 2008, 2012a; Riemer and Montgomery, 2011; Rappin and Nolan, 2012; Onderlinde and Nolan, 2014, 2016; Finocchio et al., 2016; Chen et al., 2018). As the SHIPS variables only include limited shear information, detailed environmental VWS profiles are derived from ERA-Interim reanalyses.

Many previous studies calculate the environmental VWS profile by removing the vortex out

SHIPS predictors included in the analysis		
Predictor	Units	Description
VMAX	kts	Current maximum surface wind
VMPI	kts	Current Emanuel maximum potential intensity
SHRD	kts $\times 10$	850-200hPa shear magnitude averaged from 200-800km radius
D200	$s^{-1} \times 10^{-7}$	200hPa divergence averaged from 0-1000km radius
RSST	$^{\circ}\text{C} \times 10$	Reynolds' sea surface temperature
CD26	m	Climatological depth of the 26 degree isotherm
VMFX	kg/ms $\times 10$	0-15km average vertical mass flux
HIST	hours $\times 6$	Length of time the vortex intensity has been greater than 20kts
TGRD	$^{\circ}\text{C} \times 10^{-7}$	850-700hPa temperature gradient averaged from 0-500km radius
HE05	$m^2 s^2 \times 10$	Storm motion relative helicity from 1000-500hPa and 200-800km radius
PSLV	hPa	Pressure at level where storm motion best matches the relative environmental flow
RHHI	%	750-500hPa relative humidity averaged from 200-800km radius
EPOS	$^{\circ}\text{C} \times 10$	average $\theta_e$ difference between a parcel lifted from the surface and its environment
R000	%	1000hPa relative humidity averaged from 200-800km radius
E000	$^{\circ}\text{K} \times 10$	1000hPa $\theta_e$ averaged from 200-800km radius

Table 3.2: The 15 SHIPS predictors included in the analysis. Descriptions adapted from Regional and Mesoscale Meteorology Branch (2018).

to a certain radius and interpolating for the missing points (DeMaria and Kaplan, 1999; Davis et al., 2008; Chen et al., 2018). An issue with this method is that it requires assumptions about what constitutes the vortex and environmental flow. To avoid this problem, low pass filtering is used to remove vortices from the reanalysis fields in this study. For a complete description of this process, see Appendix B. The environmental flow in the region of a TC is then calculated at each pressure level from 1000hPa to 200hPa in 50hPa intervals as the average over a 5 degree radius from the best track position at each time in the SHIPS dataset.

# Chapter 4

## Classifying TC Structure

This chapter outlines the development of a classification scheme for TC rainbands and a fully automated algorithm to implement this for the PMW dataset described in Chapter 3. Figure 4.1 provides an outline of the stages of the algorithm development. Different convective phenomena are first defined, and a classification system developed. A total of 1528 images from the 89GHz dataset between 2012 and 2014 are then used to create a validation dataset for the automated classification system. An interactive command line tool is developed for the manual classification of these images. Finally, the complete automated classification process is outlined. A total of 750 images containing at least one rainband are used to train a convolutional neural network for eyewall identification, and another 250 images used for validation against the manually classified images. These validation images are then used to test a clustering routine for rainband identification.

### 4.1 Definitions

This section outlines the definitions used in this study for the TC scale convective structure, eyewalls, SEs, rainbands and SBCs.

#### 4.1.1 TC scale convective structure

Not all TCs have a clear eyewall or rainbands. The first step in the classification scheme is therefore to classify the TC scale convective structure. Qualitative examination of the 89GHz dataset indicates that there are four main convective presentations: no rainbands, no structure, rainbands and sheared. These are summarised below and in Figure 4.2:

- **No bands:** Cases with a clear eyewall but no rainbands. This may include annular hurricanes (Knaff et al., 2003), midget typhoons (Chen et al. 2012) or alternatively cases

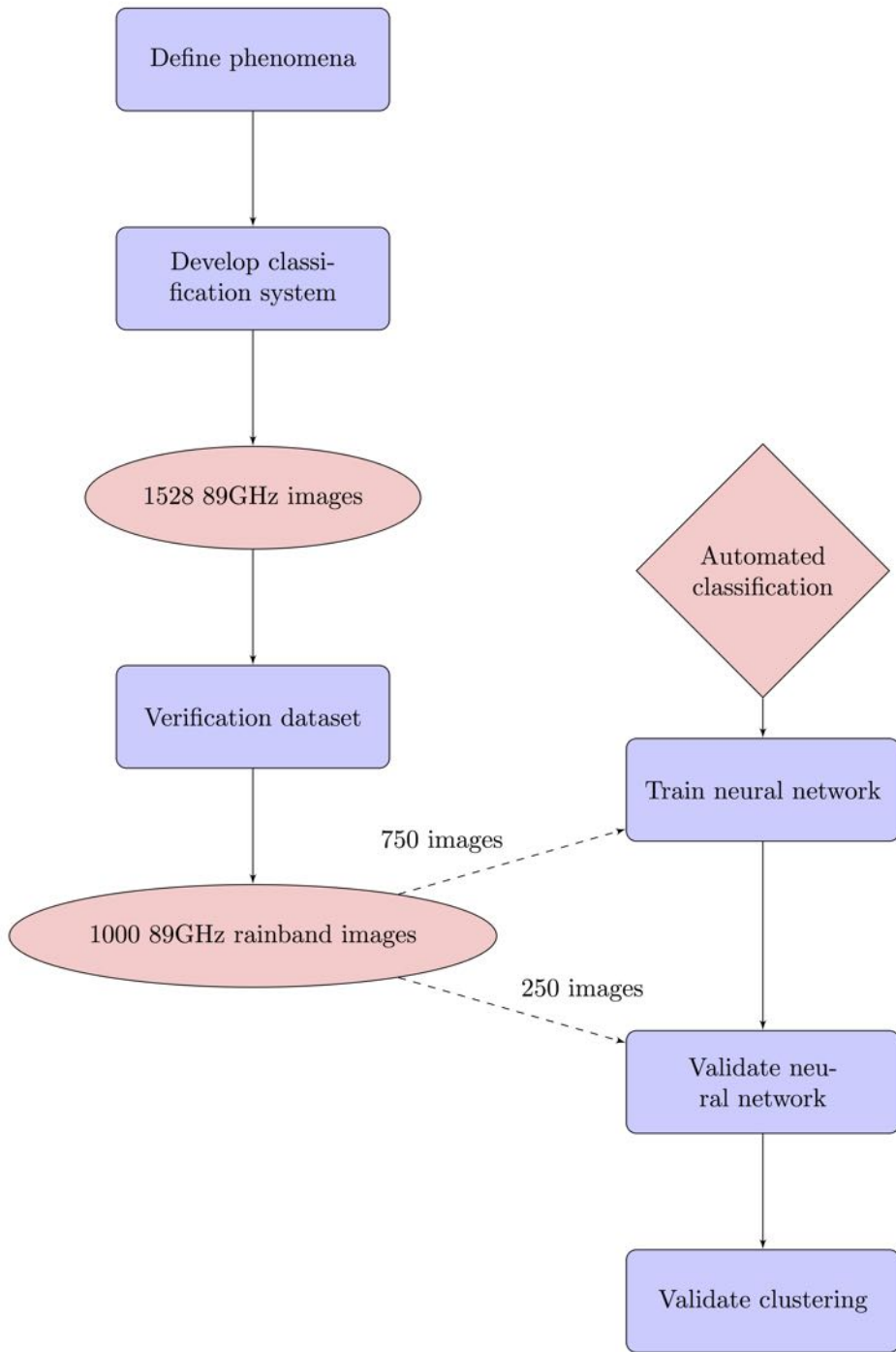


Figure 4.1: Flow chart of the TC classification process.

with convection that does not meet the definition of a rainband (Figure 4.2A).

- **Sheared:** A characteristic structure associated with TCs embedded in flow with strong VWS (Dvorak, 1975), where convection is confined to one half of the TC (Figure 4.2C).
- **Rainbands:** At least one clear spiral rainband meeting the definition of a rainband outlined in Section 4.1.3 (Figure 4.2D).
- **No class:** Cases which do not meet the criteria for any of the above classifications (Figure 4.2B). This category differs from the no bands group in that the TC does not have a clearly defined eyewall.

These categories are similar to those used in both the Dvorak technique (Dvorak, 1975; Velden et al., 2006) and recent crowdsourcing projects classifying TC morphology from IR images (Hennon et al., 2015).

#### 4.1.2 Secondary Eyewalls

Previous climatologies have used varying definitions of what constitutes a SE on PMW imagery. The majority of studies use qualitative definitions. Hawkins and Helveston (2004) used the criterion of ‘a quasi circular ring of lowered brightness temperature that is at least 1/2 complete’. Similarly, Kuo et al. (2009) required that the SE was at least 2/3 complete, with a minimum brightness temperature  $\leq 230\text{K}$ . Yang et al. (2013) proposed the first quantitative definition of a SE, based on radially and azimuthally averaged brightness temperature profiles.

Such a quantitative definition based on averages will still miss many clear SEs. SEs are often elliptical (Piech and Hart, 2008), and with radial and azimuthal averaging small or indistinct SEs will not be identified. Given the wide variety of different presentations of SEs, a qualitative definition is used in this study.

A region of lowered brightness temperature is classified as an SE if it satisfies the following three criteria:

- The image has clear inner and outer eyewalls.
- The outer eyewall is at least 1/2 complete with  $89\text{GHz PCT} < 255\text{K}$  and is quasi circular or elliptical. No constraints are placed on the appearance of the inner eyewall provided that it is visible on the satellite image.
- There is a clear moat between the two eyewalls.

Examples of SEs identified in the PMW dataset are shown in Figure 4.3. In rare cases, triple concentric eyewalls are observed (Figure 4.4). This eyewall configuration has previously been

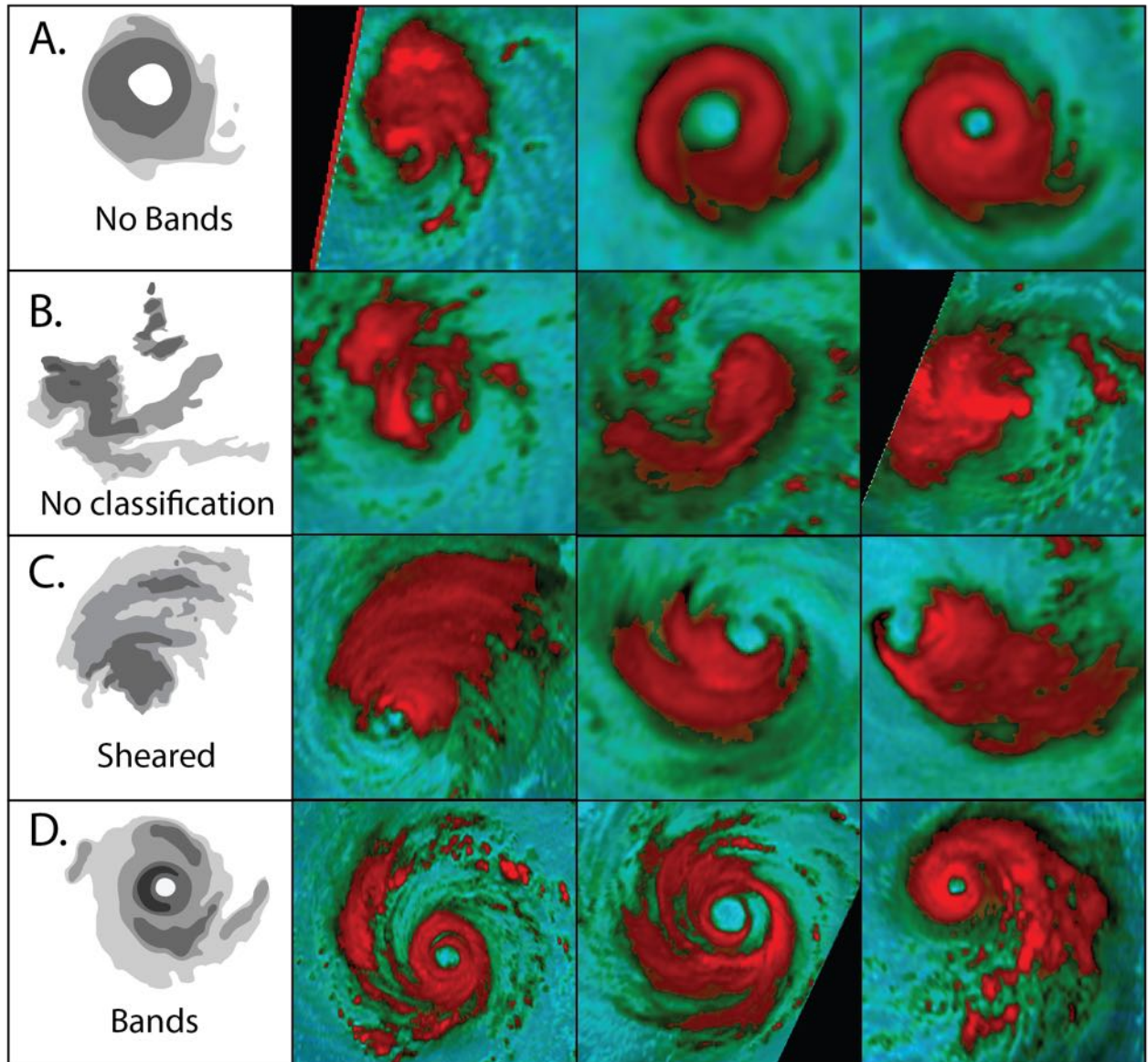
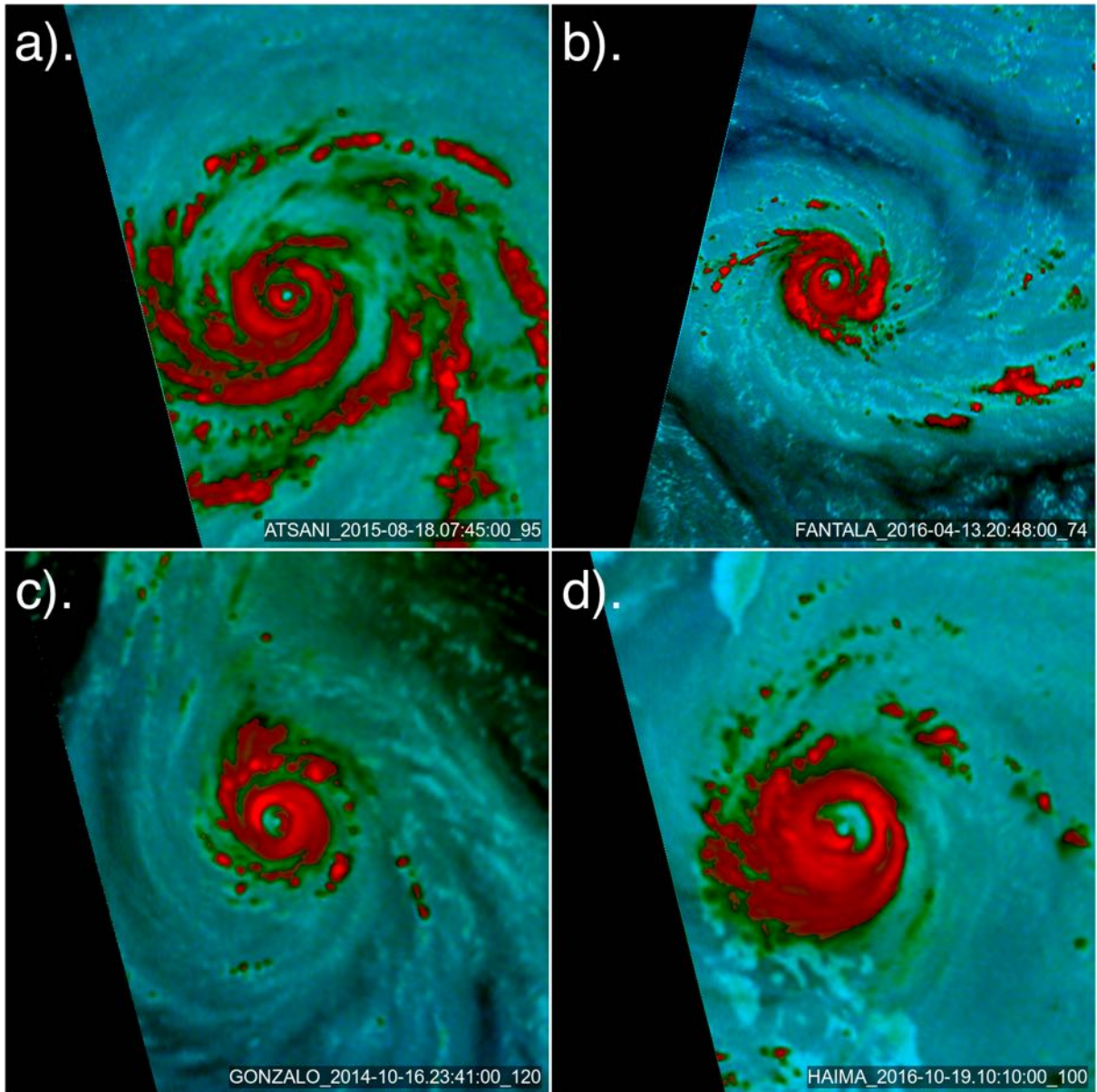


Figure 4.2: Examples of TCs classified in each of the four structural groups. (A) No bands type, showing from left to right cases with (i) convection with no clear banding structure, (ii) eyewall with no clear banding structure and (iii) annular configuration. (B) No classification type, showing three examples of cases with irregular convection and no clear eyewall structure. (C) Sheared type, showing three examples of TCs with convection confined to 180° on one side of the TC. (D) Rainbands type, showing three cases with clearly defined spiral banding structure.



*Figure 4.3: Four examples of SEs on 89GHz PMW imagery.*

documented in high resolution radar studies of Hurricane Juliette (McNoldy, 2004) and Typhoon Usagi (Zhao et al., 2016).

#### 4.1.3 Rainbands

Previous case studies of rainband structure have defined the extent of a rainband as the contour of either 25 or 30dBz reflectivity (Barnes et al., 1983; Powell, 1990a). As reflectivity is not available in the PMW dataset, for this climatology the rainband extent is defined as the region of pixels with an 89GHz PCT  $\leq 255K$  (Spencer et al., 1989).

Even after applying this threshold to isolate areas of rain, in certain scenarios it remains difficult

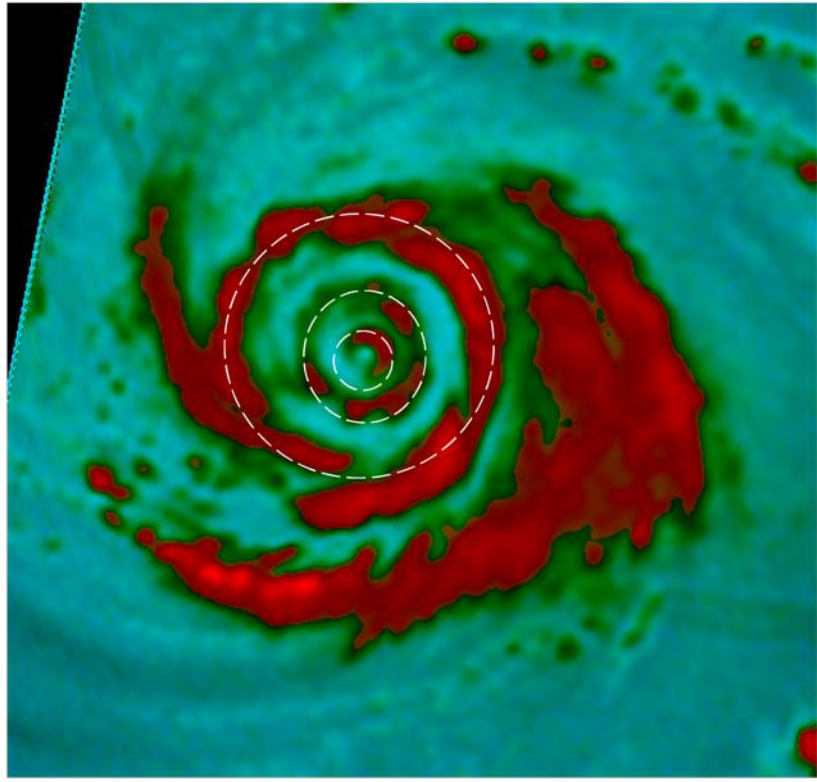


*Figure 4.4: Example of a triple concentric eyewall configuration, with concentric eyewalls indicated by white dashed lines observed in Typhoon Bolaven at 23:29UTC on the 25/08/2012.*

to identify individual bands. Occasionally, sub banding is evident within a PRB, similar to structures observed in radar studies (Hence and Houze, 2008; Tang et al., 2018). In these cases it can be difficult to ascertain whether a given band is its own unique band or part of a larger band (Figure 4.5 (c), (d)). Band identification may also be complicated in cases where the rainbands merge with an MCC upwind (Figure 4.5 (a)). Finally, although clear banding structure may be evident, it is occasionally difficult to isolate the precise extent of each rainband within the SBC (Figure 4.5 (b)).

Given these difficulties, the following definition of a rainband is suitably broad as to deal with some of the uncertainty in the precise location of the bands. In order to be classified as a rainband, a region of lowered brightness temperature must meet the following four criteria:

- The length to width ratio of the band must be greater than 2:1. This criterion filters out ambiguous band complexes and other non-band structures.
- The band must have a clear spiral structure. This also filters out irregular areas of convection.
- The band must be longer than 50 pixels (100km) of 89GHz PCT<255K.
- Gaps in the convection are only permitted if they are less than 10 pixels (20km). The

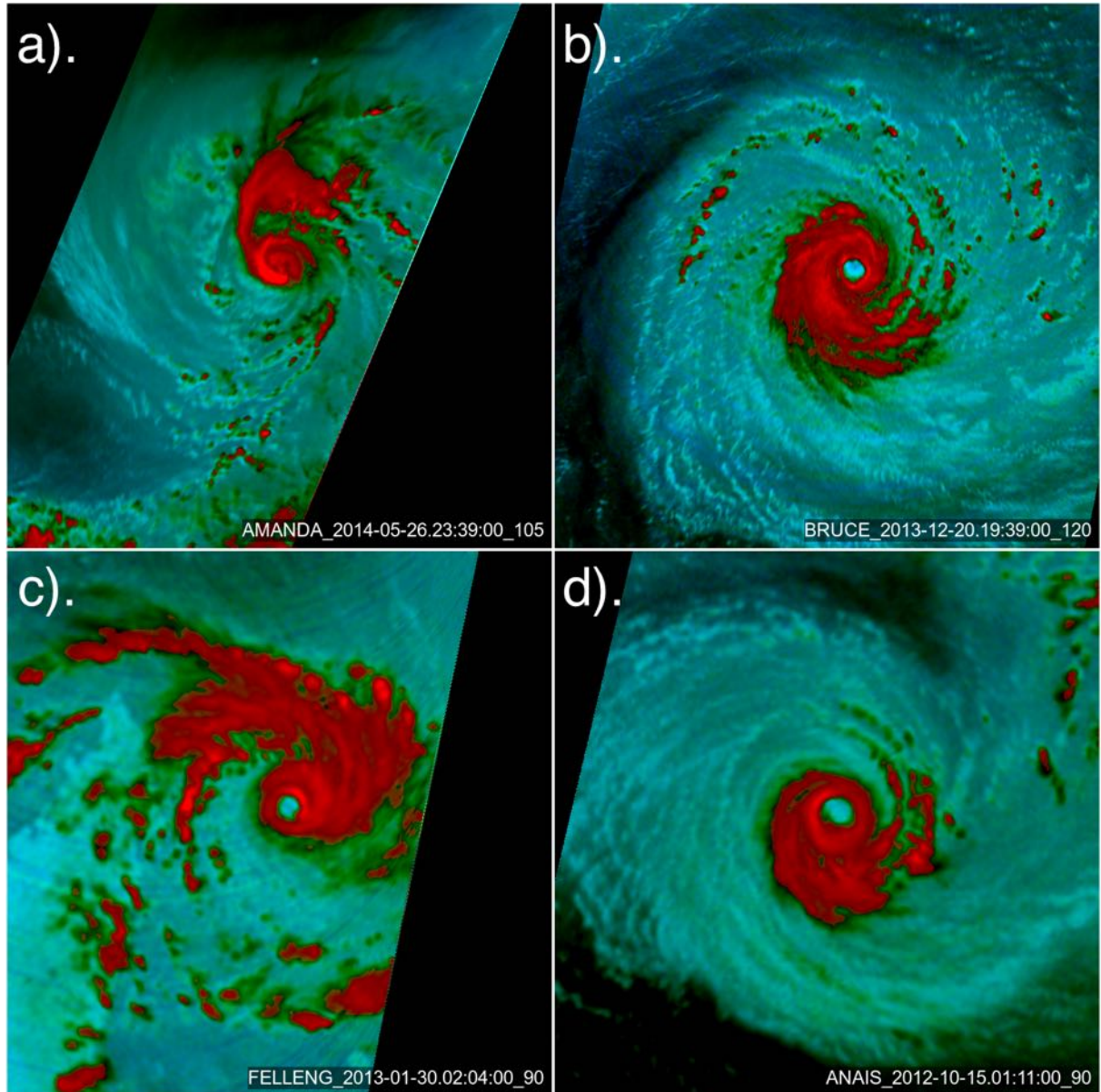


*Figure 4.5: Cases with clear spiral structure but poorly defined individual rainbands. Clockwise from top left. Example of a rainband merging with an upwind mesoscale convective complex. Example of clear spiral banding structure within which it is difficult to isolate the extent of individual bands. Two examples of sub banding structure within a PRB.*

threshold of 20km is based on qualitative comparison with the four channel 89-37GHz composite product described in Appendix A.1 with 89GHz images. This suggests that smaller gaps are usually filled with areas of warm rain, and therefore represent a continuation of the same band.

#### 4.1.4 SBCs

The PRB has variously been defined as ‘the largest and most dominant spiral band visible on satellite imagery’ (Hence and Houze, 2008), ‘a band larger than other rainbands that is stationary relative to the TC centre’ (Didlake and Houze, 2009), ‘a rainband stationary with respect to the IC with wavenumber one characteristics’ (Li et al. 2017) and a ‘prominent spiral shaped feature extending to one side of the vortex’ (Willoughby et al., 1984). Unambiguously identifying the PRB is complicated by the constantly evolving nature of the SBC (May, 1996; Li et al., 2017). This leads to uncertainty in the distinction between the amplifying inner rainbands and PRB during the PRB replacement cycle. For the purposes of this climatology, the SBC is defined as consisting of one PRB together with a number of secondary rainbands satisfying the following four criteria:

- The PRB is stationary or quasi stationary relative to the vortex.
- There is a clear wavenumber one convective asymmetry.
- The PRB is either attached to the eyewall by secondary bands, or separated by a narrow convection free moat.
- All secondary rainbands are attached to either the inner or outer edge of the PRB.

Examples of SBCs identified in the PMW dataset are shown in Figure 4.6.

## 4.2 Classification Scheme

The classification scheme has three primary aims. Firstly, it needs to differentiate between TCs with a single eyewall and those with concentric eyewalls. The identification mechanisms employed at this step must be flexible enough to account for the varying presentations of SEs on PMW imagery. Secondly, the scheme must provide some description of the TC scale convective structure, to assess whether rainbands are present in a given image. Finally, any rainbands and SBC in each image must be individually identified.

A flow chart of the classification system is shown in Figure 4.7. The classification process is implemented in the following steps:

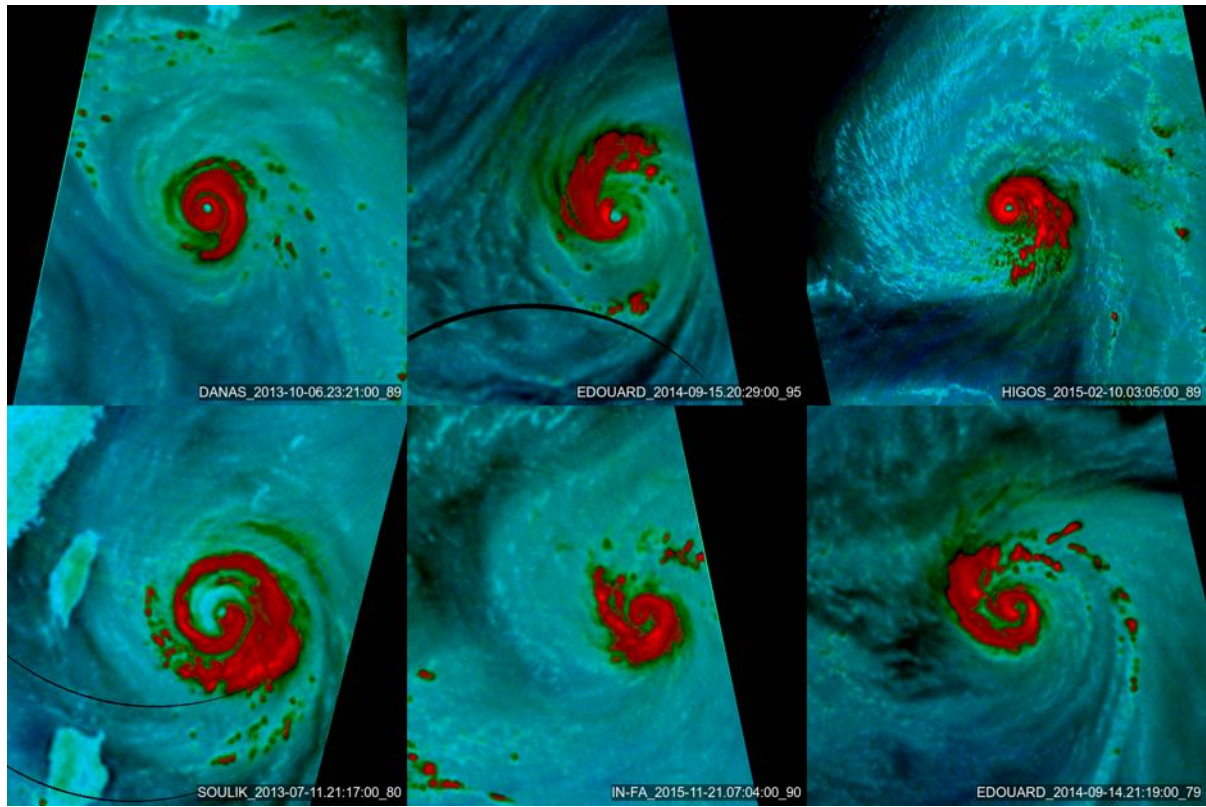


*Figure 4.6: Examples of typical SBCs included in the PMW dataset.*

### **Step 1: screening**

The image is checked to confirm that the entire TC is contained within the swath. Images not containing the entire TC are rejected. Images are also rejected if the TC is clearly extratropical, over land or has intensity <65kts based on IBTrACS data interpolated to the time of the satellite overpass.

### **Step 2: SE ID**

The image is classified as SE or no SE according to the definition in Section 4.1.4.

### **Step 3: TC scale convective classification**

The image is classified as one of the four TC scale convective categories. For all categories except for rainbands, the classification ends here.

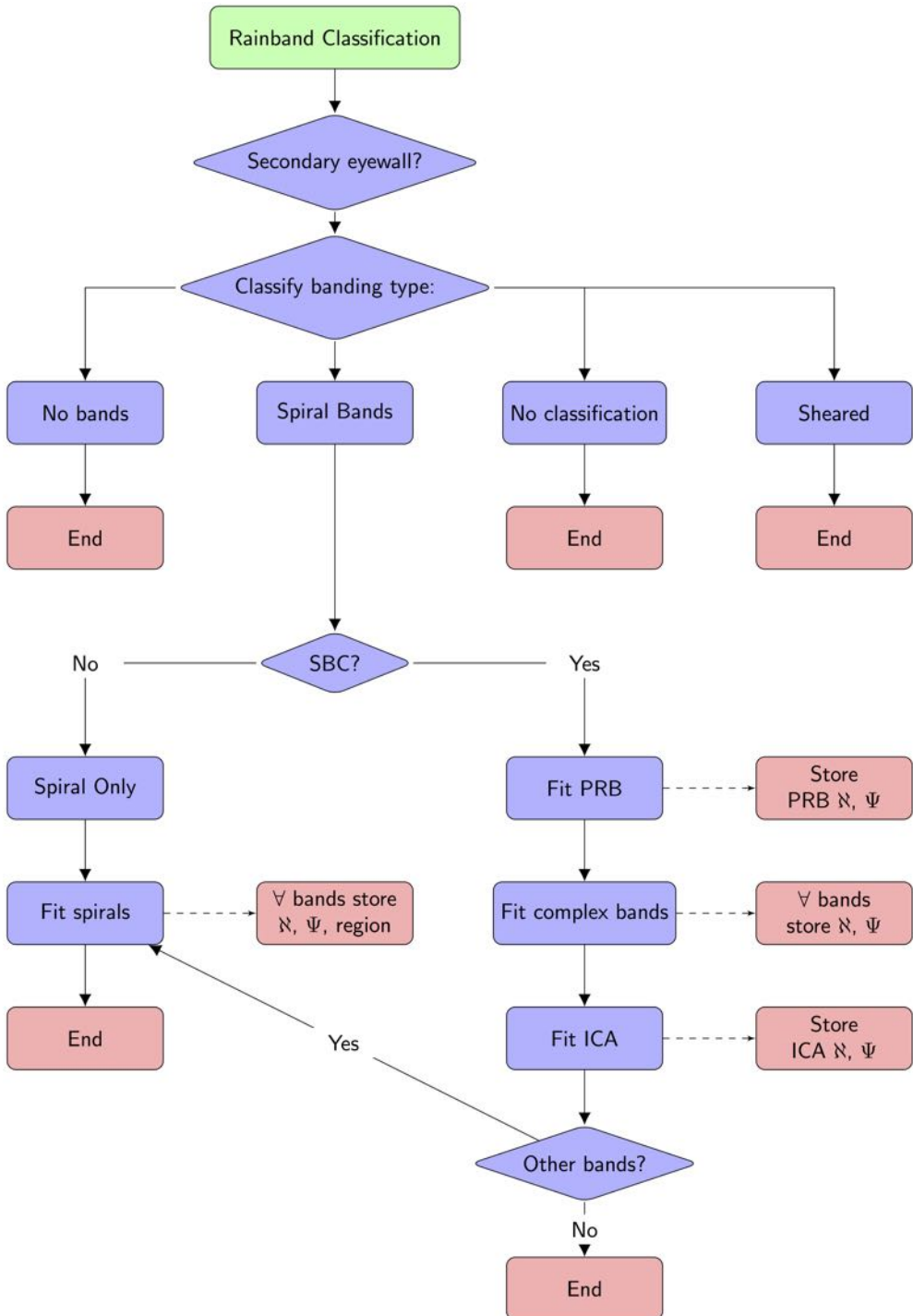


Figure 4.7: Flow chart outlining the rainband morphology classification scheme.

## Step 4: Rainband ID

All rainbands that are not part of the SBC are identified. For each rainband identified in an image, three parameters are stored. Firstly, each band is fitted with a logarithmic spiral using nonlinear least squares minimisation. A logarithmic spiral is described by the equation

$$r = a \times e^{b\theta}$$

Although other models have previously been used to describe TC rainband geometry (Anthes, 1972; Yurchak, 2007), a logarithmic spiral provides the best fit to the widest variety of rainband types (Senn et al., 1957), and has been used to model rainbands in recent work (Kepert, 2018). From the logarithmic spiral curve two parameters are used to characterise each band: the azimuthal coverage ( $\Psi$ ) and crossing angle ( $\aleph$ ). The azimuthal coverage is defined by

$$\Psi = (\theta_f - \theta_i) + 2\pi \times \text{rotations}$$

Where  $\theta_i$  and  $\theta_f$  are the start and finish angles of rainband region, and rotations is the number of 360°rotations around the TC. The crossing angle is defined by

$$\aleph = \tan^{-1}\left(\frac{1}{b}\right)$$

This provides a measure of the circularity of the band, where 0°is circular and 90°is a straight line. In the context of SEF, these parameters capture the extent to which vorticity and diabatic heating project onto the azimuthal mean, and the degree to which the band has axisymmetrised as it evolves into a SE. These parameters are preferred over using the absolute length of the band as they do not depend on the size of the vortex.

Finally, each band is classified as either IC or OC. A rainband is classified as IC if it is located within the quasi-circular region of lowered brightness temperature around the eyewall, and OC if it begins outside of this region (Figure 4.8). This classification is similar to that used in previous PMW climatologies (Cecil et al., 2002; Cecil and Zipser, 2002).

## Step 5: Banding complex ID

Images classified as rainbands are assigned a classification of either SBC or no SBC according to the definition in Section 4.3.2. A SE typically forms from the innermost band within the SBC, which may be either the PRB or an amplifying secondary band. A new parameter, termed the Inner Crossing Angle (ICA) is therefore associated with cases with a SBC. For this parameter, a logarithmic spiral is fitted to the innermost edge of the band complex that is clearly separated from the eyewall (Figure 4.9). This provides a measure of the degree of axisymmetrisation of

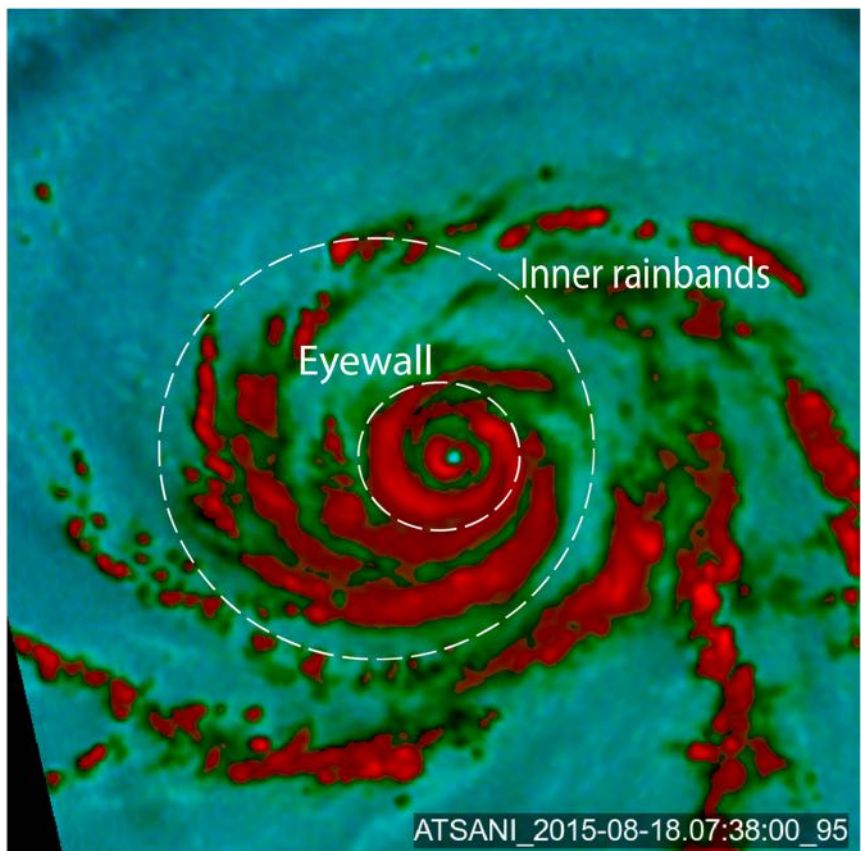
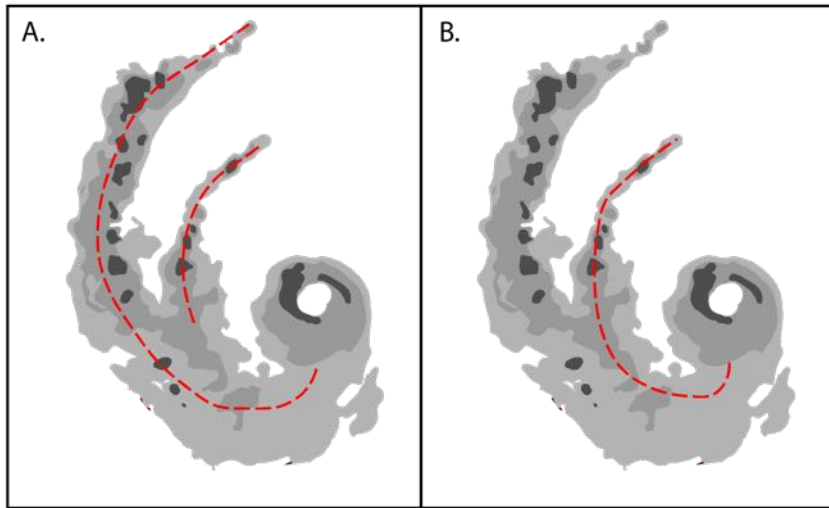


Figure 4.8: Example of the distinction between the eyewall (within the innermost dashed circle), IC (within the second dashed circle) and OC (outside of both circles) rainband regions.



*Figure 4.9: Example of a stationary banding complex with (A) one PRB and one secondary rainband identified and (B) the ICA parameter shown as red dashed lines.*

the SBC as a whole. Finally, all secondary bands in the SBC are fitted with logarithmic spirals.

### 4.3 Validation dataset

Developing a fully automated version of this algorithm is reliant on having a verification dataset to test it against. A difficulty in accurately classifying the rainbands is that, unlike for SEs there may be multiple different interpretations of the same rainband scene, of which none are inherently incorrect. A common approach to dealing with this problem is to use crowdsourcing to produce multiple independent classifications of an image, and combine this with deep learning methods to produce the best guess at the labelled training/verification data. This technique has been used successfully in the galaxy zoo project for galaxy classification (Lintott et al., 2008), for classifying geographical structures (Haklay, 2013) and in medicine (Kurtek et al., 2013). Similar methodology has also been applied to classifying TC scale convective morphology from IR imagery as part of the TC Centre project (Hennon et al., 2015; Knapp et al., 2016).

To create the validation dataset, a command line tool is developed using MATLAB to interactively implement the classification scheme. This software is available at <https://github.com/anna-184702/tc-class>. Although there is only one classification for each image in this project, this tool could easily be scaled to a large user base similar to the crowdsourcing applications described in this section to increase confidence in the verification dataset. Using this tool, images

are sequentially read in from the 89GHz dataset and shown to the user. Images are automatically rejected if the interpolated best track intensity is less than 65kts or the TC is flagged as extratropical. An example of the user interface for classifying an image of Hurricane Marie (2014) is shown in Figure 4.10.

In the first step (Figure 4.10 (a)), the user rejects the image if it does not contain the entire TC. Rejected images are deleted from the dataset and the next image is shown. If the image is accepted, then the classification continues.

In the second step (Figure 4.10 (b)), the user determines whether or not a SE is present and classifies the TC scale convective structure. If the structural classification is not rainbands then the classification ends. Otherwise, the process continues and the user is prompted to select the centre of the image. They then select whether or not a stationary banding complex is present, and input the number of secondary bands within the complex.

The user is next prompted to select the location of the PRB by marking the location on the image using the MATLAB imfreehand tool. Figure 4.10 (c) shows this selection process, with the selected band marked as a blue line. For this band, and all rainbands subsequently selected, a logarithmic spiral is fitted to the band relative to the centre selected in step 2, and the azimuthal extent and crossing angle are stored. This process is repeated for any secondary rainbands and the ICA parameter.

In the fourth step (Figure 4.10 (d)), all rainbands that are not part of the SBC are selected. In the Hurricane Marie example, there is one outer rainband. The user is then prompted to enter the region of this band.

Figure 4.10 (d), shows a summary of the interface at the conclusion of the classification process. This data is written to a .mat file for subsequent post-processing, completing the classification. This technique was applied to a total of 106 TCs between 2012 and 2014 for 1586 individually classified PMW images in the validation set.

## 4.4 Automated Classification

### 4.4.1 Image processing for TCs

A problem with the subjective classification scheme is that there is an inherent degree of uncertainty as to what precisely constitutes an eyewall or rainband. This, together with the impracticality of applying a subjective classification scheme across more than a few thousand images, motivates the development of a fully automated method of classifying TC structure. This objective technique needs to perform the following steps:

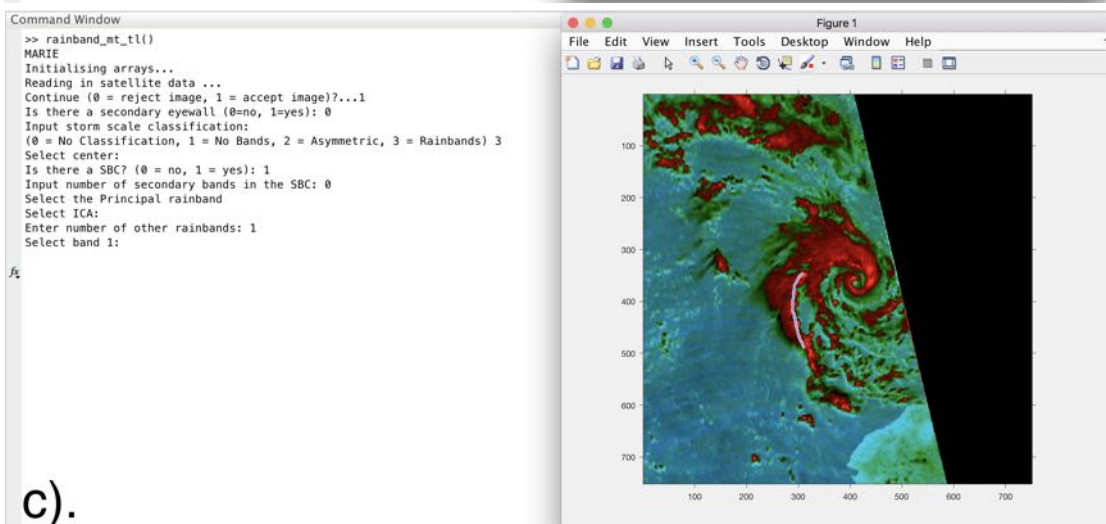
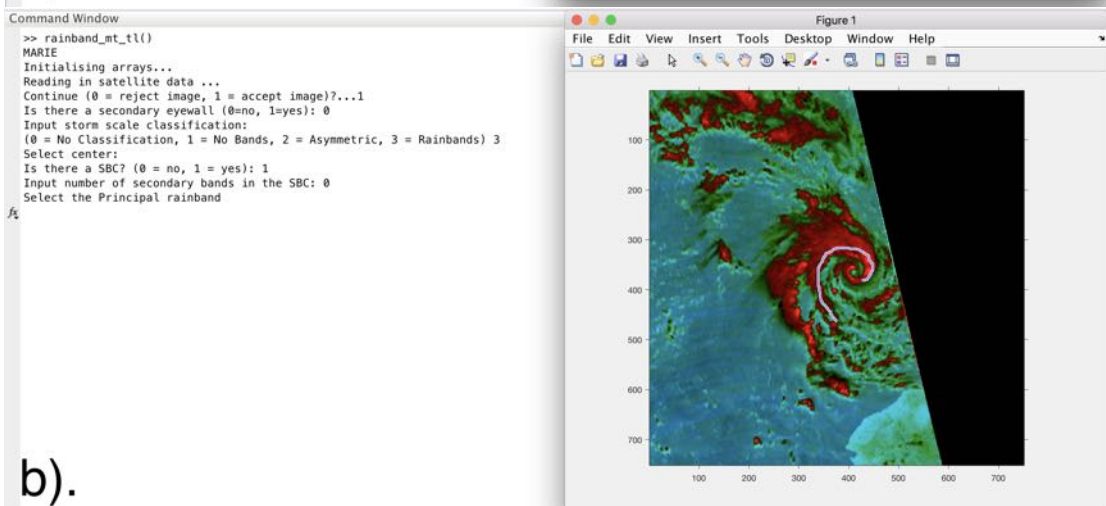
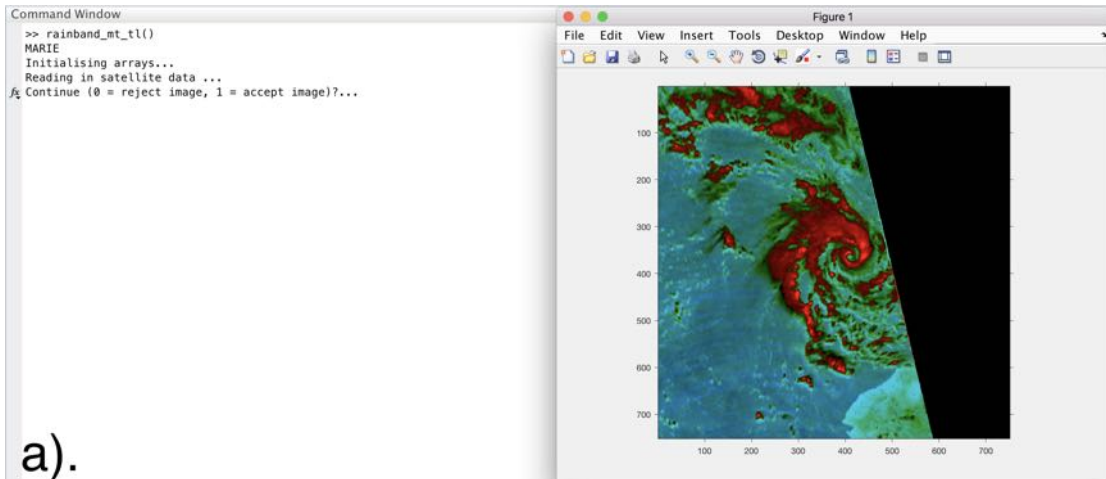


Figure 4.10: Example of the MATLAB implementation of the command line classification process on an AMSRE image of Hurricane Marie (2014) at 09:03UTC on the 23/08/2014.

1. Identify whether an eyewall and SE are present, and distinguish between no eyewall, single eyewall and concentric eyewall cases.
2. Mask out pixels classified as eyewalls.
3. Identify the pixels belonging to each rainband, and correctly reject clusters without the requisite banding structure.
4. Fit a logarithmic spiral to each band.
5. Determine whether an image contains a SBC, and if so identify the PRB and fit the ICA parameter.

Formally, this is an example of an *instance segmentation* problem (Girshick et al., 2016). This is a category of computer vision problems in which individual objects in an image are identified and pixels are assigned to an object class and a particular instance of that object. This is in contrast to *semantic segmentation*, where pixels assigned to a class but not an individual instance.

Machine learning problems are often categorised as either *supervised* or *unsupervised* (Goodfellow et al., 2016). In a *supervised learning* problem, an algorithm ‘learns’ to recognise patterns based on training with a labelled dataset. In contrast, in *unsupervised learning* an algorithm groups data with similar characteristics. The first step of the automated classification process is to handle the eyewall identification. As eyewalls and SEs are clearly defined on PMW imagery, this is best treated as a supervised learning problem. On the other hand, as discussed in Section 4.3, precisely what constitutes a rainband is often ambiguous. To eliminate possible bias resulting from human error within the training dataset, rainband identification is treated as an unsupervised problem.

The next point to consider is how to implement these two components. For the supervised learning step, the approach needs to be flexible enough to identify eyewalls of different sizes and located at different positions in an image, and capable of distinguishing between PRB moats and SEs during axisymmetrisation and generating pixel level masks. The naive approach to this problem is to employ techniques previously used in meteorology, involving centre finding and identifying SEs based on the brightness temperature profile in each quadrant. Initial attempts at implementing the classification scheme focussed primarily on this approach, using the Automated Rotational Centre Hurricane Eye Retrieval (ARCHER) centre finding algorithm to objectively determine the centre of each TC (Wimmers and Velden, 2010, 2016). This was trialled together with the Yang et al. (2013) objective definition of SEs to classify images. Three major issues arise with this approach. This method is not suitable for identifying asymmetric SEs (e.g Figure 4.3 (c)), resulting in a high number of false negatives. Secondly, the ARCHER algorithm, while reasonably accurate, is very computationally expensive, taking 30 to 40 seconds for each image. Finally, the combination of these two approaches is unsuitable for identifying

which pixels belong to eyewalls at instance level.

In computer vision applications, the most widely used technique for this type of problem is a Convolutional Neural Network (CNN; LeCun et al. 1989, Krizhevsky et al. 2012). A CNN is a subclass of Neural Networks that are optimised for dealing with multidimensional arrays - in this case RGB images. Such a network takes an array of data as input and ‘learns’ patterns in the data. The data is fed through a sequence of max pooling and convolutional layers. In the convolutional layers, the image is convolved using a set or ‘bank’ of filters to produce an array of activation maps. After several of these convolutional layers, the dimensionality is reduced by applying a convolutional ‘pooling’ filter. CNNs have multiple iterations of these layers, culminating in several fully connected layers and a classification step. During training, the network successively learns the activation patterns of smaller and smaller scale features via back propagation of the training dataset. Several recent studies have used CNNs for data analysis in meteorology, including for predicting TC intensity (Pradhan et al., 2018) and identifying hail storms (Gurung et al., 2018).

A common approach to CNN problems is to take an existing open source network architecture and modify it to work with the required dataset. Choosing a particular architecture is dependent on the characteristics of the problem. For identifying eyewalls, desired features of the network are that it is able to accurately identify features at instance level and performs well for objects spanning a range of sizes. A popular architecture for such instance segmentation problems is the Mask Region proposal Convolutional Neural Network (Mask R-CNN; He et al. 2017). Mask R-CNN was developed at the Facebook Artificial Intelligence Laboratory, and consists of a backbone CNN together with additional software to perform instance segmentation on multiple objects in an image. The network first generates region proposals, or bounding boxes where objects may be located (Girshick, 2015; Ren et al., 2017). The backbone convolutional neural network, ResNet101 (He et al., 2016), is then run on each region of interest to generate a feature map. Mask-RCNN includes an initial step in the bounding box generation known as the feature pyramid network (FPN; Lin et al. 2017) which improves the CNN performance for classes where objects span a large range of sizes. This feature makes it ideal for the PMW dataset, where there are considerable size differences between instances of eyewalls. After the feature map is generated from the backbone CNN, two separate branches generate a classification and mask for each object. For an in depth discussion of the Mask-RCNN architecture, see Appendix C.1.

Having identified and masked out the eyewalls, it is then necessary to use an unsupervised algorithm to identify instances of rainbands. Although this has not previously been attempted, it is similar to the problem of classifying spiral galaxy morphology (Figure 4.11). Although the physical mechanisms driving spiral arm formation in galaxies and rainband formation in TCs are distinct, the geometry of both of these phenomena is approximated by logarithmic spirals (Ma, 2001; Seigar et al., 2006; Davis and Hayes, 2012). Multiple classification schemes have

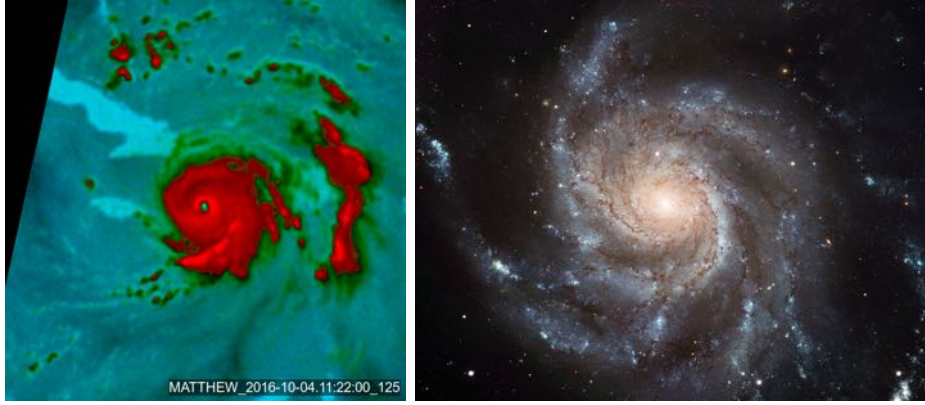


*Figure 4.11: Similarities in spiral structure between a TC and spiral galaxy M51. Image retrieved from <https://www.nasa.gov/feature/goddard/2017/messier-51-the-whirlpool-galaxy>*

been developed to classify spiral arm structure in galaxies (Peng et al., 2002; de Souza et al., 2004; Peng et al., 2010). Initial work as part of this study focussed on using Fourier transform methods (Puerari and Dottori, 1992), hough transforms (Pei and Horng, 1995) and density based clustering (Tramacere et al., 2016), however none of these frameworks proved suitable for reliably identifying rainbands at instance level.

Only one fully automated galaxy classification scheme has been developed, known as the SPiral Arc FIting and REporting algorithm (SpArcFiRe; Davis and Hayes 2012, 2014). One component of the SpArcFiRe package is a clustering routine for automatically identifying spiral arms, which is used to identify TC rainbands. The clustering consists of three stages. A multiscale orientation field (Au, 2006) is first generated for the image. Initial clusters are then generated using single-link hierarchical agglomerative clustering on the resulting field. Finally, these clusters are merged based on logarithmic spiral fits. For a complete description of the clustering scheme and alterations to the original SpArcFiRe algorithm made as part of this study, see Appendix D.

#### 4.4.2 Automated classification

The stages of the automated classification process are summarised in Figure 4.12. The eyewall structure is first classified using Mask-RCNN. The eyewalls are then masked, followed by pre-processing to enhance the contrast between rainband regions and the image background. The image is then passed through the SpArcFiRe clustering scheme to identify the rainbands, and finally the output is post-processed. This section details the software used in each step in this process, using an AMSRE image of Typhoon Megi (2016; Figure 4.13) as an example.

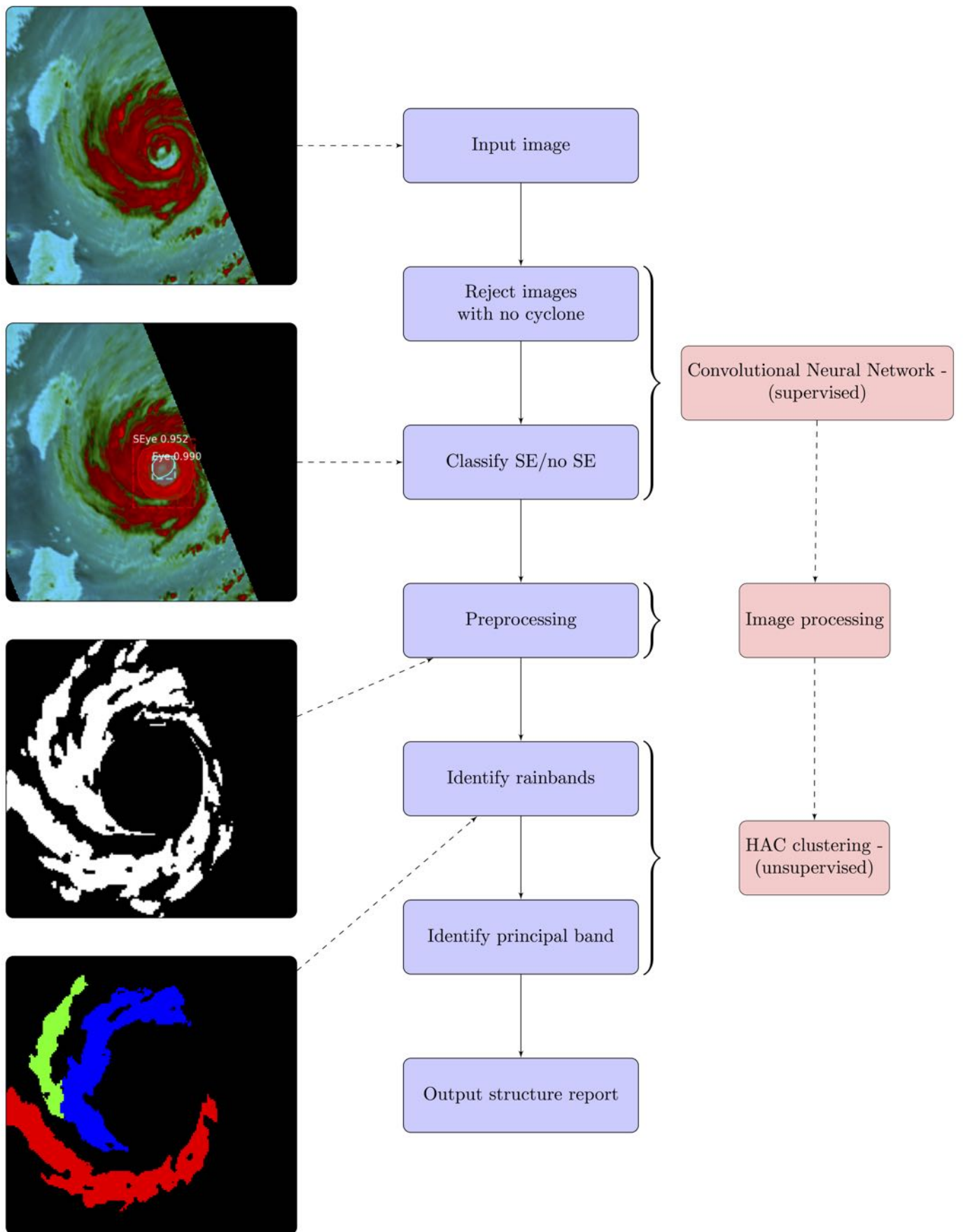


Figure 4.12: Overview of the automated classification technique.

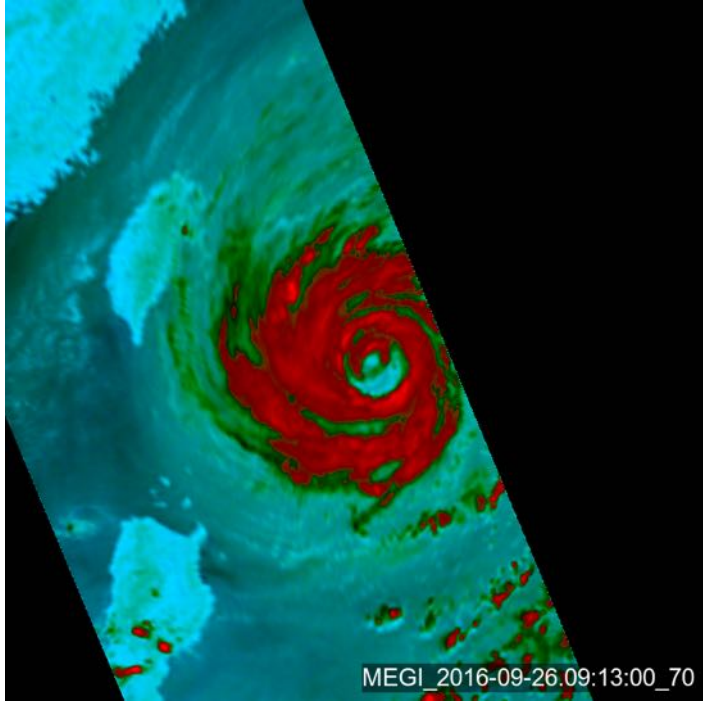


Figure 4.13: Image of Typhoon Megi at 09:13UTC on the 26/09/2016 used to demonstrate the stages of the automated classification system.

## Mask-RCNN

Several different implementations of Mask-RCNN have been developed. This study utilises the open source Matterport implementation (Abdulla, 2017), written in the Keras (Chollet et al., 2015) and Tensorflow (Abadi et al., 2015) libraries. Training and visualisation code was also adapted from an open source robotic surgery project using Mask-RCNN (Ye, 2018).

The network is trained on a dataset of 1000 images, of which 200 have been manually verified to contain a SE. A stratified training/testing split is performed with 750 (600 eyewall, 150 SE) training images and 250 (200 eyewall, 50 SE) testing images. Eyewall and SE masks are manually marked on each image of the training dataset using the VCG Image Annotator software (Dutta et al., 2016).

For full details of the network tuning, see Appendix C.2. With the small training dataset, stopping overfitting is a significant challenge. Transfer learning, image augmentation and a shallower backbone network are used to prevent overfitting. Transfer learning refers to initialising the model with weights from previous training runs. As model is already trained to identify certain patterns, it is then able to generalise this information to new classes more efficiently (Pan et al., 2010). For this project, the network backbone was initialised using pre-trained Microsoft Common Objects in COntext (MS-COCO; Lin et al., 2014) weights included in the Matterport Mask-RCNN distribution. A ResNet50 backbone CNN was used rather than the deeper ResNet100 version included in the original MaskRCNN paper. Although this network

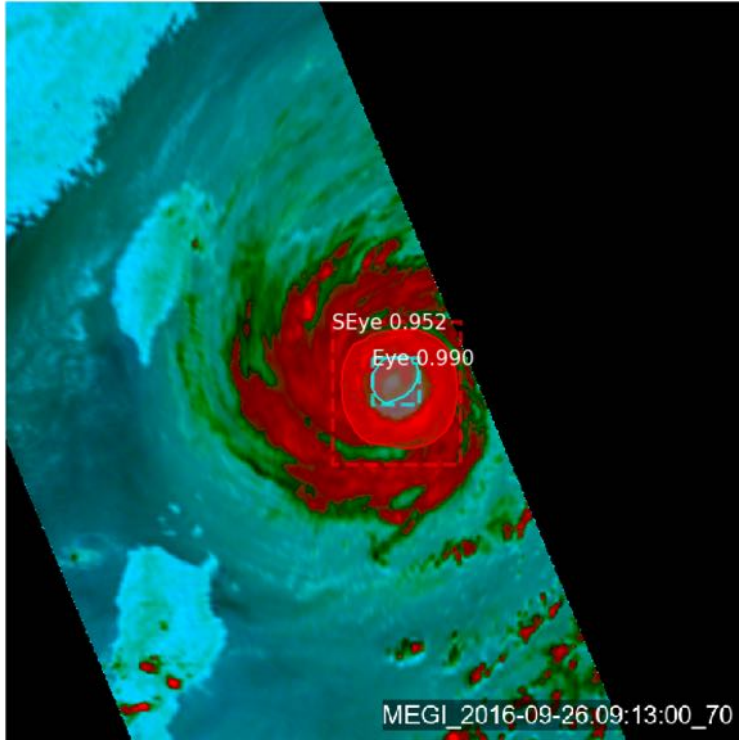


*Figure 4.14: Example of Mask-RCNN output for identifying an eyewall and SE in the example image. Eyewall masks and bounding boxes displayed using code adapted from Ye (2018).*

is typically less accurate, limiting the number of degrees of freedom allows for more robust fitting on a small dataset. Finally, image augmentation was implemented with the python imgaug library (Jung, 2018) to artificially increase the size of the training dataset. Artificial images were generated by randomly flipping an image up/down or flipping left/right each time it was fed through the network during training. The network was trained for 26 epochs on two NVIDIA K80 GPUs. Output for the example image is shown in Figure 4.14.

## Image preprocessing

Identifying rainbands based on unsupervised clustering relies on the rainbands being clearly defined against the image background. This is frequently not the case in the raw PMW images (e.g Figure 4.5). As the clustering relies on orientation filters, the size of the images also needs to be standardised. A three stage preprocessing technique is used, consisting of eyewall masking and resizing, two successive convolutions using contrast limited adaptive histogram equalisation (CLAHE; Pizer et al. 1987) and finally linear Gaussian unsharp masking. Stages of the preprocessing for the example image is shown in Figure 4.16.

Eyewalls in the image are first masked using the mask output from the Mask-RCNN step, and the centre identified by taking the centroid of the eyewall mask (Figure 4.16-2). The image is then re-centred and resized to  $200 \times 200$  pixels (4.16-3). A common issue in the images is that convection may be present in the image that is not part of the spiral banding structure. These

regions must be filtered out prior to the clustering step. The TC and rainbands are extracted from the image using a combination of clustering and binary dilation. Binary dilation using a  $10 \times 10$  circular pixel wise element is first applied to all pixels with  $R > 0$  to group rainfall areas within 20km of each other. The image is then broken into connected components, and the closest component to the centre is taken to be the TC.

Enhancing the contrast in an image is often accomplished using histogram equalisation. Traditional histogram equalisation enhances the global contrast of an image by dividing pixels into bins based on their intensity. Let

$$p_n = \frac{|\text{pixels of intensity } n|}{|\text{total pixels}|}$$

In histogram equalisation, the intensity of each pixel  $i_{mn}$  of the 255 values is then mapped to a new intensity

$$I(i_{mn}) = \lfloor 255 \sum_{n=0}^k p_n \rfloor$$

This enhances the global contrast of the image. To enhance rainband contrast, it is necessary to increase the local contrast of the image. This is accomplished using CLAHE, which applies histogram equalisation sequentially on local patches of an image. In order to limit amplification of noise in homogenous areas of the image, clipping is applied where an upper limit is imposed on the number of counts in any one bin. CLAHE is therefore defined by

$$p_n = \begin{cases} \lfloor 255 \sum_{n=0}^k p_n \rfloor, & p_n < c_{val} \\ p_n, & p_n \geq c \end{cases}$$

For the 89GHz dataset, optimum results were obtained applying CLAHE to an image twice with a  $9 \times 9$  pixel filter (Figure 4.16-4,5). A further example of how this improves contrast in an image with poorly defined banding structure is shown in Figure 4.15.

Gaussian unsharp masking is then used to isolate the rainband pixels (Figure 4.16-6). Unsharp masking is a method of image sharpening where the image is blurred using convolution with a Gaussian blur, with the  $i, j$ th pixel given by:

$$I_{blur}^{ij} = \frac{1}{9} \sum_{n=i-4}^{i+4} \sum_{m=j-4}^{j+4} \frac{1}{2\pi\sigma} e^{-\frac{x^2+y^2}{2\sigma^2}} x_{mn}$$

The resulting image ( $I_{blur}$ ) is then subtracted from the original using a weighted sum a

$$I_{sharp} = 2.5 \times I - 0.5 \times I_{blur}$$

This step is similar to the preprocessing component of the SpArcFiRe software (Davis and

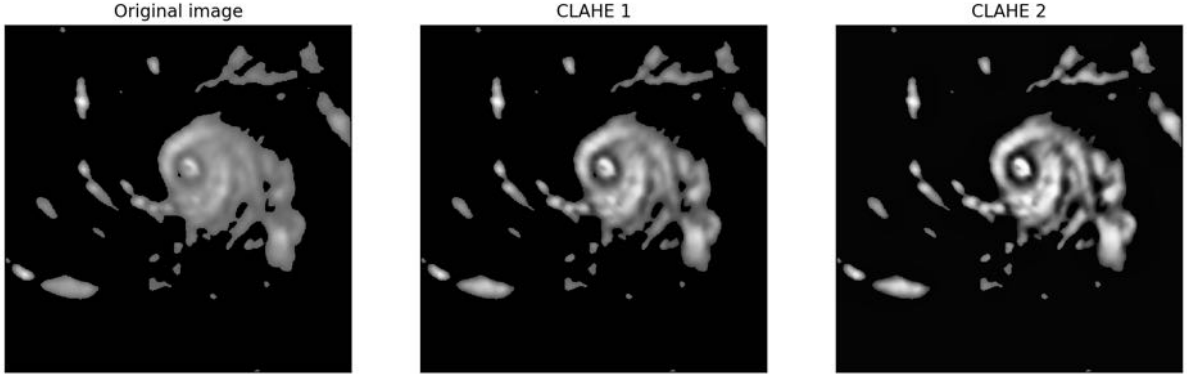


*Figure 4.15: The three stages of CLAHE pre-processing, from left to right: the original image, output after the first application of the CLAHE filter and output after the second application of the CLAHE filter.*

Hayes, 2012). Finally, the intersection of the all pixels classified as raining ( $PCT < 255K$ ) in the initial image and the unsharp mask region is taken to give the preprocessed image (Figure 4.16-6).

$$I_{final} = (I_{initial} \geq 255) \cap (I_{sharp} > 0)$$

This reverts back to the physically justified threshold for rainfall, as the sequence of transformations distort the image brightness.

### SpArcFiRe rainband identification

The final step in the processing is to apply the SpArcFiRe clustering to the preprocessed image set. Each image from the preprocessed dataset is fed through this clustering step, which identifies each rainband, fits a logarithmic spiral and outputs a list of rainbands together with their crossing angles and azimuthal extents (Table 4.1).

Based on the clustering output, an image is classified as PRB or no PRB. A cluster is marked as a PRB if it is at least twice as large as all other clusters. From this, the SBC is identified by including all rainbands that are simply connected to the PRB, and the ICA parameter is calculated from the inner edge of the SBC pixels.

### 4.4.3 Output

The complete process outputs a structural report of the image to a .csv file. Output for each image consists of whether a TC, eyewall, SE and PRB were found in the image, how many rainbands were identified and the crossing angle and azimuthal extent for each band. Output for the example image is shown in Table 4.1.

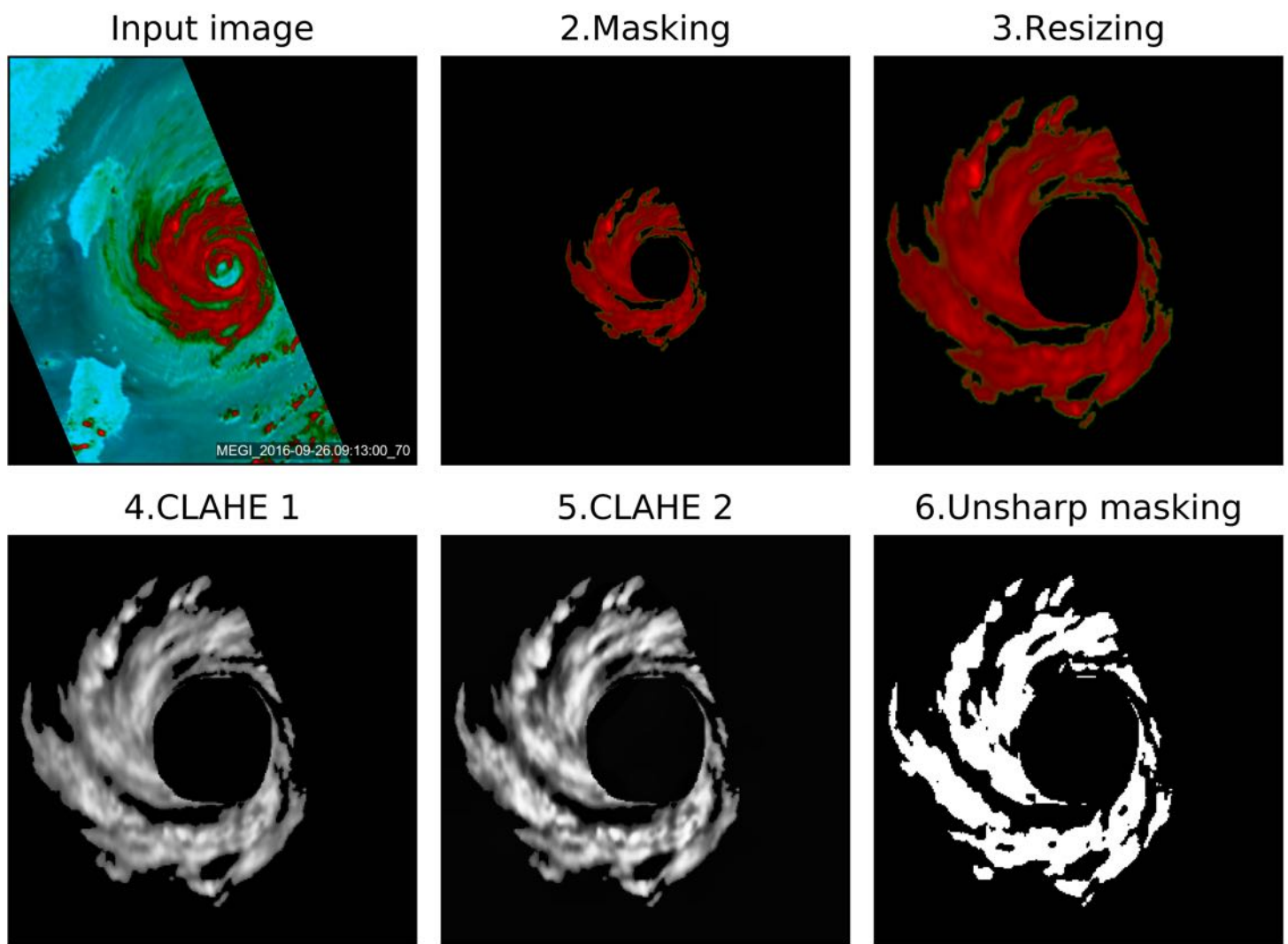


Figure 4.16: Stages of image pre-processing, showing (1) the original image, (2) original image R channel after eyewall masking using mask output from mask-RCNN, (3) resized image, (4) after first application of CLAHE, (5) after second application of CLAHE and finally (6) the preprocessing output after unsharp masking and thresholding.

Output for image: Typhoon MEGI		
TC included	YES	
Eyewall	YES	
SE	YES	
PRB	NO	
Number of rainbands	3	
Band 1 (GREEN)	$\aleph = 16.53$	$\Psi = 178$
Band 2 (BLUE)	$\aleph = 14.25$	$\Psi = 45$
Band 3 (RED)	$\aleph = 7.41$	$\Psi = 191$

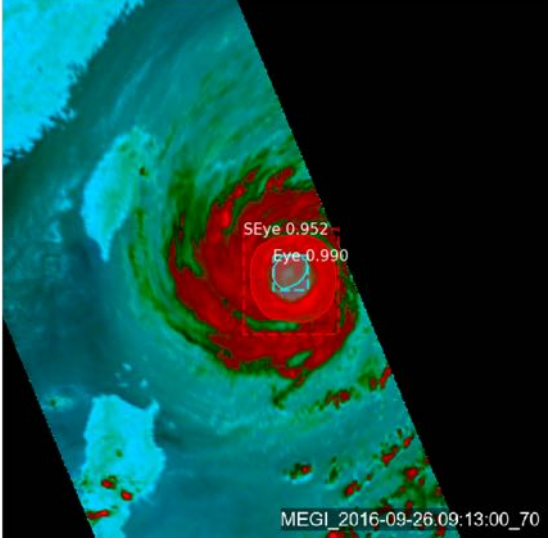
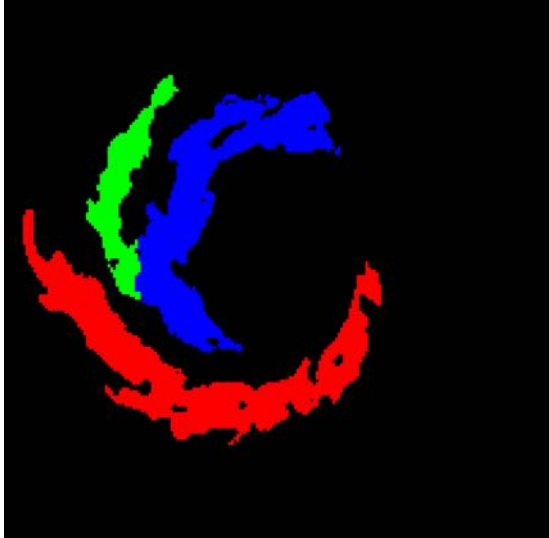



Table 4.1: Output from the classification algorithm, showing each rainband in a different colour, together with the crossing angle and azimuthal extent of each band. Rainband clusters are shown using software adapted from the SpArcFiRe project (Davis and Hayes 2014). Eyewall masks and bounding boxes are displayed using software adapted from (Ye, 2018).

## 4.5 Verification

### Eyewall identification

In validating the Mask-RCNN portion of the classification scheme, an identification is counted as a hit if

- The Mask-RCNN classification is correct
- At least 80% of pixels in the Mask-RCNN generated mask overlap with the manually selected mask in the validation set.

As the class sizes are unbalanced, accuracy statistics for eyes and eyewalls are presented separately.

Four metrics are used in evaluating the model performance for each class: accuracy, precision (also known as probability of detection) recall and false alarm rate (FAR). These are defined in terms of the true positives (TP), true negatives (TN), false positives (FP) and false negatives (FN) for each model. The accuracy is defined as the ratio of correct outcomes to total outcomes

$$Accuracy = \frac{TP + TN}{TP + TN + FP + FN}$$

The precision is the ratio of true positives to all positives, and is therefore the percentage of correct positive identifications.

$$Precision = \frac{TP}{TP + FP}$$

The recall is the ratio of correctly identified true positives to all positives

$$Recall = \frac{TP}{TP + FN}$$

Finally, the FAR is the ratio of false positives to all negatives

$$FAR = \frac{FP}{FP + TN}$$

The total accuracy over multiple classes is assessed using the (unweighted) Macro-F1 score, defined by.

$$F_{macro} = \sum_{classes} \frac{2 \times precision \times recall}{precision + recall}$$

Values of these parameters for each of the two classes are shown in Table 4.2.

For the eyewall class, the network has an accuracy of 100%, precision of 100%, recall of 96% and false alarm rate of 0%. The model performs well detecting eyewalls across multiple scales (Figure 4.17 (a, b)). Though the mask accuracy was not fully evaluated, qualitatively fits are

---

Mask-RCNN verification

---

Class: EYEWALL,  $n_{val} = 200$

---

	Predict True	Predict False
Observed True	96%	4%
Observed False	0%	100%
Accuracy	100%	
Precision	100%	
Recall	96%	
FAR	0%	

---

Class: SE,  $n_{val} = 50$

---

	Predict True	Predict False
Observed True	88%	12%
Observed False	5%	95%
Accuracy	85%	
Precision	83%	
Recall	88%	
FAR	5%	
Macro F1	91%	

---

*Table 4.2: Validation statistics for Mask-RCNN eyewall identification.*

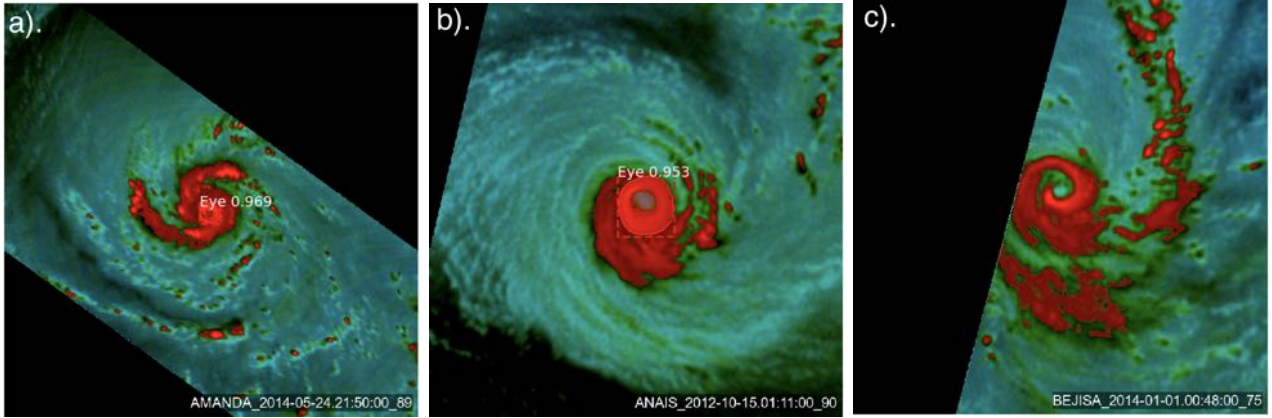


*Figure 4.17: Examples of successful identifications of (a) a small eyewall and (b) A large eyewall and (c) example of a false negative with a banding eyewall. Eyewall masks and bounding boxes are displayed using software adapted from Ye (2018).*

excellent. The one situation in which eyewalls are not identified by the model is when they appear to form part of a rainband (Figure 4.17 (c)). In this case, the objective classification scheme classes the convection as part of a rainband rather than an eyewall.

For the SE class, verification values are slightly lower, with 85% accuracy, 83% precision, 88% recall and a 5% false alarm rate. The network performs well generating accurate region proposals for clear SEs (Figure 4.18 (a)), elliptical SEs (Figure 4.18 (c)) and partial SEs (Figure 4.18 (b)). The most common scenario resulting in false positives is a strong PRB with a very symmetric moat (Figure 4.18 (e)). In most cases, however, the model is successfully able to distinguish between moats and SEs (Figure 4.18 (f)). False negatives occur in situations where the inner eyewall is indistinct, particularly as it begins to decay during an eyewall replacement cycle (Figure 4.18 (c)). In many of these cases, the model identifies the SE as an ROI, however the probability assigned to the SE class is below the detection threshold.

## Rainband identification

Results of the clustering component of the classification were verified for the 250 training images in the validation set for Mask-RCNN. A rainband identification was classed as a hit if it either matched the band configuration in the validation set or if the chosen rainband configuration was also a possible interpretation. Quantitative comparisons were not made at a pixel level as the precise extent of the rainbands is often ambiguous. For this stage of the process, eyewalls and SEs not correctly masked in the initial steps were manually removed in order to evaluate the performance of the rainband identification independently from the eyewall verification step.

Verification statistics for rainband identification are shown in Table 4.3. The percentage of images where all rainbands were correctly identified was 81%. Using a more relaxed verification statistic where one band can be missed or incorrect, the percentage of correct identifications

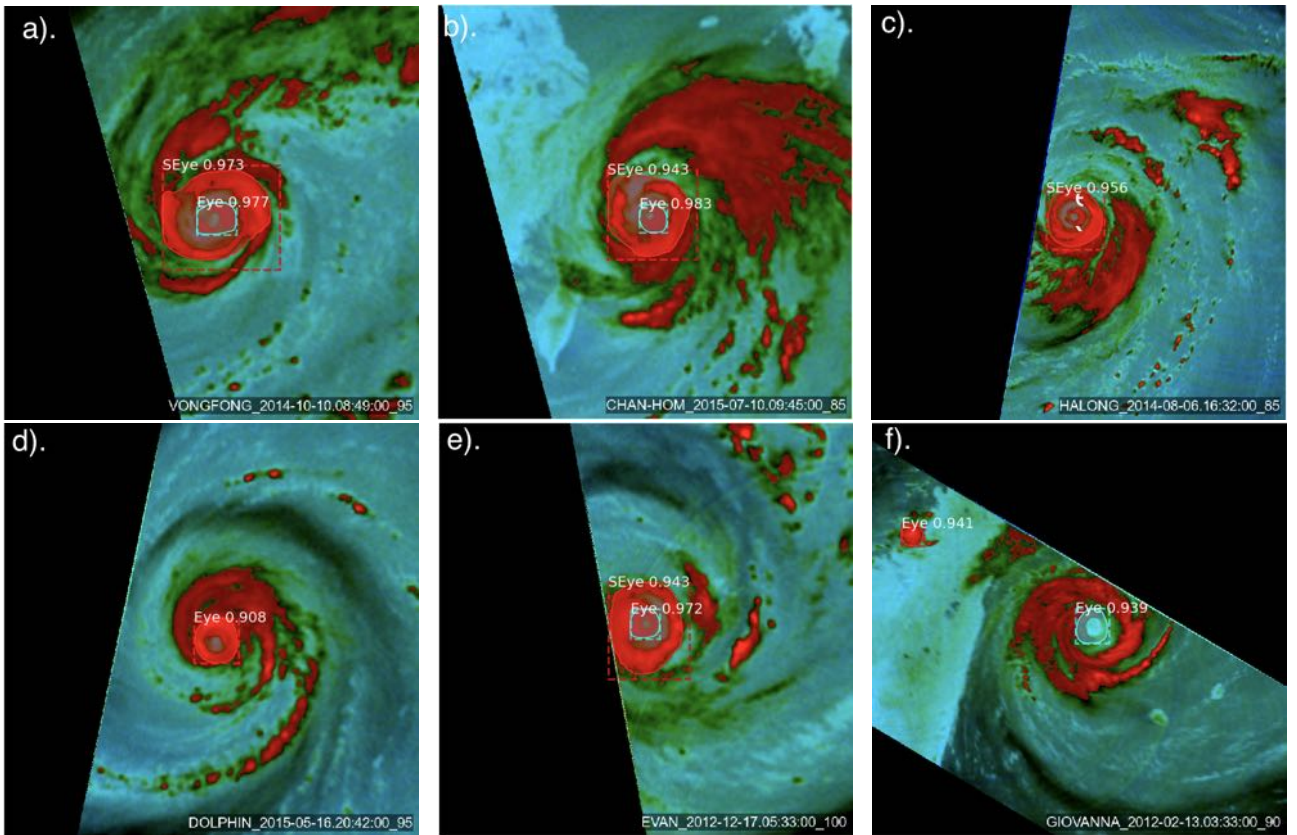


*Figure 4.18: Examples of MASK-RCNN output for (a) a large elliptical SE, (b) an incomplete SE, (c) a classical circular SE, (d) example of false negative with indistinct inner eyewall, (e) example of a false positive in a PRB with a symmetric moat, (f) example of model successfully rejecting a moat as a SE. Eyewall masks and bounding boxes are displayed using software adapted from (Ye, 2018).*

---

Rainband clustering verification	
All bands	
% sample all bands correct	81%
% sample all bands correct or one incorrect	90%
% sample no bands identified	2%
Principal bands	
% SBCs successfully identified	56%

---

*Table 4.3: Validation statistics for rainband identification.*

rises to 90%. No bands are successfully identified in just 2% of images. Examples of successful segmentations are shown in Figure 4.19.

Of the false negatives, common scenarios where the clustering does not perform well are rainbands with poor spiral structure, fine scale or weak bands and merged rainbands. For cases with structure that is not well approximated by a logarithmic spiral, the clustering algorithm is poorly equipped to accurately merge clusters into a band. An example of such a case is shown in Figure 4.20 (a), with a poor clustering fit to a PRB. For very weak bands, the band is often partially obscured at the unsharp masking stage, even after applying CLAHE (e.g light blue band in Figure 4.20 (b)). In this case, the fainter, irregular band is not identified. Finally, the algorithm does not perform well in cases where the banding structure is poorly defined (e.g Figure 4.20 (c))

The SBC identification technique does not perform as well, with a POD of 56%. This is primarily because the definition used here only takes cluster size into account, not the presence of a moat or relationship to the other rainbands. This results in high numbers of false alarms for clusters that are large but do not have a well defined moat, and missed identifications where the principal band is of comparable scale to an amplifying secondary band. In future versions of this technique, this problem will be solved by incorporating PRB/SBC identification at the Mask-RCNN stage rather than as a post processing step.

### Total accuracy and benchmarking

In the previous two verification sections the classification performance was evaluated separately for each step of the algorithm. For the overall accuracy, an image is classed as a hit if both the eyewall and all rainbands are correctly identified, and a miss if the classification fails at any stage of the process. The percentage of images with both the eyewall and all rainbands successfully identified was 76%. Given the complexity of this process, and the fact that the vast majority of other cases still contain useful information this is an exceptional result. An advantage of this scheme is that it is relatively fast, taking an average of 3.01 seconds per image for step one and 4.87 seconds for step 2. This technique is therefore both accurate and efficient enough to create a climatology using a large sample of images.

## 4.6 Conclusion

This chapter presented a classification system for TC convective structure, the development and implementation of a command line tool to manually classify 89GHz images and the development of a fully automated classification algorithm. This fully automated algorithm uses a combination of a CNN and unsupervised clustering to quantify the TC structure. It was

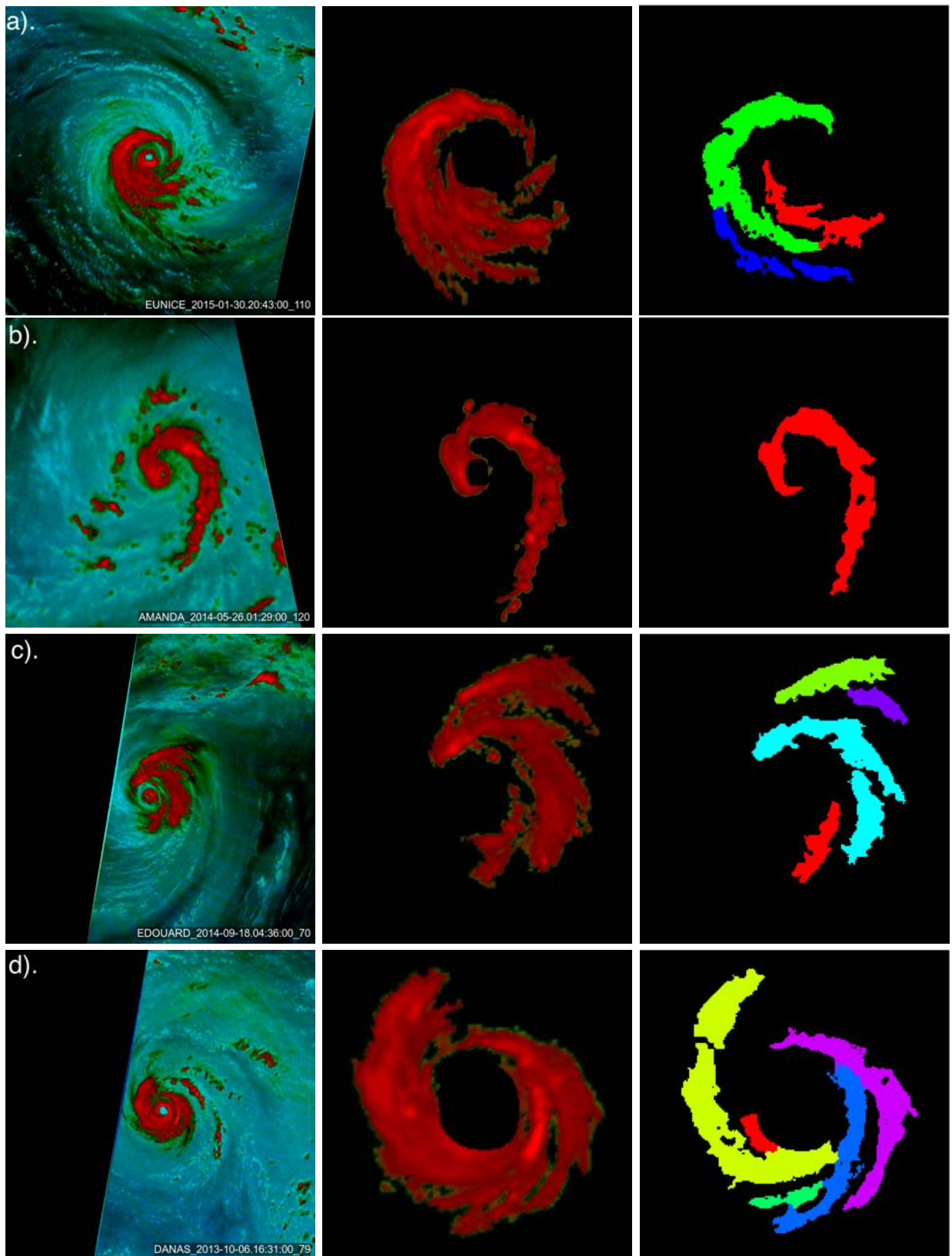


*Figure 4.19: Examples of successful rainband segmentations. Different rainbands are shown in different colours using code adapted from the SpArcFiRe project (Davis and Hayes 2014). Images show (L-R original 89GHz satellite image, cropped and masked image prior to preprocessing to demonstrate rainband locations and output of the rainband clustering. Examples show (a) successful clustering of a poorly defined bands within a SBC, (b) successful identification of a lone PRB and (c, d) successful segmentation of multiple spiral bands.*

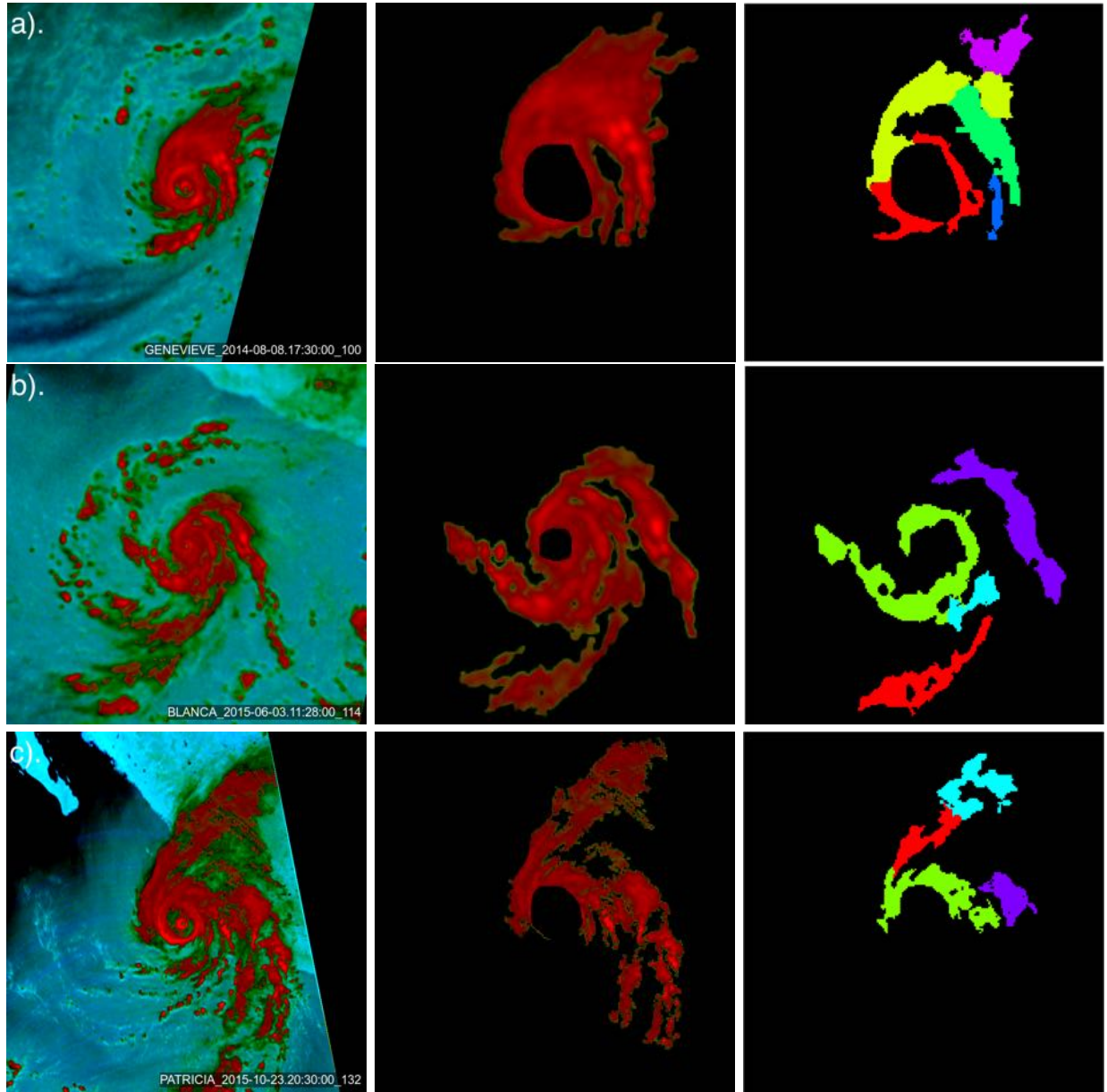


*Figure 4.20: Examples demonstrating limitations of the clustering scheme. As in Figure 4.18, in clustering images each rainband is identified by a different colour, with clustering plots produced using the SpArcFiRe software (Davis and Hayes, 2014). For each case, images show (L-R original 89GHz satellite image, cropped and masked image prior to preprocessing to demonstrate rainband locations and output of the rainband clustering. Images show examples of (a) difficulties in accurately identifying rainbands where the geometry varies significantly along the band, (b) a rainband with highly irregular geometry that is not correctly identified, (c) poorly defined diffuse rainbands that are not accurately identified.*

demonstrated that the algorithm is capable of identifying eyewall structure with a macro F1 score of 0.91 together with identifying all rainbands correctly on 81% of images. In the next chapter, these tools are used to construct a first climatology of TC rainband morphology.

# Chapter 5

## Results chapter: Climatology of rainband morphology

This chapter presents a first climatology of rainband structure in TCs. Preliminary results are presented for the validation dataset, and will be extended to the whole sample prior to publication. Four specific scientific questions are addressed:

1. How often does a TC have well defined rainbands, and how does the storm scale convective structure vary geographically?
2. What is the climatological incidence of principal rainband formation (PRBF)?
3. What is the typical geometry of different types of rainbands?
4. Is there a preferred evolution of the storm morphology leading up to SEF?

### 5.1 Dataset

Between 2012 and 2014, a total of 106 TCs developed globally that were captured by at least one microwave pass at over 65 knots intensity and included in the image set. A total of 1540 PMW images and 2569 individual rainbands were included. Differences in TC intensity, lifespan, size (Knaff et al., 2014), incidence (Klotzbach, 2006) and structure (Hawkins and Helveston, 2004) have been documented between basins. These differences motivate an analysis of how rainband characteristics differ geographically in this climatology. Figure 5.1 shows the tracks of all 106 TCs included in this study together with the approximate geographic location of each basin. Sample sizes of total images and different band types within each basin are presented in Table 5.1.

Overall, a significantly higher number of rainbands (43% of the total sample) and images (37%

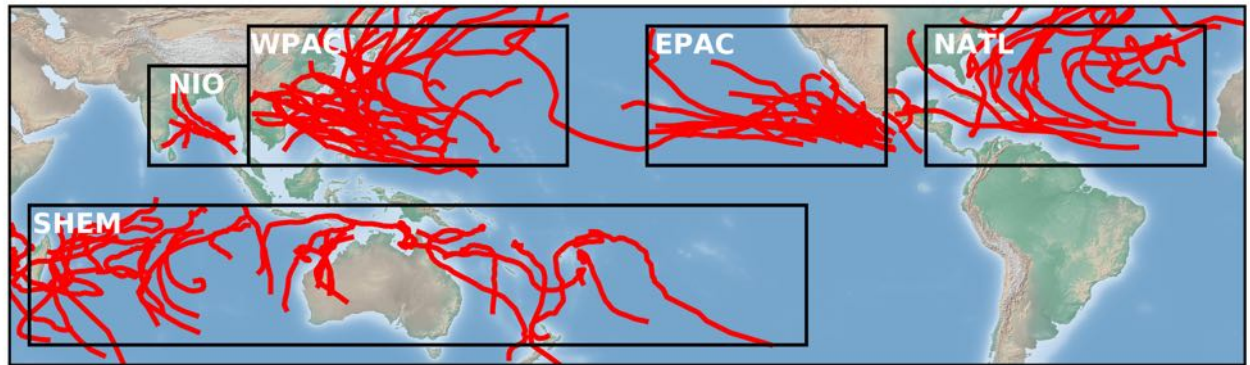
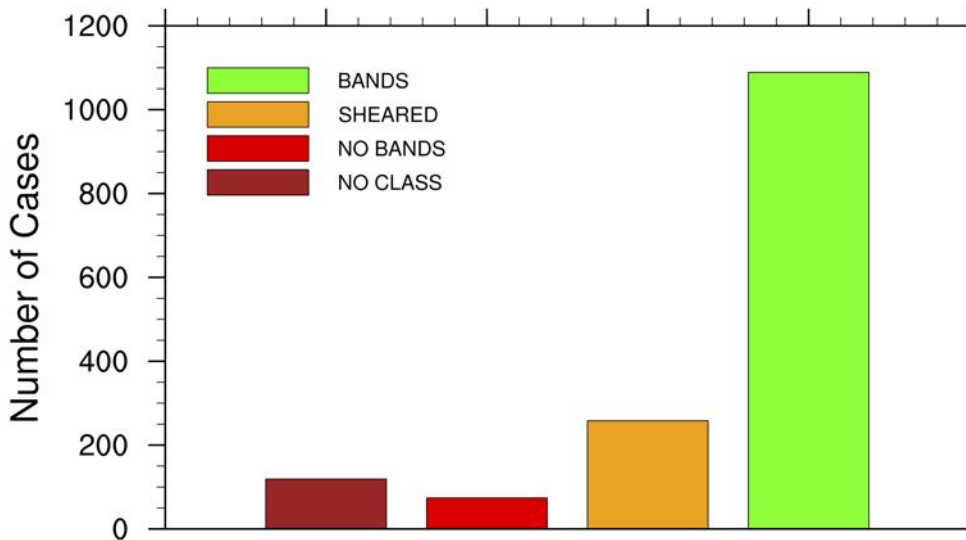


Figure 5.1: Tracks of the 106 TCs included in the sample, together with approximate locations of the basins considered in this climatology. Tracks are taken from the IBTrACS dataset (Knapp et al. 2010).

2012-2014 global climatology - sample sizes						
Variable	NATL	EPAC	WPAC	SHEM	NIO	Total
Storms	28	25	29	31	4	106
Total images	403	326	568	357	28	1540
Bands	543	478	1113	612	49	2569
SBCs	119	113	219	129	10	543
IC	211	204	457	280	14	1072
OC	78	63	166	85	12	371

Table 5.1: Sample sizes for the climatology, showing the total numbers of TCs, PMW images, total rainbands, SBCs, IC and OC bands for each of the five basins analysed.



*Figure 5.2: TC scale convective classifications for the climatology, showing the number of PMW images classed as no classification, no bands, sheared and bands.*

of the total sample) were observed in the Western Pacific (WPAC) basin. This can be attributed to the fact that WPAC TCs are typically more intense and longer lasting as a result of favourable environmental conditions. In contrast, TC formation in the Northern Indian Ocean (NIO) is a comparatively rare event, and most TCs in this basin are weak and short lived (Wahiduzzaman et al., 2017). Given that only four storms and 28 satellite passes are included for this region over the study period, the analysis in this chapter concentrates on the North Atlantic (NATL), Eastern Pacific (EPAC), WPAC and Southern Hemisphere (SHEM) basins only. As can be seen from Figure 5.1, a TC will occasionally cross from one basin into another. In these cases the TC is assigned to the basin where the first 65kt overpass occurred.

One point of interest is that surprisingly few bands are classified as OC (371 in total) given that OC bands are noted in almost all radar studies of TCs (e.g Yu et al., 2018). This is probably because the weak ice scattering signal in the OC bands is not picked up in the 89GHz images (see Appendix A.2). In reality, it is likely that many more squall line-like outer bands are present that do not meet the 100 pixel continuity criterion to be considered rainbands in this climatology.

## 5.2 Storm scale classifications

The incidence of different storm scale classifications for all images is shown in Figure 5.2. The majority (66%) of all cases have at least one spiral rainband, while comparatively few images have no bands (4.81%), no classification (7.73%) or are sheared (16.75%). The incidence of different classification types varies with both basin and latitude.

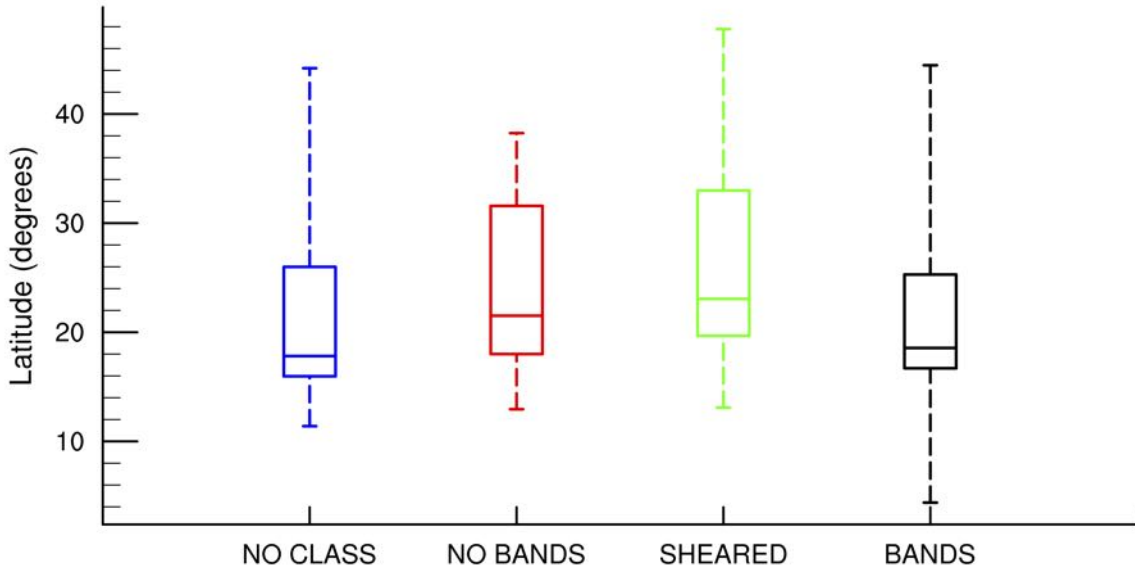


*Figure 5.3: Latitude distributions (taken from IBTrACS) for the no classification, no bands, sheared and bands groups.*

Figure 5.3 shows differences in the latitudinal distributions of images in each classification category. Differences between all distributions are significant at the 99% level using a 2-sample Kolmogorov-Smirnov (KS) test. This demonstrates that TCs are more likely to have an asymmetric structure at higher latitude, consistent with climatologically stronger vertical shear (Finocchio and Majumdar, 2017). Cases with no bands are also more likely to occur at higher latitudes. A possible explanation for this is that the drier environment as the TC moves away from the tropics suppresses banding activity (e.g Wang, 2009). Figure 5.4 shows the differences in classifications between basins. TCs in the NATL have the highest percentage of asymmetric classifications (24% of all PMW images), most likely associated with strong shear as they recurve in the midlatitude westerlies and climatologically stronger vertical shear in this basin (Finocchio et al., 2017). The percentage of PMW passes with no classification is also the highest of any basin (11%). A similar pattern is seen in the EPAC. This can be attributed to the prevalence of smaller, weaker storms in the EPAC and NATL compared to other basins (Merrill, 1984; Wada et al., 2012), and associated lack of well-defined banding structure. The Western Pacific is markedly different to other basins with 80% of images containing at least one rainband, and only 14% classified as sheared, 4% as no classification and 3% as no bands, suggesting that the environmental conditions within the WPAC are more conducive to spiral rainband formation. This is consistent with studies indicating that the size, and hence extent of the rainband field, is greater in the WPAC (Knaff et al., 2014).

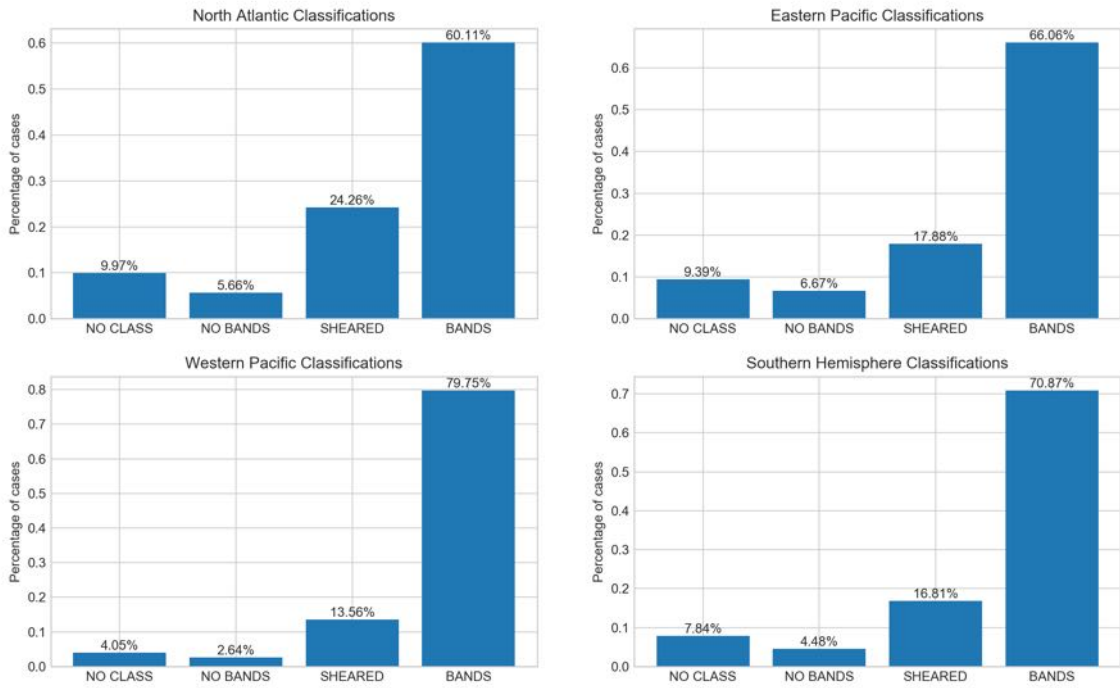


*Figure 5.4: Percentages of PMW images classified as no classification, no bands, sheared and bands in the NATL, EPAC, WPAC and SHEM basins.*

### 5.3 TC scale convective classifications

This section focusses on the set of images containing at least one spiral rainband (66% of the total sample/1098 images). Of this group, considerable variations are apparent in the number and type (SBC, IC and OC) of rainbands in different basins and at different latitudes.

Of all images in the bands group, 56.66% contain a SBC, or just 35.6% of the total image sample. The incidence of SBCs does not vary significantly between basins, ranging from 53.81% of overpasses in the NATL to 58.35% in the WPAC.

Within the image classification set, both the principal band and any secondary bands in a given SBC are identified. Of all cases, 35.54% of SBCs consist of a PRB only. This varies somewhat between basins, from 30.34% in the WPAC to 40.00% in the EPAC. The increased secondary banding activity within the WPAC probably results from enhanced IC CAPE (Wada et al. 2012, Li et al. 2017), and increased filamentation time in the strain-dominated moat due to the broader wind profile (Rozoff et al. 2006).

In certain cases, the SBC may coexist with separate IC and OC bands. Table 5.2 shows the percentage of images with IC only, OC only, IC and OC or no banding for cases with and without an SBC. This demonstrates that for the group with an SBC, no other banding is

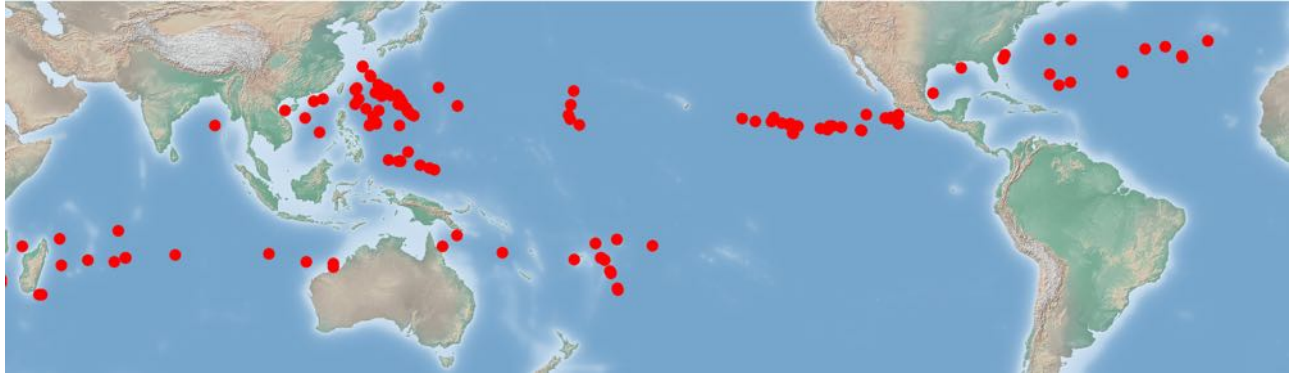


*Figure 5.5: Geographic locations of PRBF events included in the sample, marked in red. Locations taken from the IBTrACS dataset linearly interpolated to the time of the first PMW overpass classified as containing a PRB.*

apparent in a majority (64.29%) of cases. In 16.03% of cases, other IC bands are observed, probably corresponding to amplifying VRWs that may eventually propagate outwards across the moat to join onto the banding complex if the environmental conditions are favourable. In contrast, for images with no SBC, 61.73% have only IC rainbands, and 92% have at least one IC rainband. The incidence of OC rainbands is significantly lower (19.68%) for cases with a SBC than for cases without (40.12%).

The temporal resolution of the PMW dataset is sufficient to identify instances of PRBF. As PRBs are known to persist on a timescale of at least 6 hours (Powell et al. 1990a,b; Hence and Houze, 2006; Wang et al., 2016), a PRBF event is defined as a sequence of two 89GHz satellite images within 6hrs of each other where the first is classified as no SBC and the second is classified as SBC. This allows for the timing of each event to be estimated to within 6hrs, with the caveat that some PRBF events will not be included if there is a gap in the PMW coverage. This gives a total of 106 PRBF events in the climatology, of which 41 (39%) are in the WPAC, 18, (17%) are in the NATL, 24 (23%) are in the EPAC and 26 (25%) are in the SHEM (Figure 5.5). The incidence of PRBF does not vary significantly between basins. PRBF is significantly more likely at lower latitudes (KS-test,  $p < 0.01$ ), with a median latitude of  $17.96^{\circ}$ for TCs at the time of PRBF, compared with  $19.36^{\circ}$ for TCs classified as spiral bands with no SBC where no PRB develops within 6hrs.

It is instructive to consider the storm scale classification prior to PRBF. The majority (73.56%) of the PRBF events occur in a storm with active rainband activity. The second most common transition is from no classification to rainbands with an SBC (14.15%). This may result from disorganised outer convection in a developing TC organising into a coherent SBC as the low level circulation strengthens. Transitions from a TC classified as sheared or no bands to an SBC occur in just 5.67% and 6.60% of cases respectively.

Coincidence of different rainband types				
Category	IC only	OC only	IC+OC	None
SBC	16.03%	17.07%	2.61%	64.29%
NO SBC	61.73%	07.97%	30.30%	-

Table 5.2: Coincidence of different banding types including IC only, OC only, IC and OC (IC+OC) and neither inner or OC (None) for images with and without a SBC.

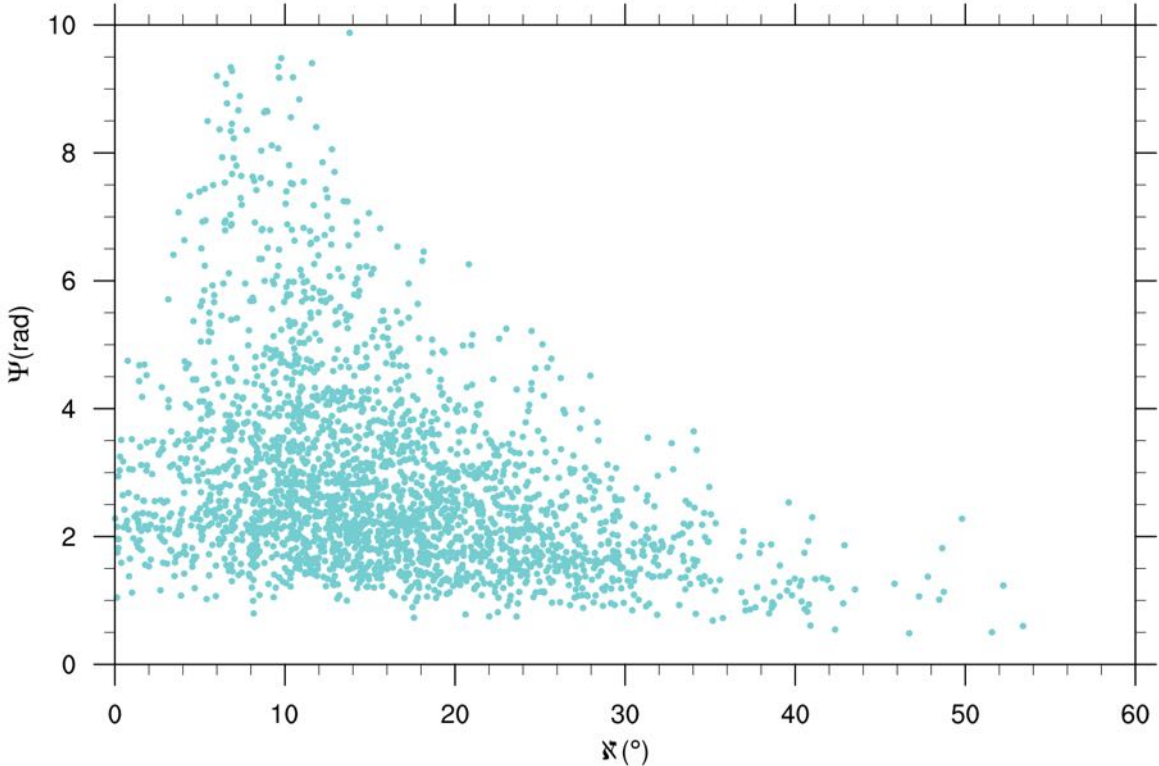


Figure 5.6: Scatter plot showing the relationship between crossing angle ( $\kappa$ ) and azimuthal extent ( $\Psi$ ) for all rainbands in the sample.

## 5.4 Rainband geometry

This section discusses the climatological variation of PRB geometry, quantified by the crossing angle and azimuthal extent. Clearly, there is a geometric relationship between these two parameters, with lower (higher) crossing angle contributing to a higher (lower) azimuthal extent. As demonstrated in Figure 5.6, however a considerable range of azimuthal extents are observed for bands with a given crossing angle. The crossing angle and azimuthal extent are therefore analysed separately. For the remainder of this study, all statistically significant differences are determined using a 2-sample Kolmogorov-Smirnov test unless otherwise stated.

Mean RMS errors for different band types (km)	
ALL	8.08km
PRB	11.42km
ICA	9.40km
IC	5.78km
OC	12.3km

Table 5.3: Mean RMS errors (km) for logarithmic spiral fits for different band types.

### 5.4.1 Logarithmic spiral fit verification

The average root mean square (RMS) errors between the rainband clusters identified on each image and fitted logarithmic spirals are shown in Table 5.3. For all bands in the sample, the mean RMS error is low, at 8.08km compared to a typical band length of around 300km. Average RMS errors for PRBs (11.2km) and OC bands (12.3km) are significantly higher than those for the IC bands (5.78km). Higher RMS errors in the PRB group arise as a result of cases with a spiral geometry downwind and quasi straight geometry upwind. Errors in the OC group primarily arise because logarithmic spirals provide poorer fits for bands beginning at larger radii. Senn et al. (1959) and Anthes (1972) demonstrated that modified log spirals with varying crossing angle provide better fits to both of these classes of bands.

### 5.4.2 Crossing angle

The crossing angle distribution for all bands in images classified as containing rainbands is shown in Figure 5.7. The distribution is lognormal with a median crossing angle of 14.46 degrees for all bands. Crossing angles range from a minimum of 0.02 degrees, or close to circular, to a maximum of 53.2 degrees. Examples of PRBs with crossing angles at each extreme of the distribution are shown in Figure 5.7.

Variations in crossing angle distributions arise between different band types and basins. Crossing angle distributions for different band types and the ICA parameter are shown in Figure 5.8. The median crossing angle is lower for the IC and PRB groups at  $13.70^\circ$  and  $13.75^\circ$  respectively than for the OC group at  $15.66^\circ$ . Differences between all groups except for IC and PRB are statistically significant. A possible reason for this is that PRBs within an SBC can form from amplifying IC VRWs or Shear Induced Deformation waves (Li, 2017; May et al., 1996; see Chapter 2). In many cases, the precise distinction between a principal and IC rainband is therefore unclear. Differences between the OC distribution and IC and PRB distributions are consistent with previous work indicating that the OC rainbands form outside of the region governed by vortex dynamics, and their geometry is therefore governed by a different flow regime (e.g Houze, 2010). Differences in crossing angle distributions between the ICA parameter and

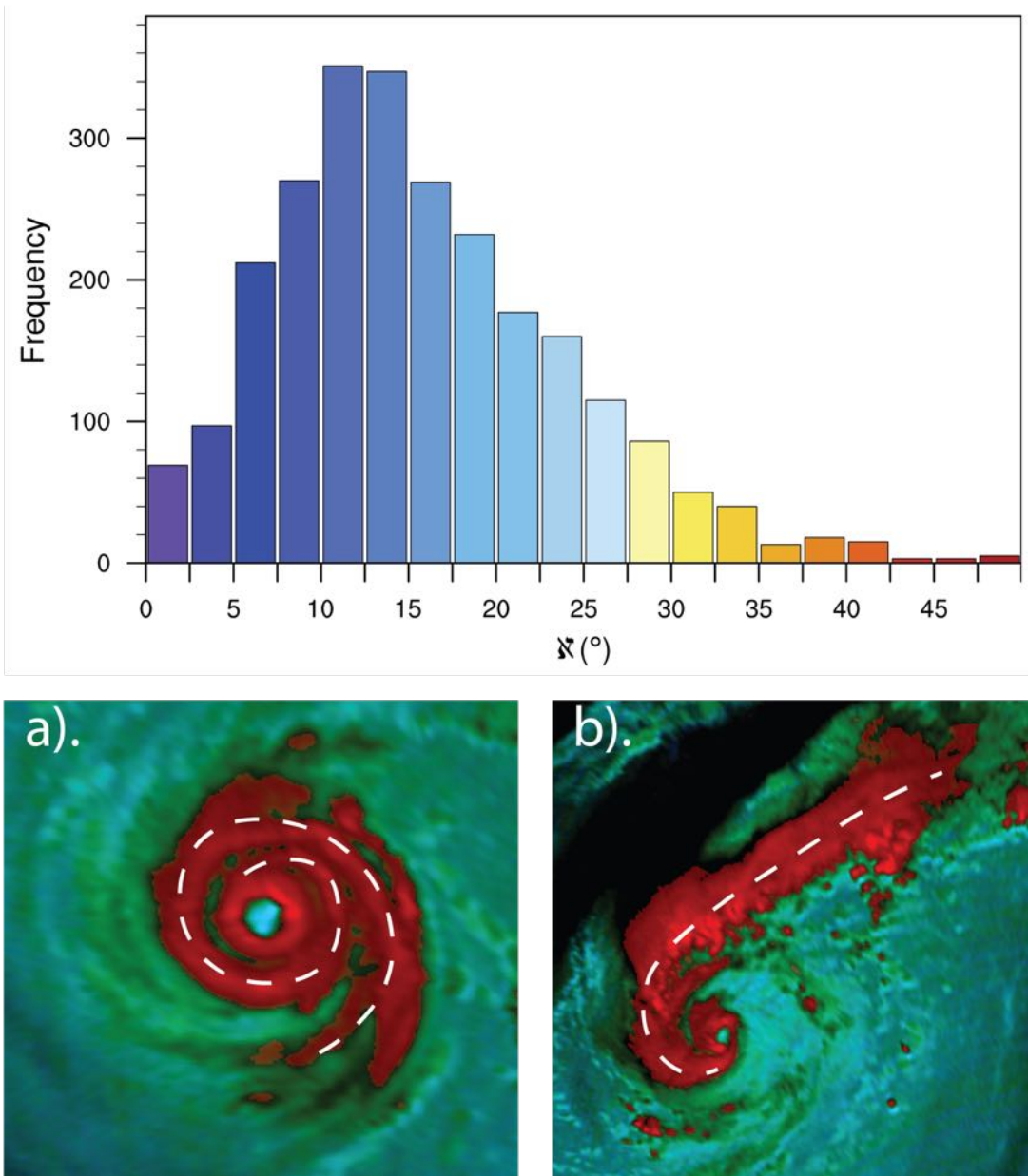


Figure 5.7: Crossing angle ( $\aleph$ ) distribution for all bands (top), together with (a) Example of a TC with crossing angle  $4.59^\circ$  and (b) Example of a TC with a crossing angle of  $49^\circ$ .

all band types are statistically significant. The median crossing angle is significantly lower for this parameter than the three band types at 10.33 degrees. These differences are primarily due to the definition of the ICA crossing angle.

Crossing angle distributions for different band types and the ICA parameter in different basins are shown in Figure 5.9. For the IC and OC groups no statistically significant differences are found between basins. For the IC bands, this is consistent with the banding structure being controlled by IC vortex dynamics. It is unclear why there are no significant differences in the OC band distributions, however this suggests that the crossing angle of the OC bands is independent of the large scale environmental conditions.

For the all band, ICA and PRB groups, differences are apparent between the WPAC and other basins. Figure 5.10 shows histograms of the differences in crossing angle distributions between basins for both the PRB group and the ICA parameter. For the all bands group, the median crossing angle for the WPAC is 13.62°, lower than 16.71°, 15.63° and 16.64° for the EPAC, NATL and SHEMA basins respectively. Differences between the WPAC and all basins are statistically significant at the 99% level. For the PRB group, differences in between the WPAC and both the NATL and EPAC basins are significant at the 95% level. The median crossing angle is lowest in the WPAC at 12.56°, compared to 15.13°, 15.62° and 13.49° in the NATL, EPAC and SHEMA basins respectively. For the ICA parameter, differences between the WPAC and all other basins are statistically significant. The ICA crossing angle is lowest in the WPAC is 9.03° compared to 12.06°, 11.66° and 11.61° for the NATL, EPAC and SHEMA basins respectively. This demonstrates that the conditions within the WPAC are conducive to more circular PRBs and SBCs.

These crossing angle distributions are consistent with the limited previous work that has investigated rainband geometry. From case studies of radar data, Senn et al. (1957) found that crossing angles for the majority of bands were between 10° and 20°. This is consistent with the median value of 14.46° for all bands observed in this sample. Their work also noted that, on average, bands closer to the centre of the vortex had lower crossing angle. That is consistent with this climatology, with a median crossing angle of 13.70° for the IC group compared with 15.66° for the OC group. Previous case studies of PRBs have primarily investigated rainbands with a crossing angle between 8° and 10° (Barnes et al. 1983, Powell 1990a,b, Hence and Houze 2008, Didlake et al. 2018). The crossing angle of these bands is therefore considerably lower than the median of 13.75° for PRBs in this study. As understanding of the kinematics and thermodynamics of PRBs is primarily based on these case studies of bands with crossing angles within the first quartile of the sample, this motivates further investigation of SBCs with different geometry.

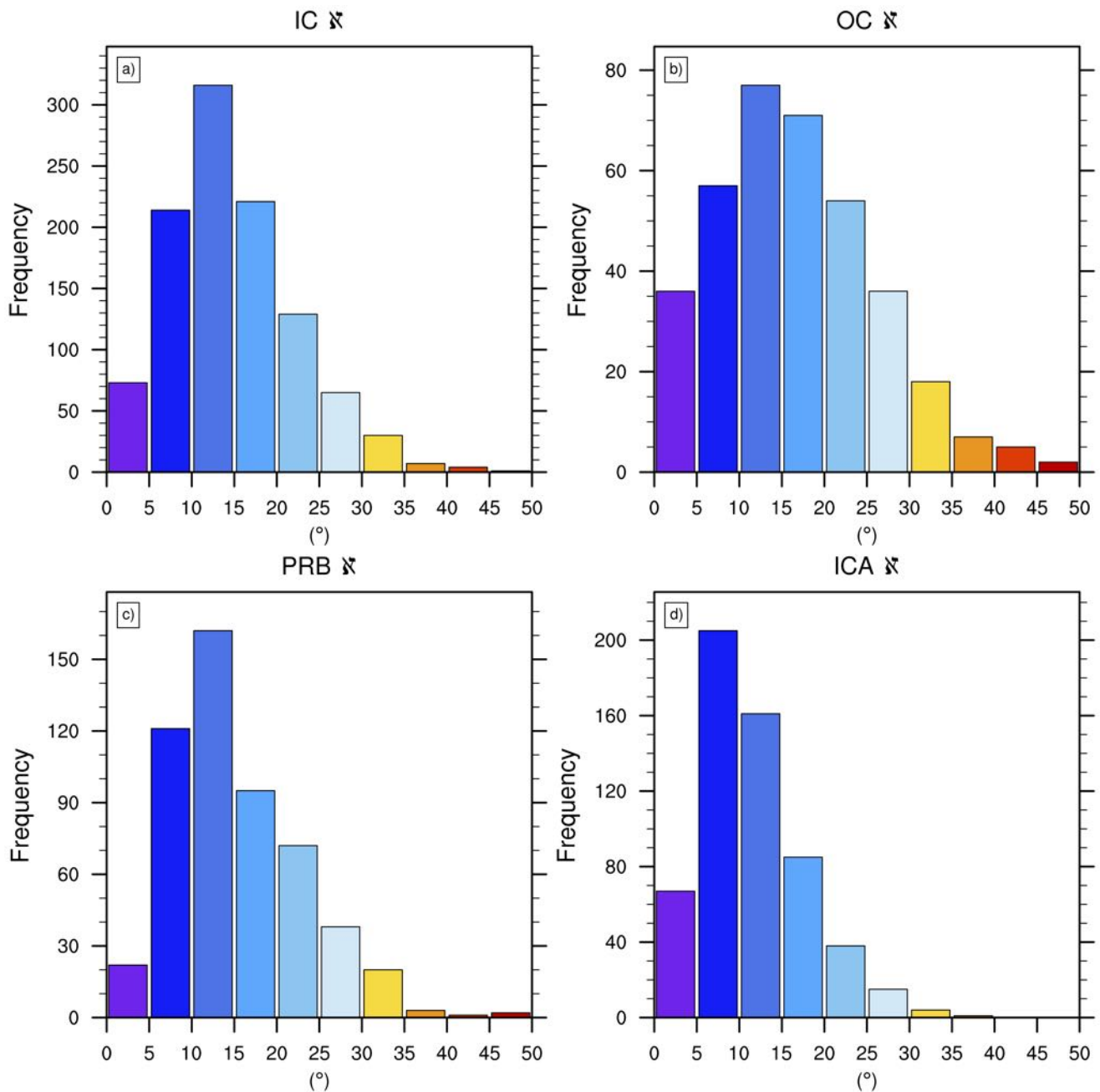


Figure 5.8: Crossing angle distributions for the IC, OC, PRB and ICA groups.

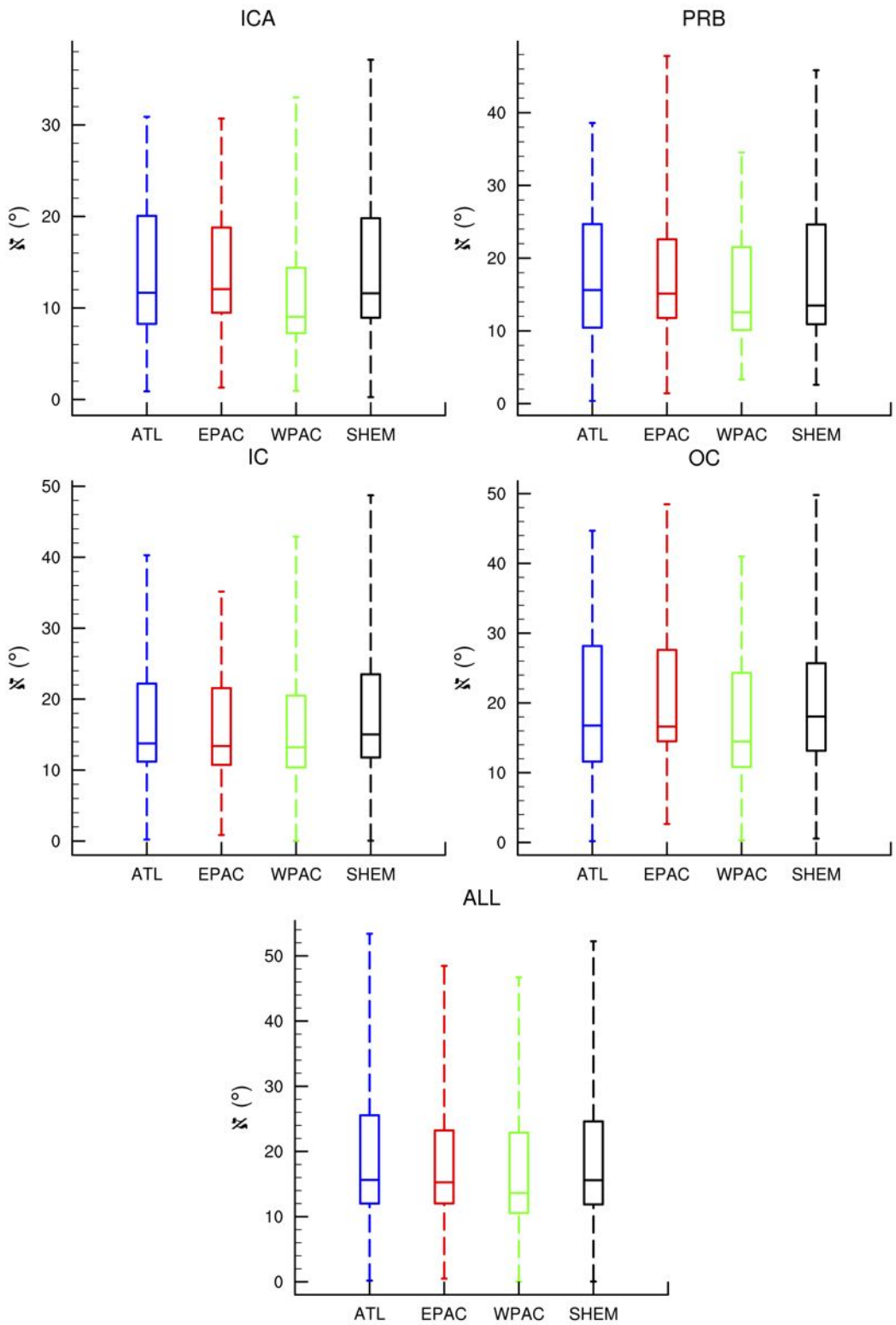


Figure 5.9: Crossing angle ( $\text{N}$ ) distributions for different band types in the NATL, EPAC, WPAC and SHEM basins for the IC, OC and PRB groups, together with the ICA parameter and all bands group. Note the different scales for different band types.

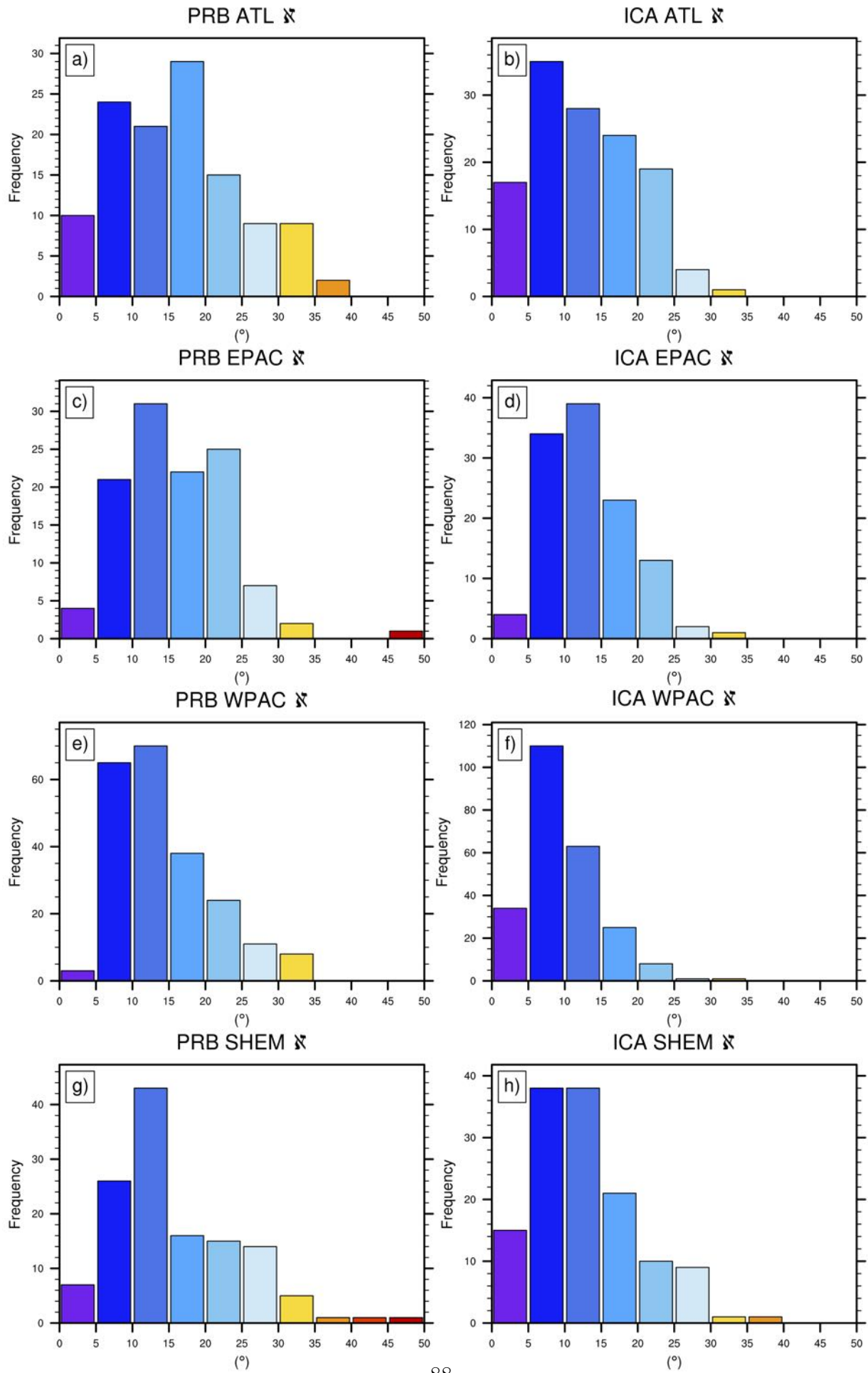


Figure 5.10: Crossing angle ( $\aleph$ ) distributions by basin for PRB (Left) and ICA (Right).

### 5.4.3 Azimuthal extent

The distribution of azimuthal extents for all bands in the sample is shown in Figure 5.11, with distributions for different basins and band types shown in Figure 5.13. Values range from a minimum of 0.49 radians to a maximum of 9.89 radians, with a median of 2.46 radians. Examples of bands with azimuthal extents at the extremes of the distribution are shown in Figure 5.11.

As for the crossing angle, differences in azimuthal extent are observed between different band types and basins. Azimuthal extent distributions for different band types are shown in Figure 5.12. Differences between all distributions are statistically significant at the 99% level. The IC and OC groups have the lowest median azimuthal extent, at 2.33 and 2.15 radians respectively. For the IC group, this is dynamically consistent with the bands being rapidly sheared apart within the rapid filamentation zone before they can propagate around the vortex, limiting their azimuthal extent (Montgomery and Kallenbach 1997, Rozoff et al. 2006). This behaviour is consistent with previous observational analyses of VRW structure (Corbosiero and Molinari, 2002). For the OC group, the azimuthal extent is low because the bands are by definition further away from the vortex centre, and geometrically must therefore be longer to project substantially onto the azimuthal mean. The median values for the PRB and ICA groups are significantly higher, at 3.89 and 4.12 radians respectively.

Differences arise in the distributions of rainband azimuthal extent in different basins. For the OC bands, the only statistically significant difference at the 99% confidence level is between the WPAC and NATL, with higher azimuthal extent in the WPAC. It is in some ways surprising that there is not a clearer signal, as the environmental conditions in the WPAC would be expected to be more conducive to convective development and enhanced OC rainbands. For the IC bands, differences between the WPAC and all other basins are significant at the 95% level, with higher values in the WPAC. This is probably associated with increased filamentation time in the WPAC resulting from favourable environmental conditions, allowing convection to propagate further around the IC.

As with the crossing angle, the largest differences between basins are seen for the PRB and ICA groups. Histograms of PRB and ICA azimuthal extent in each basin are shown in Figure 5.14. For both groups, differences in the distributions between all basins are significant at the 95% level, with the exception of between the NATL and EPAC. For the PRB group, the median azimuthal extent is lowest in the EPAC and NATL at 3.22 and 3.19 radians respectively, and higher in the WPAC and SLEM basins at 4.3 and 3.9 radians. A similar pattern emerges for the ICA parameter. Markedly higher azimuthal extents are observed for the WPAC at 5.02 radians compared to the NATL, EPAC and SLEM at 3.22, 3.19 and 3.9 radians respectively. The high azimuthal extents in the WPAC can partly be attributed to the lower crossing angles in this basin, and partly to the increased absolute band length.

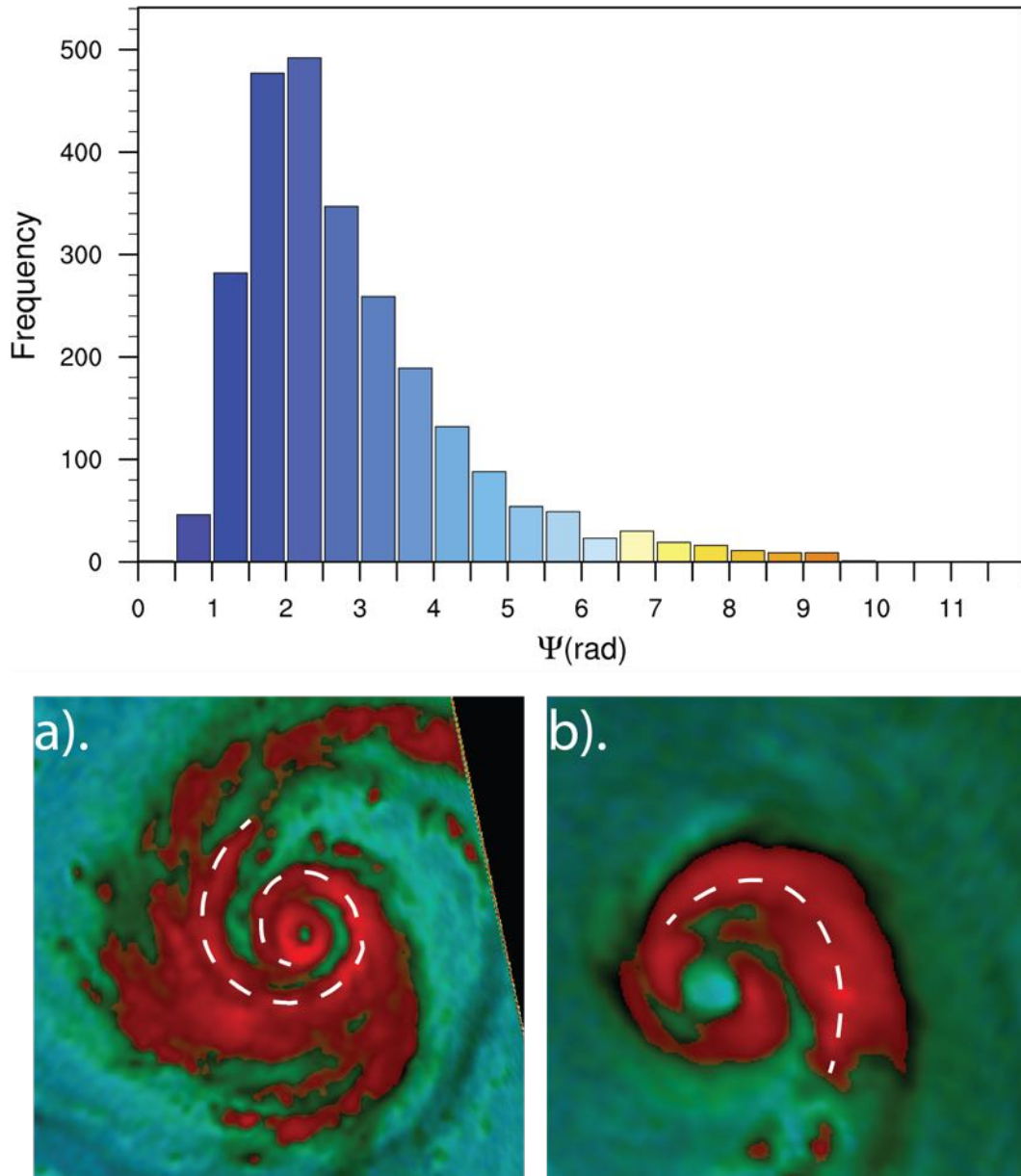


Figure 5.11: Azimuthal extent ( $\Psi$ ) distribution for all bands (top), together with (a) Example of a TC with azimuthal extent 7.01 radians and (b) Example of a TC with an azimuthal extent of 3.12 radians.

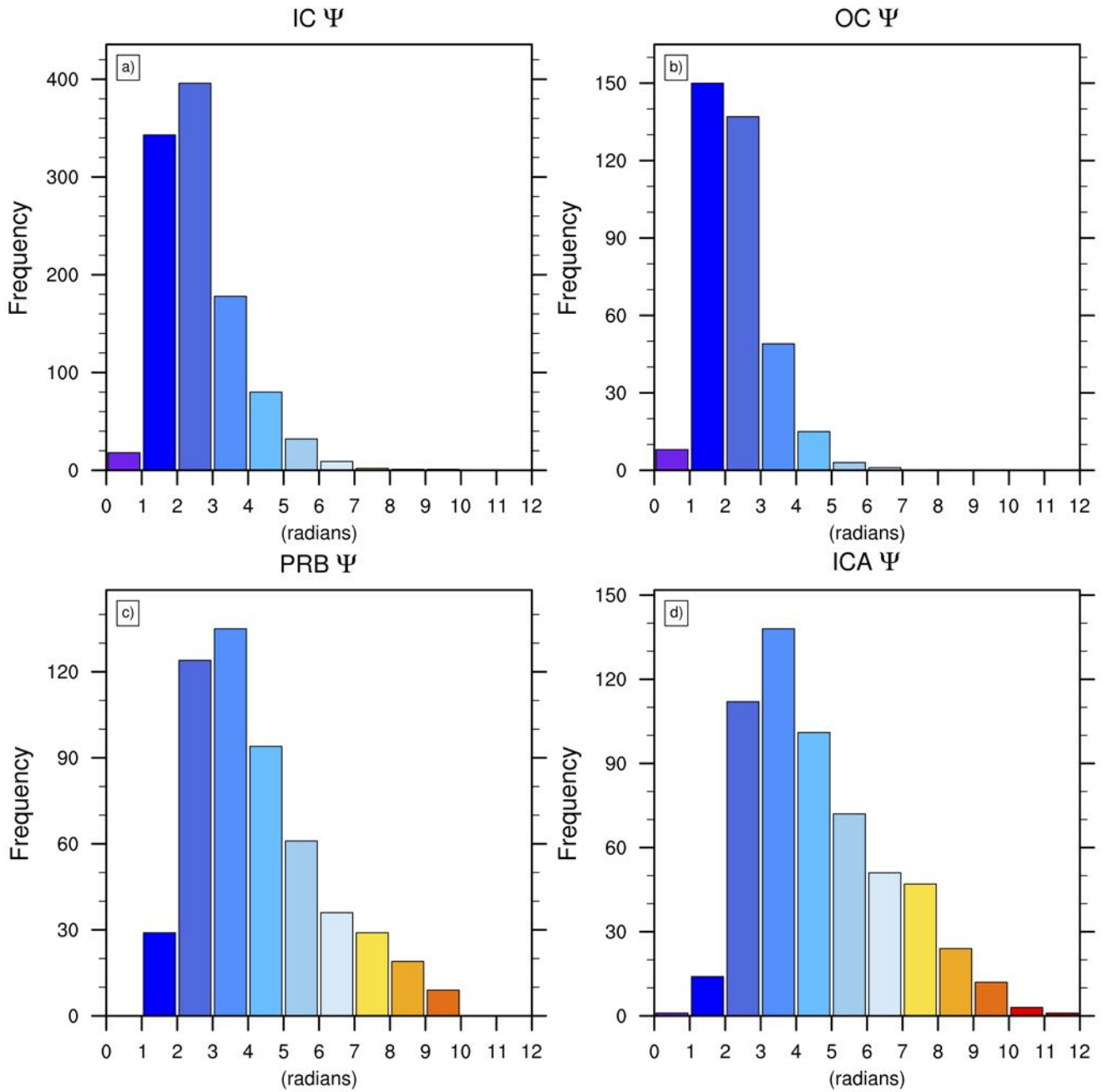


Figure 5.12: Azimuthal extent ( $\Psi$ ) distribution for the IC, OC, PRB and ICA groups.

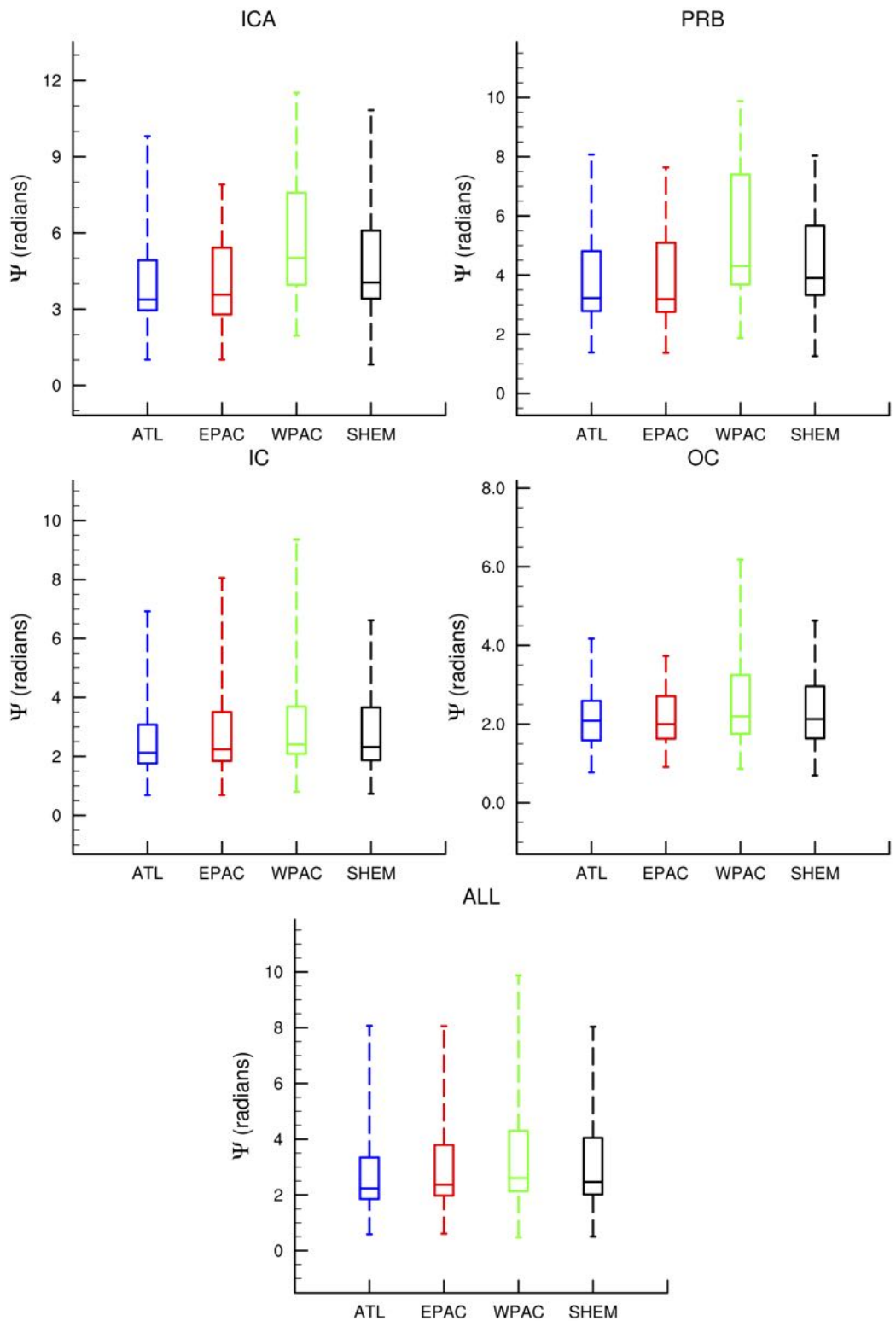


Figure 5.13: Azimuthal extent ( $\Psi$ ) distributions for different band types in the NATL, EPAC, WPAC and SHEM basins for the IC, OC and PRB groups, together with the ICA parameter and all bands group. Note the different scales for different band types.

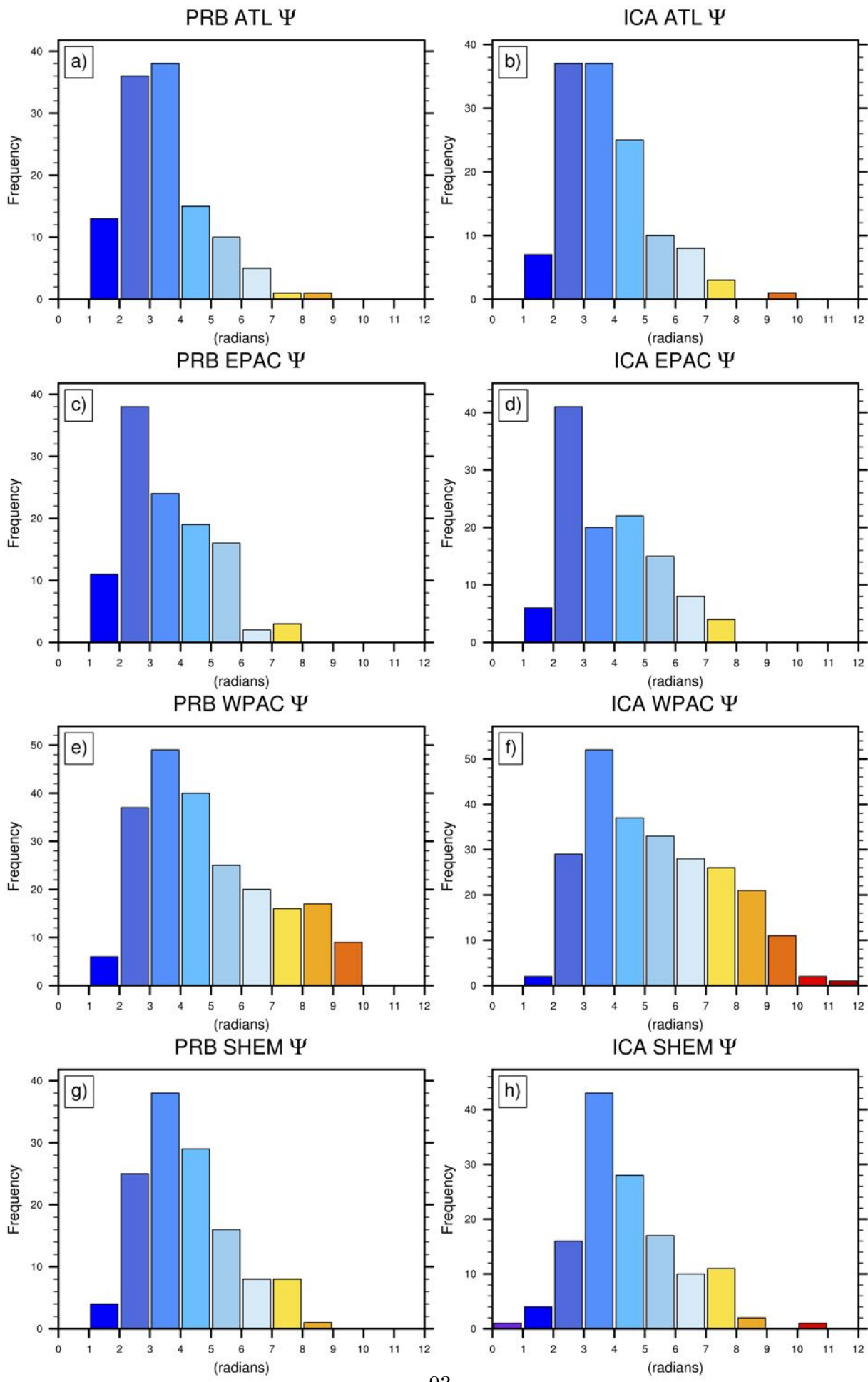


Figure 5.14: Azimuthal extent ( $\Psi$ ) distributions by basin for PRB (Left) and ICA (Right).

## 5.5 SEF

A total of 66 unique SEF events are included in the climatology. Of the 106 storms in the sample, 38 undergo SEF, with 66% of WPAC, 18% of NATL, 12% of EPAC and 32% of SHEM storms included developing at least one SE. These percentages differ from the climatology of Hawkins et al. (2004), which estimated that 80% of WPAC, 60% of EPAC and NATL and 40% of SHEM storms have at least one SEF event in their lifetime. This is likely primarily because their analysis was restricted to storms over 110kts, when SEF is more likely to occur (Kossin et al., 2007), whereas the current study includes all storms over 65kts.

As with identifying PRBF, SEF events were included in the final sample only if there was a satellite pass within 6hrs of the first pass with the SE visible. This ensures that the formation times of all SE events are accurate to within 6hrs, with the timescale chose to be consistent with the PRBF identification. As the timescale of evolution of a SE is approximately 12 hours (Sitkowski et al., 2011), SEF events occurring within 12 hours after another event are discarded from the sample. Of the 66 SEF events in the climatology, 41 meet these criteria to be included in the sample. The geographic locations of each of these events are shown in Figure 5.15. Although this is a relatively small sample for a climatology, it is important to note that many previous SEF studies have included fewer than 30 cases (Sitkowski et al., 2011; Kossin et al., 2012; DeMaria et al., 2016). Several TCs in the sample underwent multiple SEF events, for example Typhoon Francisco (2013) with 3 individual SEF events. While unusual, large numbers of sequential SEF events have previously been documented in individual TCs, for example in hurricane Ike (2004) with 7 consecutive SEF events (Kossin et al., 2008).

### 5.5.1 Rainbands prior to SEF

Given the discontinuous nature of the 89GHz PMW coverage, it is impossible to track the evolution of rainbands leading up to SEF with the current dataset. Images are therefore binned in different time periods prior to SEF to investigate the average structure of the TC at intervals prior to SEF. PMW overpasses within 24hrs of the SEF events described above are divided into four groups: 0-6hrs, 6-12hrs, 12-18hrs and 18-24hrs prior to SEF. Total numbers of images, TCs and events in each time period are shown in Table 5.4. As the mean revisit time of the GPM constellation is approximately 3hrs, some SEF events will have multiple images in each time period. In this case all images are included in the sample, as the TC structure is evolving on a timescale much faster than 6hrs during axisymmetrisation (e.g Willoughby et al., 1984), and retaining all images allows for a larger sample of structures to be included in each time period.

	PMW overpasses in the SEF sample			
Variable	0-6hrs	6-12hrs	12-18hrs	18-24hrs
storms	29	18	24	23
SEF events	41	24	34	31
Images	56	40	62	52

Table 5.4: Number of TCs, individual SEF events and total PMW overpasses included in each time period prior to SEF.

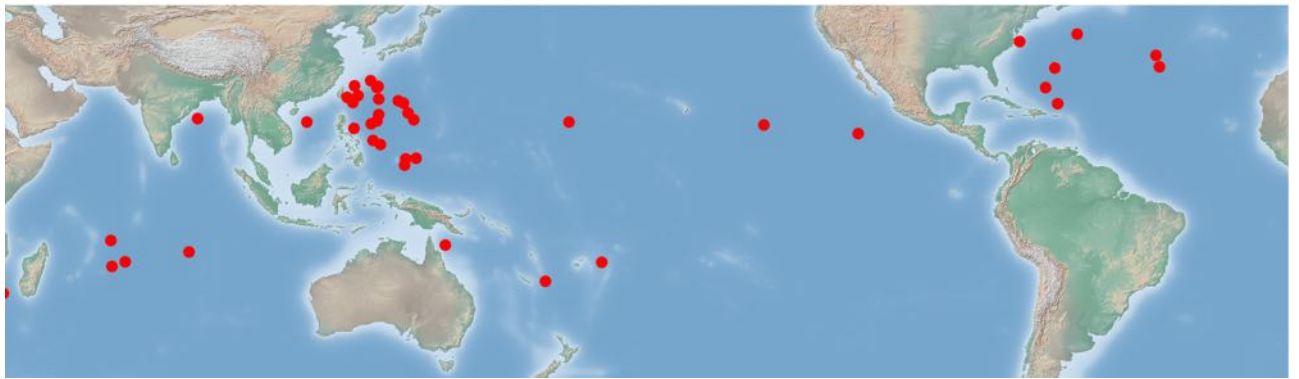


Figure 5.15: Locations of the 41 SEF events included in the sample. Locations are taken from IBTrACS interpolated to the time of the first PMW overpass containing the SEF.

The percentage of cases with an SBC increases as the TC approaches SEF. Within 0-6hrs, 6-12hrs, 12-18hrs and 18-24hrs prior to the beginning of SEF, 82%, 66%, 64% and 50% of TCs are classified as having an SBC, compared to 56.6% of all images classified as containing rainbands and 37% of the total image set. This indicates that the preferred pathway to SEF is the axisymmetrisation of a SBC.

For cases where a SBC is observed prior to SEF, the median ICA crossing angle and azimuthal extent in each time period is shown in Table 5.5. Kernel density estimation (KDE) plots of the differences between the azimuthal extent and crossing angle distributions at different times prior to SEF are shown in Figure 5.16. Differences between the 0-6 hours and 6-12 hours and all other groups are statistically significant at the 99% confidence level using a two dimensional Kolmogorov-Smirnov test. Differences between the 12-18 hours and 18-24 hours groups and the no SEF sample are not significant. This suggests that the most important changes in the rainband geometry occur within 12hrs of SEF. Between 0 and 6 hrs, the median crossing angle is almost 5 degrees less than the median for the whole sample, and the median azimuthal extent over 2 radians greater. Interestingly, the median crossing angle at 6-12 hrs prior to SEF is higher than the median for all bands at 12.01 degrees. For the azimuthal extent the median is higher than the average at 6-12 hours prior to SEF. This suggests the formation of a PRB at 6-12hrs prior to SEF, which is then axisymmetrised into the SE. An interesting observation

ICA parameters prior to SEF			
Time	Median $\aleph$ (°)	Median $\Psi$ (rad)	% SBC
6-0hrs	5.93	6.3	82%
12-6hrs	7.55	4.7	66%
18-12hrs	8.73	4.88	64%
24-18hrs	6.59	4.18	51%
All bands	14.46	4.12	

Table 5.5: Median ICA crossing angle ( $\aleph$ ), azimuthal extent ( $\Psi$ ) and percentage of images with an SBC at different times prior to SEF.

from Figure 5.16 is that there are bands in the no SEF group that have a low crossing angle and high azimuthal extent, but fail to evolve into SEs. This suggests that while rainband geometry plays an important role in this structural transition, other dynamical or environmental factors must also contribute.

This is first time that a preferred convective pathway to SEF has been observed. It is instructive to consider these results in the context of previously proposed hypotheses relating to the dynamics of SEF. The formation of an SBC within 12hrs of SEF in 72% of cases strongly suggests that asymmetric processes are important in SEF, for instance asymmetric stratiform processes (Didlake et al., 2018) and boundary layer inflow forcing (Qiu and Tan, 2013). The preference for higher azimuthal extent in the 12 hours prior to SEF provides observational evidence that the projection vorticity accumulation and diabatic heating within the rainbands onto the azimuthal mean may contribute to the development of the SE, as suggested in previous work (Judt and Chen, 2010; Rozoff et al. 2012). These observations strongly suggest that symmetric processes such as VRWs and beta skirt axisymmetrisation alone are insufficient to explain SEF. This is an important result, as a considerable number of previous studies of SEF have been conducted within an axisymmetric framework.

## 5.6 Summary

In summary, systematic differences arise in the storm scale morphology, incidence of SBCs and geometry of individual bands in different basins. Analysis of SEF events demonstrates that there is a preferred convective evolution prior to SEF:

1. An SBC develops in a TC with pre-existing spiral rainband structure.
2. The geometry of the SBC evolves with time
3. In cases where the SBC has sufficiently high azimuthal extent and low crossing angle, it may evolve into a SE.

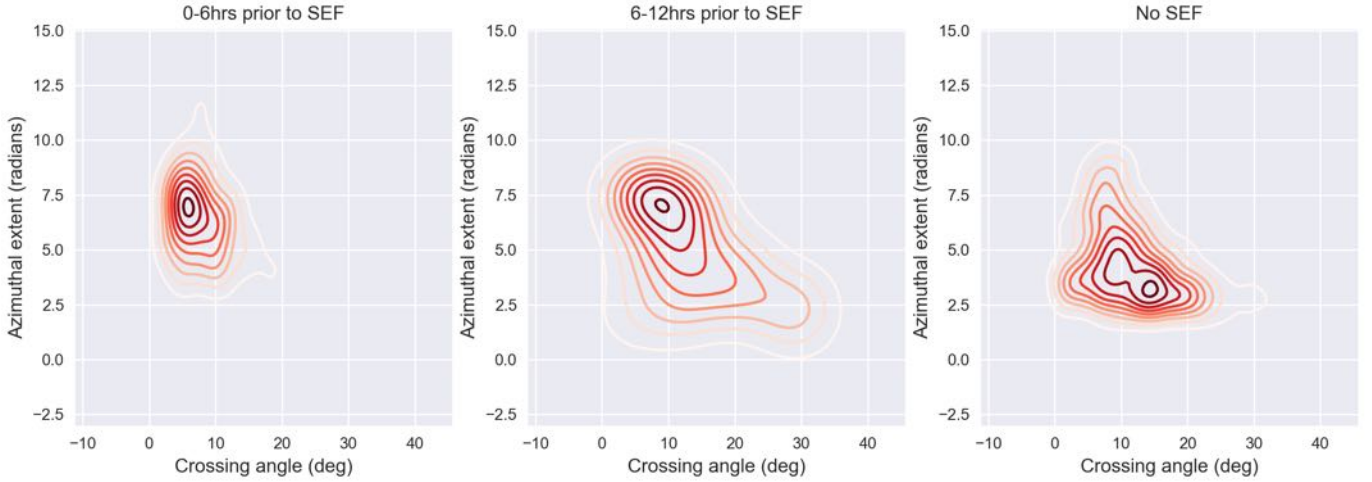


Figure 5.16: KDE probability plots showing distributions of ICA parameter geometry for (from left to right): Images 0-6 hours prior to SEF, images 6-12hrs prior to SEF, all images with a PRB that do not evolve into a SE within 24hrs.

The existence of this preferred convective evolution leading up to SEF, together with the demonstrated variation in rainband morphology between basins naturally motivates the question of to what extent this process is controlled by the large scale environmental conditions. In the next chapter, the impact of the environmental conditions on each stage of the axisymmetrisation process is discussed in detail.

# Chapter 6

## Results chapter: Impact of Environmental Conditions on Rainband Evolution

This chapter aims to quantify the impact of the large scale environmental conditions on rainband evolution leading up to SEF. Specifically, the two scientific questions addressed are:

1. At each of the four stages of the axisymmetrisation process, to what extent does the large scale environment impact the morphological evolution?
2. Given information about the large scale environment and the current TC morphology, is it possible to predict imminent SEF events?

The characteristics of the large scale environment are quantified using the datasets described in Chapter 3. This information is used to create a statistical model to predict SEF given information about the current banding morphology and environment using gradient boosted decision tree learning with the XGBoost algorithm (Chen and Guestrin, 2016).

### 6.1 Methodology

The impact of the environmental conditions on each of the following four stages of the axisymmetrisation process is quantified individually. The first two stages concern processes occurring on a large scale:

1. Comparison of TCs with and without a well defined banding structure.
2. Of TCs with no SBC, comparison between those where an SBC develops within 6 hours and those where no SBC develops within 6 hours.

The second two concern processes occurring in TCs with a SBC:

3. Comparison of PRBs with high and low crossing angle/azimuthal extent.
4. Comparison between SBCs that develop into a SE within 24hrs and those with high circularity where SEF does not occur within 24hrs.

As discussed in Chapter 3, the PMW dataset has irregular temporal resolution. For processes occurring on long timescales, it is therefore logical to standardise the structural record to a regular temporal resolution to avoid uneven sampling of individual events. As the SHIPS predictors and shear profiles are both at 6 hourly resolution, the structural record is standardised to six hourly. The SHIPS data points are available at 00UTC, 06UTC, 12UTC and 18UTC respectively. Each satellite overpass in the dataset is assigned to a bin around these times: 21UTC-03UTC, 03UTC-09UTC, 09UTC-15UTC or 15UTC-21UTC. A time period is assigned to missing if no satellite overpasses occurred, or to the structural classification of the image if one overpass occurred. If multiple satellite passes occur within one time period, the classification is taken from the latest overpass.

For the latter two stages, the geometry of individual SBCs is considered. Analysis of crossing angle variations in bins with multiple PRB images in the 6 hourly dataset reveals that the crossing angle and azimuthal extent of an individual band evolve on timescales much faster than 6 hours, with variations of up to 13.8 degrees and 2.91 radians occurring within a 6 hour time period. All image classifications are therefore included, with the understanding that this represents a random sampling of a quickly evolving phenomenon. For each image in the 2012-2014 sample, the 15 SHIPS predictors and ERA-I shear profiles are linearly interpolated to the time of each satellite overpass.

A difficulty in comparing the shear profiles between different groups is determining to what extent variations in the shear are associated with differences in the geographic distributions, and to what extent they actually cause changes in the convective morphology. In order to limit this uncertainty as much as possible, only TCs within the WPAC are included in the shear composite profiles. The shear profiles are further standardised by considering the flow at each level relative to the deep layer shear direction. Deep layer shear is defined as the vector difference between the 850hPa and 200hPa flow. For this analysis, the direction of the flow at height  $h$  is therefore given by

$$\theta_{hrel} = \tan^{-1}\left(\frac{v_{850} - v_{200}}{u_{850} - u_{200}}\right) - \theta_h$$

where  $\theta_{hrel}$  is the deep layer shear relative flow direction at height  $h$ ,  $\theta_h$  is the flow direction at height  $h$  and all other symbols have their usual meaning. Profiles created using this method will hereafter be referred to as the VWS relative flow.

## 6.2 Dynamics

### 6.2.1 TC scale Convective structure

The first stage of the axisymmetrisation process is the development of spiral banding structure. In order to assess which environmental conditions are conducive to the development of rainbands, the 6 hourly dataset is divided into four groups based on the storm scale convective classification: no classification, no bands, sheared and rainbands. The rainbands category is compared to each of the three other categories.

Between the rainbands and no classification groups, differences between the two groups are significant at the 99% level for the VMAX, SHRD, PSLV and E000 parameters (Figure 6.1 (a,b)). TCs in an environment with higher (lower) values of the steering flow level and shear magnitude (intensity) are associated with a greater likelihood of spiral banding. This is consistent with observations that the median intensity for a TC to have a well defined eye structure is 97 knots (Knapp et al., 2018), and that higher values of shear lead to the distortion of the convective structure (Frank and Ritchie, 1999).

Differences between the rainbands and no rainbands groups are significant at the 99% level for the VMAX, CD26, E000, VMPI, RSST, E000 and EPOS parameters. Median values for all parameters are lower for cases with no bands (Figure 6.1 (c,d,e,f)). In contrast to the no classification group, the environmental differences are therefore primarily thermodynamic. This is consistent with observations that the size of the TC, a proxy for the activity of the rainband field is smaller for TCs in an environment with lower relative SST (Lin et al., 2015) and humidity (Hill and Lackmann, 2009). Greater depth of the 26 degree isotherm is associated with higher CAPE (Wada et al., 2012), providing favourable conditions for rainband development. The 200hPa divergence and intensity are also lower for the no rainbands group, likely because the conditions are less favourable for intensification (Emanuel, 1986), and the overturning circulation is subsequently weaker.

Finally, differences between the sheared and rainbands groups are significant for all predictors. Sheared group TCs have higher median values of shear, and lower median VMAX (Figure 6.1 (g,h)). Median values of all thermodynamic parameters are lower for the sheared group. Given that the sheared group TCs develop at significantly higher latitudes (Figure 5.3), it is probable that these differences are associated with the cooler and drier environment in the midlatitudes, suppressing rainband formation. The characteristic asymmetric structure occurs primarily as a result of VWS (Chen et al., 2006).

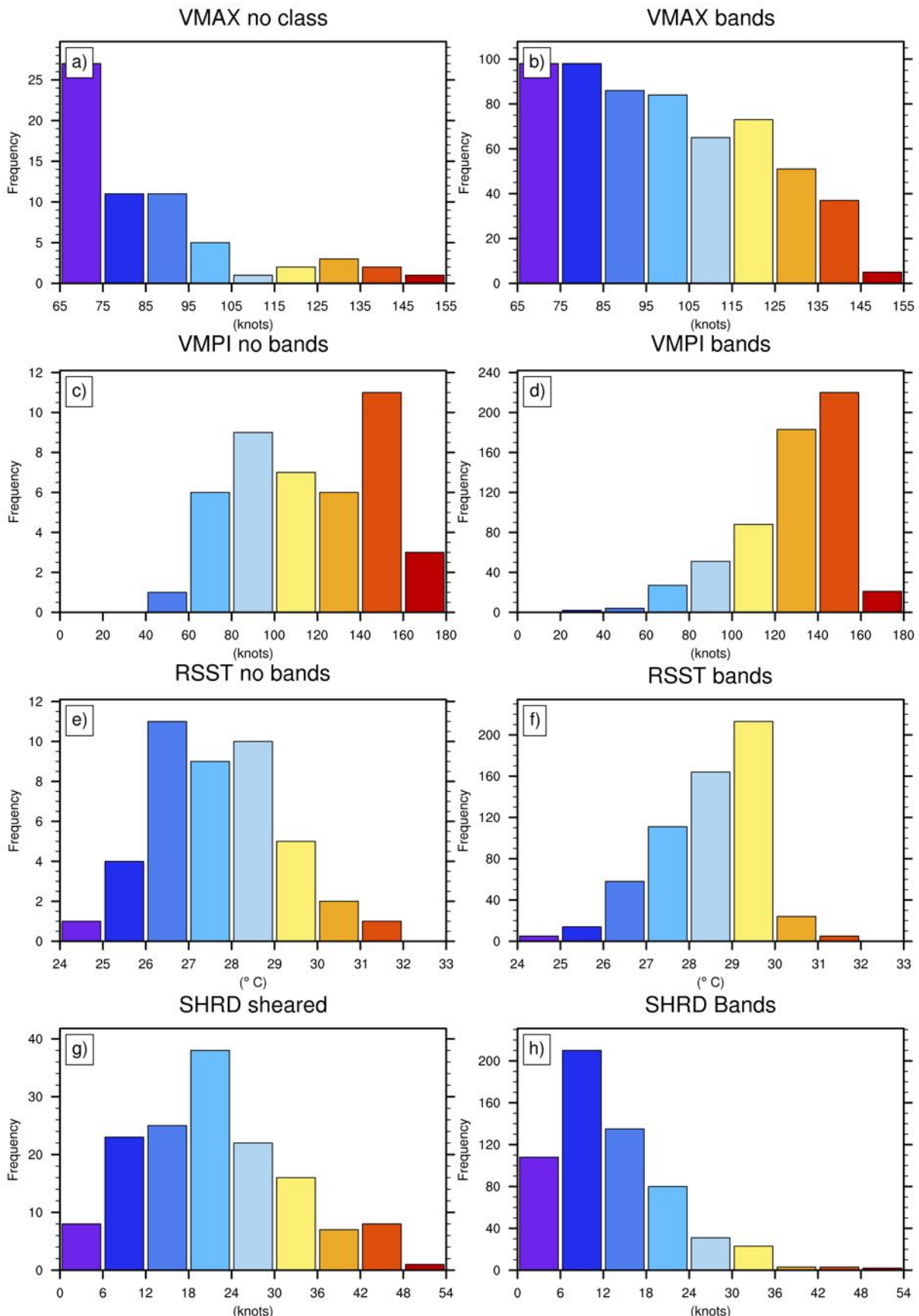


Figure 6.1: Examples of differences in distributions in SHIPS parameters between TC scale convective classifications. (a,b) No classification compared to rainbands for VMAX. (c,d) No bands compared to rainbands for VMPI. (e,f) No bands compared to rainbands for RSST. (g,h) Sheared compared to rainbands for SHRD.

Bands vs. No classification			
Predictor	PRBF median	No PRBF median	KS test p-value
VMAX (kts)	95	90	0.02
CD26 (m)	57	52	0.01
VMPI (kts)	129	133	0.05
PSLV (hPa)	561	581	0.05
R000 (%)	76	77	0.02

Table 6.1: Differences in statistically significant SHIPS predictors between the PRBF and no PRBF groups.

### 6.2.2 Principal rainband formation (PRBF)

The second stage of the SEF process is the formation of an SBC. All data points classified as having rainbands but no SBC are divided into two groups: cases where an SBC develops within 6 hours and those where an SBC does not develop within 6 hours.

Comparisons are made between the two groups for each of the 15 SHIPS predictors. Differences are significant at the 95% level for VMAX, CD26, R000, VMPI and PSLV (Figure 6.2). Higher (lower) values of VMAX, CD26, (VMPI PSLV, R000) are associated with PRBF (Table 6.1). Higher values of VMPI and CD26 indicate that the TC is in a favourable environment for convection and intensification, resulting in higher VMAX. A somewhat surprising result is that lower 1000hPa outer core relative humidity results in enhanced chance of PRBF. It is emphasised that this predictor is referring to the relative humidity outside of 200km radius, as the IC relative humidity is typically around 80% (Emanuel, 1995). The relationship between lower 1000hPa relative humidity and PRBF is not immediately clear. One possible explanation is that the upwind end of PRBs in larger storms will often extend past 200km radius. This end is convective (Hence and Houze, 2008) and associated with downdrafts reducing the low level humidity (Powell, 1990a; Riemer and Laliberté, 2015).

The limited previous work that has investigated PRBF has suggested that the PRB forms as a result of the asymmetric vortex response to deep layer shear (Willoughby et al., 1984; Riemer and Montgomery, 2011; Riemer, 2016). From this perspective, it would be expected that PRBF is more likely in an environment with stronger VWS. Surprisingly, this is not observed, with no significant differences between the no PRBF/PRBF deep layer shear magnitude distributions ( $p\text{-value}=0.28$ ). A more in depth analysis of the shear is conducted using the ERA-I profiles. For completeness, the VWS magnitudes calculated from this dataset are compared, again yielding no significant differences ( $p\text{-value}=0.86$ ). Composite plots of the u and v components of the VWS relative flow from 850hPa to 200hPa for the two groups are shown in Figure 6.3. Differences in the mean u-component are statistically significant at the 90% level from 850-

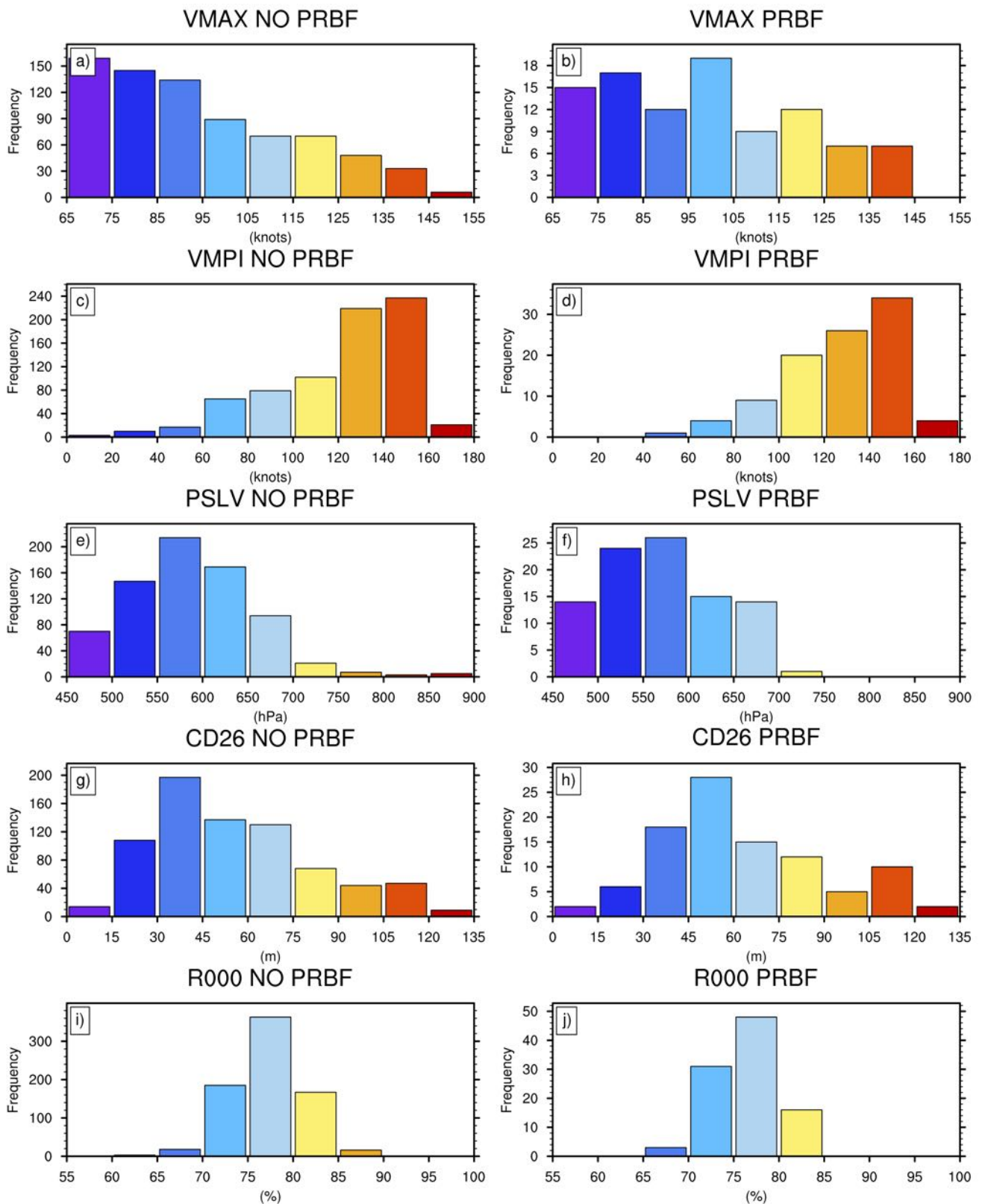
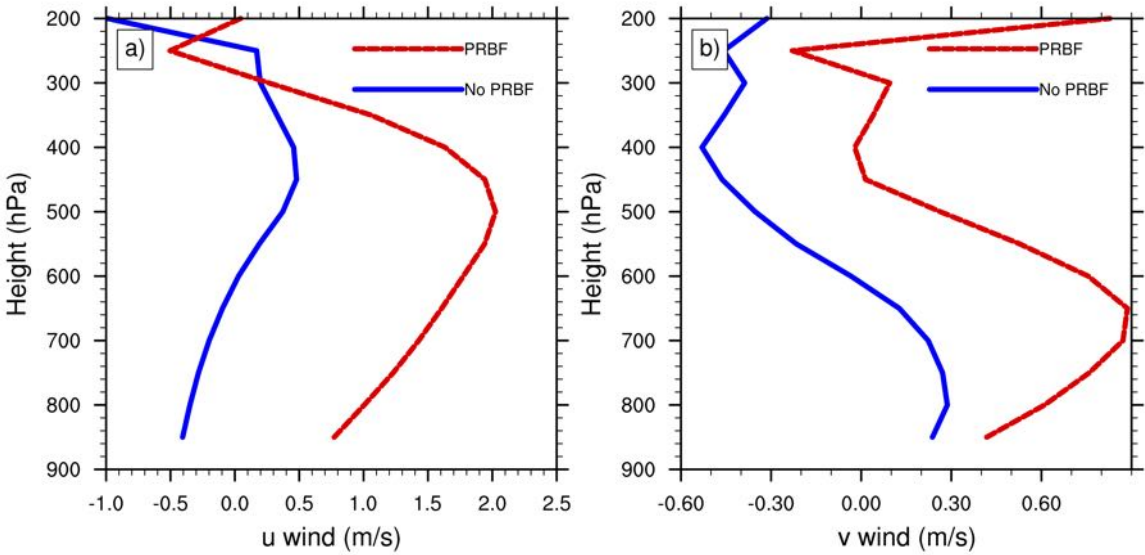


Figure 6.2: SHIPS histograms comparing the PRBF and no PRBF groups for (a, b) VMAX, (c, d) VMPI, (e, f) PSLV, (g, h) CD26, (i, j) R000.



*Figure 6.3: Mean shear profiles for the (a) u-component and (b) v-component of the wind relative to the 850-200hPa deep layer shear vector for the no PRBF group (blue) and PRBF group (red).*

400hPa, and at the 95% level from 800-400hPa using a Mann-Whitney-U test. Differences in the v component are not significant.

Three notable differences are apparent between the shear profiles. One is the direction of the low level (850hPa) flow. For the composite PRBF (no PRBF) profile, the u-component of the low level flow is aligned (counter aligned) with the deep layer shear vector. Though differences in the magnitude of the deep layer shear are not significant, there are clear variations in the low level shear magnitude, with substantially stronger shear in the PRBF group below 600hPa. Differences between the 850-600hPa shear magnitudes are significant at the 99% level. Finally, the mean directional change in the flow is in opposite directions between the two groups (Figure 6.4). For the PRBF (no PRBF) group the flow direction rotates clockwise (anticlockwise) with height.

These results suggest that it is the shear profile as opposed to simply the shear magnitude that controls PRBF. Based on these results and previous work, a new paradigm for PRBF is proposed. Numerical studies have demonstrated that in an environment with vertical shear the vortex tilts downshear left, leading to a positive upper level PV anomaly down tilt and lower level PV anomaly up tilt (Jones, 1995, 2000a,b; Reasor et al., 2004; Riemer, 2016). The IC moist envelope is also distorted, resulting in a positive mid tropospheric  $\theta_e$  anomaly downshear (Riemer 2016). As discussed by Riemer (2016), this creates a favourable environment for deep convection to develop in the downshear right quadrant and propagate cyclonically around the vortex.

The results presented here suggest that the characteristics of the shear depth and the low level flow direction act in conjunction with these mechanisms to drive PRBF. A possible explanation

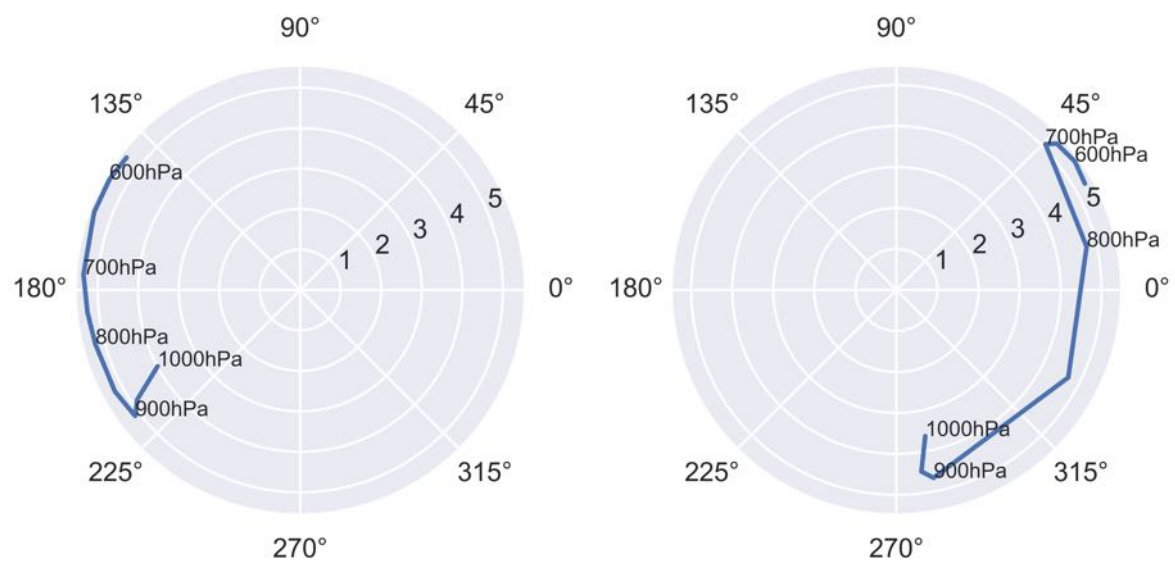


Figure 6.4: Deep layer shear relative mean direction at different heights for (left) PRBF and (right) No PRBF.

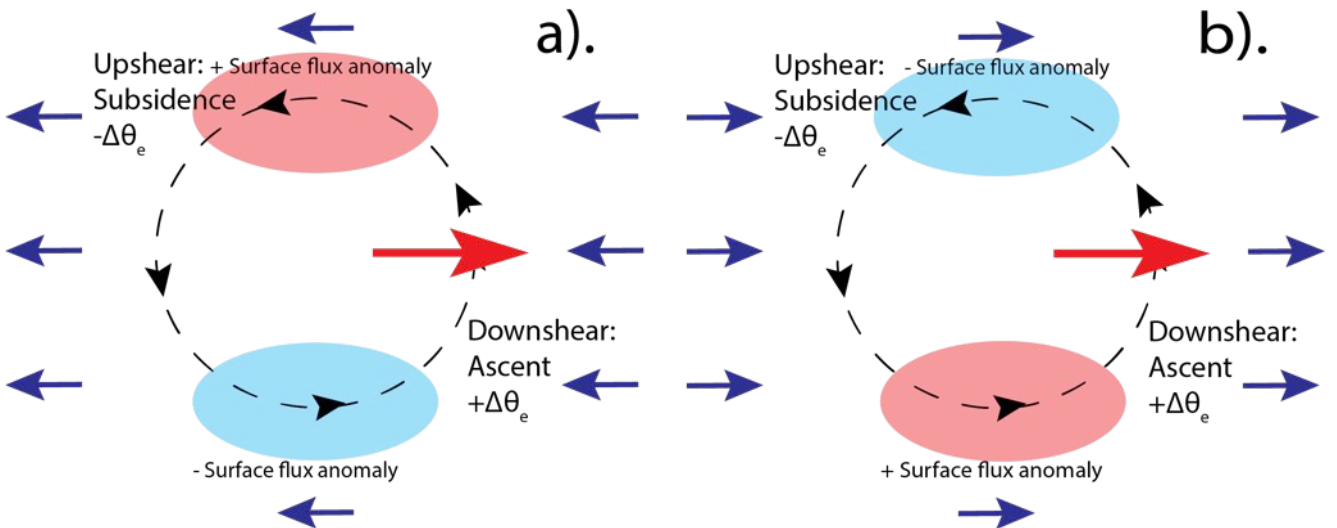


Figure 6.5: Schematic of flux asymmetries in the vortex under the influence of VWS for (a) counter aligned low level environmental flow and (b) aligned low level environmental flow. The vortex circulation is shown in black, low level environmental flow in blue and the deep layer shear vector in red. Positive (negative) surface flux anomalies are indicated with red (blue) shading.

is that PRBF is associated with strong low level shear and flow aligned with the deep layer shear vector at 850hPa. The superposition of the vortex and environmental flows results in a positive surface flux anomaly to the right of shear vector, and a negative anomaly to the left of the shear vector (Figure 6.5). This negative anomaly left of shear limits the cyclonic advection of the convection developing downshear right, and hence the precession of the vortex upshear. In contrast, when the shear and low level flow are counter aligned, the surface flux anomalies are reversed, leading to favourable conditions for the precession of the vortex upshear and the development of IC convection. This building symmetric convection further increases the vortex resilience, (Mallen et al., 2005), limiting the downshear tilt and hence the convective asymmetry. A similar mechanism has previously been shown to play a role in determining the timescale of tropical cyclogenesis (Rappin and Nolan, 2012) and asymmetries in rainfall composites in the WPAC basin (Chen et al., 2018). Although the absolute magnitude of the differences in low level flow between the two groups is only 2m/s, it is important to note that this is of the same order of magnitude as the numerical simulations conducted by Rappin and Nolan (2012).

The depth of the shear is also important in modulating the magnitude of the vortex tilt. Both numerical (Finocchio et al., 2016) and observational (Zeng et al., 2010; Wang et al., 2015) analyses have suggested that the magnitude of the vortex tilt increases with stronger shear below 500hPa. In this case, stronger shear below 600hPa (Figure 6.3) enhances the vortex tilt, enhancing the  $\theta_e$  and PV anomalies and hence the convective forcing in the downshear right quadrant. Another potential mechanism for enhancing convection downshear right is the concentration of shear relative helicity in the downshear right quadrant as a result of the differing helicities in the shear profiles(Onderlinde and Nolan, 2014, 2016).

Clearly, this process will be complicated by processes occurring on a convective scale. The tilt configuration of the vortex depends on the radial PV structure at the VRW stagnation radius (Reasor and Montgomery 2001, Reasor et al. 2004) and vortex size (Jones, 2000a). The response of the vortex to VWS, and associated asymmetries, are therefore dependent on pre-existing convection within the IC and the evolution of the shear profile and convective distribution with time. It is therefore difficult to quantify what threshold of vortex tilt is required for PRBF to occur. It is likely that the formation of the moat depends on the development of sufficiently strong, persistent convection concentrated in one area to suppress any pre existing convection as the TC transitions from a symmetric to asymmetric configuration. Other processes including the TC motion (Shapiro, 1983; Thomsen et al., 2015) and beta gyres (Ritchie and Frank, 2007) also impact on the vortex alignment and convective asymmetries.

### 6.2.3 PRB geometry

For all cases with a SBC, the geometry of the PRB is examined. For this analysis all images are used, with the SHIPS variables interpolated to the time of the satellite overpass.

#### Crossing angle

Pearson correlations between the crossing angle and individual parameters are low, primarily as a result of nonlinear interactions between different variables and the number of competing dynamical factors influencing the rainband geometry. The impact of environmental conditions on crossing angle extremes is therefore considered. Environmental conditions are compared between cases with crossing angle in the first quartile of the distribution (less than 9.63°) and those in the fourth quartile (greater than 19.99°).

For the intensity and thermodynamic variables, differences are statistically significant between the VMAX, VMPI, TGRD, R000 and E000 parameters (Table 6.2). PRBs in an environment with lower (higher) TGRD (VMAX, VMPI, R000 and E000) are associated with higher (lower) crossing angle (Figure 6.6). In general, storms with a higher VMAX will be in a lower shear environment, resulting in a more symmetric structure. Higher values of R000 and E000 are associated with lower crossing angles. This is likely related to VMAX, and the fact that more intense TCs are more likely to be located in a more thermodynamically favourable environment. Differences are also apparent in the environmental flow parameters. Lower crossing angles are associated with lower SHRD, PSLV and HE05.

The role of environmental conditions in determining the crossing angle is therefore not immediately clear. The geometry of the PRB is likely related to the topology of the low level flow controlling where developing convection is advected within the vortex. A possible mech-

Predictor	Low $\aleph$ vs high $\aleph$		p-value
	low $\aleph$ median	high $\aleph$ median	
VMAX (kts)	99	90	0.02
VMPI (kts)	130	133	0.01
SHRD (kts)	11	14	0.001
HIST (hrs $\times$ 6)	22	18	0.0004
TGRD ( $^{\circ}$ C $\times 10^{-7}$ )	15	19	0.02
PSLV (hPa)	552	568	0.03
HE05 ( $m^2 s^2 \times 10$ )	-4	1	0.03
R000 (%)	77	75	$9.27 \times 10^{-7}$
E000 ( $^{\circ}$ K $\times 10$ )	352	350	0.03

Table 6.2: Differences in statistically significant SHIPS predictors between the low crossing angle and high crossing angle groups.

anism for the role of the storm averaged environmental conditions is that thermodynamically favourable conditions increase VMAX, and hence the strength of the tangential circulation. This leads to more circular flow, and a lower crossing angle. Weaker VWS results in reduced tilt, which lessens the distortion to the wind field, and subsequently the crossing angle. Negative HE05 is associated with a more symmetric, intense storm (Onderlinde and Nolan, 2014), consistent with these arguments. These arguments would clearly be complicated by the topology of the environmental flow, and the radial profile of the vortex. Observations using high resolution datasets would therefore be required to determine the precise relationship between the flow topology and the crossing angle, as discussed in Chapter 7.

## Azimuthal extent

Pearson correlations between azimuthal extent and the SHIPS parameters are higher than for the crossing angle, with values of up to 0.4 for CD26 and 0.38 for VMAX. For consistency with the crossing angle analysis, however, this analysis is conducted in the same manner comparing high and low azimuthal extent groups. PRBs with an azimuthal extent less than 2.92 radians (1st quartile) are compared to those with azimuthal extents greater than 5.33 radians (4th quartile).

Differences are statistically significant between all variables, with the exception of R000 and HIST (Table 6.3, Figure 6.7). Higher azimuthal extent is associated with substantially greater VMAX, with median values of 106.9kts compared to 86.4kts. Part of the reason that the VMAX is higher for the high azimuthal extent group may be that this group is located in a more thermodynamically favourable environment. Cases with higher azimuthal extent have higher VMPI at 133.29 knots compared to 119.60 knots, and correspondingly greater values of CD26, RSST, RHRI, EPOS and E000. The magnitude of the deep layer shear is significantly

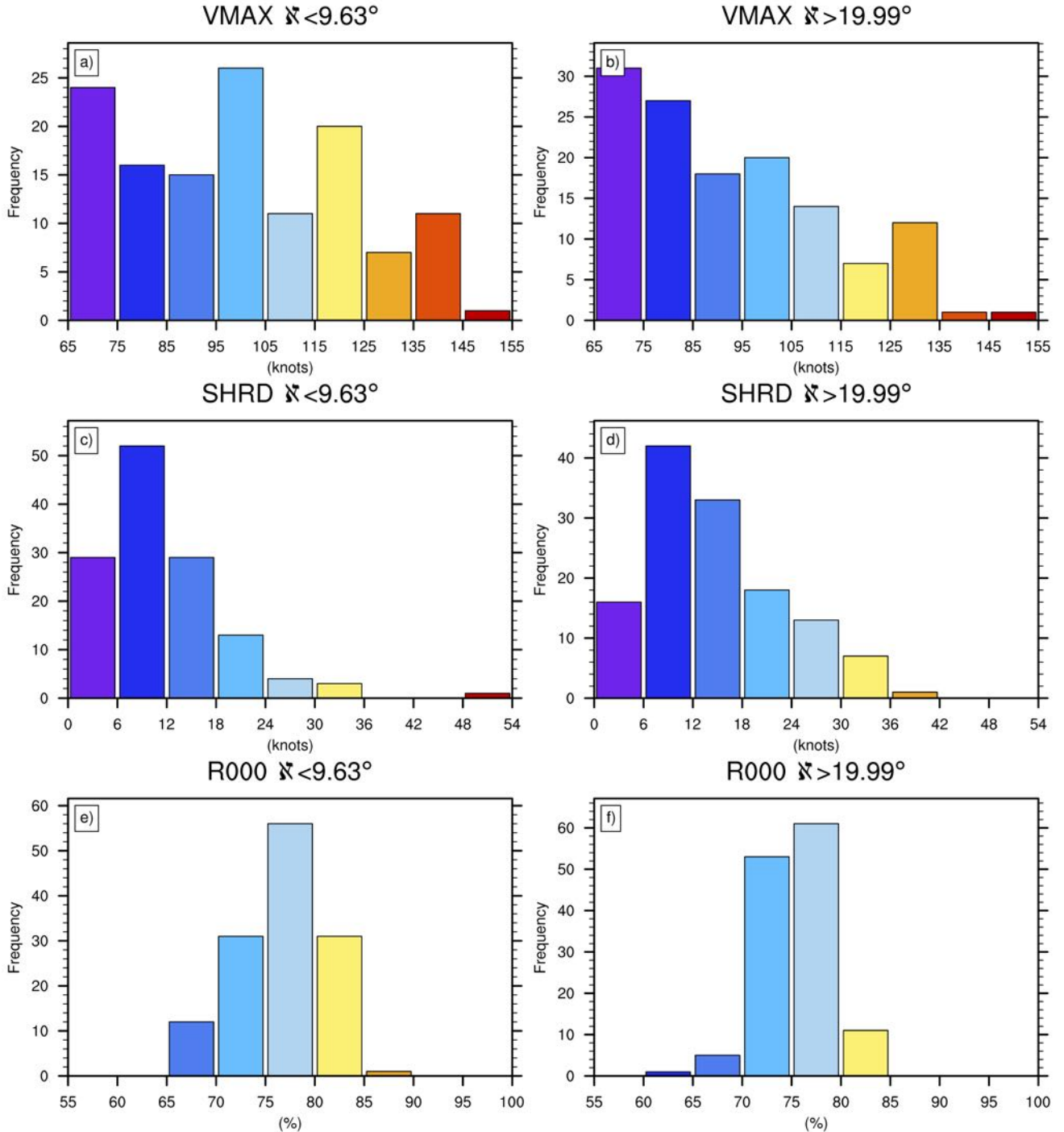


Figure 6.6: SHIPS histograms comparing cases with crossing angles in the first quartile (left) fourth quartile (right) for (a, b) VMAX, (c, d) SHRD and (e, f) R000.

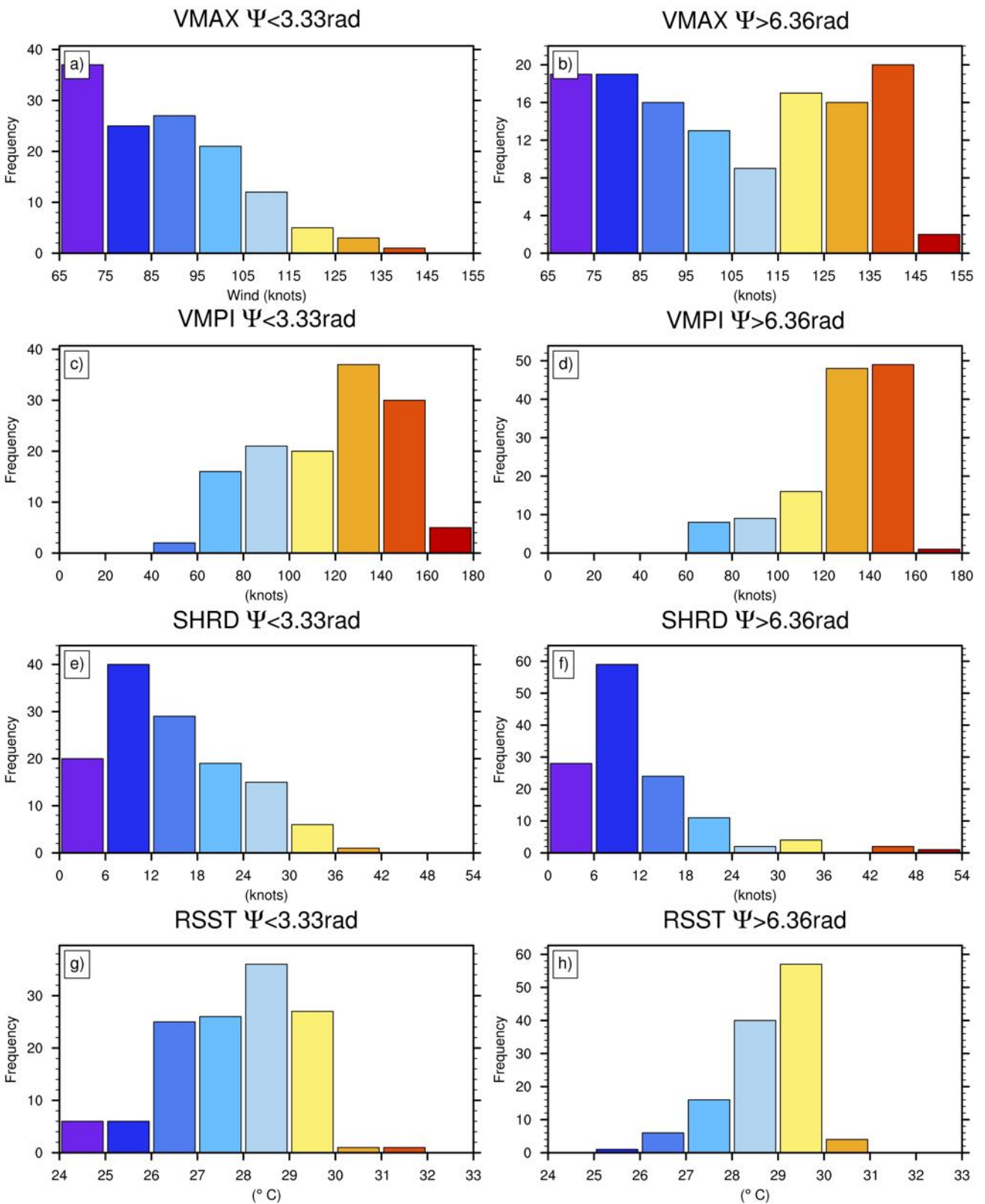
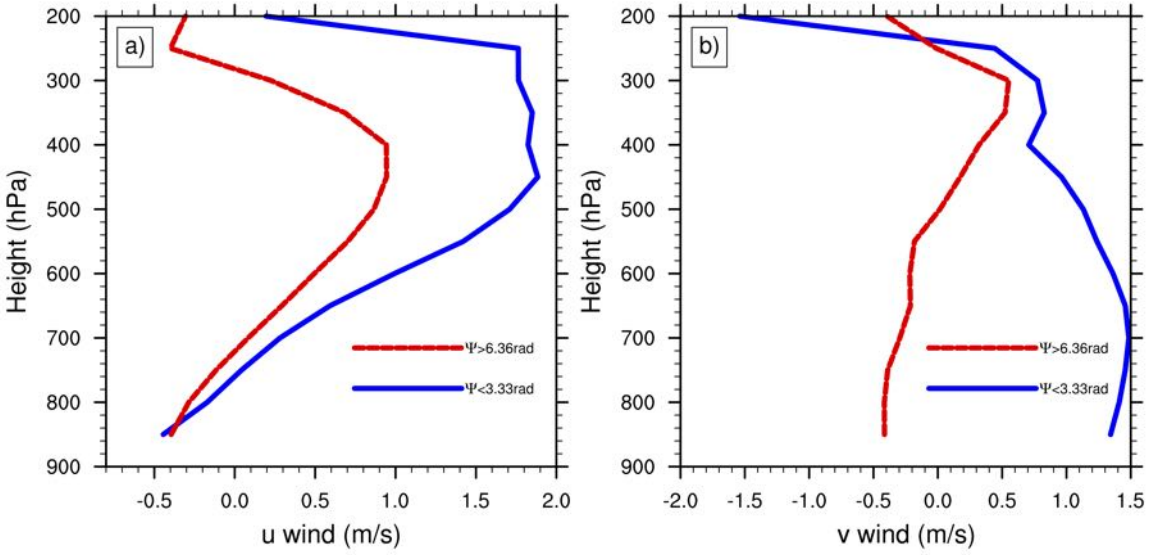


Figure 6.7: SHIPS histograms comparing cases with PRB azimuthal extent in the first quartile (left) and fourth quartile (right) for (a, b) VMAX, (c, d) VMPI, (e, f) SHRD and (g, h) RHHI.



*Figure 6.8: Mean shear profiles for the (a) u-component and (b) v-component of the wind relative to the 850-200 hPa shear vector for the low azimuthal extent group (blue) and high azimuthal extent group (red).*

lower for the high azimuthal extent group.

Clear differences are apparent between the shear profiles for the high and low azimuthal extent groups. Again considering just the WPAC cases, the difference in deep layer shear magnitudes calculated from the ERA-I profiles is significant at the 99% level. The u and v components of the composite VWS relative profiles are shown in Figure 6.8. Differences between the v-component of the winds for the two groups are significant at the 99% level below 550 hPa using a Mann-Whitney-U test. For low azimuthal extent cases, the mean v-component of the 850 hPa wind is positive, while for high extent cases it is negative.

Based on these observations and previous work, a mechanism for determining the azimuthal extent of the band is suggested. Numerical studies of PRBF (Riemer, 2016; Li et al., 2017) have suggested that the geometry of the principal band is determined by convection developing downshear right and being passively advected into the downshear left quadrant. This explanation is inconsistent with explaining how a PRB can develop an azimuthal extent greater than 180 degrees. One previously proposed explanation for how the band grows upwind is that the circulation associated with the convective upwind end of the band triggers boundary layer convergence, forcing new convection upwind (Didlake et al. 2013b). Another is that PRBs are associated with corridors of moisture that are entrained into the TC circulation (Zick and Matyas, 2014).

In the context of this previous work, the results presented here suggest that the azimuthal extent of the band is controlled by both the thermodynamic conditions and the shear profile. One possible mechanism is the surface flux asymmetry, similar to that discussed in the PRBF section. In cases with high azimuthal extent (Figure 6.8), the surface wind is to the right of

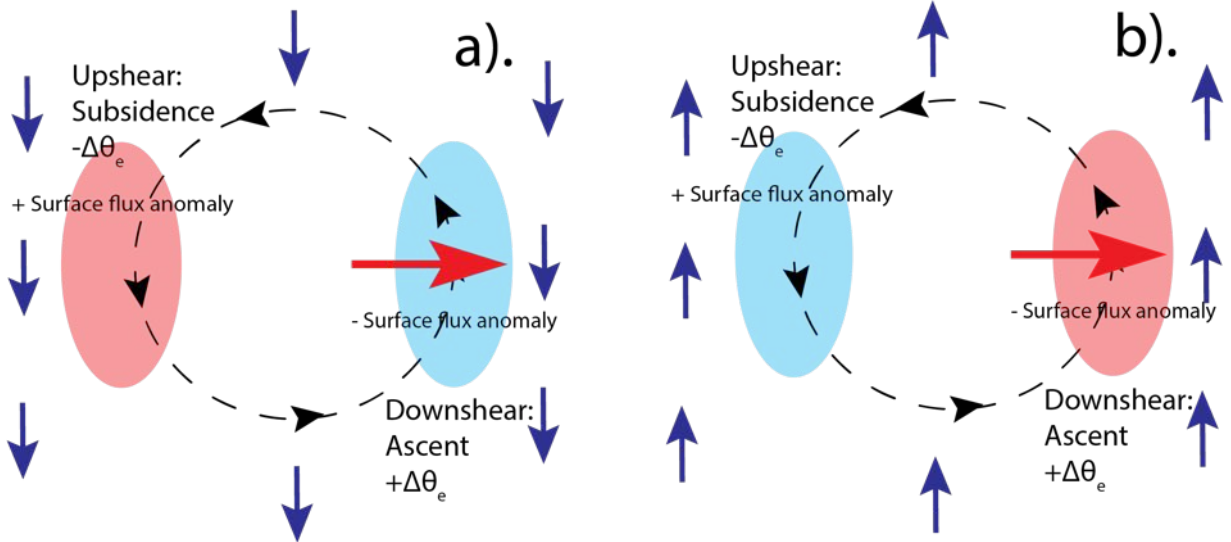


Figure 6.9: Schematic of different azimuthal extents for (a) low level flow to the right of the deep layer shear and (b) low level flow to the left of the deep layer shear. The vortex circulation is shown in black, low level environmental flow in blue and the deep layer shear vector in red. Positive (negative) surface flux anomalies are indicated with red (blue) shading.

the shear vector, creating a positive surface flux anomaly on the dry upshear side of the vortex. This provides more favourable conditions for the development of deep convection as the PRB grows upwind (Figure 6.9 (a)). This has a secondary effect, as the growth of the rainband into the upshear quadrants will tend to increase the vortex resilience (Reasor et al. 2004), reducing the tilt induced asymmetries. In contrast, for left of shear 850hPa flow a negative surface flux anomaly develops upshear, further inhibiting convection from building upwind (Figure 6.9 (b)).

A more favourable thermodynamic environment plays two roles in determining the azimuthal extent of the SBC. Firstly, regardless of the mechanism via which the PRB grows upwind, a more favourable thermodynamic environment increase the likelihood of convective development. Associated decreases in static instability can also act to reduce the vortex tilt by modulating the effect of the PV anomalies. For a symmetric vortex, the penetration depth is given by (Hoskins et al., 1985; Jones, 1995)

$$d = \sqrt{(f + \frac{2v_T}{r})(f + \zeta)} \times \frac{L}{N}$$

where  $v_T$  is the tangential component of the velocity vector,  $L$  is the horizontal length scale of the anomaly,  $N$  is the static stability and all other symbols have their usual meaning. Decreased static stability therefore results in a higher penetration depth, and greater vortex resiliency (Reasor et al. 2004).

Predictor	High $\Psi$ vs low $\Psi$		
	low $\Psi$ median	high $\Psi$ median	KS p-value
VMAX (kts)	86	104	$6.36 \times 10^{-9}$
VMPI (kts)	124	138	$1.28 \times 10^{-7}$
SHRD (kts)	14	10	$2.35 \times 10^{-4}$
D200 ( $s^{-1} \times 10^{-7}$ )	27	55	$5.25 \times 10^{-7}$
RSST (deg)	28	29	$1.04 \times 10^{-6}$
CD26 (m)	45	67	$2.62 \times 10^{-7}$
TGRD ( $^{\circ}\text{C} \times 10^{-7}$ )	19	13	$6.65 \times 10^{-3}$
PSLV (hPa)	585	547	$7.28 \times 10^{-6}$
RHHI (%)	50	64	$5.66 \times 10^{-10}$
EPOS ( $^{\circ}\text{C} \times 10$ )	75	94	$2.02 \times 10^{-6}$
E000 ( $^{\circ}\text{K} \times 10$ )	349	355	$6.20 \times 10^{-8}$

Table 6.3: Differences in statistically significant SHIPS predictors between the low azimuthal extent and high azimuthal extent groups.

#### 6.2.4 SEF

The final step in the SEF process is to consider which SBCs develop into SEs. In Chapter 5, it was shown that between 0-6 hours prior to SEF, SBCs that evolve into SEs have significantly lower crossing angle and higher azimuthal extent than the sample mean. There are, however, many SBCs with these characteristics that do not become SEs (Figure 5.16). This is surprising, as based on previously proposed axisymmetric theories of PV accumulation and diabatic heating (Rozoff et al., 2012; Judt and Chen, 2010), asymmetric inflow forcing (Sun et al., 2013; Qiu and Tan, 2013) and boundary layer feedbacks (Huang et al., 2012; Kepert, 2013; Kepert and Nolan, 2014; Kepert, 2017), it would be expected that these bands would develop into SEs.

In order to assess which environmental conditions result in SEF in cases with circular banding geometry, two groups of images are identified. The first group (SEF) consists of all images with a PRB where the TC develops a SE within 24 hours, regardless of the geometry of the band. The second group (No SEF) consists of images with a PRB with a crossing angle less than  $9.0^{\circ}$  and an azimuthal extent greater than 6.36 radians (i.e within the first quartile for crossing angle and fourth quartile for azimuthal extent) where the band does not develop into a SE within 24hrs.

SHIPS parameters for which differences are significant between the two groups are shown in Table 6.4. Cases where an SE develops within 24 hours have significantly lower VMAX, SHRD, D200, RHHI and E000 (Figure 6.10). Lower VMAX together with lower boundary layer potential temperature suggests that convection within the PRB is stronger in cases where SEF ensues. This will reduce the boundary layer potential temperature by inducing downdrafts (Powell, 1990a), subsequently limiting the intensity of the TC (Riemer and Laliberté, 2015).

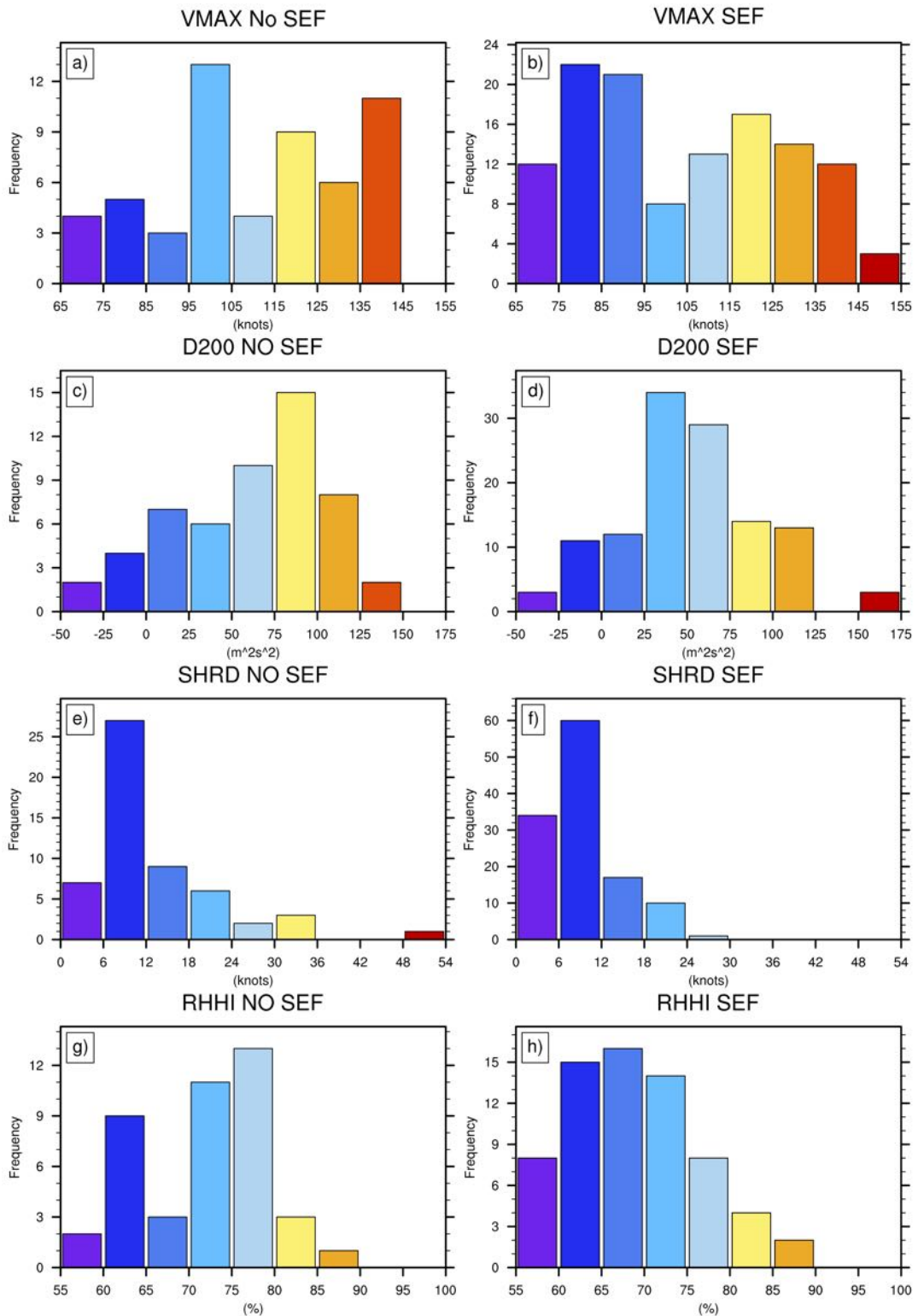


Figure 6.10: SHIPS histograms comparing the SEF (left) and no SEF (right) groups for (a, b) VMAX, (c, d) D200, (e, f) SHRD, (g, h) RHII.

SEF vs. no SEF			
Predictor	SEF median	No SEF median	KS p-value
VMAX (kts)	99.94	109.23	0.02
SHRD (kts)	8.21	11.24	0.003
D200 (kts $\times 10$ )	48.17	66.4	0.005
RHHI (g/kg)	57.05	71.15	0.002
E000 (K)	352.9	354.5	0.04

Table 6.4: Differences in statistically significant SHIPS predictors between the SEF and no SEF groups.

Higher values of SHRD will enhance the shear induced asymmetry, inducing subsidence over the upshear half of the TC and limiting the development of the SE upshear. ERA-I shear profiles were compared for the two groups, showing that the shear is significantly stronger between all levels for the no SEF group (not shown).

Interestingly, SEF is associated with lower RHHI. The role of outer core relative humidity in the circularity of rainbands has previously been noted in case studies of hurricanes Rita and Katrina. Ortt and Chen (2006, 2008) suggested that more circular rainbands develop in cases with lower outer core humidity. As all rainbands in this case are already circular, this suggests that a stronger outer core humidity gradient may be conducive for SEF. A possible mechanism for this would be the generation of baroclinic instability at the radius of the incipient SE.

## 6.3 A Statistical Model for SEF

From the perspective of operational forecasting, an important question is whether it is possible to apply this information to predict SEF events. Though there are isolated examples of successful forecasts using dynamical models (DiCatarina et al., 2018), in general forecasting SEF events remains difficult (Kossin and DeMaria, 2016). Recent work has demonstrated that in ensemble simulations with VWS, the onset of SEF varies by up to 72hrs between ensemble members as a result of machine error alone (Zhang et al., 2017a). These difficulties motivate the use of statistical models in predicting SEF. One previous statistical model been developed to predict SEF events using the SHIPS predictors. Kossin and Sitkowski (2009) used a Naive Bayes classifier to forecast the probability of SEF occurring within 12 hours (hereafter referred to as the KS09 model). This model included the IR SHIPS predictors, but no other information about the TC morphology, giving a recall of 30% and FAR of 2%. Given the relationship between rainband geometry and SEF demonstrated in this study, it is natural to ask whether statistical predictions of SEF can be improved by including information about the rainband structure.

### 6.3.1 Model description

For the SEF model, the predictor set consists of the 15 SHIPS variables, the ICA crossing angle and the ICA azimuthal extent. For consistency between reanalysis products, information about the shear profile is not included. Restricting predictors to the SHIPS variables has the added advantage that this product is available in real time, making it feasible to apply this model in an operational capacity.

This is an example of a binary classification problem. Given the recognised nonlinear relationships between the different predictors, Extreme Gradient Boosting is used to construct the models with the XGBoost algorithm (Chen and Guestrin, 2016). XGBoost has been applied extensively in chemistry (Zhang et al., 2017b), medicine (Aibar et al., 2017) and physics (Tamayo et al., 2016), however has not previously been used in meteorology. An XGBoost model consists of an ensemble of decision trees, where the residuals of each tree are minimised using stochastic gradient descent.

A difficulty with complex machine learning models such as gradient boosting is feature attribution, or assessing which predictors are the most important in determining the model prediction. Unlike for linear models, there is no simple method for ranking the importance of different features. A frequently utilised method is to assign importance based on how often different variables occur at each level of the trees, however recent work has demonstrated that this is inconsistent (Lundberg and Lee, 2017). The only consistent feature attribution framework for decision tree learning is the Shapely Additive Explanation (SHAP) values (Lundberg and Lee, 2017; Lundberg et al., 2018). A SHAP value quantifies the impact of individual predictors on determining the model prediction. For each datapoint and each predictor, the SHAP value ( $\xi$ ) is defined as

$$\xi_i(p) = \sum_{S \subseteq N \setminus i} \frac{|S|!(M - |S| - 1)!}{M!} [f_{xgb}(S \cup i) - f_{xgb}(S)]$$

where S is the powerset of  $N \setminus i$ , M is the total number of predictors in the model, N is the set of all input features, p is a data point, i is a predictor, and  $f_{xgb}$  represents the prediction of the classifier trained on predictor set S. This quantifies the impact of omitting the  $i^{th}$  predictor from the model on the model prediction of the  $p^{th}$  data point. The total impact of that feature on the model can then be determined by taking the mean SHAP value over all data points. SHAP values can also be extended to higher order interactions. For two predictors i and j, the SHAP interaction value  $\xi_{ij}$  provides a measure of the impact of omitting both predictors together from the model, and allows for visualisation of nonlinear interactions between predictors within a

gradient boosting framework.

$$\xi_{ij}(p) = \sum_{S \subseteq \{i,j\}} \frac{|S|!(M - |S| - 2)!}{2(M - 1)!} \nabla_{ij}(S) \quad (6.1)$$

where

$$\nabla_{ij}(S) = f_{xgb}(S \cup \{i, j\}) - f_{xgb}(S \cup \{i\}) - f_{xgb}(S \cup \{j\}) + f_{xgb}(S)$$

and all other symbols have the same meaning as for Equation 6.1. In this chapter, SHAP values are used to assess whether model behaviour is physically consistent.

### 6.3.2 SEF Model

The SEF XGBoost model takes any image of a TC and associated SHIPS values as input, and outputs the probability that SEF will occur within the next 12 hours. Class sizes are n=96 (SEF) and n=1034 (no SEF). Model skill is assessed using stratified k-fold cross validation with five folds. An important assumption of this process is that data in the test and training datasets are fully independent. Calculation of the decorrelation timescales for each of the SHIPS variables in the dataset reveals that the timescale is up to 72hrs for CD26 and RSST. To ensure that the independence assumption is not violated, an extra condition is imposed on the k-fold splitting that all images from each storm must be in the same fold. As there is a significant class imbalance, the minority (SEF) class is upsampled to parity in the training set using the Synthetic Minority Oversampling Technique (SMOTE; Chawla et al. 2002). This upsampling is performed after the test training split for each round of the validation to ensure that samples remain fully independent.

The tree depth and ensemble size of the classifier are tuned by evaluating the model performance with ensemble sizes ranging from 50 to 500 trees in steps of 25 and depths from 3 to 6. Model skill is benchmarked using the Macro F1 score. Variation in model performance over different ensemble sizes and depths is shown in Figure 6.11. Even after upsampling, limiting overfitting remains a significant challenge. Overfitting for a given tree depth can be detected by noting the point at which the Macro F1 score levels out or begins to decrease. Optimum model performance is achieved for a tree depth of 5 and ensemble size of 200.

The confusion matrix for the model is shown in Table 6.5. The model detects 66 out of 96 SEF events, and 1274 out of 1307 no SEF events. One measure of model performance is to compare the model to a dummy classifier which classifies data based on a random guess and information about the class sizes. For the dummy classifier, the model identifies just 6 out of the 96 events, with 104 false alarms. The model developed here is therefore skilful. A more interesting measure of skill is comparison to the KSR09 classifier. The confusion matrix for this classifier is shown in Table 6.3, with a POD of 39% and a FAR of 2%. The new model

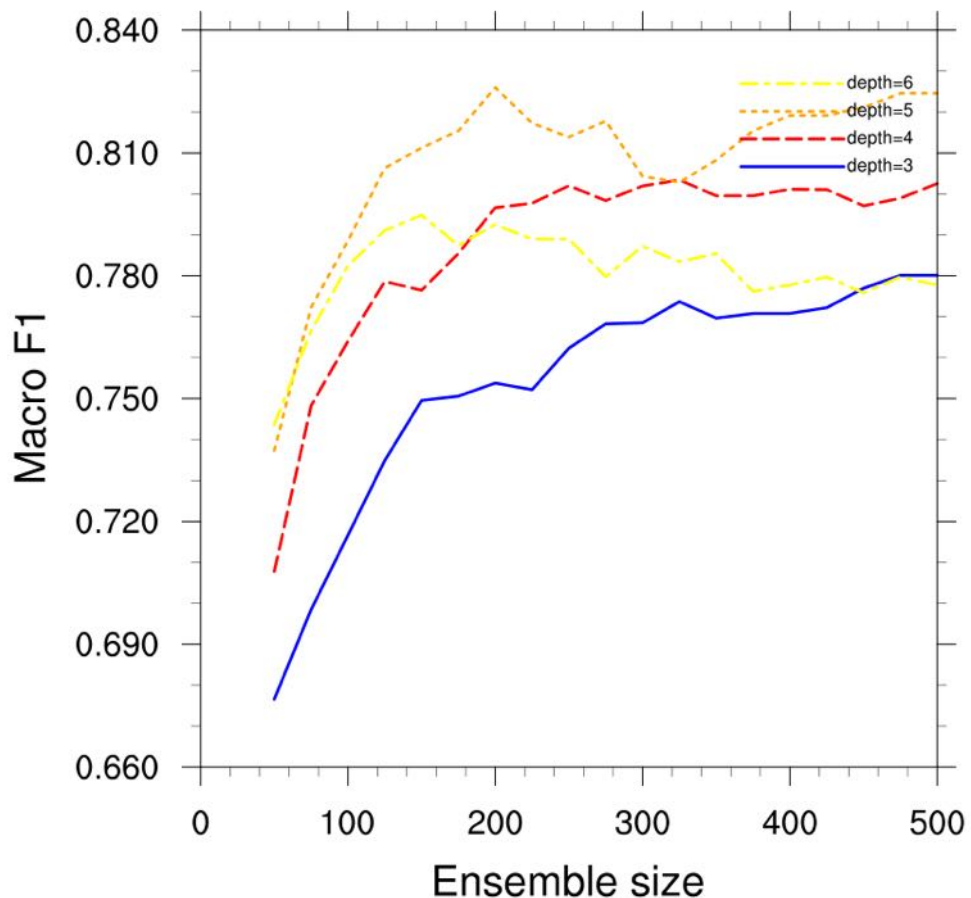


Figure 6.11: Macro-F1 score evolution for SEF model tuning with tree depths ranging from 3-6 and ensemble sizes from 50-500.

therefore has the same FAR, but detects 40% more SEF events, a significant improvement.

In order to assess the contribution of the rainband geometry predictors to the model predictions, the model is retrained with identical configuration but with the band geometry predictors excluded. For this set up, the model has a similar detection rate, correctly identifying 66 events as opposed to 69. The main difference is in the number of the false alarms, with 67 compared to 33 for the model with rainband predictors included. This is presumably because many of the false alarms are located in a favourable thermodynamic environment but do not have banding geometry conducive to SEF.

SHAP values are calculated to assess whether the model behaviour is physically justified (Figure 6.12). The most important variable in determining model output is the azimuthal extent, with higher (lower) values increasing (decreasing) the probability of a prediction of SEF. This is consistent with the known role of axisymmetric processes in SEF, and justifies the inclusion of the rainband geometry predictors in the model. Though the crossing angle does not have as big an impact on model output, this is possibly because much of the variance in this parameter is explained by the connection to azimuthal extent. Assessing the SHAP interaction values for the crossing angle and azimuthal extent demonstrates that increased decreased crossing angle and increased azimuthal extent result in a higher probability of SEF, as expected (Figure 6.13). Other important variables are VMAX, RHII, and CD26, with higher (lower) values of VMAX and CD26 (RHII) leading to a greater probability of SEF. These differences are all consistent with the physical mechanisms discussed in Section 6.2.4 (Table 6.3). The processes captured within this model are therefore dynamically consistent with understanding of SEF.

As an example, the model is shown correctly predicting two SEF events in Typhoon Jelawat (2012; Figure 6.14). For this demonstration, Typhoon Jelawat is excluded from the training set and the model is trained on all other data to ensure that the prediction is fully independent. The model successfully predicts both SEF events, with 94% (Figure 6.15 (a)) and 89% (Figure 6.15 (b)) probabilities assigned to the passes immediately prior to each event. Figure 6.15 (c) shows an example of a pass with a SE together with a PRB with azimuthal extent close to 360 degrees. The model recognises that this is conducive to SEF, assigning a 64% probability.

## 6.4 Conclusion

In summary, the large scale environmental conditions have been shown to impact each stage of the axisymmetrisation process. These results were applied to demonstrate that information about the rainband morphology can improve statistical predictions of SEF. Based on the results presented in this chapter, a paradigm for environmental control on SEF is proposed.

1. A TC develops a banding and eyewall structure as it intensifies, provided that it remains

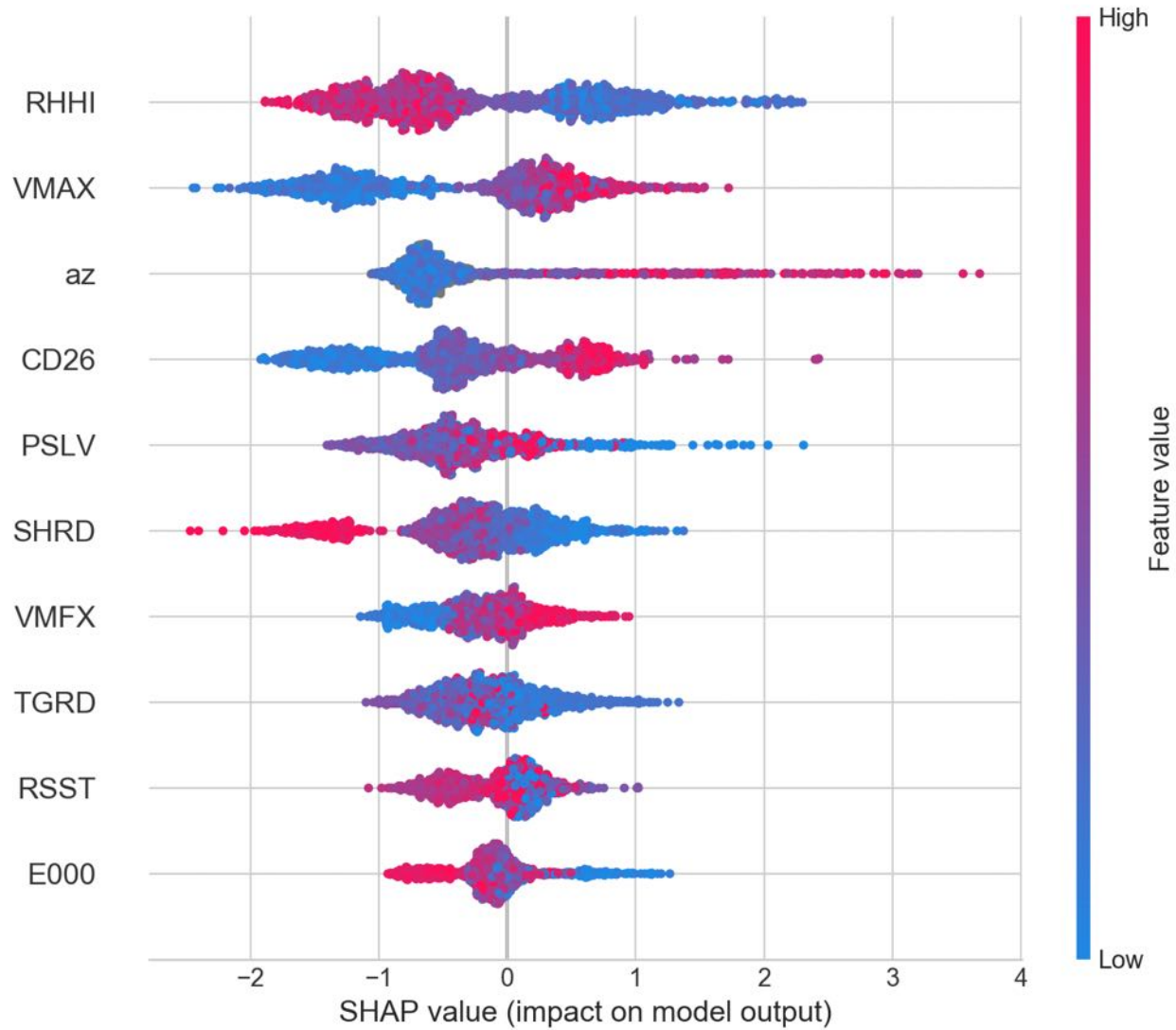


Figure 6.12: SHAP values for the SHIPS predictors, ICA crossing angle (*ca*) and ICA azimuthal extent (*az*) in the SEF model. Graphic generated using the python SHAP library Lundberg and Lee (2017).

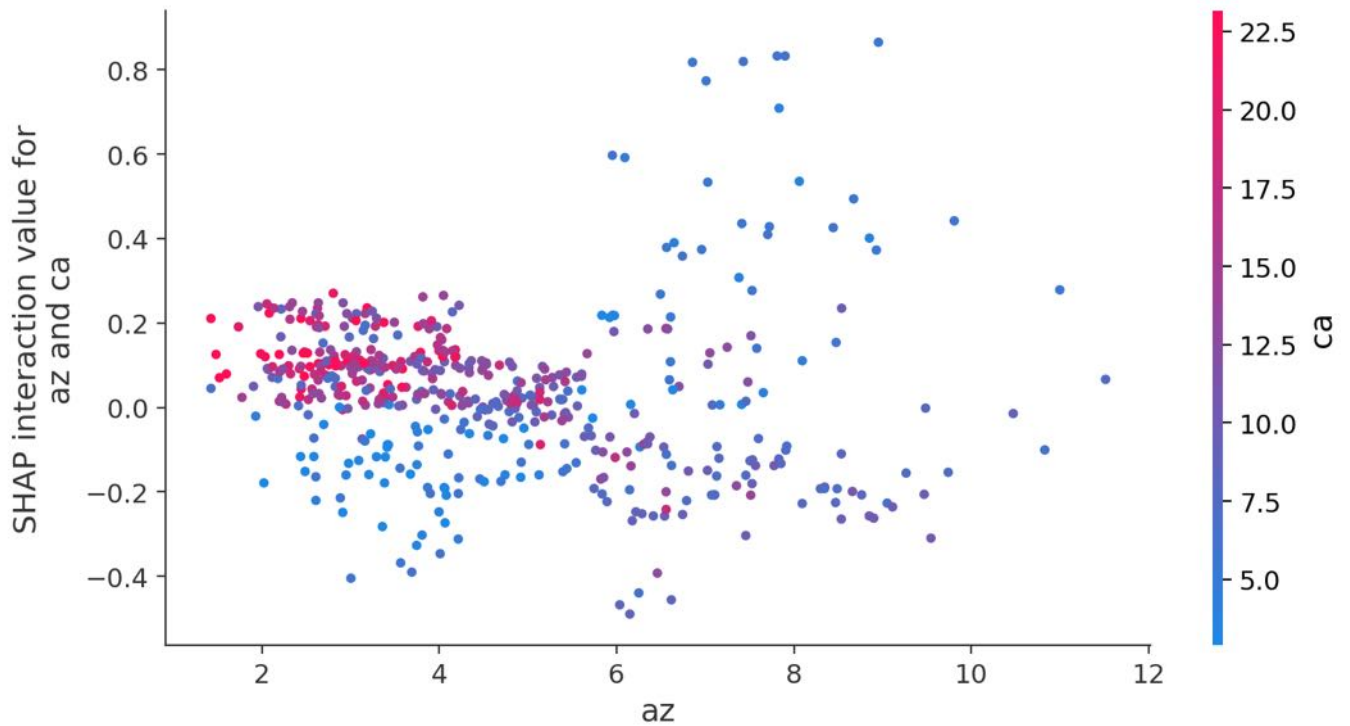
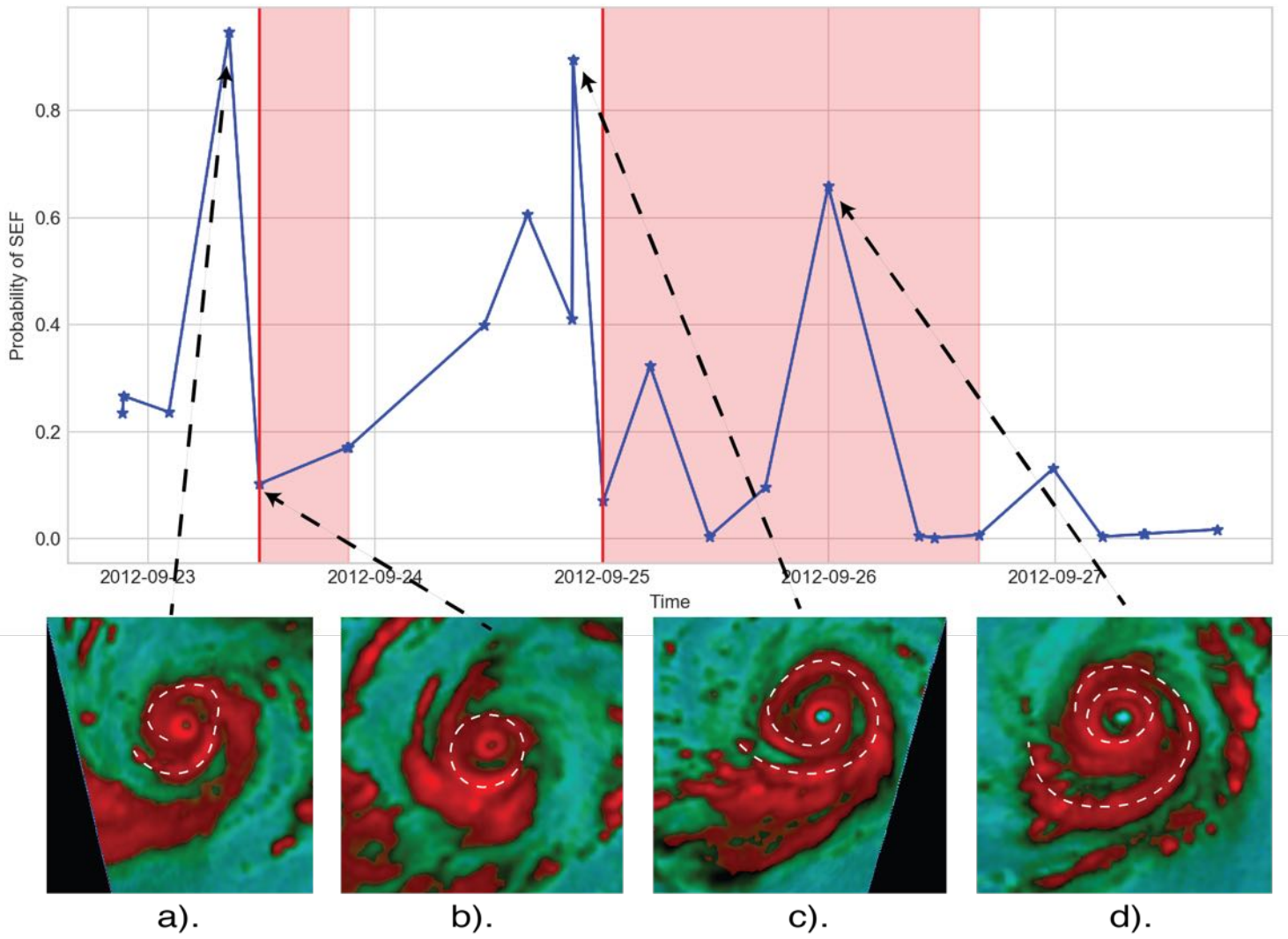


Figure 6.13: SHAP interaction values for ICA crossing angle ( $ca$ ) and azimuthal extent ( $az$ ). Graphic generated using the python SHAP library Lundberg and Lee (2017)

Dummy classifier		
	Predict NSEF	Predict SEF
Observe NSEF	1203	104
Observe SEF	90	6
KS09 classifier (SHIPS+GOES)		
	Predict NSEF	Predict SEF
Observe NSEF	915	21
Observe SEF	90	39
Model - SHIPS only		
	Predict NSEF	Predict SEF
Observe NSEF	1240	67
Observe SEF	33	63
Model - Rainband geometry+SHIPS		
	Predict NSEF	Predict SEF
Observe NSEF	1274	33
Observe SEF	30	66

Table 6.5: Confusion matrices for SEF models using a dummy classifier, the KS09 classifier, the new model with rainband predictors excluded and the new model with all predictors.



*Figure 6.14: Example of the SEF model correctly predicting two SEF events in Typhoon Jelawat (2012), showing (top) model predictions of the probability of SEF occurring within 24 hours as a function of time, and (bottom) selected PMW images corresponding to different predictions. Blue marks indicate the time of each satellite overpass, red lines indicate the time of SEF and red shading the duration of the SE. On the PMW images, white dashed lines indicate the extent of the PRB or SE.*

in a sufficiently favourable thermodynamic environment.

2. SBC formation is triggered by the vortex response to a deep layer shear profile with low level flow aligned with the deep layer shear vector and strong low level shear.
3. The geometry of the band evolves. The crossing angle is most strongly dependent on the deep layer shear. In contrast, the azimuthal extent depends on both the thermodynamic environment and shear profile. A shear profile with low level flow to the right of the shear vector and weak shear magnitude is more conducive to rainbands with a high azimuthal extent.
4. Finally, as the azimuthal extent of the band increases, SEF ensues provided that convection in the band is sufficiently intense and the TC remains in an environment with low deep layer VWS.

This suggests that the most important environmental variable in the axisymmetrisation process is therefore the deep layer VWS, consistent with current understanding of TC structure. Interestingly, strong low level shear is favourable for PRBF, however weak low level shear is then favourable for the low crossing angle and high azimuthal extent required for axisymmetrisation. This suggests that SEF may be initiated by a reduction in deep layer VWS, which has previously been observed in a radar case study of Hurricane Bonnie (Hogsett and Zhang, 2009). More work using high resolution observations and numerical models is required to assess these hypotheses. Preliminary results in these areas are discussed in the next chapter.

# Chapter 7

## Conclusion and Future Work

### 7.1 Conclusion

In conclusion, each of the aims outlined in Section 1.2 have been addressed through the development of a first climatology of TC rainband morphology.

1. TC rainbands included in the sample have crossing angles (azimuthal extents) ranging between 0.02 and 53.40 degrees (0.49 and 9.89 radians) with a median of 14.45 degrees (2.46 radians). Morphology varies with band type, with PRBs having significantly higher crossing angle and higher azimuthal extent than IC and OC bands, and PRB and IC bands having lower crossing angle than OC bands. Band morphology varies significantly between the WPAC and all other basins for the PRB group, with higher azimuthal extent and lower crossing angle in the WPAC.
2. SEF is preceded by the formation and axisymmetrisation of an SBC in 79% of cases. In contrast, climatologically, an SBC is identified in just 37% of PMW overpasses. For the ICA parameter, which quantifies the degree of axisymmetrisation of the SBC, the average crossing angle (azimuthal extent) at 0-6 hours prior to SEF is 5.93 degrees (6.3 radians), compared to the climatological average of 11.26 degrees (4.12 radians).
3. Different large scale environmental conditions are associated with the different stages of the axisymmetrisation process. In contrast to previous work, PRBF is hypothesised to be related to the profile of the vertical wind shear as opposed to the magnitude. Higher azimuthal extent is associated with more favourable thermodynamic conditions, reduced magnitude of the vertical wind shear and a shear profile with low level flow to the right of the deep layer VWS vector. Low crossing angle is associated with reduced shear and stronger tangential circulation. For rainbands with high circularity, SEF ensues when the convection within the rainbands is sufficiently intense, and the magnitude of the VWS

remains low.

4. Using the XGBoost algorithm, a statistical model was developed using environmental predictors together with information about the morphology of the SBC. This model is capable of predicting SEF events with a recall of 0.66 and FAR of 0.02, a significant improvement over previous classifiers.

## 7.2 Application of Methodology

A large component of this thesis was devoted to developing a novel dataset and methodology to analyse satellite imagery. These will both have considerable future application.

### 7.2.1 Satellite dataset

Two primary archives exist for TC specific 89GHz PMW data: the Hurricane Satellite (HURSAT) PMW database (Knapp, 2008) and the Naval Research Laboratory (NRL) PMW image archive (Hawkins et al., 2001). The PMW dataset developed for this study includes more sensors and covers a longer time period than HURSAT-PMW, and has more stringent intercalibration between instruments and quality control than the NRL archive. The PMW dataset compiled as part of this study will therefore have future application in satellite climatologies of TC convective structure. In particular, the new 4-channel composite 89GHz and 37GHz PMW product developed for this study described in Appendix A.1 will have application in improving understanding of banding structure as PMW instrument resolution improves.

### 7.2.2 Structural classification methodology

Chapter 4 described the development of an automated classification system to identify rainbands and eyewalls. This technique has considerable potential application for extending understanding of TC structure, as it presents a first opportunity to study the evolution of individual convective disturbances as opposed to using statistical averages. The methodology described here is easily extended to higher resolution datasets such as Doppler Radar to study the lifecycle of individual bands. This technique will also be suitable for application to model output archives, building on recent work attempting to identify SEF events in model output such as the Hurricane Weather Research and Forecast Model (HWRF) archive (Wu et al., 2018). Furthermore, these techniques are suitable for developing climatologies of other meteorological phenomena, for example identifying tornadoes in radar datasets.

## 7.3 Future work

Future work is required in three primary areas: extending the climatology presented in Chapter 5, idealised modelling simulations to assess the mechanisms proposed in Chapter 6 and high resolution observational work to study the axisymmetrisation process on a convective scale. Preliminary work in each of these three areas is briefly summarised below.

### 7.3.1 Extension of the climatology

The first step in future work will be to extend these results to the complete PMW dataset. This will involve applying the automated classification scheme outlined in Chapter 4 to the complete 89GHz PMW dataset. These results will increase confidence in the statistical results presented in this thesis, and provide the scope for a more detailed climatology.

### 7.3.2 Numerical simulations

In Chapter 6, mechanisms are proposed to relate the impact of various environmental parameters to the SEF process. Of the mechanisms hypothesised to impact the axisymmetrisation process, the most important is the role of the deep layer VWS profile. A series of modelling experiments are being carried out using the Weather Research and Forecasting Model (WRF; Skamarock et al. 2008). SEF has been reproduced in a quasi-idealised WRF simulation, using an initial condition based on that described by Wang et al. (2016). Important physical parameterisations include the WRF single moment 6 (WSM6) class microphysics scheme (Hong and Lim, 2006) and Yonsei State University (YSU) boundary layer scheme (Hong et al., 2006). The simulation is initialised with an axisymmetric vortex (Xiaofan Li, 1992), with four nests with highest resolution 1km and 35 vertical levels. For more information on the initial condition, see Wang et al. (2016).

In the control simulation, the model is integrated for 10 days. PRBF occurs at 186 hours, and SEF at 196 hours. These events are identified by tracking the simulated radar reflectivity of the TC at the lowest model level (Figure 7.1). Four sensitivity runs are then conducted with shear profiles with a constant magnitude of 5m/s, but low level flow to the right, left, counter aligned and aligned with the deep layer shear vector. In each sensitivity run, the shear profile is imposed at 181 hours using point downscaling (Nolan, 2011).

Preliminary results indicate differences in the timing and incidence of PRBF and SEF with different shear profiles. These results will be further analysed to quantify the impact of vertical wind shear at each stage of the axisymmetrisation process.

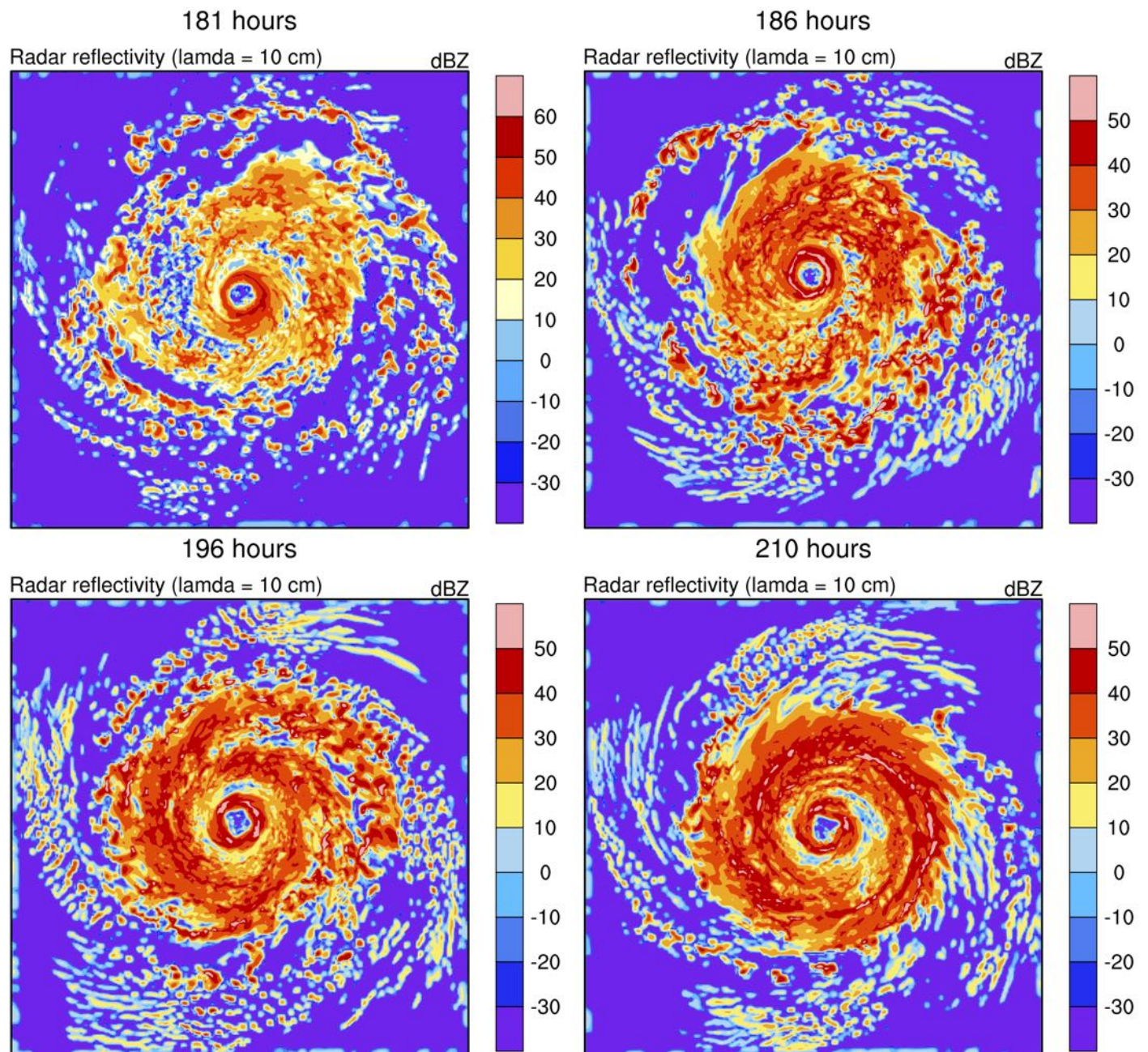


*Figure 7.1: WRF output showing evolution towards a secondary eyewall in the control simulation. Fields are model calculated reflectivity in dBz at the lowest model level.*

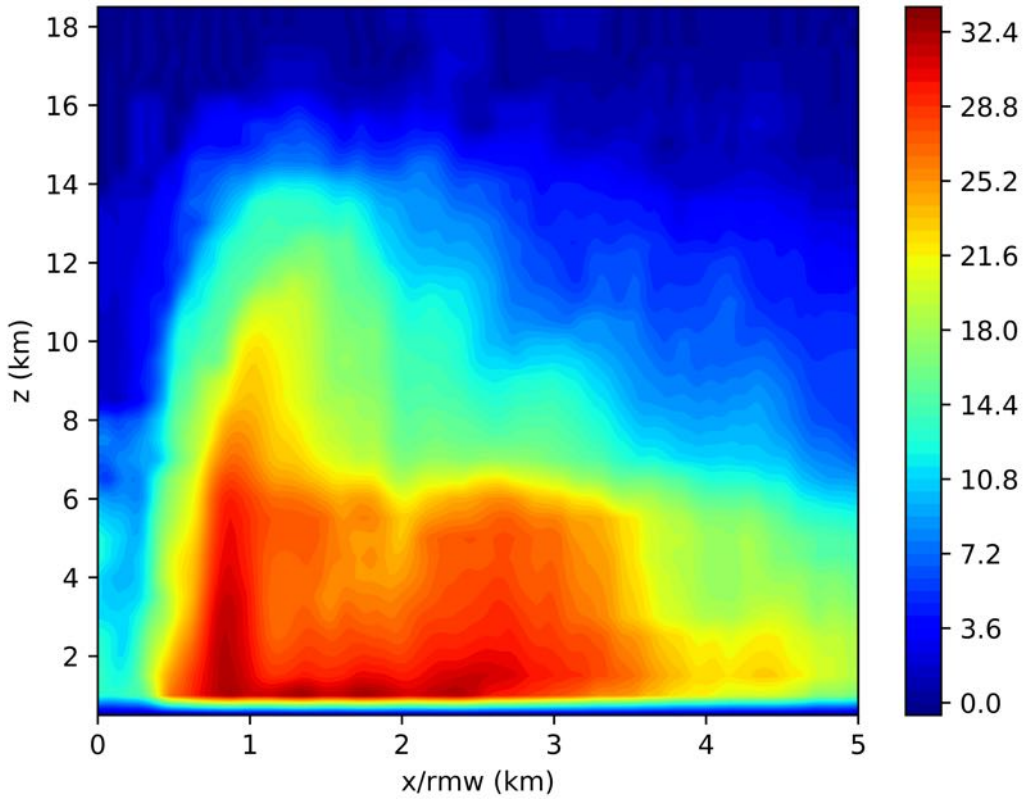


*Figure 7.2: Example of a composite radar image for normalised downshear left radar reflectivity (dBz) at 0-6 hours prior to SEF.*

### 7.3.3 High resolution observations

The third question to be addressed is how the morphology observed on PMW imagery relates to the kinematic and thermodynamic structure of the TC. This is being investigated using a combination of high resolution NOAA-P3 radar data for kinematic structure, together with composites of flight level data taken from the Flight+ dataset (Vigh et al., 2015) for thermodynamic parameters. These datasets are being used to create band-relative composites in shear relative quadrants at each stage of the axisymmetrisation process and for different rainband geometries. An example of one of these radar composites is shown in Figure 7.2.

Together, these three future projects will build on the work presented in this thesis to clarify the importance of rainbands in SEF, and further understanding of the dynamical processes responsible for this phenomenon.

# Appendices

# Appendix A

## Multichannel satellite products

Chapter 3 describes the development of an 89GHz microwave satellite dataset for observing TCs. This appendix provides justification for the use of this product in identifying rainbands, together with a discussion of some of the limitations of the dataset.

### A.1 Multichannel satellite products

The 89 and 37GHz PMW bands have been used extensively in observing TC morphology. The 85-92GHz signal is associated with ice scattering and is therefore suitable for areas of convective or stratiform precipitation (Spencer et al., 1989). In contrast, the 36.5-37GHz channels are sensitive to the liquid water path, showing areas of low level clouds and precipitation (Cecil and Zipser, 2002). Each of the six instruments utilised in this study has four channels in these bands: 37GHz horizontal polarisation ( $37_{hpol}$ ), 37GHz vertical polarisation ( $37_{vpol}$ ), 89GHz horizontal polarisation ( $89_{hpol}$ ) and 89GHz vertical polarisation ( $89_{vpol}$ ). Different combinations of these channels have previously been used to retrieve convective structure (Turk et al., 1999; Lee et al., 2002). An issue with both these frequencies is that the ocean surface has high emissivity which can appear as lowered brightness temperature, distorting the ice scattering signal of the rainband field. This effect can be eliminated through the use of polarisation corrected temperature (PCT). The PCT is defined as a linear combination of the horizontal and vertical channels. Definitions for the 37GHz and 89GHz PCT are (Spencer et al., 1989; Cecil and Zipser, 2002):

$$PCT_{37} = 2.18 \times 37_{vpol} - 1.18 \times 37_{hpol}$$

$$PCT_{85} = 1.818 \times 85_{vpol} - 0.818 \times 85_{hpol}$$

For this dataset, it is important that the images are suitable for the identification of both SEs and rainbands. Three separate multichannel products are constructed from the raw brightness

temperature data. The first two of these are separate 89GHz and 37GHz multichannel products based on the NRL false colour image products combining the horizontal and vertically polarised channels with the derived PCT (Turk et al., 1999; Lee et al., 2002). The third is a novel four channel composite developed as part of this study for improved rainband identification.

## 89GHz false colour

The 89GHz product is based on the specifications outlined by Lee et al. (2002). The red (R) blue (B) and green (G) channels of the colour image are constructed according to the following specifications:

$$R = (290 - PCT_{85}) \times \frac{255}{130}, R < 160 = 255, R > 290 = 0$$

$$G = 255 - (290 - 85_{vpol}) \times \frac{255}{20}, G < 270 = 0, G > 270 = 255$$

$$B = 255 - (300 - 85_{hpol}) \times \frac{255}{60}, B < 240 = 0, B > 300 = 255$$

Note that the scaling of the red channel is different to the original scaling used in the NRL images. Here, the lowest temperature is reduced to 160K, which provides greater contrast between rainbands and eyewalls, and allows for easier discrimination between individual bands in intense storms where the original NRL product saturates. A PCT of less than 255K has been established as the cutoff for precipitation (Spencer et al., 1989). A final constraint is then imposed that the PCT must be less than 255K for a pixel to be classified as raining:

$$PCT_{85} < 255K$$

An example of one of the resulting RGB images is shown in Figure A.2. In this image, red pixels indicate areas of rain where there is an ice scattering signal, and green and blue may indicate low level warm clouds or the underlying surface.

## 37GHz false colour

The 37GHz channel product is identical to that proposed by Lee et al. (2002).

$$R = (280 - PCT_{37}) \times \frac{255}{20}, R < 260 = 255, R > 280 = 0$$

$$G = 255 - (300 - 37_{vpol}) \times \frac{255}{140}, G < 160 = 0, G > 300 = 255$$

$$B = 255 - (310 - 37_{hpol}) \times \frac{255}{130}, B < 180 = 0, B > 310 = 255$$

An example of one of these 37GHz images is shown in Figure A.1 (b). In this image, pink or red indicates intense convection, blue low level warm rain or rough ocean surface and green clear air (Lee et al., 2002; Kieper and Jiang, 2012; Harnos and Nesbitt, 2016). Note that there is no cutoff value for precipitation in these images, as it is impossible to unambiguously identify precipitating pixels from the 37GHz channels alone (Harnos and Nesbitt, 2016).

### 89GHz+37V false colour

Finally, as part of this study a new four channel composite product was developed. Previous multichannel products have combined different frequencies on microwave instruments to create estimates of precipitation (Huffman et al., 2007). However, many of these algorithms use the lowest frequency channels, and hence have resolution too coarse for viewing TC rainbands. Individually, both the 37GHz and 89GHz multipolarisation products have potential limitations for rainband observation. For the 37GHz case, it is impossible to distinguish between pixels with warm rain and those with strong surface winds leading to lowered brightness temperatures (Harnos and Nesbitt, 2016). For the 89GHz product, although it is easier to determine where precipitation is occurring, a signal is only seen if the pixel has a sufficiently strong ice scattering signal. Although in many cases this will be the case, it is possible that some weaker rainbands are primarily composed of warm cloud, and will therefore be resolved on 37GHz imagery but not 89GHz imagery.

This product consists of a composite of the three 89GHz channels and the 37GHz vertical polarisation channel. Recent work using radiative transfer modelling has suggested that pixels with  $PCT_{85} > 255$  and  $37_{vpol} > 255K$  are associated with warm rain (Harnos and Nesbitt, 2016). As mentioned for the 89GHz product, an 89GHz  $PCT < 255K$  is indicative of rain with an ice scattering signature. A combined product showing areas of both convective and warm rain is created, with four channels defined by:

$$R = (290 - PCT_{85}) \times \frac{255}{130}, R < 160 = 255, R > 290 = 0$$

$$G = 255 - (290 - 85_{vpol}) \times \frac{255}{20}, G < 270 = 0, G > 270 = 255$$

$$B = 255 - (300 - 85_{hpol}) \times \frac{255}{60}, B < 240 = 0, B > 300 = 255$$

$$Grey = (280 - 37_{vpol}) \times \frac{255}{25}, 255 < 37_{vpol} < 280 \wedge PCT_{89} > 260$$

This product therefore consists of the rescaled 89GHz RGB product together with a separate greyscale overlay. An example of the four channel product is shown in Figure A.1 (c). Here the RGB image is interpreted as for the 89GHz image, while the greyscale overlay shows regions

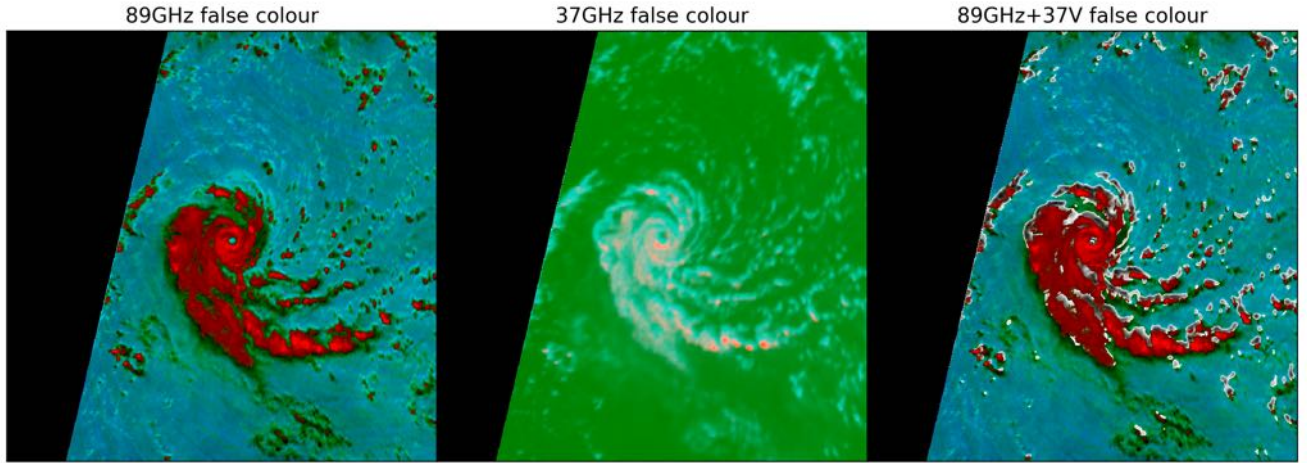


*Figure A.1: AMSR-2 satellite images of Typhoon Nepartak at 04:02UTC on the 0507/2016, showing from left to right, mutichannel 89GHz, multichannel 37GHz and novel four channel composite.*

of warm rain. It is noted that, since the thresholds for warm rain and convective rain are mutually exclusive there is by definition no overlap between these quantities. The use of these three products in identifying convective structure is explored in the following section. National Aeronautics and Space Agency (2018)

## A.2 Observing convective structure

It is necessary to justify whether the convective structure is sufficiently well represented for a climatology. There is no objective definition of what constitutes an eyewall, SE or rainband. The majority of studies use either land based or airborne radar reflectivity thresholds to objectively delineate between different structures. To assess which microwave product is best for identifying rainbands and eyewalls, we therefore take the 25dBz contour of radar reflectivity as the ground truth and compare one years worth of satellite data to all available land based radar products. Radar products are derived from the University of Miami Radar Archive (available at <http://andrew.rsmas.miami.edu/bmcnoldy/tropics/radar/>) were qualitatively compared to coincident 89GHz satellite images to assess whether all features captured by radar were also observed in the coarser resolution satellite imagery.

### SEF

As the microphysical structure of eyewalls consists of large ice particles, hail, and graupel (Cecil and Zipser, 2002), 89GHz microwave imagery is ideally suited to identifying eyewalls and SEs. The NRL false colour product that the images described in the previous section are based on has been used in multiple climatologies investigating SEs (Hawkins and Helveston, 2004;

Hawkins et al., 2006; Hawkins and Helveston, 2008; Kuo et al., 2009; Yang et al., 2013). An example of a SE identified in PMW imagery is shown in Figure A.2.

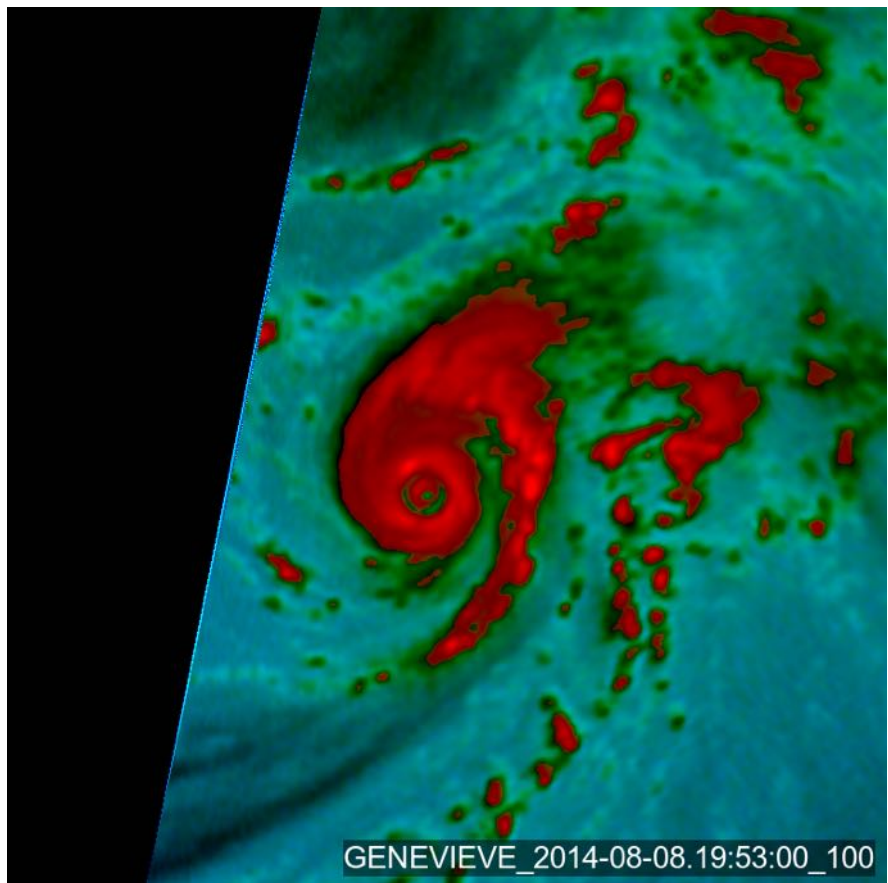
Interestingly, comparison of the three satellite products with airborne and land based radar reveals that both the timing and incidence of SEF differs between products. The first reason for this is the coarse resolution of the microwave sensors (ranging from 5km for AMSRE to 12.5km for SSMIS). As the moat of a compact SE may be on the order of 15km (Sitkowski et al., 2011), it is therefore possible that some SEs may not be resolved on PMW imagery. Comparison of the three satellite products to land based and airborne radar reveals that in 25 percent of cases with a clear radar SE, nothing is observed on satellite imagery (Figure A.3). This is primarily related to resolution, though vortex tilt and upper level advection of ice particles within the IC may also contribute.

In those cases where a SE is visible on satellite, a ring structure is visible in the 37GHz satellite images prior to the 89GHz images. The reason for this is that the SE builds from the bottom up (Hence and Houze, 2012b), with the incipient SE taking time to develop an ice scattering signal sufficient to show up on 89GHz imagery. Land/airborne radar is therefore able to detect a low level ring of reflectivity when the SE is at an earlier stage of formation. A ring of enhanced emissivity is also visible on 37GHz imagery prior to the establishment of a ring in the corresponding 89GHz image. This may be due to low level warm cloud in the developing SE. It is, however, important to note that the primary control on PCT brightness temperature at 37GHz is sea surface roughness and hence surface wind speed (Harnos and Nesbitt, 2016). Numerical experiments indicate that the boundary layer inflow asymmetries forced by an asymmetric rainband or SBC can enhance inflow on the opposite side of the storm (Moon and Nolan, 2010; Qiu and Tan, 2013). It is therefore ambiguous whether this ring is caused by low cloud, enhanced surface wind speeds or a combination of the two.

Given that all previous large scale climatologies of SEF are based on 89GHz imagery, these results suggest that SEF is a much more common process than previously thought, and motivates future climatologies as higher resolution satellite and radar data becomes more widely available.

## Rainbands

Observing rainbands is more difficult. Unlike eyewalls, rainbands may be composed of convective cloud, stratiform cloud or warm cumulus (Didlake and Kumjian, 2017; Ryzhkov et al., 2014). Previous studies tracking rainbands have all utilised either airborne or land based radar, identifying the rainbands based on the 20 or 25dB<sub>Z</sub> reselectivity contour (Barnes et al., 1983; Powell, 1990a; Samsury and Zipser, 1995; Tang et al., 2014, 2018). Radar data of the banding patterns can therefore be regarded as the ‘ground truth’ for rainband identification. Extensive



GENEVIEVE\_2014-08-08.19:53:00\_100

Figure A.2: Example of clear concentric eyewalls together with a PRB viewed on PMW imagery in Hurricane Genevieve at 19:53 on the 08/08/2014.

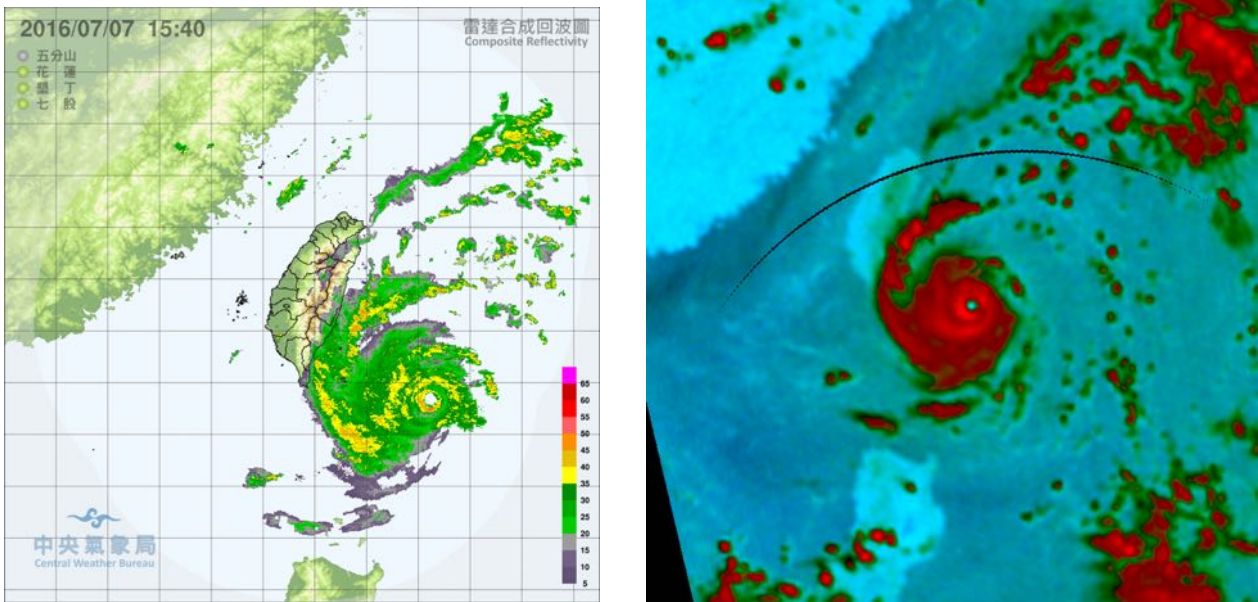


*Figure A.3: Example of poor agreement between radar and satellite for outer rainband and SE identification. Images are of typhoon Nepartak at 03:40UTC on 07/07/2016 as seen on land based radar (left) and 89GHz SSMI (right). Both the outer rainbands and the SE observed on the radar image are not evident on the coarse resolution SSMI image.*

comparison of 85-92GHz satellite images with concurrent land based radar coverage reveals that in the majority of cases the bands on radar are the same as those observed by satellite at 85-92GHz. The coarser resolution of 85-92GHz instruments (approximately 10km compared to 100m for radar) means that smaller bands will not be resolved, however the large scale features of the banding structure are clearly defined.

Three notable exceptions to this agreement occur. The first is in cases with warm rainbands, which do not have a clear ice scattering signal. Wang et al. (2018a) documented the evolution of a PRB, noting that in the early stages of formation the band consisted of warm rain with limited ice content. This warm rain is visible on 37GHz but not 89GHz images. Evaluating this technique on one year of AMSR-2 data, several cases were identified where a clear warm rainband forms in the absence of any signal in the 85GHz PCT (Figure A.5). Similarly, apparent ‘gaps’ in bands on 85GHz imagery are often filled by areas of warm rain (Figure A.4). The presence of complete bands of warm rain that do not have any signal at 89GHz is comparatively rare, however, occurring in only 0.8% of the AMSR2 images evaluated. Dynamically, these bands are probably in the early stages of development, prior to the establishment of sufficiently deep convection to create a coherent ice scattering signal. Two difficulties arising in the identification of warm rainbands are the low dynamic range of the 37GHz instrument (4mm/hr), and the extremely coarse resolution of the SSMIS 37GHz channel at 37km.

The second situation in which rainbands are visible on radar that do not have a clear ice scattering signal is in outer rainbands (Figure A.3) Again, these rainbands are captured well in

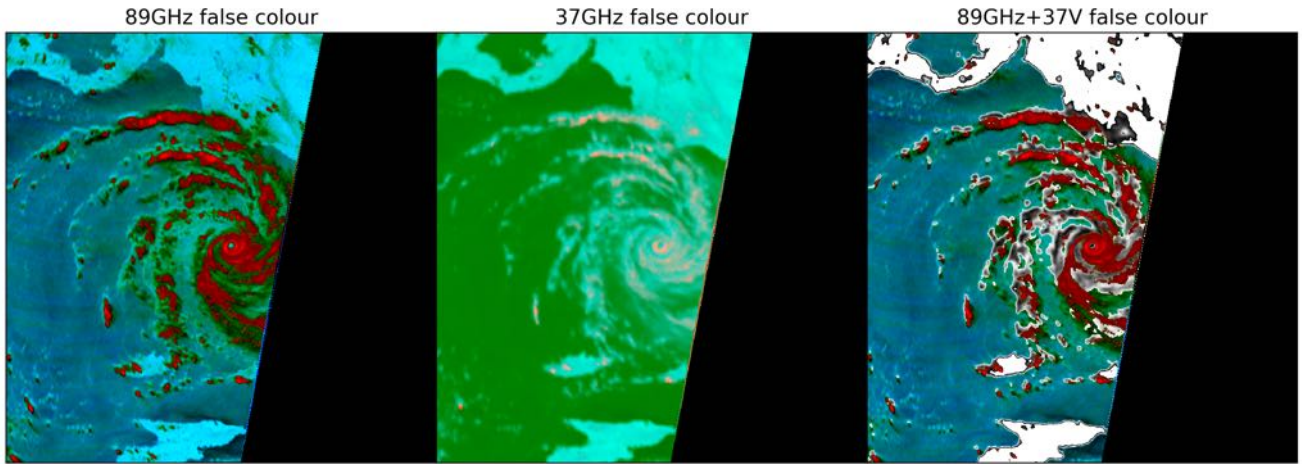


*Figure A.4: Example of rainbands visible on multichannel imagery but not on 89GHz imagery in hurricane Matthew at 18:43UTC on 02/10/2016.*

the four channel images. This is consistent with precipitation observations that these rainbands are more traditionally convective in nature, and ice is therefore not advected along the band as it is in the inner regions of the storm (Hence and Houze, 2012b).

Given that warm IC rainbands are uncommon, the poor (37km) resolution of SSMIS instruments at 37GHz, low dynamic range and interference in the 37GHz signal from surface wind (Harnos and Nesbitt, 2016), the 85-92GHz channels alone are utilised to detect rainbands in this study. It is noted, however, that with future increases in satellite resolution, the four channel product developed here will provide a more accurate product for observing rainbands.

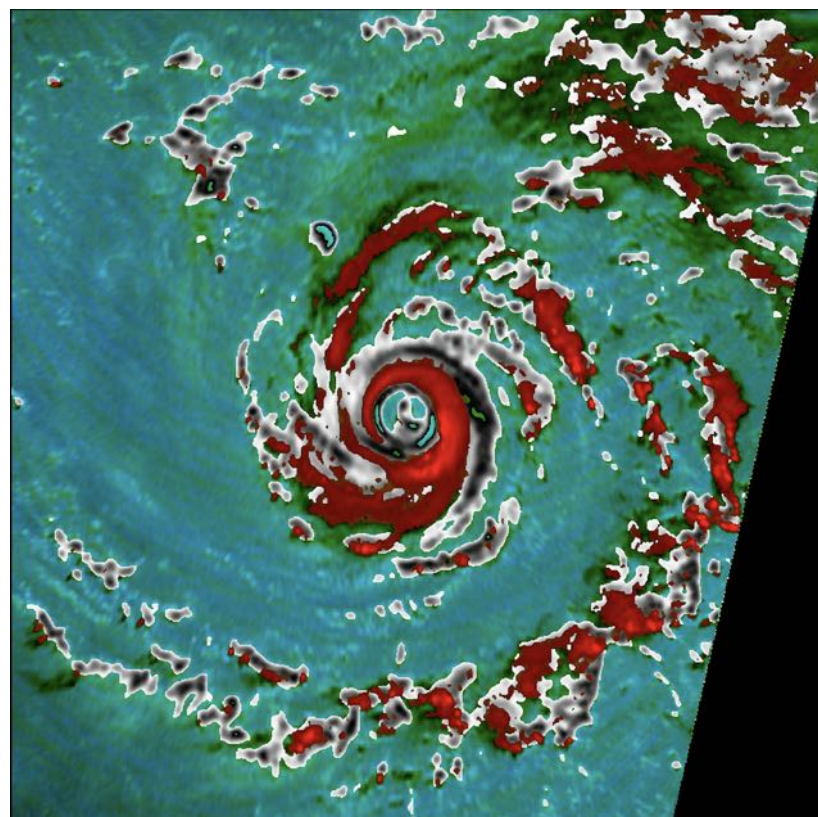


Figure A.5: Example of a warm rainband observed on an AMSR-2 image that has no signal at the 89GHz wavelength.

# Appendix B

## Shear Profiles

In latitude-longitude coordinates, the vector harmonic expansion for the u and v components of the wind field is (Adams and Swartztrauber, 1997):

$$u(\lambda, \theta) = \sum_{n=0}^N \sum_{m=0}^n [W_n^M (bi_m^n \cos(m\lambda) - br_m^n \sin(m\lambda)) + V_n^M (cr_m^n \cos(m\lambda) - ci_m^n \sin(m\lambda))]$$

$$v(\lambda, \theta) = \sum_{n=0}^N \sum_{m=0}^n [V_n^M (br_m^n \cos(m\lambda) - bi_m^n \sin(m\lambda)) + W_n^M (ci_m^n \cos(m\lambda) - cr_m^n \sin(m\lambda))]$$

Where

$$W_n^m(\theta) = \frac{m}{\cos(\theta)\sqrt{n(n+1)}} P_n^m$$

$$V_n^m(\theta) = \frac{1}{\cos(\theta)\sqrt{n(n+1)}} \frac{dP_n^m}{d\theta}$$

Where the  $P_n^m$  are the associated Legendre polynomials, and the coefficients are defined by

$$br_{m,n} = \alpha_{m,n} \int_0^{2\pi} \int_{-\pi/2}^{\pi/2} [vV_n^m \cos(m\lambda) - uW_n^m \sin(m\lambda)] \cos(\theta) d\theta d\lambda$$

$$br_{m,n} = \alpha_{m,n} \int_0^{2\pi} \int_{-\pi/2}^{\pi/2} [uW_n^m \cos(m\lambda) + vV_n^m \sin(m\lambda)] \cos(\theta) d\theta d\lambda$$

$$cr_{m,n} = \alpha_{m,n} \int_0^{2\pi} \int_{-\pi/2}^{\pi/2} [uV_n^m \cos(m\lambda) + vW_n^m \sin(m\lambda)] \cos(\theta) d\theta d\lambda$$

$$ci_{m,n} = \alpha_{m,n} \int_0^{2\pi} \int_{-\pi/2}^{\pi/2} [-vW_n^m \cos(m\lambda) + uV_n^m \sin(m\lambda)] \cos(\theta) d\theta d\lambda$$

If the harmonic of the truncation has a spatial scale larger than that of a typical TC, then the TC vortex will be removed from the reanalysis field. In this study, the spectral field is truncated at wavenumber 18 or 2000km. This is the 98th percentile of all cyclone sizes in the WPAC basin, ensuring that the vortex is removed in all cases considered in this study (Knaff et al., 2014). An example of a reanalysis field with the vortex removed in hurricane Gonzalo (2014) is shown in Figure B.1. From this figure, it can be clearly seen that the vortex is satisfactorily removed after the spectral truncation, leaving the background wind field more or less unaltered. To further justify the truncation at wavenumber 18, a timeseries of shear magnitude for TC Jasmine (2012) is shown in Figure B.2. From this figure, it is clear that there is little variation in the shear values above the  $k=15$  truncation, suggesting that  $k=18$  is a reasonable approximation to the wind field.

The spectral transformation is implemented using the NCAR Spherepack library (Adams and Swarztrauber, 1997) and associated Pyspharm and Windpyspharm python libraries (Dawson, 2016; Whitaker, 2018). The wind field at each level is then averaged over a circle of radius 5 degrees from the centre of the cyclone derived from IBTrACS. The resulting dataset is then linearly interpolated to the time of each satellite overpass.

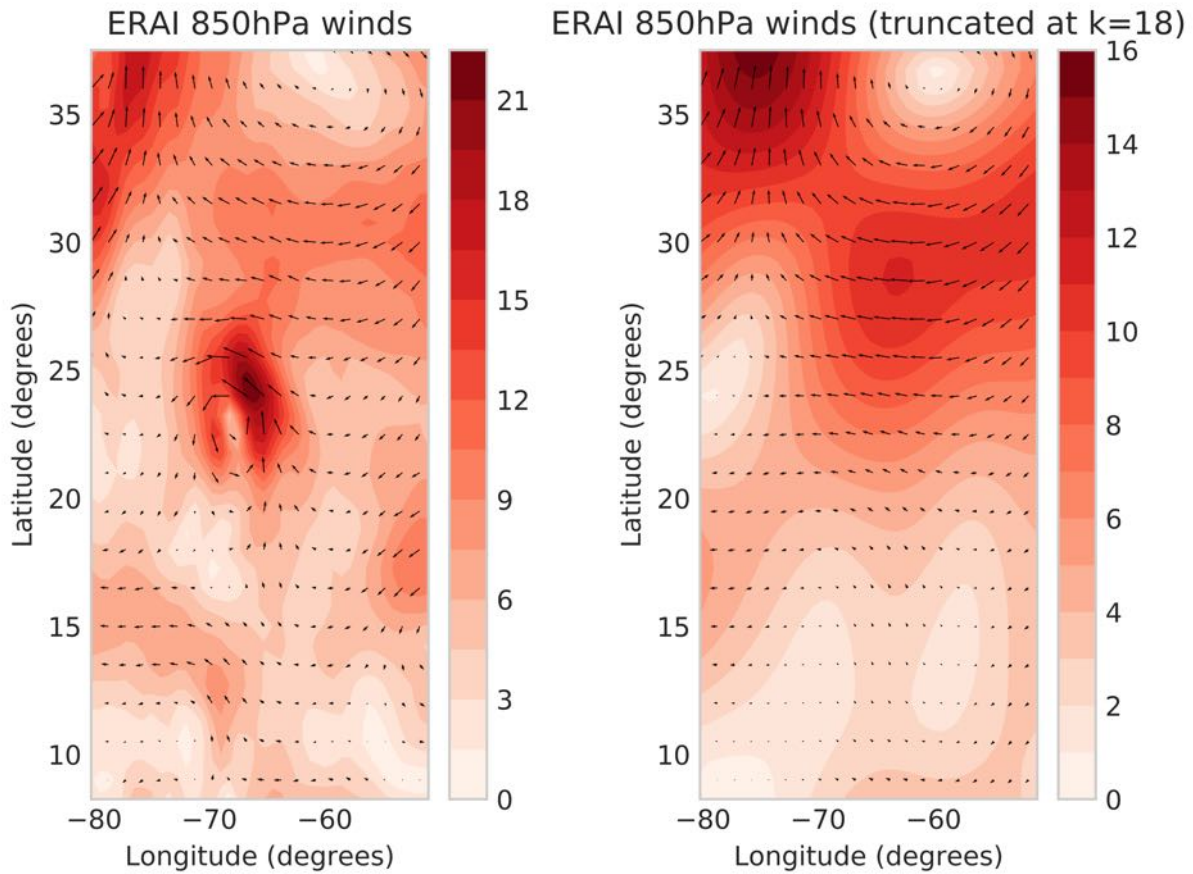


*Figure B.1: Example of vortex removal with  $k = 18$  truncation for Hurricane Gonzalo (2014), at 26.3W, 28.3N on 15/10/2014 at 18:00UTC, showing the original ERAI 850hPa reanalysis field (left) and corresponding field with the vortex removed after low pass filtering (right).*

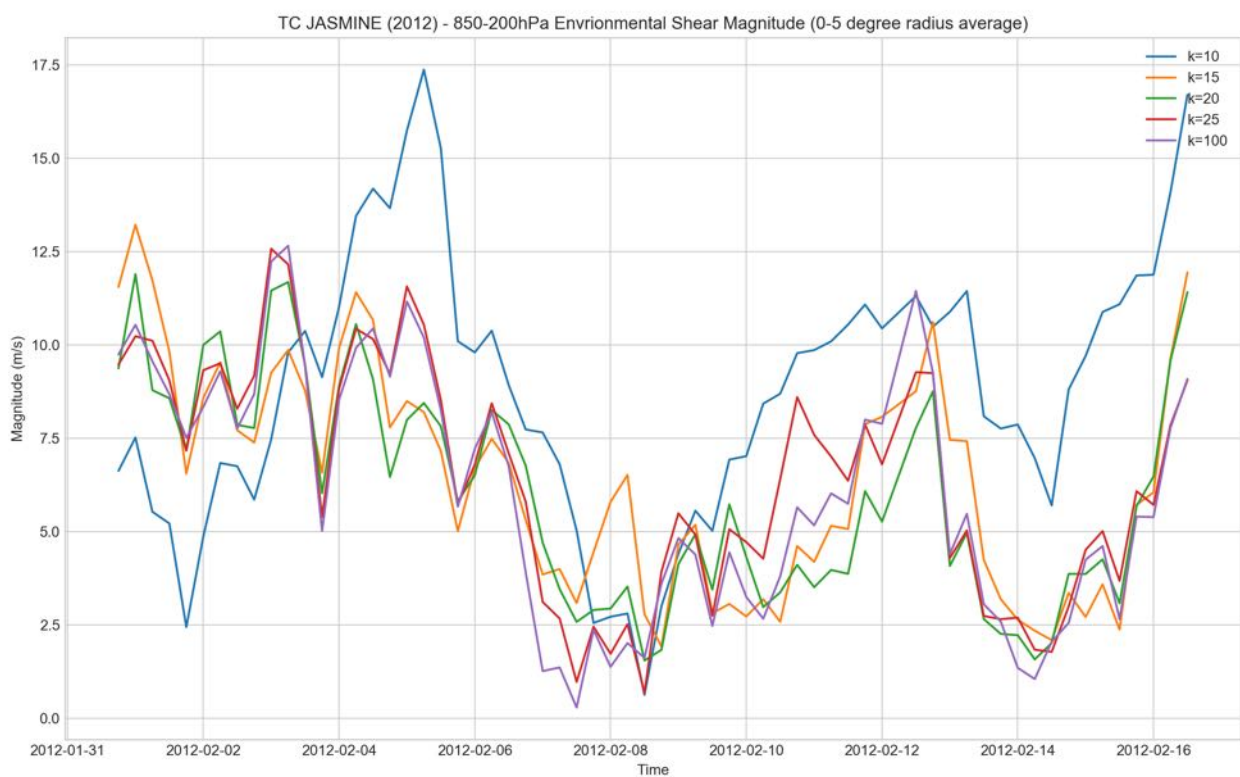


*Figure B.2: Deep layer shear magnitude time series calculated from ERA interim reanalysis for TC Jasmine (2012) at different wavenumber truncations.*

# Appendix C

## Mask-RCNN training

### C.1 Network overview

A schematic of the Mask-RCNN architecture is shown in Figure C.1. The input layer ( $751 \times 751 \times 3$  neurons for these images) is fed through the backbone Resnet101 CNN combined with the FPN (Lin et al., 2017) to generate a feature map of the image. This is then fed through a fully convolutional region proposal network to generate the object region proposals. This step is referred to as the backbone of the network. Each of the ROIs generated by the backbone are then individually run through the network head. This uses ROI align (He et al., 2017) to standardise the bounding boxes. In the next step two branches operate concurrently. The first is the prediction branch, which takes in the feature map in the standardised bounding box and assigns probabilities for each of the classes via softmax. In this study, predictions are only retained if they have a probability of  $\geq 90\%$ . A concurrent mask branch generates masks for each of the two classes. If one feature has a probability above the threshold, that is classified as a hit and the appropriate mask and classification are returned.

The different branches of the network are then trained concurrently using stochastic gradient descent optimisation (for full details of the training method, see He et al. (2017)). The loss function is a combination of three separate metrics, as described by He et al. (2017): the mask loss ( $L_{mask}$ ) on the mask branch, and bounding box loss ( $L_{bb}$ ) and class loss ( $L_{class}$ ) on the class branch. For a given instance, the mask loss is defined as the pixel sigmoid binary cross entropy loss on any mask associated with a classification, the bounding box loss is defined as the smooth L2 loss on the bounding box associated with the classification and the class loss is taken as the log loss on the correct class (Girshick et al., 2016; He et al., 2017). The total loss minimised by the model during training is then given by

$$L_{mrcnn} = L_{mask} + L_{bb} + L_{class} \quad (\text{C.1})$$

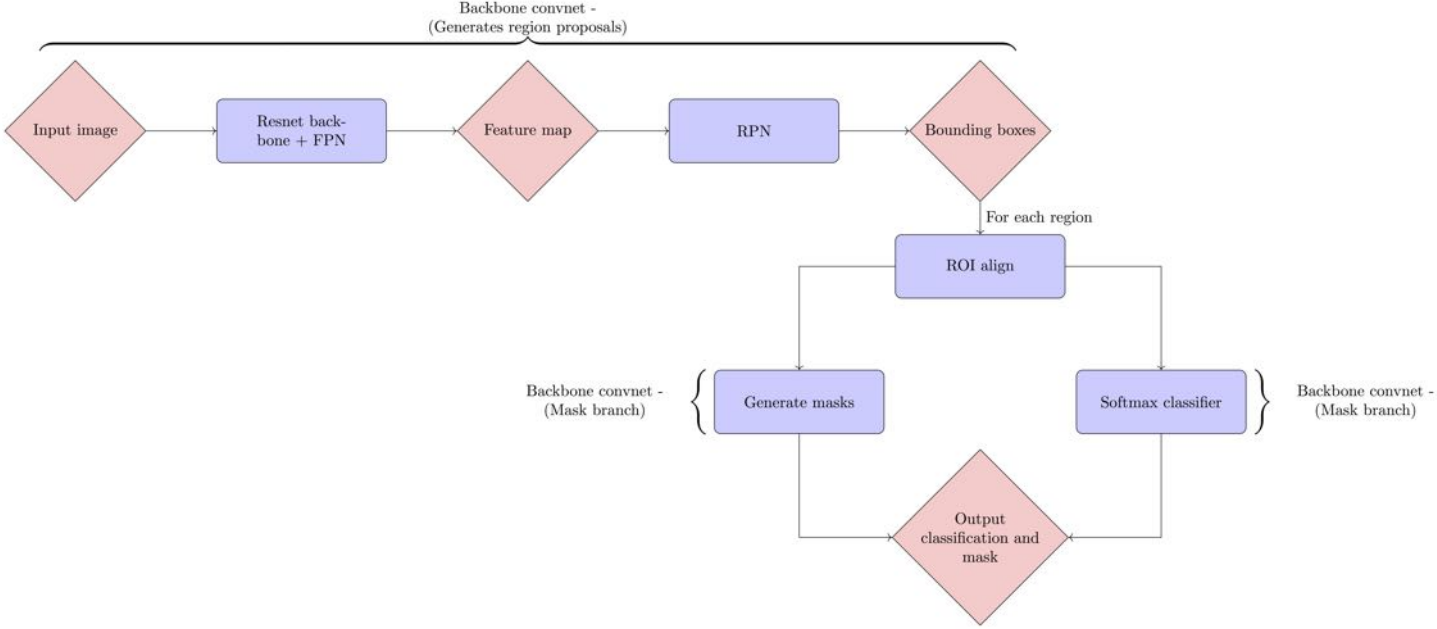


Figure C.1: Mask-RCNN network architecture.

## C.2 Network tuning

Section 4.3.2 describes the configuration of Mask-RCNN used for identifying TCs. This section outlines the tuning of this network. Mask-RCNN has a number of tuneable parameters, described in detail by Abdulla (2017).

For all runs, the learning rate and momentum were set to default values at 0.001 and 0.9 respectively. Tests were conducted to see whether using the Adams optimisation method lead to any improvements in results, however no changes were observed. Stochastic gradient descent optimisation was therefore used in all training runs. For all runs, the backbone was initialised using the Microsoft Common Objects in COntext (MS-COCO; Lin et al., 2014) dataset, while the heads were randomly initialised. Image augmentation was also used in all runs as this is known to substantially improve accuracy on small datasets.

The Mask-RCNN network offers a choice between training the entire network (including the ResNet backbone), or just training the network heads (Mask and class branches only) using the MS-COCO weights for the ResNet component. An important factor is the depth of the backbone network. A deeper backbone network has more degrees of freedom, and hence higher accuracy but correspondingly higher likelihood of overfitting. To determine the best network configuration, four separate training runs were conducted: Resnet101 all layers, Resnet101 heads only, Resnet50 all layers, Resnet50 heads only. Each case was trained on two NVIDIA-K80 GPUs for 100 epochs. Tensorflow tensorboard was used to log the losses for both the training and validation sets at the end of each epoch. Overfitting can be identified as the point where the validation loss plateaus or begins to increase while the training loss continues to

Optimum Mask-RCNN parameters				
Parameter	Resnet50 (head)	Resnet50 (all)	Resnet101 (head)	Resnet50 (all)
Min epoch	37	26	21	24
Val	0.47	0.43	0.46	0.45
Val mask	0.26	0.27	0.24	0.29
Val class	0.025	0.014	0.021	0.010
Val bbox	0.19	0.15	0.20	0.15
Train	0.33	0.27	0.42	0.26
Train mask	0.21	0.19	0.25	0.18
Train class	0.019	0.008	0.025	0.100
Train bbox	0.10	0.08	0.15	0.07

*Table C.1: Losses at the optimum network configuration for each of the four backbone options. All loss values are taken at the optimum epoch for valloss, which was the point at which the validation loss began to increase, indicating overfitting.*

decrease. This point is identified by observing the evolution of the total validation loss, which gives the optimum stopping point. The model weights are then taken for this epoch.

The evolutions of the loss metrics during training for the four configurations are shown in Figure C.2 (Resnet-50 heads), Figure C.3 (Resnet-50 all), figure C.4 (ResNet-100 heads) and figure C.5 (Resnet-100 all). Based on the total validation loss, the optimum epochs are shown to be 37, 26, 21 and 24 for Resnet-50 heads, Resnet-50 all, ResNet-100 heads and ResNet-100 all respectively. Validation values are shown in Table C.1, with loss at a minimum for the ResNet-50 with all layers after 26 epochs. This is as expected that the shallower network is more robust to overfitting, and more accurate results are obtained by training all layers. ResNet50 with all layers is therefore used as the backbone architecture in this study.

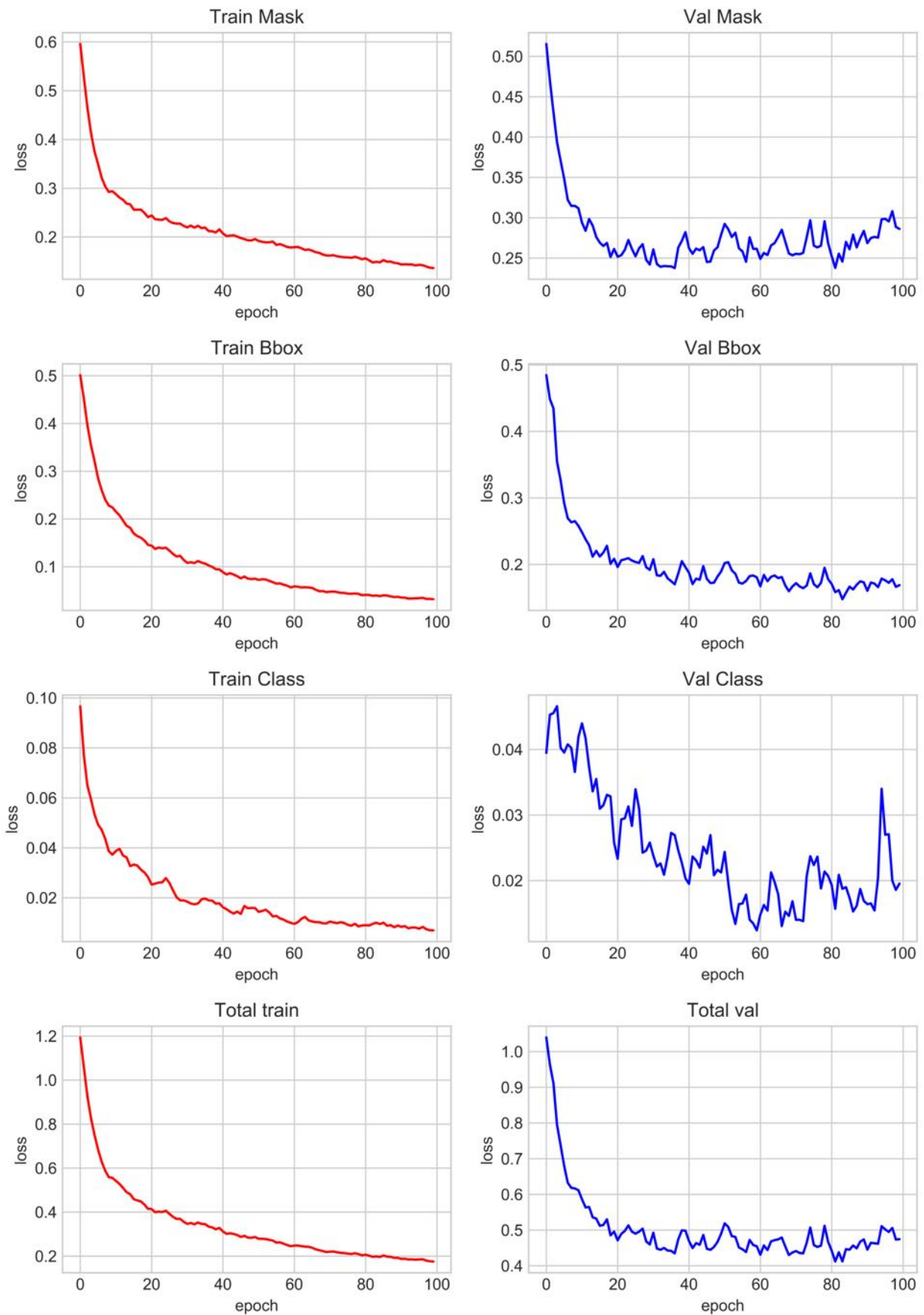


Figure C.2: Resnet 50 heads only training and validation losses. Values are smoothed with a 0.8 strength filter as used in Tensorboard.

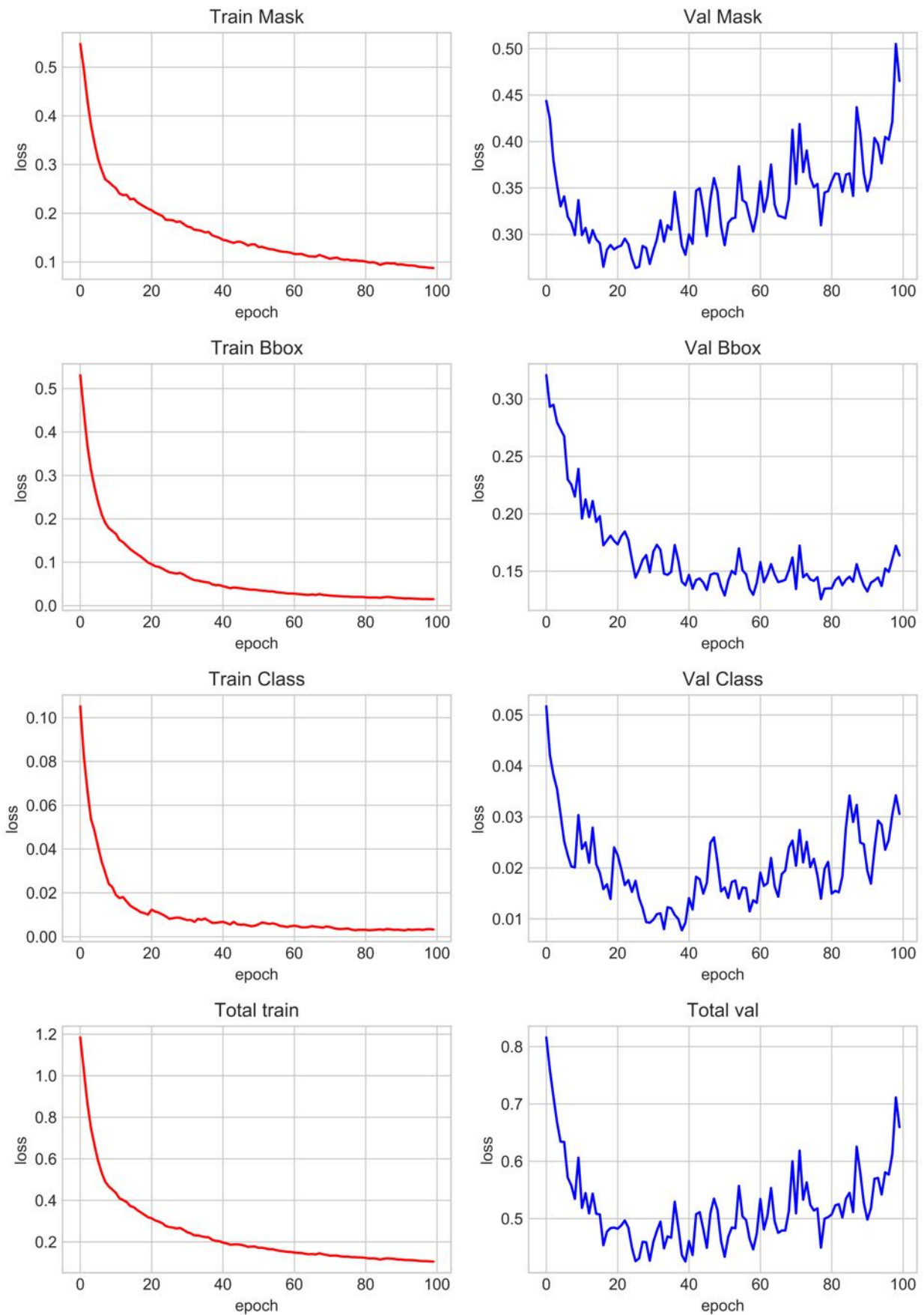


Figure C.3: Resnet 50 all layers training and validation losses. Values are smoothed with a 0.8 strength filter as used in Tensorboard.

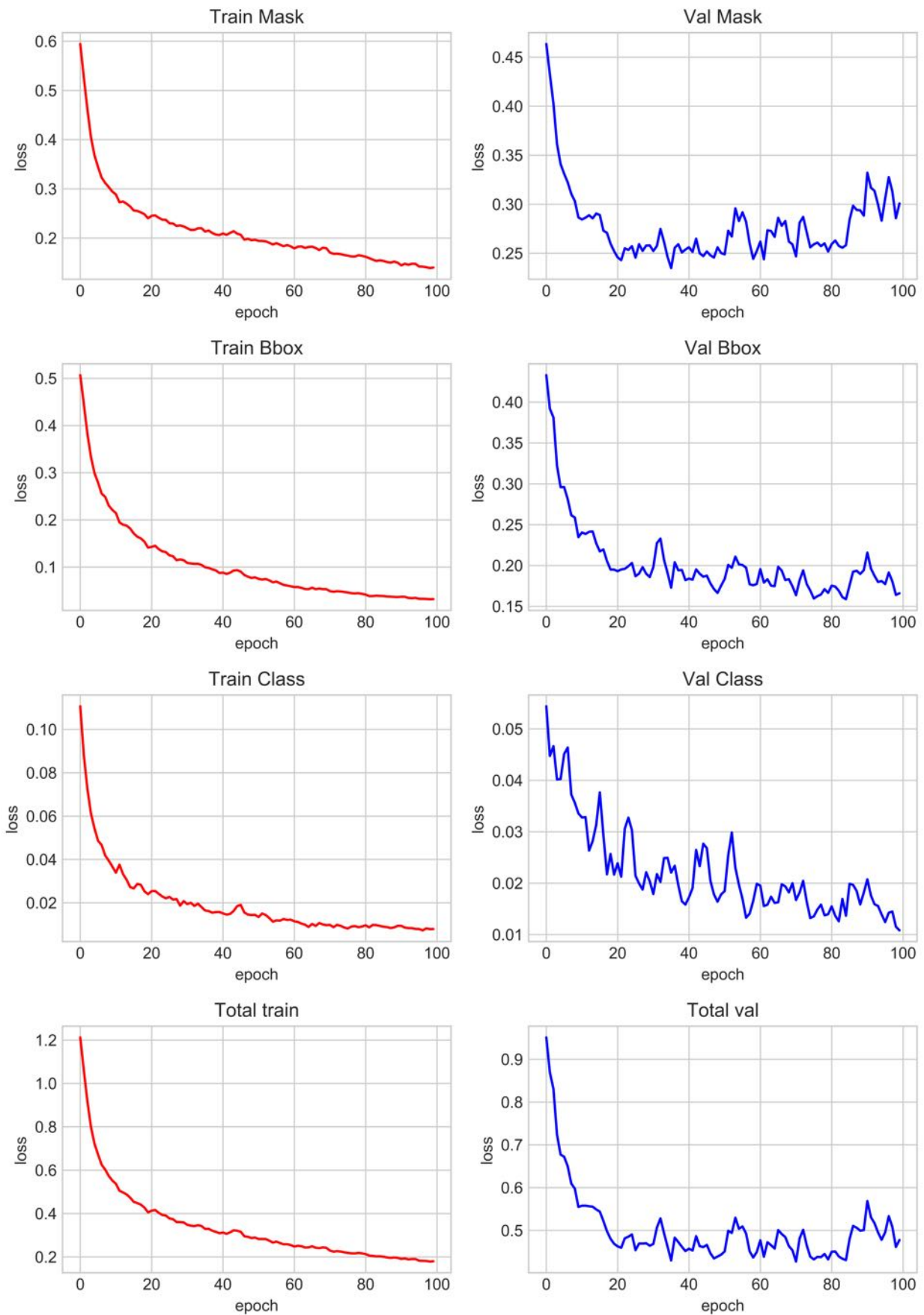


Figure C.4: Resnet 100 heads only training and validation losses. Values are smoothed with a 0.8 strength filter as used in Tensorboard.

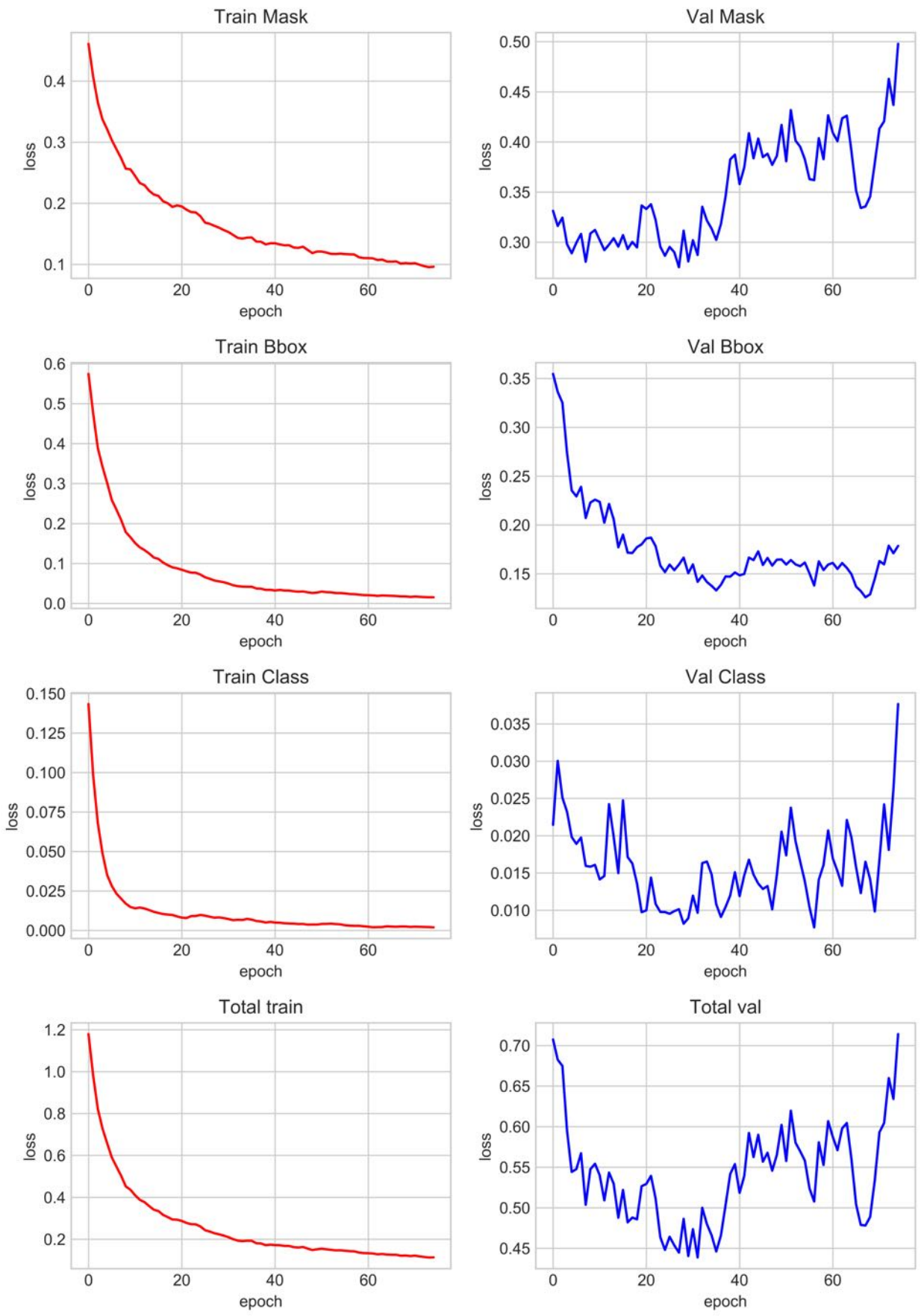


Figure C.5: Resnet 100 all layers training and validation losses. Values are smoothed with a 0.8 strength filter as used in Tensorboard.

# Appendix D

## SpArcFiRe clustering software

Section 4.4.2 describes the implementation of the SpArcFiRe clustering scheme (Davis and Hayes, 2014). This appendix describes the technical aspects of this scheme in detail, together with an outline of the minor changes made to the original scheme for this project.

### D.1 SpArcFiRe

This section provides a brief outline of the SpArcFiRe clustering software, following the outline given by Davis and Hayes (2012). A multiscale orientation field is first generated from the preprocessed image. This field consists of a combination of nine filters applied to the full half and quarter resolution image. Single-link hierarchical agglomerative clustering is then applied to the orientation field. This procedure begins with every pixel constituting a single cluster, and progressively merges them based on the orientation field similarity. The key difference between the SpArcFiRe clustering and previous schemes is that the merging is conducted with input from a logarithmic spiral fit. Prior to each merge, a logarithmic spiral is fitted to each of the clusters. If the ratio of the RMS error of the merged cluster is greater than a certain factor of the single cluster, then the merging is halted. For the PMW dataset, the optimum ratio was found to be 2.5. Preventing this merge ensures that these bands are correctly identified. A second round of merging is then performed, resulting in the final cluster output. For the PMW dataset, the cluster size threshold was set at 250 pixels.

### D.2 Alterations to the original clustering scheme

A series of minor alterations are made to the clustering scheme to optimise performance for PMW satellite images.

- During the merging process, all logarithmic spiral fits are forced to wind in the same direction (for an anticlockwise TC, with all TCs in the SDEM reflected over the horizontal). This improves the accuracy of the clustering scheme in cases where the spiral structure is ambiguous.
- At the second merging stage, an additional constraint is imposed that no clusters are merged if the resulting logarithmic spiral fit will have a crossing angle less than 0.1 radians. In cases with multiple IC bands, the bands often have similar crossing angles, meaning that they are merged into one circular band. Preventing these merges substantially improves model performance on IC bands.

# References

- Abadi, M., and Coauthors, 2015: TensorFlow: Large-scale machine learning on heterogeneous systems. URL <https://www.tensorflow.org/>, software available from tensorflow.org.
- Abarca, S. F., and K. L. Corbosiero, 2011: Secondary eyewall formation in WRF simulations of Hurricanes Rita and Katrina (2005). *Geophysical Research Letters*, **38** (7).
- Abdulla, W., 2017: Mask R-CNN for object detection and instance segmentation on Keras and TensorFlow. Github, [https://github.com/matterport/Mask\\_RCNN](https://github.com/matterport/Mask_RCNN).
- Adams, J., and P. Swarztrauber, 1997: SPHEREPACK 2.0: A model development facility. Tech. rep., National Centre for Atmospheric Research.
- Aibar, S., and Coauthors, 2017: SCENIC: single-cell regulatory network inference and clustering. *Nature methods*, **14** (11), 1083.
- Anthes, R. A., 1972: *Hurricanes*. Elsevier.
- Au, K., 2006: Phd thesis.
- Barnes, G., E. Zipser, D. Jorgensen, and F. Marks, 1983: Mesoscale and convective structure of a hurricane rainband. *Journal of the Atmospheric Sciences*, **40** (9), 2125–2137.
- Bell, M. M., M. T. Montgomery, and W.-C. Lee, 2012: An axisymmetric view of concentric eyewall evolution in Hurricane Rita (2005). *Journal of the Atmospheric Sciences*, **69** (8), 2414–2432.
- Berg, W., and Coauthors, 2016: Intercalibration of the GPM microwave radiometer constellation. *Journal of Atmospheric and Oceanic Technology*, **33** (12), 2639–2654.
- Cecil, D. J., and E. J. Zipser, 2002: Reflectivity, ice scattering, and lightning characteristics of hurricane eyewalls and rainbands. Part II: Intercomparison of observations. *Monthly Weather Review*, **130** (4), 785–801.
- Cecil, D. J., E. J. Zipser, and S. W. Nesbitt, 2002: Reflectivity, ice scattering, and lightning characteristics of hurricane eyewalls and rainbands. Part I: Quantitative description. *Monthly Weather Review*, **130** (4), 769–784.

- Chan, J., and J. Kepert, 2010: *Global perspectives on tropical cyclones: from science to mitigation*, Vol. 4. World Scientific.
- Chang, C., T. Yeh, and J. Chen, 1993: Effects of terrain on the surface structure of typhoons over Taiwan. *Monthly weather review*, **121** (3), 734–752.
- Chawla, N. V., K. W. Bowyer, L. O. Hall, and W. P. Kegelmeyer, 2002: SMOTE: synthetic minority over-sampling technique. *Journal of artificial intelligence research*, **16**, 321–357.
- Chen, B.-F., C. A. Davis, and Y.-H. Kuo, 2018: Effects of low-level flow orientation and vertical shear on the structure and intensity of tropical cyclones. *Monthly Weather Review*, **146** (8), 2447–2467.
- Chen, S. S., J. A. Knaff, and F. D. Marks, 2006: Effects of vertical wind shear and storm motion on tropical cyclone rainfall asymmetries deduced from TRMM. *Monthly Weather Review*, **134** (11), 3190–3208.
- Chen, T., and C. Guestrin, 2016: XGBoost: A scalable tree boosting system. *Proceedings of the 22nd ACM SIGKDD international conference on knowledge discovery and data mining*, ACM, 785–794.
- Cheng, C.-J., and C.-C. Wu, 2018: The role of WISHE in secondary eyewall formation. *Journal of the Atmospheric Sciences*, **75** (11), 3823–3841.
- Chollet, F., and Coauthors, 2015: Keras. <https://keras.io>.
- Corbosiero, K. L., and J. Molinari, 2003: The relationship between storm motion, vertical wind shear, and convective asymmetries in tropical cyclones. *Journal of the Atmospheric Sciences*, **60** (2), 366–376.
- Corbosiero, K. L., J. Molinari, A. R. Aiyyer, and M. L. Black, 2006: The structure and evolution of Hurricane Elena (1985). Part II: Convective asymmetries and evidence for vortex Rossby waves. *Monthly weather review*, **134** (11), 3073–3091.
- Dai, Y., S. J. Majumdar, and D. S. Nolan, 2017: Secondary eyewall formation in tropical cyclones by outflow-jet interaction. *Journal of the Atmospheric Sciences*, **74** (6), 1941–1958.
- Davis, C., and Coauthors, 2008: Prediction of landfalling hurricanes with the advanced hurricane WRF model. *Monthly weather review*, **136** (6), 1990–2005.
- Davis, D. R., and W. B. Hayes, 2012: Automated quantitative description of spiral galaxy arm-segment structure. *2012 IEEE Conference on Computer Vision and Pattern Recognition*, IEEE, 1138–1145.
- Davis, D. R., and W. B. Hayes, 2014: SpArcFiRe: Scalable automated detection of spiral galaxy arm segments. *The Astrophysical Journal*, **790** (2), 87.

- Dawson, A., 2016: Windspharm: A high-level library for global wind field computations using spherical harmonics. *Journal of Open Research Software*, **4** (1).
- de Souza, R. E., D. A. Gadotti, and S. dos Anjos, 2004: BUDDA: a new two-dimensional bulge/disk decomposition code for detailed structural analysis of galaxies. *The Astrophysical Journal Supplement Series*, **153** (2), 411.
- DeMaria, M., 1996: The effect of vertical shear on tropical cyclone intensity change. *Journal of the atmospheric sciences*, **53** (14), 2076–2088.
- DeMaria, M., and J. Kaplan, 1999: An updated statistical hurricane intensity prediction scheme (SHIPS) for the Atlantic and eastern North Pacific basins. *Weather and Forecasting*, **14** (3), 326–337.
- Deng, D., and E. A. Ritchie, 2018: A metric for rainfall asymmetry in recurving tropical cyclones. *Geophysical Research Letters*, **45** (13), 6741–6749.
- DiCatarina, F., S. Abarca, A. Mehra, and V. Tallapragada, 2018: Comparison of HWRF operational cycles with and without secondary eyewalls. *Preprints, 33rd Conf. on Hurricanes and Tropical Meteorology, Ponte Vedra, Fl., Amer. Meteor. Soc. A*, Vol. 18.
- Didlake, A. C., G. M. Heymsfield, P. D. Reasor, and S. R. Guimond, 2017: Concentric eyewall asymmetries in Hurricane Gonzalo (2014) observed by airborne radar. *Monthly Weather Review*, **145** (3), 729–749.
- Didlake, A. C., and R. A. Houze, 2009: Convective-scale downdrafts in the principal rainband of Hurricane Katrina (2005). *Monthly Weather Review*, **137** (10), 3269–3293.
- Didlake, A. C., and R. A. Houze, 2011: Kinematics of the secondary eyewall observed in Hurricane Rita (2005). *Journal of the Atmospheric Sciences*, **68** (8), 1620–1636.
- Didlake, A. C., and R. A. Houze, 2013a: Convective-scale variations in the inner-core rainbands of a tropical cyclone. *Journal of the Atmospheric Sciences*, **70** (2), 504–523.
- Didlake, A. C., and R. A. Houze, 2013b: Dynamics of the stratiform sector of a tropical cyclone rainband. *Journal of the Atmospheric Sciences*, **70** (7), 1891–1911.
- Didlake, A. C., and M. R. Kumjian, 2017: Examining polarimetric radar observations of bulk microphysical structures and their relation to vortex kinematics in Hurricane Arthur (2014). *Monthly Weather Review*, **145** (11), 4521–4541.
- Didlake, A. C., P. D. Reasor, R. F. Rogers, and W.-C. Lee, 2018: Dynamics of the transition from spiral rainbands to a secondary eyewall in Hurricane Earl (2010). *Journal of the Atmospheric Sciences*, (2018).

Dutta, A., A. Gupta, and A. Zissermann, 2016: VGG image annotator (VIA). Version: 2.0.0, Accessed: 12/09/2018, <http://www.robots.ox.ac.uk/~vgg/software/via/>.

Dvorak, V. F., 1975: Tropical cyclone intensity analysis and forecasting from satellite imagery. *Monthly Weather Review*, **103** (5), 420–430.

Elsberry, R. L., and P. A. Harr, 2008: Tropical cyclone structure (TCS08) field experiment science basis, observational platforms, and strategy. *Asia-Pac. J. Atmos. Sci.*, **44** (3), 209–231.

Emanuel, K. A., 1986: An air-sea interaction theory for tropical cyclones. Part I: Steady-state maintenance. *Journal of the Atmospheric Sciences*, **43** (6), 585–605.

Emanuel, K. A., 1995: Sensitivity of tropical cyclones to surface exchange coefficients and a revised steady-state model incorporating eye dynamics. *Journal of the Atmospheric Sciences*, **52** (22), 3969–3976.

Fang, J., and F. Zhang, 2012: Effect of beta shear on simulated tropical cyclones. *Monthly Weather Review*, **140** (10), 3327–3346.

Finocchio, P. M., and S. J. Majumdar, 2017: A statistical perspective on wind profiles and vertical wind shear in tropical cyclone environments of the Northern Hemisphere. *Monthly Weather Review*, **145** (1), 361–378.

Finocchio, P. M., S. J. Majumdar, D. S. Nolan, and M. Iskandarani, 2016: Idealized tropical cyclone responses to the height and depth of environmental vertical wind shear. *Monthly Weather Review*, **144** (6), 2155–2175.

Flaming, G. M., 2004: Measurement of global precipitation. *Geoscience and Remote Sensing Symposium, 2004. IGARSS'04. Proceedings. 2004 IEEE International*, IEEE, Vol. 2, 918–920.

Frank, W. M., and E. A. Ritchie, 1999: Effects of environmental flow upon tropical cyclone structure. *Monthly weather review*, **127** (9), 2044–2061.

Franklin, C. N., G. J. Holland, and P. T. May, 2006: Mechanisms for the generation of mesoscale vorticity features in tropical cyclone rainbands. *Monthly weather review*, **134** (10), 2649–2669.

Fudeyasu, H., and Y. Wang, 2011: Balanced contribution to the intensification of a tropical cyclone simulated in TCM4: Outer-core spinup process. *Journal of the Atmospheric Sciences*, **68** (3), 430–449.

Gardini, B., G. Graf, and G. Ratier, 1995: The instruments on ENVISAT. *Acta Astronautica*, **37**, 301–311.

- Ge, X., L. Guan, and S. Zhou, 2016: Impacts of initial structure of tropical cyclone on secondary eyewall formation. *Atmospheric Science Letters*, **17** (10), 569–574.
- Girshick, R., 2015: Fast R-CNN. *Proceedings of the IEEE international conference on computer vision*, 1440–1448.
- Girshick, R., J. Donahue, T. Darrell, and J. Malik, 2016: Region-based convolutional networks for accurate object detection and segmentation. *IEEE transactions on pattern analysis and machine intelligence*, **38** (1), 142–158.
- Goodfellow, I., Y. Bengio, and A. Courville, 2016: *Deep Learning*. MIT Press, <http://www.deeplearningbook.org>.
- Guinn, T. A., and W. H. Schubert, 1993: Hurricane spiral bands. *Journal of the atmospheric sciences*, **50** (20), 3380–3403.
- Gurung, I., C. Peng, M. Maskey, and R. Ramachandran, 2018: Deep feature extraction and its application for hailstorm detection in a large collection of radar images. *Signal, Image and Video Processing*, 1–9.
- Haklay, M., 2013: Citizen science and volunteered geographic information: Overview and typology of participation. *Crowdsourcing geographic knowledge*, Springer, 105–122.
- Harnos, D. S., and S. W. Nesbitt, 2016: Passive microwave quantification of tropical cyclone inner-core cloud populations relative to subsequent intensity change. *Monthly Weather Review*, **144** (11), 4461–4482.
- Hawkins, J., and M. Helveston, 2008: Tropical cyclone multiple eyewall characteristics. 28th Conf. on Hurricanes and Tropical Meteorology, Orlando, FL. *Amer. Meteor. Soc. B*, **14**.
- Hawkins, J. D., and M. Helveston, 2004: Tropical cyclone multiple eyewall characteristics. *Preprints, 26th Conf. on Hurricane and Tropical Meteorology, Miami, FL, Amer. Meteor. Soc. P*, Vol. 1.
- Hawkins, J. D., M. Helveston, T. Lee, F. Turk, K. Richardson, C. Sampson, J. Kent, and R. Wade, 2006: Tropical cyclone multiple eyewall configurations. *Preprints, 27th Conf. on Hurricanes and Tropical Meteorology, Monterey, CA, Amer. Meteor. Soc. B*, Vol. 6.
- Hawkins, J. D., T. F. Lee, J. Turk, C. Sampson, J. Kent, and K. Richardson, 2001: Real-time internet distribution of satellite products for tropical cyclone reconnaissance. *Bulletin of the American Meteorological Society*, **82** (4), 567–578.
- He, K., G. Gkioxari, P. Dollár, and R. Girshick, 2017: Mask r-cnn. *Computer Vision (ICCV), 2017 IEEE International Conference on*, IEEE, 2980–2988.

- He, K., X. Zhang, S. Ren, and J. Sun, 2016: Deep residual learning for image recognition. *Proceedings of the IEEE conference on computer vision and pattern recognition*, 770–778.
- Hence, D. A., and R. A. Houze, 2008: Kinematic structure of convective-scale elements in the rainbands of hurricanes Katrina and Rita (2005). *Journal of Geophysical Research: Atmospheres*, **113 (D15)**.
- Hence, D. A., and R. A. Houze, 2011: Vertical structure of hurricane eyewalls as seen by the TRMM Precipitation Radar. *Journal of the Atmospheric Sciences*, **68 (8)**, 1637–1652.
- Hence, D. A., and R. A. Houze, 2012a: Vertical structure of tropical cyclone rainbands as seen by the TRMM precipitation radar. *Journal of the Atmospheric Sciences*, **69 (9)**, 2644–2661.
- Hence, D. A., and R. A. Houze, 2012b: Vertical structure of tropical cyclones with concentric eyewalls as seen by the TRMM Precipitation Radar. *Journal of the Atmospheric Sciences*, **69 (3)**, 1021–1036.
- Hennon, C. C., and Coauthors, 2015: Cyclone center: Can citizen scientists improve tropical cyclone intensity records? *Bulletin of the American Meteorological Society*, **96 (4)**, 591–607.
- Hill, K. A., and G. M. Lackmann, 2009: Influence of environmental humidity on tropical cyclone size. *Monthly Weather Review*, **137 (10)**, 3294–3315.
- Hogsett, W., and D.-L. Zhang, 2009: Numerical simulation of Hurricane Bonnie (1998). Part III: Energetics. *Journal of the Atmospheric Sciences*, **66 (9)**, 2678–2696.
- Hollinger, J. P., J. L. Peirce, and G. A. Poe, 1990: SSM/I instrument evaluation. *IEEE Transactions on Geoscience and Remote Sensing*, **28 (5)**, 781–790.
- Hong, S.-Y., and J.-O. J. Lim, 2006: The WRF single-moment 6-class microphysics scheme (WSM6). *J. Korean Meteor. Soc.*, **42 (2)**, 129–151.
- Hong, S.-Y., Y. Noh, and J. Dudhia, 2006: A new vertical diffusion package with an explicit treatment of entrainment processes. *Monthly weather review*, **134 (9)**, 2318–2341.
- Horstmann, J., D. Thompson, F. Monaldo, S. Iris, and H. Graber, 2005: Can synthetic aperture radars be used to estimate hurricane force winds? *Geophysical Research Letters*, **32 (22)**.
- Hoskins, B. J., M. McIntyre, and A. W. Robertson, 1985: On the use and significance of isentropic potential vorticity maps. *Quarterly Journal of the Royal Meteorological Society*, **111 (470)**, 877–946.
- Hou, A. Y., and Coauthors, 2014: The global precipitation measurement mission. *Bulletin of the American Meteorological Society*, **95 (5)**, 701–722.
- Houze, R. A., 2010: Clouds in tropical cyclones. *Monthly Weather Review*, **138 (2)**, 293–344.

- Houze, R. A., S. S. Chen, B. F. Smull, W.-C. Lee, and M. M. Bell, 2007: Hurricane intensity and eyewall replacement. *science*, **315** (5816), 1235–1239.
- Houze, R. A., and Coauthors, 2006: The hurricane rainband and intensity change experiment: Observations and modelling of Hurricanes Katrina, Ophelia, and Rita. *Bulletin of the American Meteorological Society*, **87** (11), 1503–1522.
- Huang, Y.-H., M. T. Montgomery, and C.-C. Wu, 2012: Concentric eyewall formation in Typhoon Sinlaku (2008). Part II: Axisymmetric dynamical processes. *Journal of the Atmospheric Sciences*, **69** (2), 662–674.
- Huang, Y.-H., C.-C. Wu, and M. T. Montgomery, 2018: Concentric eyewall formation in Typhoon Sinlaku (2008). Part III: Horizontal momentum budget analyses. *Journal of the Atmospheric Sciences*, **75** (10), 3541–3563.
- Huffman, G. J., and Coauthors, 2007: The TRMM multisatellite precipitation analysis (TMPA): Quasi-global, multiyear, combined-sensor precipitation estimates at fine scales. *Journal of hydrometeorology*, **8** (1), 38–55.
- Irish, J. L., D. T. Resio, and J. J. Ratcliff, 2008: The influence of storm size on hurricane surge. *Journal of Physical Oceanography*, **38** (9), 2003–2013.
- Japan Aerospace Exploration Agency, 2005: *AMSRE Data Users Handbook*.
- Jones, S. C., 1995: The evolution of vortices in vertical shear. I: initially barotropic vortices. *Quarterly Journal of the Royal Meteorological Society*, **121** (524), 821–851.
- Jones, S. C., 2000a: The evolution of vortices in vertical shear. II: large-scale asymmetries. *Quarterly Journal of the Royal Meteorological Society*, **126** (570), 3137–3159.
- Jones, S. C., 2000b: The evolution of vortices in vertical shear. III: baroclinic vortices. *Quarterly Journal of the Royal Meteorological Society*, **126** (570), 3161–3185.
- Jorgensen, D. F., 1984: Mesoscale and convective-scale characteristics of mature hurricanes. Part I: General observations by research aircraft. *Journal of the Atmospheric Sciences*, **41** (8), 1268–1286.
- Judit, F., and S. S. Chen, 2010: Convectively generated potential vorticity in rainbands and formation of the secondary eyewall in Hurricane Rita of 2005. *Journal of the Atmospheric Sciences*, **67** (11), 3581–3599.
- Jung, A., 2018: imgaug. Github, <https://github.com/aleju/imgaug>.
- Kalnay, E., and Coauthors, 1996: The NCEP/NCAR 40-year reanalysis project. *Bulletin of the American meteorological Society*, **77** (3), 437–472.

- Kaplan, J., and M. DeMaria, 2003: Large-scale characteristics of rapidly intensifying tropical cyclones in the North Atlantic basin. *Weather and forecasting*, **18** (6), 1093–1108.
- Kaplan, J., M. DeMaria, and J. A. Knaff, 2010: A revised tropical cyclone rapid intensification index for the Atlantic and eastern North Pacific basins. *Weather and forecasting*, **25** (1), 220–241.
- Kaplan, J., and Coauthors, 2015: Evaluating environmental impacts on tropical cyclone rapid intensification predictability utilizing statistical models. *Weather and Forecasting*, **30** (5), 1374–1396.
- Kepert, J. D., 2013: How does the boundary layer contribute to eyewall replacement cycles in axisymmetric tropical cyclones? *Journal of the Atmospheric Sciences*, **70** (9), 2808–2830.
- Kepert, J. D., 2017: Time and space scales in the tropical cyclone boundary layer, and the location of the eyewall updraft. *Journal of the Atmospheric Sciences*, **74** (10), 3305–3323.
- Kepert, J. D., 2018: The boundary layer dynamics of tropical cyclone rainbands. *Journal of the Atmospheric Sciences*, **75** (11), 3777–3795.
- Kepert, J. D., and D. S. Nolan, 2014: Reply to comments on how does the boundary layer contribute to eyewall replacement cycles in axisymmetric tropical cyclones? *Journal of the Atmospheric Sciences*, **71** (12), 4692–4704.
- Kieper, M. E., and H. Jiang, 2012: Predicting tropical cyclone rapid intensification using the 37 GHz ring pattern identified from passive microwave measurements. *Geophysical Research Letters*, **39** (13).
- Klotzbach, P. J., 2006: Trends in global tropical cyclone activity over the past twenty years (1986–2005). *Geophysical Research Letters*, **33** (10).
- Knaff, J. A., T. A. Cram, A. B. Schumacher, J. P. Kossin, and M. DeMaria, 2008: Objective identification of annular hurricanes. *Weather and Forecasting*, **23** (1), 17–28.
- Knaff, J. A., J. P. Kossin, and M. DeMaria, 2003: Annular hurricanes. *Weather and Forecasting*, **18** (2), 204–223.
- Knaff, J. A., S. P. Longmore, and D. A. Molenar, 2014: An objective satellite-based tropical cyclone size climatology. *Journal of Climate*, **27** (1), 455–476.
- Knapp, K. R., 2008: 4B. 4 hurricane satellite (HURSAT) data sets: Low earth orbit infrared and microwave data.
- Knapp, K. R., M. C. Kruk, D. H. Levinson, H. J. Diamond, and C. J. Neumann, 2010: The international best track archive for climate stewardship (IBTrACS) unifying tropical cyclone data. *Bulletin of the American Meteorological Society*, **91** (3), 363–376.

- Knapp, K. R., J. L. Matthews, J. P. Kossin, and C. C. Hennon, 2016: Identification of tropical cyclone storm types using crowdsourcing. *Monthly Weather Review*, **144** (10), 3783–3798.
- Knapp, K. R., C. S. Velden, and A. J. Wimmers, 2018: A global climatology of tropical cyclone eyes. *Monthly Weather Review*, **146** (7), 2089–2101.
- Komaromi, W. A., and J. D. Doyle, 2018: On the dynamics of tropical cyclone and trough interactions. *Journal of the Atmospheric Sciences*, **75** (8), 2687–2709.
- Kossin, J. P., and M. DeMaria, 2016: Reducing operational hurricane intensity forecast errors during eyewall replacement cycles. *Weather and Forecasting*, **31** (2), 601–608.
- Kossin, J. P., J. A. Knaff, H. I. Berger, D. C. Herndon, T. A. Cram, C. S. Velden, R. J. Murnane, and J. D. Hawkins, 2007: Estimating hurricane wind structure in the absence of aircraft reconnaissance. *Weather and Forecasting*, **22** (1), 89–101.
- Kossin, J. P., and M. Sitkowski, 2009: An objective model for identifying secondary eyewall formation in hurricanes. *Monthly Weather Review*, **137** (3), 876–892.
- Kossin, J. P., and M. Sitkowski, 2012: Predicting hurricane intensity and structure changes associated with eyewall replacement cycles. *Weather and Forecasting*, **27** (2), 484–488.
- Krizhevsky, A., I. Sutskever, and G. E. Hinton, 2012: Imagenet classification with deep convolutional neural networks. *Advances in neural information processing systems*, 1097–1105.
- Kummerow, C., W. Barnes, T. Kozu, J. Shiue, and J. Simpson, 1998: The tropical rainfall measuring mission (TRMM) sensor package. *Journal of atmospheric and oceanic technology*, **15** (3), 809–817.
- Kuo, H.-C., C.-P. Chang, Y.-T. Yang, and H.-J. Jiang, 2009: Western North Pacific typhoons with concentric eyewalls. *Monthly Weather Review*, **137** (11), 3758–3770.
- Kurihara, Y., 1976: On the development of spiral bands in a tropical cyclone. *Journal of the Atmospheric Sciences*, **33** (6), 940–958.
- Kurtek, S., J. Su, C. Grimm, M. Vaughan, R. Sowell, and A. Srivastava, 2013: Statistical analysis of manual segmentations of structures in medical images. *Computer Vision and Image Understanding*, **117** (9), 1036–1050.
- Lafore, J.-P., and M. W. Moncrieff, 1989: A numerical investigation of the organization and interaction of the convective and stratiform regions of tropical squall lines. *Journal of the atmospheric sciences*, **46** (4), 521–544.
- Lazarus, S. M., S. T. Wilson, M. E. Splitt, and G. A. Zarillo, 2013: Evaluation of a wind-wave system for ensemble tropical cyclone wave forecasting. Part II: Waves. *Weather and Forecasting*, **28** (2), 316–330.

- LeCun, Y., Y. Bengio, and G. Hinton, 2015: Deep learning. *nature*, **521** (7553), 436.
- LeCun, Y., B. Boser, J. S. Denker, D. Henderson, R. E. Howard, W. Hubbard, and L. D. Jackel, 1989: Backpropagation applied to handwritten zip code recognition. *Neural computation*, **1** (4), 541–551.
- Lee, C.-S., B.-F. Chen, and R. L. Elsberry, 2012: Long-lasting convective systems in the outer region of tropical cyclones in the western north pacific. *Geophysical Research Letters*, **39** (21).
- Lee, I. K., A. Shamsoddini, X. Li, J. C. Trinder, and Z. Li, 2017: Extracting hurricane eye morphology from spaceborne SAR images using morphological analysis. *Hurricane Monitoring With Spaceborne Synthetic Aperture Radar*, Springer, 119–139.
- Lee, T. F., F. J. Turk, J. Hawkins, and K. Richardson, 2002: Interpretation of TRMM TMI images of tropical cyclones. *Earth Interactions*, **6** (3), 1–17.
- Li, Q., Y. Wang, and Y. Duan, 2017: A numerical study of outer rainband formation in a sheared tropical cyclone. *Journal of the Atmospheric Sciences*, **74** (1), 203–227.
- Li, X., J. A. Zhang, X. Yang, W. G. Pichel, M. DeMaria, D. Long, and Z. Li, 2013: Tropical cyclone morphology from spaceborne synthetic aperture radar. *Bulletin of the American Meteorological Society*, **94** (2), 215–230.
- Liang, S., 2017: *Comprehensive Remote Sensing*. Elsevier.
- Lin, T.-Y., P. Dollár, R. B. Girshick, K. He, B. Hariharan, and S. J. Belongie, 2017: Feature pyramid networks for object detection. *CVPR*, Vol. 1, 4.
- Lin, T.-Y., M. Maire, S. Belongie, J. Hays, P. Perona, D. Ramanan, P. Dollár, and C. L. Zitnick, 2014: Microsoft COCO: Common objects in context. *European conference on computer vision*, Springer, 740–755.
- Lin, Y., M. Zhao, and M. Zhang, 2015: Tropical cyclone rainfall area controlled by relative sea surface temperature. *Nature communications*, **6**, 6591.
- Lintott, C. J., and Coauthors, 2008: Galaxy zoo: morphologies derived from visual inspection of galaxies from the Sloan Digital Sky Survey. *Monthly Notices of the Royal Astronomical Society*, **389** (3), 1179–1189.
- Lundberg, S. M., G. G. Erion, and S.-I. Lee, 2018: Consistent individualized feature attribution for tree ensembles. *arXiv preprint arXiv:1802.03888*.
- Lundberg, S. M., and S.-I. Lee, 2017: A unified approach to interpreting model predictions. *Advances in Neural Information Processing Systems*, 4765–4774.
- Ma, J., 2001: A method of obtaining the pitch angle of spiral arms and the inclination of galactic discs. *Chinese Journal of Astronomy and Astrophysics*, **1** (5), 395.

- Maclay, K. S., M. DeMaria, and T. H. Vonder Haar, 2008: Tropical cyclone inner-core kinetic energy evolution. *Monthly Weather Review*, **136** (12), 4882–4898.
- Maeda, T., Y. Taniguchi, and K. Imaoka, 2016: GCOM-W1 AMSR2 level 1R product: Dataset of brightness temperature modified using the antenna pattern matching technique. *IEEE Transactions on Geoscience and Remote Sensing*, **54** (2), 770–782.
- Mallen, K. J., M. T. Montgomery, and B. Wang, 2005: Reexamining the near-core radial structure of the tropical cyclone primary circulation: Implications for vortex resiliency. *Journal of the Atmospheric Sciences*, **62** (2), 408–425.
- Martinez, Y., G. Brunet, and M. Yau, 2010: On the dynamics of two-dimensional hurricane-like concentric rings vortex formation. *Journal of the Atmospheric Sciences*, **67** (10), 3253–3268.
- Martinez, Y., G. Brunet, M. Yau, and X. Wang, 2011: On the dynamics of concentric eyewall genesis: Space–time empirical normal modes diagnosis. *Journal of the Atmospheric Sciences*, **68** (3), 457–476.
- Matyas, C., 2007: Quantifying the shapes of US landfalling tropical cyclone rain shields. *The Professional Geographer*, **59** (2), 158–172.
- Matyas, C., 2008: Shape measures of rain shields as indicators of changing environmental conditions in a landfalling tropical storm. *Meteorological Applications*, **15** (2), 259–271.
- Matyas, C. J., 2009: A spatial analysis of radar reflectivity regions within Hurricane Charley (2004). *Journal of Applied Meteorology and Climatology*, **48** (1), 130–142.
- Matyas, C. J., 2010: Associations between the size of hurricane rain fields at landfall and their surrounding environments. *Meteorology and atmospheric physics*, **106** (3-4), 135–148.
- Matyas, C. J., 2014: Conditions associated with large rain-field areas for tropical cyclones landfalling over Florida. *Physical Geography*, **35** (2), 93–106.
- May, P. T., 1996: The organization of convection in the rainbands of Tropical Cyclone Laurence. *Monthly weather review*, **124** (5), 807–815.
- May, P. T., and G. J. Holland, 1999: The role of potential vorticity generation in tropical cyclone rainbands. *Journal of the atmospheric sciences*, **56** (9), 1224–1228.
- McNoldy, B. D., 2004: Triple eyewall in hurricane Juliette. *Bulletin of the American Meteorological Society*, **85** (11), 1663–1666.
- Menelaou, K., M. Yau, and Y. Martinez, 2012: On the dynamics of the secondary eyewall genesis in Hurricane Wilma (2005). *Geophysical Research Letters*, **39** (4).
- Merrill, R. T., 1984: A comparison of large and small tropical cyclones. *Monthly Weather Review*, **112** (7), 1408–1418.

- Metzger, E. J., and Coauthors, 2014: US Navy operational global ocean and arctic ice prediction systems. *Oceanography*, **27** (3), 32–43.
- Montgomery, M. T., and R. J. Kallenbach, 1997: A theory for vortex rossby-waves and its application to spiral bands and intensity changes in hurricanes. *Quarterly Journal of the Royal Meteorological Society*, **123** (538), 435–465.
- Moon, Y., and D. S. Nolan, 2010: The dynamic response of the hurricane wind field to spiral rainband heating. *Journal of the Atmospheric Sciences*, **67** (6), 1779–1805.
- Moon, Y., and D. S. Nolan, 2015a: Spiral rainbands in a numerical simulation of Hurricane Bill (2009). Part I: Structures and comparisons to observations. *Journal of the Atmospheric Sciences*, **72** (1), 164–190.
- Moon, Y., and D. S. Nolan, 2015b: Spiral rainbands in a numerical simulation of Hurricane Bill (2009). Part II: Propagation of inner rainbands. *Journal of the Atmospheric Sciences*, **72** (1), 191–215.
- National Aeronautics and Space Agency, 2018: Precipitation Processing System STORM Database. URL <https://storm.pps.eosdis.nasa.gov/storm/>.
- Nolan, D. S., 2011: Evaluating environmental favorability for tropical cyclone development with the method of point-downscaling. *Journal of Advances in Modeling Earth Systems*, **3** (3).
- Nong, S., and K. Emanuel, 2003: A numerical study of the genesis of concentric eyewalls in hurricanes. *Quarterly Journal of the Royal Meteorological Society*, **129** (595), 3323–3338.
- Onderlinde, M. J., and D. S. Nolan, 2014: Environmental helicity and its effects on development and intensification of tropical cyclones. *Journal of the Atmospheric Sciences*, **71** (11), 4308–4320.
- Onderlinde, M. J., and D. S. Nolan, 2016: Tropical cyclone-relative environmental helicity and the pathways to intensification in shear. *Journal of the Atmospheric Sciences*, **73** (2), 869–890.
- Ortt, D., and S. Chen, 2008: Effect of environmental moisture on rainbands in Hurricanes Katrina and Rita (2005). *Preprints, 27th AMS Conference on Hurricanes and Tropical Meteorology*.
- Ortt, D., and S. S. Chen, 2006: Rainbands and secondary eye wall formation as observed in RAINEX. *Preprints, 27th Conf. on Hurricanes and Tropical Meteorology, Monterey, CA, Amer. Meteor. Soc. A*, Vol. 12.
- Pan, S. J., Q. Yang, and Coauthors, 2010: A survey on transfer learning. *IEEE Transactions on knowledge and data engineering*, **22** (10), 1345–1359.

- Pei, S.-C., and J.-H. Horng, 1995: Circular arc detection based on Hough transform. *Pattern recognition letters*, **16** (6), 615–625.
- Peng, C. Y., L. C. Ho, C. D. Impey, and H.-W. Rix, 2002: Detailed structural decomposition of galaxy images. *The Astronomical Journal*, **124** (1), 266.
- Peng, C. Y., L. C. Ho, C. D. Impey, and H.-W. Rix, 2010: Detailed decomposition of galaxy images. II. beyond axisymmetric models. *The Astronomical Journal*, **139** (6), 2097.
- Piech, D., and R. Hart, 2008: Atlantic reconnaissance vortex message climatology and composites and their use in characterizing eyewall cycles. *Preprints, 28th Conf. on Hurricanes and Tropical Meteorology, Orlando, FL, Amer. Meteor. Soc. C*, Vol. 18.
- Pizer, S. M., and Coauthors, 1987: Adaptive histogram equalization and its variations. *Computer vision, graphics, and image processing*, **39** (3), 355–368.
- Powell, M. D., 1990a: Boundary layer structure and dynamics in outer hurricane rainbands. Part I: Mesoscale rainfall and kinematic structure. *Monthly Weather Review*, **118** (4), 891–917.
- Powell, M. D., 1990b: Boundary layer structure and dynamics in outer hurricane rainbands. Part II: Downdraft modification and mixed layer recovery. *Monthly Weather Review*, **118** (4), 918–938.
- Pradhan, R., R. S. Aygun, M. Maskey, R. Ramachandran, and D. J. Cecil, 2018: Tropical cyclone intensity estimation using a deep convolutional neural network. *IEEE Transactions on Image Processing*, **27** (2), 692–702.
- Puerari, I., and H. Dottori, 1992: Fourier analysis of structure in spiral galaxies. *Astronomy and Astrophysics Supplement Series*, **93**, 469–493.
- Qiu, X., and Z.-M. Tan, 2013: The roles of asymmetric inflow forcing induced by outer rainbands in tropical cyclone secondary eyewall formation. *Journal of the Atmospheric Sciences*, **70** (3), 953–974.
- Quilfen, Y., J. Tournadre, and B. Chapron, 2006: Altimeter dual-frequency observations of surface winds, waves, and rain rate in tropical cyclone Isabel. *Journal of Geophysical Research: Oceans*, **111** (C1).
- Raney, R. K., A. P. Luscombe, E. Langham, and S. Ahmed, 1991: RADARSAT (SAR imaging). *Proceedings of the IEEE*, **79** (6), 839–849.
- Rappin, E. D., and D. S. Nolan, 2012: The effect of vertical shear orientation on tropical cyclogenesis. *Quarterly Journal of the Royal Meteorological Society*, **138** (665), 1035–1054.
- Reasor, P. D., M. T. Montgomery, and L. D. Grasso, 2004: A new look at the problem of tropical

cyclones in vertical shear flow: Vortex resiliency. *Journal of The atmospheric sciences*, **61** (1), 3–22.

Regional and Mesoscale Meteorology Branch, 2018: SHIPS predictor files. Tech. rep., Colorado State University.

Ren, S., K. He, R. Girshick, X. Zhang, and J. Sun, 2017: Object detection networks on convolutional feature maps. *IEEE transactions on pattern analysis and machine intelligence*, **39** (7), 1476–1481.

Riemer, M., 2016: Meso- $\beta$ -scale environment for the stationary band complex of vertically sheared tropical cyclones. *Quarterly Journal of the Royal Meteorological Society*, **142** (699), 2442–2451.

Riemer, M., and F. Laliberté, 2015: Secondary circulation of tropical cyclones in vertical wind shear: Lagrangian diagnostic and pathways of environmental interaction. *Journal of the Atmospheric Sciences*, **72** (9), 3517–3536.

Riemer, M., and M. T. Montgomery, 2011: Simple kinematic models for the environmental interaction of tropical cyclones in vertical wind shear. *Atmospheric Chemistry and Physics*, **11** (17), 9395.

Ritchie, E. A., and W. M. Frank, 2007: Interactions between simulated tropical cyclones and an environment with a variable coriolis parameter. *Monthly weather review*, **135** (5), 1889–1905.

Rozoff, C. M., D. S. Nolan, J. P. Kossin, F. Zhang, and J. Fang, 2012: The roles of an expanding wind field and inertial stability in tropical cyclone secondary eyewall formation. *Journal of the Atmospheric Sciences*, **69** (9), 2621–2643.

Rozoff, C. M., W. H. Schubert, B. D. McNoldy, and J. P. Kossin, 2006: Rapid filamentation zones in intense tropical cyclones. *Journal of the atmospheric sciences*, **63** (1), 325–340.

Ryzhkov, A., M. Diederich, P. Zhang, and C. Simmer, 2014: Potential utilization of specific attenuation for rainfall estimation, mitigation of partial beam blockage, and radar networking. *Journal of Atmospheric and Oceanic Technology*, **31** (3), 599–619.

Samsury, C. E., and E. J. Zipser, 1995: Secondary wind maxima in hurricanes: Airflow and relationship to rainbands. *Monthly weather review*, **123** (12), 3502–3517.

Sanabia, E. R., B. S. Barrett, N. P. Celone, and Z. D. Cornelius, 2015: Satellite and aircraft observations of the eyewall replacement cycle in Typhoon Sinlaku (2008). *Monthly Weather Review*, **143** (9), 3406–3420.

Sawada, M., and T. Iwasaki, 2010: Impacts of evaporation from raindrops on tropical cyclones. Part II: Features of rainbands and asymmetric structure. *Journal of the Atmospheric Sciences*, **67** (1), 84–96.

- Seigar, M. S., J. S. Bullock, A. J. Barth, and L. C. Ho, 2006: Constraining dark matter halo profiles and galaxy formation models using spiral arm morphology. I. method outline. *The Astrophysical Journal*, **645** (2), 1012.
- Senn, H. V., and H. Hiser, 1959: On the origin of hurricane spiral rain bands. *Journal of Meteorology*, **16** (4), 419–426.
- Senn, H. V., H. W. Hiser, and R. C. Bourret, 1957: Studies of hurricane spiral bands as observed on radar. Tech. rep., MIAMI UNIV FLA MARINE LAB.
- Shapiro, L. J., 1983: The asymmetric boundary layer flow under a translating hurricane. *Journal of the Atmospheric Sciences*, **40** (8), 1984–1998.
- Shapiro, L. J., and H. E. Willoughby, 1982: The response of balanced hurricanes to local sources of heat and momentum. *Journal of the Atmospheric Sciences*, **39** (2), 378–394.
- Sitkowski, M., J. P. Kossin, and C. M. Rozoff, 2011: Intensity and structure changes during hurricane eyewall replacement cycles. *Monthly Weather Review*, **139** (12), 3829–3847.
- Skamarock, W. C., and J. B. Klemp, 2008: A time-split nonhydrostatic atmospheric model for weather research and forecasting applications. *Journal of Computational Physics*, **227** (7), 3465–3485.
- Smith, R. K., M. T. Montgomery, and N. Van Sang, 2009: Tropical cyclone spin-up revisited. *Quarterly Journal of the Royal Meteorological Society: A journal of the atmospheric sciences, applied meteorology and physical oceanography*, **135** (642), 1321–1335.
- Spencer, R. W., H. M. Goodman, and R. E. Hood, 1989: Precipitation retrieval over land and ocean with the SSM/I: Identification and characteristics of the scattering signal. *Journal of Atmospheric and Oceanic Technology*, **6** (2), 254–273.
- Sun, Y. Q., Y. Jiang, B. Tan, and F. Zhang, 2013: The governing dynamics of the secondary eyewall formation of Typhoon Sinlaku (2008). *Journal of the Atmospheric Sciences*, **70** (12), 3818–3837.
- Tamayo, D., and Coauthors, 2016: A machine learns to predict the stability of tightly packed planetary systems. *The Astrophysical Journal Letters*, **832** (2), L22.
- Tang, X., W.-C. Lee, and M. Bell, 2014: A squall-line-like principal rainband in Typhoon Hagupit (2008) observed by airborne doppler radar. *Journal of the Atmospheric Sciences*, **71** (7), 2733–2746.
- Tang, X., W.-C. Lee, and M. Bell, 2018: Subrainband structure and dynamic characteristics in the principal rainband of typhoon hagupit (2008). *Monthly Weather Review*, **146** (1), 157–173.

- Terwey, W. D., and M. T. Montgomery, 2008: Secondary eyewall formation in two idealized, full-physics modeled hurricanes. *Journal of Geophysical Research: Atmospheres*, **113** (D12).
- Thomsen, G. L., R. K. Smith, and M. T. Montgomery, 2015: Tropical cyclone flow asymmetries induced by a uniform flow revisited. *Journal of Advances in Modeling Earth Systems*, **7** (3), 1265–1284.
- Tramacere, A., D. Paraficz, P. Dubath, J.-P. Kneib, and F. Courbin, 2016: ASTERIsM: application of topometric clustering algorithms in automatic galaxy detection and classification. *Monthly Notices of the Royal Astronomical Society*, **463** (3), 2939–2957.
- Turk, F. J., G. D. Rohaly, J. Hawkins, E. A. Smith, F. S. Marzano, A. Mugnai, and V. Levizzani, 1999: Meteorological applications of precipitation estimation from combined SSM/I, TRMM and infrared geostationary satellite data. *Microwave Radiometry and Remote Sensing of the Earth's Surface and Atmosphere*, 353–363.
- Tyner, B., P. Zhu, J. A. Zhang, S. Gopalakrishnan, F. Marks, and V. Tallapragada, 2018: A top-down pathway to secondary eyewall formation in simulated tropical cyclones. *Journal of Geophysical Research: Atmospheres*, **123** (1), 174–197.
- Velden, C., and Coauthors, 2006: The Dvorak tropical cyclone intensity estimation technique: A satellite-based method that has endured for over 30 years. *Bulletin of the American Meteorological Society*, **87** (9), 1195–1210.
- Vigh, J., N. Dorst, C. Williams, E. Uhlhorn, H. Willoughby, and F. Marks Jr, 2015: FLIGHT+: The Extended Flight Level Dataset for Tropical Cyclones (Version 1.0). Tropical Cyclone Data Project. *National Center for Atmospheric Research, Research Applications Laboratory, Boulder, Colorado.* [Available online at: <http://dx.doi.org/10.5065/D6WS8R93>], **16**.
- Wada, A., N. Usui, and K. Sato, 2012: Relationship of maximum tropical cyclone intensity to sea surface temperature and tropical cyclone heat potential in the North Pacific Ocean. *Journal of Geophysical Research: Atmospheres*, **117** (D11).
- Wahiduzzaman, M., E. C. Oliver, S. J. Wotherspoon, and N. J. Holbrook, 2017: A climatological model of north Indian ocean tropical cyclone genesis, tracks and landfall. *Climate Dynamics*, **49** (7-8), 2585–2603.
- Wang, H., C.-C. Wu, and Y. Wang, 2016: Secondary eyewall formation in an idealized tropical cyclone simulation: Balanced and unbalanced dynamics. *Journal of the Atmospheric Sciences*, **73** (10), 3911–3930.
- Wang, M., K. Zhao, W.-C. Lee, and F. Zhang, 2018a: Microphysical and kinematic structure of convective-scale elements in the inner rainband of Typhoon Matmo (2014) after landfall. *Journal of Geophysical Research: Atmospheres*.

Wang, X., Q. Li, and N. E. Davidson, 2018b: The coupled dynamic and thermodynamic processes for secondary eyewall formation. *Journal of Geophysical Research: Atmospheres*, **123** (17), 9192–9219.

Wang, Y., 2002a: Vortex rossby waves in a numerically simulated tropical cyclone. Part I: Overall structure, potential vorticity, and kinetic energy budgets. *Journal of the atmospheric sciences*, **59** (7), 1213–1238.

Wang, Y., 2002b: Vortex rossby waves in a numerically simulated tropical cyclone. Part II: The role in tropical cyclone structure and intensity changes. *Journal of the atmospheric sciences*, **59** (7), 1239–1262.

Wang, Y., 2008a: Rapid filamentation zone in a numerically simulated tropical cyclone. *Journal of the Atmospheric Sciences*, **65** (4), 1158–1181.

Wang, Y., 2008b: Structure and formation of an annular hurricane simulated in a fully compressible, nonhydrostatic model TCM4. *Journal of the Atmospheric Sciences*, **65** (5), 1505–1527.

Wang, Y., Y. Rao, Z.-M. Tan, and D. Schönemann, 2015: A statistical analysis of the effects of vertical wind shear on tropical cyclone intensity change over the western North Pacific. *Monthly Weather Review*, **143** (9), 3434–3453.

Wexler, H., 1947: Structure of hurricanes as determined by radar. *Annals of the New York Academy of Sciences*, **48** (8), 821–845.

Whitaker, J., 2018: Pyspharm. Github, <https://github.com/jswhit/pyspharm>,

Willoughby, H., 1978: A possible mechanism for the formation of hurricane rainbands. *Journal of the Atmospheric Sciences*, **35** (5), 838–848.

Willoughby, H., and P. Black, 1996: Hurricane Andrew in Florida: Dynamics of a disaster. *Bulletin of the American Meteorological Society*, **77** (3), 543–550.

Willoughby, H., J. Clos, and M. Shoreibah, 1982: Concentric eye walls, secondary wind maxima, and the evolution of the hurricane vortex. *Journal of the Atmospheric Sciences*, **39** (2), 395–411.

Willoughby, H. E., F. D. Marks, and R. J. Feinberg, 1984: Stationary and moving convective bands in hurricanes. *Journal of the atmospheric sciences*, **41** (22), 3189–3211.

Wimmers, A. J., and C. S. Velden, 2007: MIMIC: A new approach to visualizing satellite microwave imagery of tropical cyclones. *Bulletin of the American Meteorological Society*, **88** (8), 1187–1196.

Wimmers, A. J., and C. S. Velden, 2010: Objectively determining the rotational center of

tropical cyclones in passive microwave satellite imagery. *Journal of Applied Meteorology and Climatology*, **49** (9), 2013–2034.

Wimmers, A. J., and C. S. Velden, 2016: Advancements in objective multisatellite tropical cyclone center fixing. *Journal of Applied Meteorology and Climatology*, **55** (1), 197–212.

Wu, C.-C., Y.-H. Huang, and G.-Y. Lien, 2012: Concentric eyewall formation in Typhoon Sinlaku (2008). Part I: Assimilation of T-PARC data based on the ensemble Kalman filter (EnKF). *Monthly Weather Review*, **140** (2), 506–527.

Wu, C.-C., Y.-H. Huang, and Z. Tan, 2016: Secondary eyewall formation in tropical cyclones. *Dynamics and Predictability of Large-Scale, High-Impact Weather and Climate Events*, **2**, 168.

Wu, K., S. Abarca, B. Liu, W. Wang, L. Zhu, Z. Zhang, A. Mehra, and V. Tallapragada, 2018: 2c.7 application of machine learning for secondary eyewall formation prediction in HWRF and HMON models.

Xiaofan Li, B. W., 1992: The beta drift of three-dimensional vortices: A numerical study. *Monthly weather review*, **120** (4), 579–593.

Xu, J., and Y. Wang, 2010: Sensitivity of tropical cyclone inner-core size and intensity to the radial distribution of surface entropy flux. *Journal of the Atmospheric Sciences*, **67** (6), 1831–1852.

Yang, S., J. Hawkins, and K. Richardson, 2014: The improved NRL tropical cyclone monitoring system with a unified microwave brightness temperature calibration scheme. *Remote Sensing*, **6** (5), 4563–4581.

Yang, Y.-T., H.-C. Kuo, E. A. Hendricks, and M. S. Peng, 2013: Structural and intensity changes of concentric eyewall typhoons in the Western North Pacific basin. *Monthly Weather Review*, **141** (8), 2632–2648.

Ye, S., 2018: Surgery robot detection segmentation. Github, <https://github.com/SUYEgit/Surgery-Robot-Detection-Segmentation>.

Yu, C.-K., C.-Y. Lin, L.-W. Cheng, J.-S. Luo, C.-C. Wu, and Y. Chen, 2018: The degree of prevalence of similarity between outer tropical cyclone rainbands and squall lines. *Scientific reports*, **8** (1), 8247.

Yurchak, B., 2007: Description of cloud-rain bands in a tropical cyclone by a hyperbolic-logarithmic spiral. *Russian Meteorology and Hydrology*, **32** (1), 8–18.

Zeng, Z., Y. Wang, and L. Chen, 2010: A statistical analysis of vertical shear effect on tropical cyclone intensity change in the North Atlantic. *Geophysical Research Letters*, **37** (2).

- Zhang, F., D. Tao, Y. Q. Sun, and J. D. Kepert, 2017a: Dynamics and predictability of secondary eyewall formation in sheared tropical cyclones. *Journal of Advances in Modeling Earth Systems*, **9** (1), 89–112.
- Zhang, L., and Coauthors, 2017b: CarcinoPred-EL: novel models for predicting the carcinogenicity of chemicals using molecular fingerprints and ensemble learning methods. *Scientific reports*, **7** (1), 2118.
- Zhao, K., Q. Lin, W.-C. Lee, Y. Qiang Sun, and F. Zhang, 2016: Doppler radar analysis of triple eyewalls in typhoon Usagi (2013). *Bulletin of the American Meteorological Society*, **97** (1), 25–30.
- Zhou, Y., and C. J. Matyas, 2017: Spatial characteristics of storm-total rainfall swaths associated with tropical cyclones over the Eastern United States. *International Journal of Climatology*, **37** (S1), 557–569.
- Zhu, Z., and P. Zhu, 2014: The role of outer rainband convection in governing the eyewall replacement cycle in numerical simulations of tropical cyclones. *Journal of Geophysical Research: Atmospheres*, **119** (13), 8049–8072.
- Zick, S. E., and C. J. Matyas, 2014: 14B. 1 Evolving synoptic-scale precipitation patterns in US landfalling tropical cyclones.
- Zick, S. E., and C. J. Matyas, 2016: A shape metric methodology for studying the evolving geometries of synoptic-scale precipitation patterns in tropical cyclones. *Annals of the American Association of Geographers*, **106** (6), 1217–1235.
- Zipser, E., 1977: Mesoscale and convective-scale downdrafts as distinct components of squall-line structure. *Monthly Weather Review*, **105** (12), 1568–1589.